UNIVERSITY OF OKLAHOMA

GRADUATE COLLEGE

THE BOOTSTRAP DUAL POLARIMETRIC SPECTRAL DENSITY ESTIMATOR

A THESIS

SUBMITTED TO THE GRADUATE FACULTY

in partial fulfillment of the requirements for the

Degree of

MASTER OF SCIENCE

By

ARTURO YOSHIYUKI UMEYAMA MATSUMOTO
Norman, Oklahoma
2016

THE BOOTSTRAP DUAL POLARIMETRIC SPECTRAL DENSITY ESTIMATOR

A THESIS APPROVED FOR THE
SCHOOL OF ELECTRICAL AND COMPUTER ENGINEERING

BY

Dr. Robert Palmer, Chair

Dr. Sebastián Torres

Dr. Boon Leng Cheong

Dr. Caleb Fulton

Dr. Tian-You Yu

© Copyright by ARTURO YOSHIYUKI UMEYAMA MATSUMOTO 2016
All Rights Reserved.

Acknowledgments

I would like to thank my advisors, Dr. Sebastián Torres, and Dr. Boon Leng Cheong, for their excellent mentoring, guidance and constant support. I appreciate the time and effort they dedicated to ensure my academic, professional, and personal success. Thanks to Dr. Robert Palmer, Dr. Caleb Fulton and Dr. David Bodine, with whom I worked under the NSF Debris project, for providing insightful comments on my research. Special thanks to Dr. Palmer and Dr. Torres for encouraging me to pursue other research experiences, and to Dr. Cheong for training me and allowing me to participate in the development of SimRadar. I would also like to thank Dr. Tian-You Yu for making his time and effort available to become a member of the thesis committee. Additional thanks to my friends for making being away from home a blissful experience. And last but not least, I am forever grateful to my family, especially my parents, for always encouraging me to take the next step, and for enabling me to continue my graduate education abroad.

This work was supported by the National Science Foundation under research grant AGS-1303685.

Table of Contents

List Of Tables

List Of Figures

Abstract

Weather radar moments and polarimetric variables provide useful information about the characteristics and motion of hydrometeors. However, the bulk information may be masked when the meteorological signal of interest is contaminated by clutter. The dual-polarimetric spectral densities (DPSD) may unveil additional information about the polarimetric characteristics of groups of scatterers moving at different Doppler velocities in a given radar resolution volume. Previous DPSD estimation methods required averaging a large number of spectra (obtained from different range gates, radials, or scans), or averaging in frequency to get accurate estimates; though by doing so, the resolution is degraded, and important features of the meteorological phenomenon may be masked, potentially affecting the ability to perform a good spectral analysis. In an attempt to overcome these limitations, the Bootstrap DPSD estimator is developed, which allows the estimation of DPSDs from a single dwell, with minimal resolution loss. Briefly, the estimator pre-processes the weather radar I/Q time-series signals and generates I/Q pseudo-realizations through bootstrap resampling, which are then used to compute PSD estimates that are averaged to obtain the DPSD estimate. Then, a post-processing stage applies a bias correction to the estimates. The Bootstrap DPSD estimator's performance is compared to that of conventional methods for single-dwell as well as for multiple-dwell estimates. Additionally, the performance and limitations of the Bootstrap and conventional DPSD estimators are assessed when identifying signals of different polarimetric signatures

of scatterers moving at different radial velocities in the radar volume. The advantages of the Bootstrap DPSD estimator as a tool for polarimetric spectral analysis is demonstrated with a few examples of polarimetric spectral signatures in data from tornado cases, and from a physically-based simulator. It is expected that, with the Bootstrap DPSD and polarimetric spectral analysis, it will be possible to better understand tornado dynamics and their connection to weather radar measurements, as well as to elucidate important scientific questions that motivated this work.

Chapter 1

Introduction

A summary of natural hazard statistics for the year 2013 by the National Weather Service registered the fatalities, injuries and damages caused by severe weather (NCDC 2014). Among the different weather events, tornadoes were responsible for: 55 fatalities accounting for 12.33% of the total coming in 4th place, 756 injuries for 27.33% of the total - 2nd place, and $3,642.18 million in property damage for 41.34% of the total - 1st place. These statistics highlight the potential impacts of tornadoes, which are one of the greatest weather-related threats to life and property in the U.S. Part of these tornado-related fatalities are victims struck by airborne debris (Bohonos and Hogan 1999), which can also inflict major structural damage and increase the damage potential of the tornado as they are lofted along (Marshall 2002). Therefore, they are important in the study of tornadoes.

Continuous efforts have been led by the scientific community to improve the knowledge about tornadoes with the goal of increasing their predictability and to mitigate consequences. Despite this, many aspects of tornado mechanics are still not completely understood (Cheong et al. 2015). In this context, weather radars have proven to be an essential tool in tornado studies as their remote sensing capability allows retrieving information in a way that would otherwise be extremely difficult

and dangerous. Furthermore, advances in weather radar technology have played a critical role by providing better measurements of the underlying phenomena.

The first meteorological application of a pulsed-Doppler radar was made in the 1950's, and since then it has become increasingly important for remote measurements of precipitation (Doviak and Zrnić 2006). However, it was not until the 1970's that tornadoes were observed with pulsed-Doppler weather radar (Zrnić and Doviak 1975). The discovery of the tornadic vortex signature (TVS) (Brown et al. 1978), which is a pattern of tornado formation before it is visible on the ground, suggested a potential for improved warning for severe weather. This eventually led to the nationwide deployment of a pulsed-Doppler weather radar (WSR-88D) network as a joint effort of the U.S. Departments of Commerce (DOC), Defense (DOD), and Transportation (DOT) –the NEXRAD (Crum and Alberty 1993). The original WSR-88D network provided three main radar variables: radar reflectivity factor (Z), mean radial velocity ($\bar{v}_{\mathrm{r}}$), and spectrum width (σ_v). By 2013, the WSR-88D network was upgraded to dual polarization, which provides new information about the scatterers within the radar resolution volume through an additional polarization channel (Doviak et al. 2000). With the simultaneous transmission and reception of the H- and V-polarized waves, three additional polarimetric products were made available: differential reflectivity (Z_{DR}), correlation coefficient (ρ_{HV}), and differential phase (ϕ_{DP}). Consequently, discrimination of meteorological and non-meteorological scatterers was possible, with potential application in tornado detection (Ryzhkov et al. 2005).

In light of the improved observation capabilities introduced by polarimetric radar measurements, the detection of tornadic debris signatures (TDS) was possible (Ryzhkov et al. 2005). TDS are tornado-scale signatures with distinctive polarimetric characteristics collocated near a tornado vortex that are visible in radar observations after a tornado touches ground (Ryzhkov et al. 2002), that is related to the ejection and centrifuging of hydrometeors and debris by the cyclone (Dowell et al. 2005). Since debris lofted by tornadoes can have polarimetric signatures that depend on their electrical size, shape, orientation and concentration (Bodine 2014), these signatures can be noticeably different from those of hydrometeors and can be used for polarimetric tornado detection (Ryzhkov et al. 2005). Additionally, they are clear indicators of tornadoes when ground observation is limited or impossible (e.g., at night or during heavy rainfall) (Kumjian and Ryzhkov 2008). A set of values typically found to be associated with TDS is suggested in Ryzhkov et al. (2005) and Bodine et al. (2013), though it is still unknown exactly how the characteristics of different debris types affect different polarimetric radar measurements.

Nevertheless, in recent years, research on TDS has shown promising results in different applications. Schultz et al. (2012*a*) and Schultz et al. (2012*b*) explore the use of TDS as a tool for forecasters to improve the warning decision-making process and to assess the potential threat of a tornado in a near-real time operational environment, while Scharfenberg et al. (2005) reported TDS were used to enhance the confidence of tornado detection. TDS may also provide information about the damage potential and the intensity of a tornado (Bodine et al. 2013). Several studies (Ryzhkov et al. 2005; Bluestein et al. 2007; Bodine et al. 2011) have shown evidence

of negative $Z_{\rm DR}$ values in TDS from different tornado cases, suggesting a possible common alignment of the debris within the tornadic vortex, or a scattering in the Mie regime due to large debris. In Bodine et al. (2014), a statistical analysis of TDS is performed using dual-frequency observations in an attempt to better characterize debris scattering and polarimetric signatures. Logically, important scientific questions about the dynamics of a tornado, and the relationship between them and the radar measurements arise: How do tornado dynamics affect debris centrifuging? How does the centrifuging of tornadic debris vary for debris with different characteristics? How do the size and concentration of lofted debris relate to tornado intensity and damage severity and extent? What causes negative $Z_{\rm DR}$ in tornadoes? The answers to these questions could provide a better understanding of tornadoes, which would potentially aid in the nowcasting and detection of imminent threats, as well as to provide better near real-time estimation of the tornado intensity and damage severity and extent. However, any attempt to exploit the advantages of the TDS detection will come with its challenges.

While TDS can be helpful in the detection of tornadoes (Scharfenberg et al. 2005; Schultz et al. 2012*a*,*b*), there are clear limitations when assessing tornado intensity through radar observations, and thus it is still a topic of much ongoing research. One such limitation is due to the effects of centrifuging, which causes hydrometeors and debris to move at slightly different velocities within a tornado vortex. In addition, Doppler radars measure the scatterers' motion rather than the actual wind speed and as such, significant biases can be introduced in wind radar measurements (Dowell et al. 2005). This can occur whether the signal scattered

by debris is stronger than that of hydrometeors or vice versa. Moreover, TDS are more likely to be seen in observations due to the debris signal power dominating in a particular radar resolution volume (Ryzhkov et al. 2005), thus measurements of mean radial velocity in volumes with TDS are more prone to centrifuging bias. Hypothetically, this error in measurement can be corrected if the velocity of the debris is known and can be separated from the velocity of hydrometeors which passively trace the wind. Since the radar variables are computed by averaging the contribution of all scatterers within a radar resolution volume, an alternative way to retrieve the velocities must be employed. This can be achieved through spectral analysis.

The power spectral density (PSD) of weather radar signals is the power-weighted distribution of the radial velocities in a radar resolution volume (Doviak and Zrnić 2006). In a PSD, the power return of scatterers moving at different Doppler velocities within a given resolution volume is shown. Janssen and Van Der Spek (1985) found that approximately 75% of the spectra observed with a phased array system from precipitation at close ranges were Gaussian-shaped. For the other 25% of the cases with non-Gaussian spectra, spectral analysis can provide important information about the distribution of radial velocities in the radar resolution volume (Yu et al. 2009). When assuming a Gaussian distribution, however, spectral analysis is only useful when there is a multimodal signal composition, with each scatterer group having its own velocity in the resolution volume; i.e., more than one peak in the PSD. In the case where the weather signal is mixed with ground clutter, the spectra will show the distribution of both signals as a function of their Doppler velocities with

two peaks corresponding to each type of scatterer, where the ground clutter signal is at zero and the weather signal can be moving at any Doppler velocity (Doviak and Zrnić 2006). Provided that the weather signal does not have a zero mean velocity, the ground clutter can be filtered from the spectra without significantly corrupting the weather signal (Torres and Zrnić 1999). In the cases where the signals overlap in the spectra, techniques have been developed to mitigate the clutter influence and reconstruct the weather signal to provide better radar estimates (Cao et al. 2012; Torres and Warde 2014). However, it is difficult to discriminate the nature of the non-static scatterers contained in the spectra since the peaks in a PSD do not contain any information other than the power returns and their velocity towards the radar. Without further information about the distribution of scatterers, any attempt to classify them would be difficult.

Additional spectral information can be gathered from the dual polarimetric spectral densities (DPSD). The DPSD depicts the polarimetric characteristics of scatterers moving at different Doppler velocities within a radar resolution volume. These tools for polarimetric spectral analysis provide three additional spectral variables: the spectral differential reflectivity (sZ_{DR}), the spectral correlation coefficient ($s\rho_{\mathrm{HV}}$), and the spectral differential phase ($s\phi_{\mathrm{DP}}$). Although a universal definition of the spectral polarimetric variables has not been established, the term DPSD used herein can refer to any one spectral polarimetric variable or a set of them. Provided that the polarimetric characteristics of the scatterers are known, it is hypothesized that discrimination of scatterer type in the spectra would be possible by correlating the DPSD values to known polarimetric characteristics of different scatterer types,

though identification and characterization of all scatterers in the volume would not be possible.

Previous work in DPSD have used different methods for their estimation as well as other spectral variables. Some works have dealt with classification of scatterers to filter out non-meteorological targets. In Bachmann and Zrnić (2007), different biological scatterers were discriminated using Daniell's method to estimate the PSD, which is a three-point moving average filter on the power spectra estimate, and averaging over several adjacent range gates. Additionally, an enhanced version of the velocity-azimuth display (VAD), the spectral VAD was explored, showing promising results for separating bird and insect flight speeds. In Moisseev and Chandrasekar (2009), a filter for adaptive clutter and noise suppression based on the spectral polarimetric variables was presented. This work used additional spectral variables such as textures of spectral differential reflectivity and spectral differential phase. The spectra were averaged in range to reduce the variance of spectral estimates. Alku et al. (2015) expanded on Moisseev and Chandrasekar (2009) by proposing the classification of a wide variety non-meteorological echoes based on thresholds set by the DPSD values and strategies to mitigate such signal contaminants. The spectra were estimated by averaging over four range gates. In a similar application, Unal (2009) studied the use of the spectral linear depolarization ratio and found improved measurements of atmospheric returns. The DPSD was estimated using time averaging of up to 40 spectra, for an observation time of 1 minute. Other works used DPSD estimates to study the microphysics and dynamics of weather

events. Yanovsky (2011) studied the retrieval of microphysical and turbulence characteristics of rain using phenomenological models and through the analysis of the spectral differential reflectivity and spectral linear depolarization ratio. Here, the DPSD were estimated with spectra averaged in time over an observation time of 15 minutes. Dufournet (2010) and Spek et al. (2008) assessed the retrieval of ice and mixed-phase cloud microphysics characteristics using models for ice particles with spectral differential reflectivity, spectral linear depolarization ratio and spectral correlation coefficient. The spectra were averaged in time to obtain the DPSD using 10 observations. Moisseev et al. (2006) and Moisseev and Chandrasekar (2007), retrieved the drop-size distribution (DSD) through the spectral differential reflectivity using the average of independent simulated spectra. Yu et al. (2013) analyzed a hailstorm at a low elevation angle using spectral polarimetry to verify shear-induced size sorting mechanisms, which was further validated with simulations. Finally, there is only one work in the literature that studies the quality of the DPSD estimates. In Yu et al. (2012), a much needed, thorough analysis of the statistical quality of the spectral polarimetric variables was performed, yielding the number of independent observations needed to ensure the errors of the polarimetric variables are within the desired limits. It is important to note that all of these studies have used, in one way or another, the averaging of the PSD to obtain the DPSD estimate. In this study, focus is directed to the spectral differential reflectivity and the spectral correlation coefficient, while the spectral differential phase is not analyzed because it may not convey as much information to discriminate hydrometeors from debris.

While the idea of analyzing the spectral signatures of TDS –whether it is for a better characterization of the scattering properties of debris or to discriminate debris from hydrometeors in the spectra– might seem simple at first, there are many constraints that prevent an adequate analysis. The main limitation for a polarimetric spectral analysis for tornado observations is the large amount of independent observations needed to achieve the required accuracy and precision, shown in Yu et al. (2012) as approximately 20 independent observations to achieve optimal statistical quality. Currently, the operational WSR-88D can provide one scan for an elevation angle every few minutes (Crum and Alberty 1993). It is essential to average more than one spectra to get useful DPSD estimates. Furthermore, it is easy to show that with one independent observation the estimator fails to yield useful results for the spectral correlation coefficient. To account for this limitation, additional data may be obtained from adjacent gates in radial, range, different dwells, or even by smoothing the spectral estimates, but they ultimately end up reducing the spatial, time, or frequency resolution, and thus far, an optimal solution to this problem has not been proposed in the previous literature. Since tornadoes are events that evolve fast in time, in a relatively small spatial extent, with different scatterers contained within the tornadic vortex (Bodine et al. 2013), it is in our interest to preserve the best resolution possible in all dimensions.

To overcome these constraints, a new estimator of the DPSD is developed. In this work, the Bootstrap DPSD estimator is presented, which accounts for the aforementioned limitations and computes the DPSD using one dwell with minimal resolution

loss. In Chapter 2, the concepts of polarimetric radar I/Q time-series signal processing, TDS, spectral analysis and estimation of spectral variables are presented. Also, an assessment of the advantages and limitations of currently available methods of PSD and DPSD estimation is included. A complete description of the fundamental concepts and considerations taken in the design of the Bootstrap DPSD estimator is presented in Chapter 3. Thorough analysis of the quality of the Bootstrap DPSD estimator under different scenarios by comparing the ideal and conventional methods are presented in Chapter 4. Chapter 5 shows the results of using the Bootstrap DPSD estimator on data sets of real weather events, and data obtained from simulations of hydrometeors and debris in a tornado vortex from a physical polarimetric radar time-series simulator (Cheong et al. 2015). Finally, concluding remarks and recommendations for future work are presented in Chapter 6.

Chapter 2

Background

The context of the problem, as established in Chapter 1, would be incomplete without a detailed description of the concepts. This chapter synthesizes the fundamental theory required to properly understand the problem. In Section 2.1, the basics of the polarimetric weather radar time-series signal processing are presented. A description of the TDS and a hypothesis about their spectral polarimetric characteristics are presented in Section 2.2. Section 2.3 presents methods to estimate the PSD and assesses the advantages and limitations of each method. Section 2.4 focuses on DPSD estimators in a similar manner. This chapter concludes with a summary highlighting key aspects of each section.

2.1 Polarimetric Radar Signal Processing

A complete review on the principles of Doppler weather radar can be found in Doviak and Zrnić (2006), and with additional details on polarimetric Doppler weather radars in Bringi and Chandrasekar (2001). This section will focus on the signal processing aspects of a polarimetric radar.

2.1.1 I/Q Time-Series Signals

As the radar sends out a pulse of electromagnetic waves, energy is radiated to the scatterers along the path which reflect a portion of this energy back to the radar. A weather signal is composed of the returns of a large number of hydrometeors in a sub-volume of the atmosphere. Since the individual returns cannot be resolved, the weather signal is sampled at discrete range-time delays with the use of gating circuits which convert the analog backscattered returns to digital numbers. The range gates define the approximate range of a resolution volume in space where the scatterers have the largest contribution to the weather signal sample. The resolution volume is determined by a range weighting function related to the radar filter's amplitude response and the transmitted pulse envelope, and an angular weighting function related to the antenna's radiation pattern. The echoes of each scatterer in the resolution volume add constructively or destructively (depending on their position within a wavelength) producing a composite complex voltage sample (Figure 2.1). For a particular range time delay τ_s and the m-th transmitted pulse this is

$$V(\tau_s, mT_s) = \sum_{i=0}^{N-1} A_i e^{-j\gamma_i}, \tag{2.1}$$

$$\gamma_i = \frac{4\pi r_i}{\lambda} + \frac{4\pi v_i T_s}{\lambda} - \psi_{si}, \tag{2.2}$$

where A_i is the amplitude of the i-th scatterer, r_i is the range to the scatterer, λ is the radar wavelength, v_i is the radial velocity of the scatterer, T_s is the pulse repetition time (PRT), ψ_{si} is the phase shift imposed by the i-th scatterer, and N

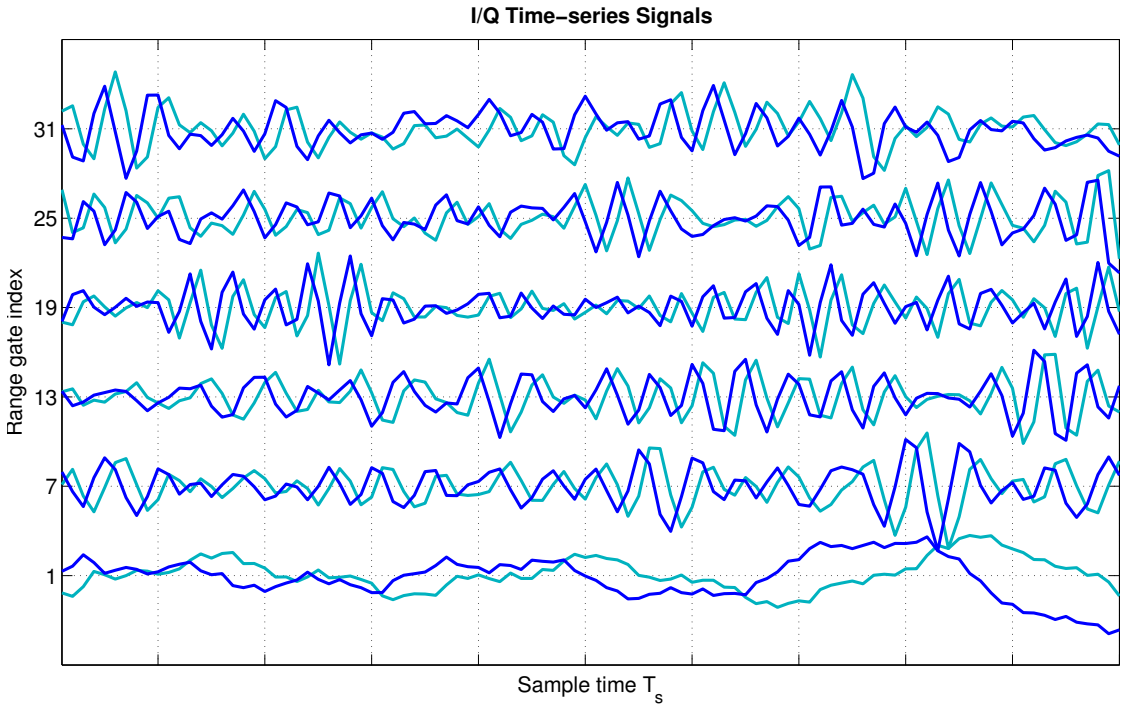

Figure 2.1: I/Q signals for different range gates as a function of sample time T_s, with $I(m)$ shown in blue and and $Q(m)$ shown in cyan.

is the total number of scatterers. The amplitude of each scatterer is related to the radar constants and the backscattering cross section (σ_b) by:

$$A_i \propto \sqrt{\frac{P_\mathrm{t}\sigma_\mathrm{b}}{(4\pi)^3}}\frac{\lambda g}{r^2}W_\mathrm{a}W_\mathrm{r}, \tag{2.3}$$

where P_t is the peak transmitted power, σ_b is the backscattering cross section of the scatterer, g is the antenna gain, W_a is a weighting function due to the antenna pattern, and W_r is a range-weighting function. Alternatively, for a given range resolution volume,

$$V(m) = I(m) + jQ(m), \tag{2.4}$$

$$I(m) = \sum_{i=0}^{N-1} |A_i| \cos\gamma_i, \tag{2.5}$$

$$Q(m) = -\sum_{i=0}^{N-1} |A_i| \sin \gamma_i, \tag{2.6}$$

represent the I/Q signal, for a dwell defined by M consecutive pulses as $m = 0, \ldots, M-1$. Hereafter, the range time delay and the pulse repetition time shall be ignored for the sake of simplicity.

2.1.2 Polarimetric Radar Variables

Typical radar moments that can be estimated from the I/Q signals are: reflectivity factor (Z), mean radial velocity ($\bar{v}_r$), and spectrum width (σ_v). Also, with the simultaneous transmission and reception of H- and V-channel polarized waves (with the WSR-88D), polarimetric radar variables can be estimated, providing more information about the scatterers in a radar resolution volume; these are: differential reflectivity (Z_{DR}), magnitude of the lag-0 cross-correlation coefficient (ρ_{HV}, herein referred to as the correlation coefficient), and differential phase (ϕ_{DP}). The polarimetric I/Q signals shall be represented as

$$V_{\mathrm{H,V}}(m) = I_{\mathrm{H,V}}(m) + jQ_{\mathrm{H,V}}(m). \tag{2.7}$$

Weather radar signals can be considered to be stationary processes because no significant changes in the statistical properties occur during the short observation time of tens of milliseconds; also, they are assumed to be ergodic, i.e., the statistical properties of the ensemble can be inferred from sample-time averages. Furthermore, since they are random in nature, to make inferences about the properties of the

received signals, we must rely on estimating average statistical parameters. We recall the autocorrelation function of a stationary process $V(m)$ which is defined as: (Doviak and Zrnić 2006)

$$R_{\mathrm{H,V}}(l) = E[V^*_{\mathrm{H,V}}(m)V_{\mathrm{H,V}}(m+l)] = \lim_{M\to\infty} \frac{1}{M} \sum_{m=0}^{M-|l|-1} V^*_{\mathrm{H,V}}(m)V_{\mathrm{H,V}}(m+l), \quad (2.8)$$

where l is the time lag, with H or V indicating the polarization channel. Because there is a finite number of samples, only an estimate of the autocorrelation function can be obtained as

$$\hat{R}_{\mathrm{H,V}}(l) = \frac{1}{M-|l|} \sum_{m=0}^{M-|l|-1} V^*_{\mathrm{H,V}}(m)V_{\mathrm{H,V}}(m+l), \quad (2.9)$$

for $|l| \leq M-1$, which is the unbiased autocorrelation function estimator. An estimate of the average returned power can be obtained from the autocorrelation function at lag 0 as

$$\hat{R}_{\mathrm{H,V}}(0) = \frac{1}{M} \sum_{m=0}^{M-1} V^*_{\mathrm{H,V}}(m)V_{\mathrm{H,V}}(m) = \hat{P}_{\mathrm{H,V}}. \quad (2.10)$$

By subtracting the noise power N, an estimate of the signal power can be obtained as

$$\hat{S}_{\mathrm{H,V}} = \hat{P}_{\mathrm{H,V}} - N_{\mathrm{H,V}}. \quad (2.11)$$

Also, an estimate of the autocorrelation function at lag 1 ($l = 1$) is used for calculating estimates of the mean velocity and spectrum width using the autocovariance estimator (as will be shown later), which can be computed as

$$\hat{R}_{\mathrm{H}}(1) = \frac{1}{M-1} \sum_{m=0}^{M-2} V_{\mathrm{H}}^{*}(m) V_{\mathrm{H}}(m+1). \tag{2.12}$$

Additionally, the cross-correlation between the H- and V-channel signals is represented as

$$\hat{R}_{\mathrm{X}}(l) = \frac{1}{M-|l|} \sum_{m=0}^{M-|l|-1} V_{\mathrm{H}}^{*}(m) V_{\mathrm{V}}(m+l). \tag{2.13}$$

Brief descriptions of the polarimetric radar variables and their estimators are given next.

The general radar terminology for the backscattering cross section per unit volume is reflectivity (η), and it is important to relate this measure to factors that have meteorological significance. If the raindrops are spherical and have small diameters compared to the radar wavelength, the radar reflectivity is related to the reflectivity factor (Z) by (Doviak and Zrnić 2006)

$$\eta = \frac{\pi^5}{\lambda^4} |K_{\mathrm{w}}|^2 Z, \tag{2.14}$$

where K_{w} is the dielectric factor for water. The reflectivity factor measures of the power returned from the scatterers in a radar resolution volume for a given dwell

and it is typically used, along with an assumed DSD, to estimate the rainfall rate and the liquid water content. The reflectivity factor can be estimated as

$$\hat{Z}_{\mathrm{H}} = 10 \log \hat{S}_{\mathrm{H}} + 20 \log r + 10 \log C, \tag{2.15}$$

in dBZ, ignoring any losses, where r is the range to the radar volume and C is a constant that depends on characteristics of the radar system such as the wavelength, transmitted power, pulse-width, antenna gain, and antenna weighting patterns, as well as the dielectric factor of the hydrometeor, and other scaling factors. The reflectivity factor is related to the physical properties of the scatterers, so, high returns are expected for higher concentration of particles and larger electrical sizes.

The mean radial velocity ($\bar{v}_r$) is the power-weighted average of the radial velocities of the scatterers in the radar resolution volume. It can be estimated using the autocovariance estimator (Doviak and Zrnić 2006) as

$$\hat{v}_{\mathrm{r}} = -\frac{v_{\mathrm{a}}}{\pi} \arg(\hat{R}_{\mathrm{H}}(1)), \tag{2.16}$$

where v_a is the radar's maximum unambiguous velocity, the argument of $\hat{R}_{\mathrm{H}}(1)$ is in radians and $\hat{v}_r$ is in m/s. The radar's maximum unambiguous velocity is the maximum range of radial velocity that can be observed by a Doppler radar and is related to the radar's wavelength and PRT by

$$v_a = \pm \frac{\lambda}{4T_{\mathrm{s}}}. \tag{2.17}$$

The spectrum width (σ_v) is a measure of the spread of the radial velocities about the mean, and it is a function of radar system parameters such as beamwidth, bandwidth, and pulse width, and the meteorological parameters that describe the distribution of hydrometeor density and velocity within the resolution volume (Doviak and Zrnić 2006). There are many mechanisms that can broaden the spectrum width. Meteorological factors include turbulence and wind shear, which can cause relative motion of the scatterers in the volume. Antenna rotation can additionally broaden the spectrum width as the location of the resolution volume changes from pulse to pulse causing a decorrelation of signal samples and subsequent increase in spectrum width. Additionally, depending on the data window used in spectral processing, the spectrum width may also vary. More aggressive windows have wider main lobe width, resulting in broader spectrum widths than with less aggressive windows. The spectrum width can be simply estimated as

$$\hat{\sigma}_v = \frac{\sqrt{2}v_{\mathrm{a}}}{\pi}\sqrt{\left|\ln\left(\frac{\hat{S}}{|\hat{R}(1)|}\right)\right|}. \tag{2.18}$$

However, NEXRAD uses a hybrid spectrum width estimator (Meymaris et al. 2009) that uses the lags 0/1, 1/2, and 1/3 estimators for wide, medium, and narrow spectrum widths, respectively.

The differential reflectivity Z_{DR} is the ratio of the power in the H-channel to the V-channel and it provides an insight about the shape of the scatterers. It can be estimated as

$$\hat{Z}_{\mathrm{DR}} = 10\log\left(\frac{\hat{S}_{\mathrm{H}}}{\hat{S}_{\mathrm{V}}}\right). \tag{2.19}$$

Small raindrops are typically spherical in shape and have a Z_{DR} of zero due to the power returns in both channels being equal. Larger raindrops tend to become more oblate in shape, corresponding to the horizontal backscattered power being larger than the backscattered power in the vertical channel, and result in a positive Z_{DR}. Other hydrometeors, such as ice crystals, can have a prolate shape, producing the opposite effect and thus having a negative Z_{DR} (Bringi and Chandrasekar 2001). The Z_{DR} of debris can largely depend on its electrical properties, orientation, size and concentration and it can vary in a wide range (Bringi and Seliga 1977).

The correlation coefficient ρ_{HV} is a measure of how similar the H-channel voltage return is, in average, to the V-channel return. Therefore, it is a measure of the homogeneity of the returns from scatterers in the radar volume. To estimate the correlation coefficient, the cross-correlation function between the H- and V-channels at lag 0 is obtained from (2.13), then

$$\hat{\rho}_{\mathrm{HV}} = \frac{|\hat{R}_{\mathrm{X}}(0)|}{\sqrt{\hat{S}_{\mathrm{H}}\hat{S}_{\mathrm{V}}}}. \tag{2.20}$$

The returns in the H- and V-channels for any set of homogeneous scatterers will have a high ρ_{HV} (e.g., only raindrops). When the voltage returns from different types of scatterers are mixed (e.g., hydrometeors and debris), the scattering can become less homogeneous, resulting in a lower ρ_{HV}.

The differential phase ϕ_{DP} is defined as the backscattered differential phase between the voltage returns from the H- and V-channels (from the scatterers in the

resolution volume) and propagation differential phase (from the path the pulse travelled). It can be estimated using the cross-correlation function between the H- and V-channels at lag 0 as

$$\hat{\phi}_{\mathrm{DP}} = \arg\left(\frac{\hat{R}_{\mathrm{X}}(0)}{\sqrt{\hat{S}_{\mathrm{H}}\hat{S}_{\mathrm{V}}}}\right). \tag{2.21}$$

The differential phase is a measure of the resistance experienced by the electromagnetic waves as they travel through the atmosphere (Kumjian 2013). For example, waves traveling through a spherical scatterer would experience the same amount of resistance in both polarization channels ($\phi_{\mathrm{DP}} = 0°$), while non-spherical scatterers would experience a positive difference if they are oblate ($\phi_{\mathrm{DP}} > 0°$) and a negative difference if they are prolate ($\phi_{\mathrm{DP}} < 0°$). It also provides an insight about the concentration of the scatterers, as it is proportional to the number concentration of particles and tends to increase with increasing particle size (Kumjian 2013).

2.1.3 Spectral Analysis

In addition to the radar moments and polarimetric radar variables, there are tools which provide information about the Doppler velocities of the scatterers within a radar resolution volume. Hereafter, the term 'bulk' will be used to simply refer to both radar moments and polarimetric variables, and to distinguish them from the spectral variables. The power spectral density (PSD) represents the power-weighted distribution of radial velocities of the scatterers within a resolution volume (Doviak and Zrnić 2006). The Wiener-Khinchin theorem states that if a process is wide-sense

stationary, the autocorrelation function and the PSD form a Fourier transform pair (Papoulis and Pillai 2002). The PSD is defined as

$$sS_{\mathrm{H,V,X}}(kf_0) \equiv \lim_{M\to\infty} T_s \sum_{l=-(M-1)}^{M-1} R_{\mathrm{H,V,X}}(l) e^{-j2\pi k f_0 T_s l}, \tag{2.22}$$

where $f_0 = 1/MT_s$, and $k = 0, \ldots, M-1$ is the spectral component index. The preceding s denotes spectral variables as opposed to bulk variables, and hereafter, f_0 will be omitted for simplicity. Methods to estimate the PSD will be presented in Section 2.3.

In a similar way, the DPSD represents the distribution of the polarimetric variables as a function of the radial velocities of the scatterers within a resolution volume. For example, the spectral differential reflectivity is the extension of the differential reflectivity in the frequency domain. It is defined as the ratio between the horizontal PSD sS_{H} and the vertical PSD sS_{V}:

$$sZ_{\mathrm{DR}}(k) = \frac{sS_{\mathrm{H}}(k)}{sS_{\mathrm{V}}(k)}. \tag{2.23}$$

The spectral correlation coefficient and the spectral differential phase are likewise defined using the corresponding PSDs instead of the polarimetric radar variables. This is,

$$s\rho_{\mathrm{HV}}(k) = \frac{|sS_{\mathrm{X}}(k)|}{\sqrt{sS_{\mathrm{H}}(k) sS_{\mathrm{V}}(k)}}, \tag{2.24}$$

$$s\phi_{\mathrm{DP}}(k) = \arg\left(\frac{sS_{\mathrm{X}}(k)}{\sqrt{sS_{\mathrm{H}}(k) sS_{\mathrm{V}}(k)}}\right). \tag{2.25}$$

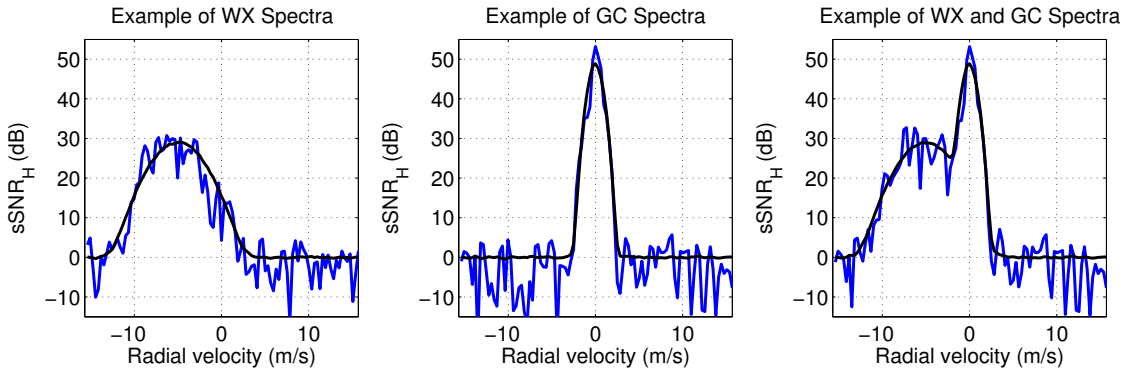

Figure 2.2: Power spectral densities of typical signals. Weather (WX, left), ground clutter (GC, center), weather and ground clutter (right). The PSDs correspond to returns from the H channel and are normalized to the noise power. Hence, the y-axis represents signal-to-noise ratio in the H channel ($s\mathrm{SNR}_\mathrm{H}$).

The DPSD estimators will be presented in Section 2.4.

To highlight the importance of spectral analysis in weather radar signal processing, typical signatures found in observations are briefly discussed. Referring to Figure 2.2, the power spectrum of weather is Gaussian-like with relatively wide spectrum width and power that depends on the strength of the echoes and the radar sensitivity (Zrnić 1975). For ground clutter, the power spectrum is also Gaussian-like with narrow spectrum width, relatively high power, and centered at $v_\mathrm{r} = 0$ m/s (Doviak and Zrnić 2006). If the resolution volume contains weather but is contaminated by ground clutter, the spectrum will be a combination of both.

For a single signal in the resolution volume (i.e., either weather only or ground clutter only) and with the assumption of a Gaussian model, spectral analysis does not provide additional information about the scatterers since the estimates of the radar variables already reflect this. However, for a composite signal, the radar variables are biased (e.g., they can be skewed towards the dominant signal). In the case where the ground clutter signal is completely dominant over the weather

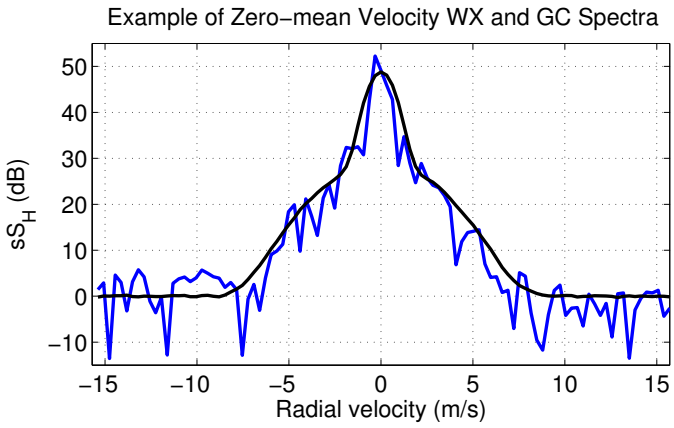

Figure 2.3: Power spectrum of zero mean radial velocity weather mixed with ground clutter.

signal, information about the hydrometeors will be lost. With spectral analysis, the signals can be separated with minimal biases introduced in the radar estimates. Even in the case where the weather signal has a zero mean radial velocity and it is mixed with a ground clutter signal (Figure 2.3), information about the weather signal can still be extracted because the ground clutter signal is spectrally narrower. The separation of a ground clutter signal from others is relatively easy because of the distinct characteristics seen in the power spectra, namely, the high power return, the narrow spectrum width and a mean radial velocity about zero. However, when dealing with groups of scatterers move independently with different radial velocities, it becomes harder to separate them in the PSD alone because of the lack of information to distinguish them from one another, as is the case in resolution volumes with hydrometeors and debris. In such cases, the DPSDs provide additional spectral information that could be used to identify groups of scatterers moving with different radial velocities that have distinct polarimetric characteristics. It is

hypothesized that these type of spectra could be found near TDSs, which is discussed next.

2.2 Tornadic Debris Signatures

As mentioned previously, TDS are tornado-scale signatures with distinctive polarimetric characteristics collocated near a tornado vortex that are visible in radar observations (Figure 2.4) after a tornado touches ground (Ryzhkov et al. 2002). It is hypothesized that they are related to the lofting, ejection and centrifuging of debris by the tornado vortex (Dowell et al. 2005). Since debris have polarimetric signatures that depend on their electrical size, shape, orientation and concentration (Bodine 2014), these signatures can be noticeably different from those of hydrometeors and can be used for polarimetric tornado detection (Ryzhkov et al. 2005). In addition, they improve the detection of tornadoes (Wang and Yu 2015) when ground observation is limited or impossible (e.g., at night or during heavy rainfall) (Kumjian and Ryzhkov 2008).

Due to centrifuging in a tornado vortex, debris move at different velocities than hydrometeors. Since Doppler radars measure the mean scatterers motion rather than the actual wind speed, significant biases can be introduced in the radar measurements (Dowell et al. 2005). This can occur whether the debris signal is stronger than the weather signal or not. To effectively assess the potential damage (Bodine et al. 2013), it is important to have accurate measurements to estimate the intensity of the tornado. Ryzhkov et al. (2005) catalogued typical values of the polarimetric

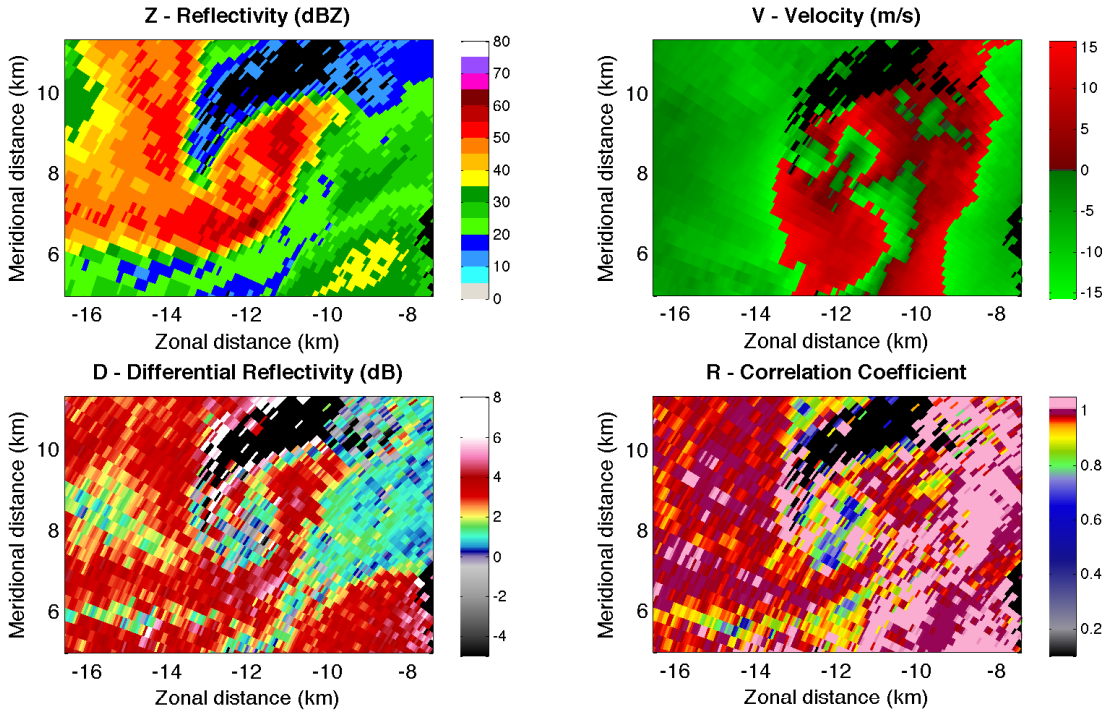

Figure 2.4: Tornadic debris signatures in observations of 20 May 2013 Moore, OK tornado at 20:04:03 UTC with the PX-1000 radar. Reflectivity factor Z_{H} (top left), mean radial velocity $\bar{v}_{\mathrm{r}}$ (top right), differential reflectivity Z_{DR} (bottom left), correlation coefficient ρ_{HV} (bottom right).

radar variables associated to the TDS as $Z > 45$ dBZ, $Z_{\mathrm{DR}} < 0.5$ dB, and $\rho_{\mathrm{HV}} < 0.8$, while Bodine et al. (2013) use more stringent sets of values for Z and ρ_{HV}: either $Z < 43$ dBZ and $\rho_{\mathrm{HV}} < 0.82$, or $Z < 51$ dBZ and $\rho_{\mathrm{HV}} < 0.72$. With these criteria, it can be inferred that TDS are more likely to be seen in observations due to the debris signal dominating in a particular radar resolution volume (Ryzhkov et al. 2005), thus the mean radial velocities in volumes with TDS are more prone to centrifuging biases. Furthermore, it is hypothesized that this error in measurement can be corrected if the velocity of the debris is known and can be separated from the velocity of hydrometeors, which are passive tracers of the wind. It is argued in this work that such information could be retrieved through spectral analysis.

With a Gaussian assumption, the PSD does not provide additional information if there is only one type of scatterer in the radar resolution volume. In the case where there is more than one type of scatterer, discrimination might be possible provided that neither signal is completely obscuring the other signal. However, the additional information provided by the DPSD is needed to appropriately classify the signals. Because the DPSD shows the distribution of polarimetric variables as a function of the radial velocities, it may be possible to determine the type of the scatterers by correlating the DPSD values to known polarimetric characteristics of the different groups of scatterers. However, identification of all scatterer types would be impossible.

As an example, a sketch of a bimodal DPSD for a combination of weather and debris signals is shown in Figure 2.5 (Cheong et al. 2015). The representation of the spectral variables of debris may be exaggerated, but it illustrates a possible

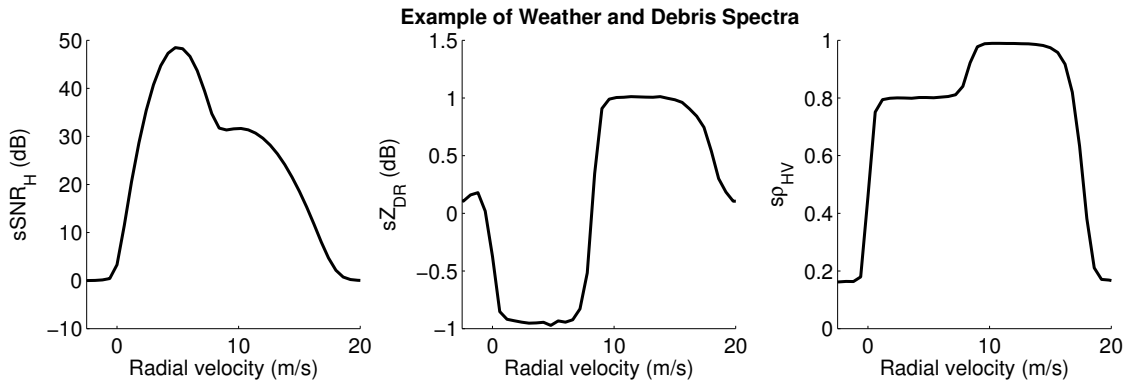

Figure 2.5: Sketch of spectral polarimetric variables for a combination of weather and debris. Spectral power sS_{H} (left), spectral differential reflectivity sZ_{DR} (center), spectral correlation coefficient $s\rho_{\mathrm{HV}}$ (right). Adapted from Cheong et al. (2015).

way to retrieve the actual velocity of the raindrops from DPSD estimates. In this scenario, raindrops are moving faster, with a wider spectrum width, positive sZ_{DR}, and $s\rho_{\mathrm{HV}}$ high and close to 1. Conversely, debris is slower, with a narrower spectrum width, negative sZ_{DR} and lower $s\rho_{\mathrm{HV}}$. It is expected that the spectral variables of the scatterers would follow the polarimetric radar variables somewhat closely in value. Without the DPSD, there would be a higher uncertainty in determining which spectral components of the PSD correspond to weather and which to debris. However, by inspecting the spectral polarimetric variables it should be possible to separate the different scatterer types. Although the debris signal is depicted as a Gaussian-shaped signal, it should be noted that such assumption is not realistic. Nonetheless, it is a simple model that successfully illustrates the idea of the presence of signals with different polarimetric characteristics in the spectra.

2.3 Estimation of Power Spectral Densities

For PSD estimation, there are non-parametric and parametric methods. The former type makes no assumptions about the structure of the underlying phenomena, while the latter assumes their structure can be described with certain models by using different parameters. The atmosphere is constantly changing, and only over 75% of the observed power spectra are Gaussian shaped (Janssen and Van Der Spek 1985), in addition to non-hydrometeor scatterers being present in the radar volume. Thus, the uncertainty in determining the nature of the event would be high and extremely difficult to parameterize a model for each case. Therefore, non-parametric methods are better suited for this work.

Two common non-parametric methods to compute the PSD are the periodogram and the correlogram methods. The periodogram consists in applying the discrete Fourier transform (DFT) to the I/Q time-series signal to obtain

$$Z(k) = \sum_{m=0}^{M-1} V(m) e^{-j2\pi mk/M}, \tag{2.26}$$

where the signal V corresponds to either the H- or V-channel. Then an estimate of the PSD can be obtained as

$$s\hat{S}(k) = \frac{|Z(k)|^2}{M}, \tag{2.27}$$

where M is the total number of samples in the dwell, and k is the frequency component index. The correlogram method (Stoica and Moses 1997) consists in estimating

the autocorrelation function of the I/Q time series and then applying the DFT. An estimate of the PSD with the correlogram can be computed as

$$s\hat{S}(k) = \sum_{l=-(M-1)}^{(M-1)} \hat{R}(l) e^{-j2\pi lk/M}. \tag{2.28}$$

It can be shown that the periodogram and the correlogram estimators are equivalent under certain conditions (Doviak and Zrnić 2006). The method preferred herein is the periodogram because of its relative simplicity and low computational cost. In spite of its advantages, the periodogram comes with limitations regarding the accuracy and precision of the PSD estimates. Many variants of the periodogram (Hayes 1996; Stoica and Moses 1997) have been proposed in the literature to address these issues, some of which will be described later in this chapter.

2.3.1 Modified Periodogram

Since the DFT assumes the underlying signal to be periodic, the discontinuities associated with the periodic extension of an I/Q dwell introduce frequency components that are not related to the underlying phenomenon. This effect is known as spectral leakage (Harris 1978). The modified periodogram is a generalized variation of the periodogram which accounts for this effect by applying a data window or tapering function to smooth out the discontinuities associated with the periodic extension of the time-series signal (Hayes 1996).

$$Z(k) = \sum_{m=0}^{M-1} d(m) V(m) e^{-j2\pi mk/M}, \tag{2.29}$$

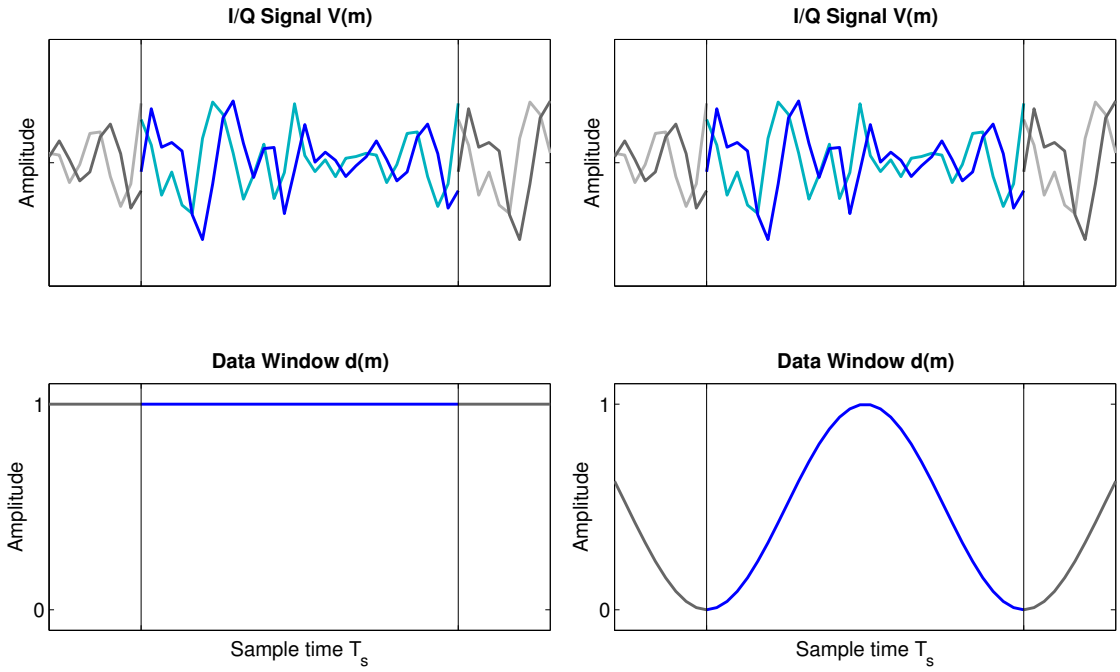

(a) (b)

Figure 2.6: Effects of data windowing in (a) the periodogram, and (b) the modified periodogram. Whereas the former uses a rectangular window (i.e., no window), the latter uses a tapered window (the von Hann window in this example). The in-phase component $I(m)$ shown in blue and the quadrature component $Q(m)$ shown in cyan.

where $d(m)$ is the data window function. Figure 2.6 shows how the data windowing function is applied for the periodogram and for the modified periodogram. It is important to note that by applying the taper the signal power is attenuated. To compensate for this loss, the PSD is normalized by:

$$\alpha = \frac{1}{M} \sum_{m=0}^{M-1} |d(m)|^2. \tag{2.30}$$

Then, the modified periodogram estimate becomes

$$s\hat{S}(k) = \frac{1}{\alpha} \frac{|Z(k)|^2}{M}. \tag{2.31}$$

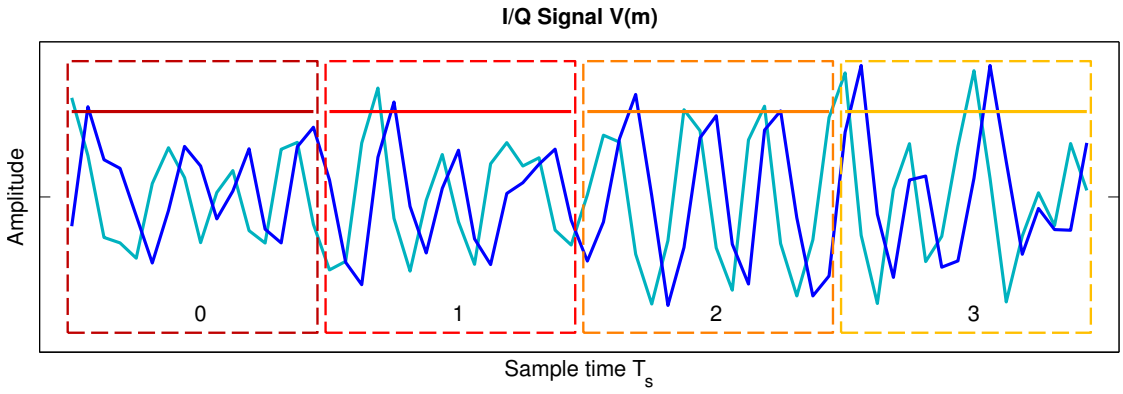

Figure 2.7: Bartlett's method makes non-overlapping segments of the I/Q signal, and computes the PSD for each segment using a rectangular data window. In this case, the length of each segment is $L = M/4$, and each segment is enumerated.

The choice of the data windowing function can reduce the spectral leakage in exchange for frequency resolution (Harris 1978). Typical choice of windows include the Bartlett window (SLL -25 dB), the von Hann window (SLL -32 dB), the Hamming window (SLL -43 dB), and the Blackman window (SLL -58 dB), among others. From here on, this method will be simply referred to as the periodogram.

2.3.2 Bartlett's Method

The method proposed by Bartlett (1950), consists in dividing the time-series signal into non-overlapping segments. The PSD of each segment is computed with the periodogram using a rectangular data window (Figure 2.7), and then these partial estimates are averaged to reduce the variance of the frequency component estimates (Stoica and Moses 1997). The PSD estimate of a single dwell with Bartlett's method is computed as

$$Z_i(k) = \sum_{m=0}^{L-1} V(m + iL)e^{-j2\pi mk/L}, \tag{2.32}$$

$$s\hat{S}_i(k) = \frac{|Z_i(k)|^2}{L}, \tag{2.33}$$

$$s\hat{S}(k) = \frac{1}{N}\sum_{i=0}^{N-1} s\hat{S}_i(k), \tag{2.34}$$

for $m = 0, \ldots, L-1$, $k = 0, \ldots, L-1$ and $i = 0, \ldots, N-1$, where $N = \lfloor M/L \rfloor$ is the number of segments, L is the segment length, and $\lfloor \cdot \rfloor$ is the floor function.

Although Bartlett's method computes a smoother PSD estimate because the partial estimates are independent, it comes with its limitations and tradeoffs. The method, by definition, does not make use of data windowing functions and thus is less flexible compared to other methods. Since it reduces the number of samples to compute the partial PSD estimates, the frequency resolution gets degraded significantly, although the variance is also reduced by a factor of N. This tradeoff between frequency resolution and variance is clear (Stoica and Moses 1997). Moreover the method has no control over the spectral leakage which makes it unsuitable for the dynamic range of weather signals.

2.3.3 Welch's Method

A variant of Bartlett's method was proposed by Welch (1967) and it allows the segments to overlap (Figure 2.8), as well as introducing an extra degree of freedom when selecting the data windowing function for each segment (Stoica and Moses 1997). Bartlett's method is reduced to a specific case of the Welch's method when the data window function used is the rectangular window and the segments do not overlap. The PSD estimate of a single dwell with Welch's method is obtained as

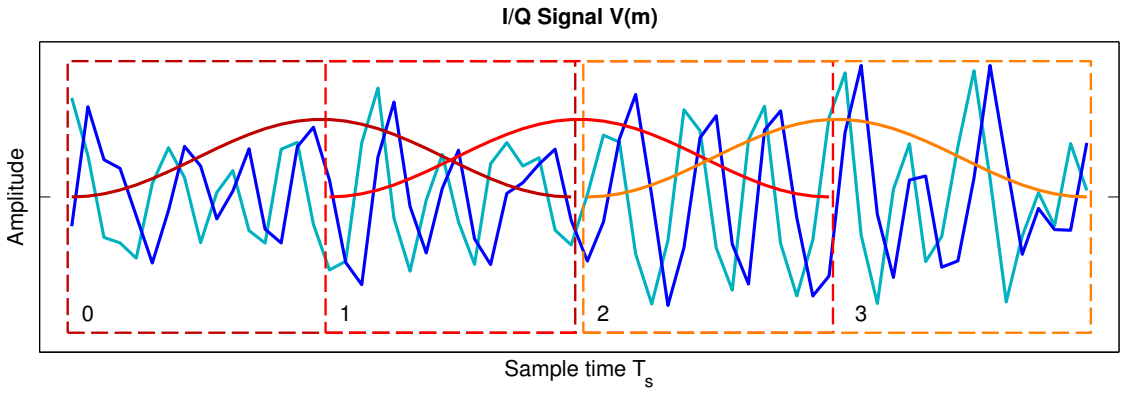

Figure 2.8: Welch's method makes overlapping segments of the I/Q signal, and computes the PSD for each segment using a particular data window. In this case, the length of each segment is $L = M/2$ with a 50% overlap and the von Hann window. Each segment is enumerated.

follows:

$$Z_i(k) = \sum_{m=0}^{L-1} d(m)V[m + i(L - O)]e^{-j2\pi mk/L}, \tag{2.35}$$

$$\alpha = \frac{1}{L}\sum_{m=0}^{L-1} |d(m)|^2, \tag{2.36}$$

$$s\hat{S}_i(k) = \frac{1}{\alpha}\frac{|Z_i(k)|^2}{L}, \tag{2.37}$$

$$s\hat{S}(k) = \frac{1}{N}\sum_{i=0}^{N-1} s\hat{S}_i(k), \tag{2.38}$$

for $m = 0, \ldots, L-1$, $k = 0, \ldots, L-1$ and $i = 0, \ldots, N-1$, where $N = \lfloor \frac{M-O}{L-O} \rfloor$ is the number of segments, O the amount of segment overlap, and L is the segment length.

Welch's method accounts for the limitations of Bartlett's method by adding more flexibility in the selection of the appropriate parameters that improves the statistical performance of the estimator. However, by allowing the overlap of the time-series signal segments, the partial PSD estimates are no longer independent even though

the windowing function works to "decorrelate" these estimates. The resolution and the variance of Welch's method are better than Bartlett's method (Stoica and Moses 1997). The performance of the method is analyzed in Chapter 4.

2.3.4 Daniell's Method

The smoothed periodogram method proposed by Daniell (1946) reduces the variance of the estimate in a different manner than in the methods described above. In this method, a moving average filter is applied to the "raw" periodogram estimate (Stoica and Moses 1997) (See Figure 2.9). To obtain the PSD estimate with Daniell's method, we first get an estimate using Equations (2.29)-(2.31). Then, a moving average filter is applied as

$$s\hat{S}(k) = \frac{1}{2p+1} \sum_{k'=\langle k-p \rangle_M}^{\langle k+p \rangle_M} s\hat{S}(k'), \tag{2.39}$$

where $2p+1$ is the length of the filter, and $\langle \cdot \rangle_M$ is the modulo M operator. Clearly this method trades spectral resolution for reduction of variance, and it may lead to higher bias as it smoothes out the raw PSD. Additionally, when the frequency components of the signals of interest are too close, the ability to resolve them individually may be lost due to this smearing effect. The method can be extended to a more general version which reduces the spectral leakage by using a weighted moving average filter. However, such implementation is not analyzed in this study. The performance of the method is analyzed in Chapter 4.

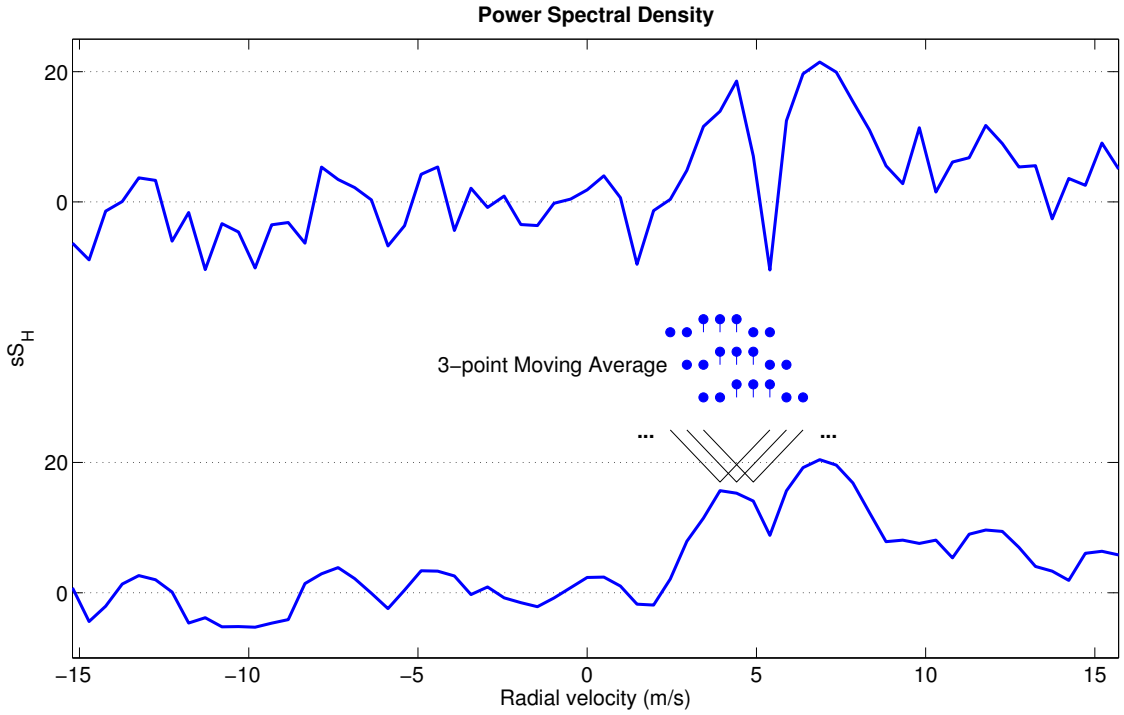

Figure 2.9: Daniell's method smooths the raw PSD estimate. The length of the moving average filter used here is $2p + 1 = 3$.

2.4 Estimation of Dual-Polarimetric Spectral Densities

To estimate the DPSDs, the co- and cross-polar power spectra must be obtained first as

$$Z_{\mathrm{H,V}}(k) = \sum_{m=0}^{M-1} d(m) V_{\mathrm{H,V}}(m) e^{-j2\pi mk/M}, \tag{2.40}$$

$$s\hat{S}_{\mathrm{H,V}}(k) = \frac{1}{\alpha} \frac{|Z_{\mathrm{H,V}}(k)|^2}{M}, \tag{2.41}$$

$$s\hat{S}_{\mathrm{X}}(k) = \frac{1}{\alpha} \frac{Z_{\mathrm{H}}(k) Z_{\mathrm{V}}^*}{M}, \tag{2.42}$$

To illustrate this, the expressions for the modified periodogram are shown, but it should be noted that the estimates $s\hat{S}_{\mathrm{H}}$, $s\hat{S}_{\mathrm{V}}$ and $s\hat{S}_{\mathrm{X}}$ may be obtained with any PSD estimator.

The polarimetric spectral estimates are obtained in a similar way to the polarimetric radar variables but using the PSD estimates as:

$$s\hat{Z}_{\mathrm{DR}}(k) = \frac{\sum_{i=1}^{K} s\hat{S}_{\mathrm{H}}^{(i)}(k)}{\sum_{i=1}^{K} s\hat{S}_{\mathrm{V}}^{(i)}(k)}, \tag{2.43}$$

$$s\hat{\rho}_{\mathrm{HV}}(k) = \frac{\left|\sum_{i=1}^{K} s\hat{S}_{\mathrm{X}}^{(i)}(k)\right|}{\sqrt{\sum_{i=1}^{K} s\hat{S}_{\mathrm{H}}^{(i)}(k) \sum_{i=1}^{K} s\hat{S}_{\mathrm{V}}^{(i)}(k)}}, \tag{2.44}$$

$$s\hat{\phi}_{\mathrm{DP}}(k) = \arg\left(\frac{\sum_{i=1}^{K} s\hat{S}_{\mathrm{X}}^{(i)}(k)}{\sqrt{\sum_{i=1}^{K} s\hat{S}_{\mathrm{H}}^{(i)}(k) \sum_{i=1}^{K} s\hat{S}_{\mathrm{V}}^{(i)}(k)}} \right), \tag{2.45}$$

where K is the number of independent spectra that are averaged to obtain useful DPSD estimates. As previously stated, the spectral differential phase will not be part of the analyses because it does not convey as much information to discriminate hydrometeors from debris.

Operational weather radars perform a scan every few minutes, which yields one independent spectra ($K = 1$) for each radar resolution volume. Using the periodogram estimator, for the spectral differential reflectivity, the frequency components of the PSD have significantly large variance, providing a poor sZ_{DR} estimate.

Additionally, it can be shown that the spectral correlation coefficient estimate fails to produce any useful results. By combining (2.44) and (2.41)-(2.42) for $K = 1$:

$$s\hat{\rho}_{\mathrm{HV}}(k) = \frac{|s\hat{S}_{\mathrm{X}}(k)|}{\sqrt{s\hat{S}_{\mathrm{H}}(k)s\hat{S}_{\mathrm{V}}(k)}} = \frac{|Z_{\mathrm{H}}(k)Z_{\mathrm{V}}^{*}(k)|}{\sqrt{|Z_{\mathrm{H}}(k)|^2|Z_{\mathrm{V}}(k)|^2}}$$
$$= \frac{|Z_{\mathrm{H}}(k)||Z_{\mathrm{V}}^{*}(k)|}{|Z_{\mathrm{H}}(k)||Z_{\mathrm{V}}(k)|} = 1, \tag{2.46}$$

which shows how the $s\rho_{\mathrm{HV}}$ estimate always equals 1.

This limitation can be overcome in different ways. Perhaps the most obvious solution is to average more independent spectra to reduce the statistical errors of the estimates and to produce meaningful $s\hat{\rho}_{\mathrm{HV}}$. To this end, data can be obtained from different sources such as adjacent radar resolution volumes in azimuth, range, or scans. Alternatively, the methods described in Section 2.3 provide estimates with better statistical performance than the periodogram estimator, and these could be used to obtain more reliable DPSD estimates with data from one dwell. Previous works (Bachmann and Zrnić 2007; Moisseev and Chandrasekar 2009; Alku et al. 2015; Unal 2009; Yanovsky 2011; Dufournet 2010; Spek et al. 2008; Moisseev et al. 2006; Moisseev and Chandrasekar 2007; Yu et al. 2013, 2012) have used one or more of the previously mentioned methods.

The DPSD can be used as tool for polarimetric spectral analysis, and it has been applied in the retrieval of microphysical parameters (Yanovsky 2011; Dufournet 2010; Spek et al. 2008; Moisseev et al. 2006; Moisseev and Chandrasekar 2007; **?**), as well as for detecting and suppressing clutter signals (Bachmann and Zrnić 2007; Moisseev and Chandrasekar 2009; Alku et al. 2015; Unal 2009). Ideally, it is desired

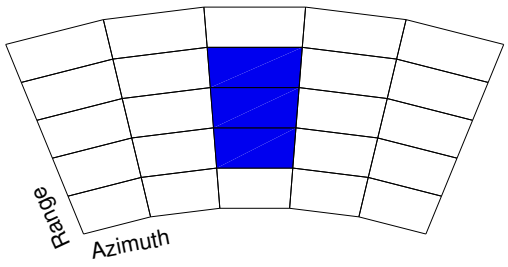

Figure 2.10: Range averaging scheme. Radar bins of three consecutive resolution volumes along range are averaged in this example.

to obtain reliable DPSD estimates out of an individual dwell for polarimetric spectral analysis to be both useful for interpretation and operationally feasible. Furthermore, it is preferred that resolution loss in any dimension is kept to the minimum in order to retrieve meaningful information for tornado observations. The advantages and disadvantages of averaging in different dimensions is briefly discussed next.

2.4.1 Range Averaging

More spectra may be acquired from spatially correlated radar resolution volumes. If the range gates of a particular radial are chosen to be averaged (Figure 2.10), the range resolution is degraded by at least a factor of two (e.g., two adjacent range gates). Depending on the range resolution of the radar, this could be quite significant as important spatial features of the weather event may be masked by averaging. Additionally, since the range dimension of the resolution volume remains constant although the resolution volume increases in size with range due to the antenna's beamwidth and range may be oversampled, range averaging may be a less compromising option in regard to resolution loss.

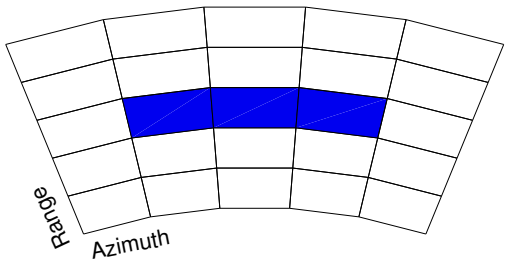

Figure 2.11: Azimuthal averaging scheme. Radar bins of three consecutive azimuths are averaged in this example.

2.4.2 Azimuth Averaging

A different spatial averaging can be performed using independent spectra from adjacent radar resolution volumes in azimuth (Figure 2.11). Similar to range averaging, the azimuthal resolution is degraded at the very least by a factor of two (e.g., resolution volumes from two adjacent rays). At farther ranges, the radar resolution volume gets wider in azimuth resulting in degraded spatial resolution, while for a constant range, resolution volumes will be similar in size. Thus, averaging in azimuth may be favored over range averaging at closer ranges. Additionally, if the azimuth is oversampled or if signal processing techniques such as the super-resolution (Torres and Curtis 2006) are used, the impact of azimuth averaging may be acceptable.

2.4.3 Scan-to-Scan Averaging

Averaging spectra from different scans (Figure 2.12) can also be performed to obtain better DPSD estimates, provided the spectra are correlated in time (i.e., slow moving phenomena or short scan times). By doing so, it must be ensured that the observations are based on the same location in space for a given event. However, to correctly capture the evolution of certain weather events, such as tornadoes, the time

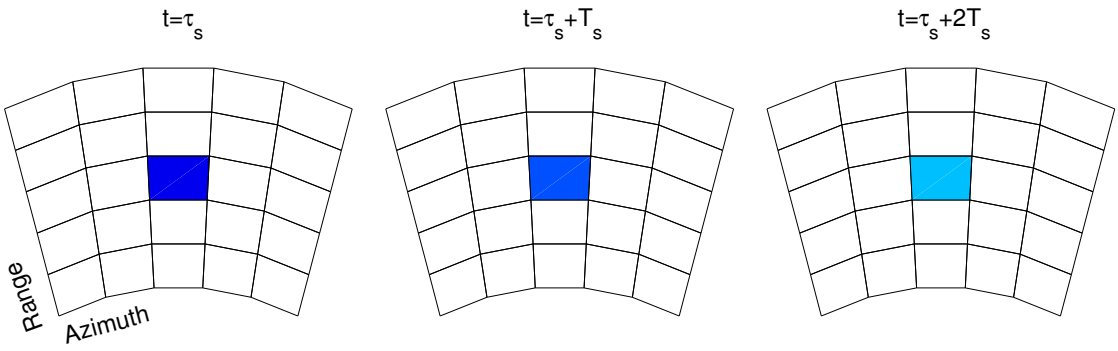

Figure 2.12: Dwell averaging scheme. Radar bins of three consecutive dwells are averaged in this example.

between consecutive scans for a given radar resolution volume must be considerably short.

2.4.4 Frequency Averaging

Some of the PSD estimation methods described in the previous section can provide decent DPSD estimates using data from a single dwell by reducing the statistical errors through averaging in the frequency domain. Albeit useful in cases where no other type of averaging can be performed, these methods degrade the frequency resolution (Bartlett, Welch) or add additional spectral "smearing" (Daniell). As a consequence, the quality of these estimates are usually not enough to be used in any quantitative analysis.

2.5 Summary

While the radar variables provide the "big picture" of a weather event, measurements can be biased by the presence of dominant clutter (i.e., non-meteorological

targets). In such cases, a spectral analysis may be useful to infer the characteristics for groups of scatterers moving at different Doppler velocities. A potential application for polarimetric spectral analysis is in radar resolution volumes with TDS, where the measurements are more prone to errors due to the weather signal being dominated by the debris signal. The correction of these biases is important when estimating tornado intensity and damage potential through radar observations. However, the quality of the DPSD estimates is limited by the number of independent observations that are needed to obtain accurate estimates. Polarimetric spectral analysis of tornado observations is additionally hindered by the fact that tornadoes evolve fast in time in a relatively small spatial extent, and because debris are centrifuged in the tornadic vortex. This means that good temporal and spatial resolutions are required to capture important features of the tornado, as well as a good frequency resolution to discriminate the velocities of hydrometeors and debris. Currently available techniques for DPSD estimation are not sufficient to overcome these constraints. In the following chapter, the Bootstrap DPSD estimator is introduced which is capable of estimating reliable DPSDs with minimal resolution loss.

Chapter 3

The Bootstrap Dual-Polarimetric Spectral Density Estimator

Obtaining radar-variable estimates with low errors is important to correctly characterize the underlying meteorological phenomena. The estimators presented in Chapter 2 yield estimates of sufficient quality provided that the number of independent measurements is large (Melnikov and Zrnić 2004; Yu et al. 2012). In practice, however, it may be extremely difficult to obtain the required number of measurements due to numerous reasons, some of which were mentioned in the previous chapter. In this chapter, the Bootstrap DPSD estimator is presented as an alternative method that overcomes some of the limitations of the conventional PSD and DPSD estimators. The bootstrap concept and definitions of non-dependent and dependent data bootstrap are presented in Section 3.1. Section 3.2 presents applications of these methods to weather radar I/Q time-series signals and explores the utility of each method for this application. In Section 3.3, the considerations taken into account in the design of the Bootstrap DPSD estimator are presented. The criteria to evaluate the performance of the methods and a few signal conditioning strategies that improve the quality of the estimates are explained. Section 3.4 presents the rationale behind the selection of the best strategies and parameters for the Bootstrap DPSD

estimator. The algorithm of the Bootstrap DPSD estimator is described in Section 3.5. And finally, a summary of this chapter is presented in Section 3.6.

3.1 Bootstrap Resampling

In a statistical investigation, samples of an unknown distribution can be obtained to make inferences about the actual distribution. In other words, the sample distribution is an estimate of the real distribution. It is explained by the law of large numbers that the accuracy of an estimate improves as the number of samples increases. Logically, as the sample size increases, the sample distribution will converge to the real distribution. However, obtaining a large number of samples may not always be feasible or practical, in which case there is no choice other than to work with the available data. In such situations, resampling methods can provide a better estimate of the sample distribution because the distribution, albeit small and discrete, is known and thus can be treated as a parent distribution (Hall 1992). In this sense, the statistical characteristics of the resample distribution inferred from the sample distribution can be compared to those of the sample distribution inferred from the unknown, real distribution (Efron and Tibshirani 1994). Consequently, more accurate inferences about the real distribution can be made, provided that the sample distribution is reasonably representative of the underlying distribution (Varian 2005). According to Efron and Tibshirani (1994): "The bootstrap is a computer-based method for assigning measures of accuracy to statistical estimates". This concept was first introduced in Efron (1979) as the random resampling with

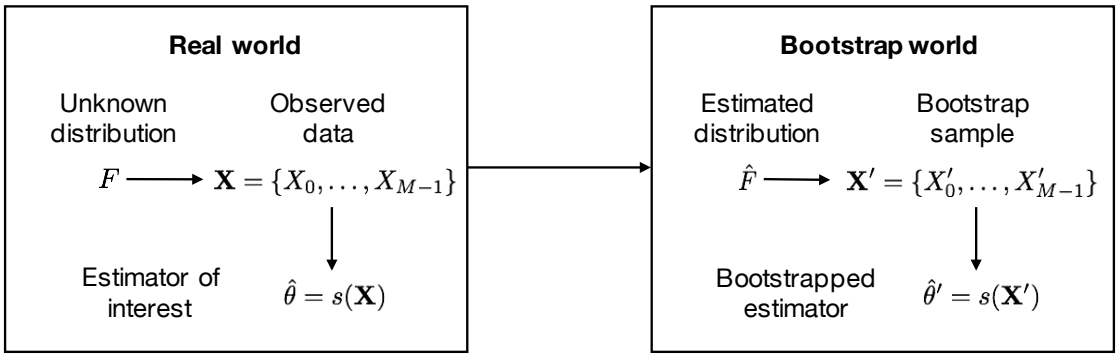

Figure 3.1: Bootstrap resampling. Adapted from Zoubir and Iskander (2004).

replacement of a given set of samples, and it is typically used to estimate statistical properties of estimators (e.g., variance, confidence intervals). The bootstrapping procedure is similar to a Monte Carlo simulation, where independent samples are drawn from a known distribution, and by drawing a large number of them, an approximation to the real distribution is obtained. The difference is that the bootstrap generates a large number of resamples from the sample distribution to obtain a bootstrap distribution with which the statistical quality of an estimator can be assessed (Varian 2005). Intuitively, the bootstrap simulates the probabilistic aspect of the real world by substituting unknowns with estimates from the available data (Zoubir and Iskander 2004). Figure 3.1 shows a diagram of the bootstrap concept, where the mechanisms of the real world are compared to the bootstrap world. A proper description will be presented later.

Although the bootstrap in its simplest form can fail under certain conditions (e.g., correlated data), with proper modification it can be widely extended to many applications (Hall 1992). The bootstrap has been used in many different areas of engineering, including radar signal processing (Zoubir and Iskander 2004) and some

applications related to radar meteorology include rainfall modeling through spatial bootstrapping (Overeem et al. 2009), cloud radar observations and tests for similarities between cloud occurrence profiles (Marchand et al. 2006), the determination of the likelihood of TDS parameters observed in two different wavelengths having the same parent distribution Bodine et al. (2014), and the analysis of tornado strength through skill scores (Kingfield and LaDue 2015). However, to our knowledge, the bootstrap has not been applied to weather radar signal processing.

There are bootstrap methods for non-dependent and dependent data, a brief description of the methods is provided hereafter. In a later section, the bootstrap methods are applied to I/Q signals, and it will be clear that only the dependent data methods can yield meaningful results for spectral estimation.

3.1.1 Non-Dependent Data Bootstrap

For non-dependent data, i.e., data without structure, the independent and identically distributed (IID) bootstrap can be formulated as follows (Efron and Tibshirani 1994). Let

$$\mathbf{X} = \{X_0, X_1, \ldots, X_{M-1}\} \tag{3.1}$$

be the measured M-point sample set from a given distribution F. A resample

$$\mathbf{X}' = \{X'_0, X'_1, \ldots X'_{M-1}\} \tag{3.2}$$

of $\mathbf{X}$ is obtained by reassigning the samples of $\mathbf{X}$ randomly and with replacement with probability

$$P(X'_i = X_j|\mathbf{X}) = \frac{1}{M}, \tag{3.3}$$

for $0 \leq i, j \leq M-1$. Then, a number K' of resamples is generated, $\mathbf{X}'_0, \ldots, \mathbf{X}'_{K'-1}$, of which the distribution is $\hat{F}$, an estimate of the distribution F. Hereafter, the terms resample and bootstrap sample will be used interchangeably. It is shown in Hall (1992) that as M goes to infinity, $\hat{F}$ approaches F. In other words, the sample distribution converges to the real distribution as the number of samples increases. The number K' of resamples needed varies depending on various factors which can be application- or estimator-specific (Zoubir and Iskander 2004). From these resamples, measures of the accuracy of a statistical property of interest $\hat{\theta}' = s(\mathbf{X}')$ can be obtained. For example, if the sample mean estimator is used with a single set, only one estimate of the mean could be computed. However, by bootstrapping the sample mean estimator, the distribution of the mean can be obtained to assess the errors of the measurement.

3.1.2 Dependent Data Bootstrap

For dependent data, such as the I/Q time-series signals from weather radars, the former definition is inadequate. However, it can be extended to fit the definition if the resampling is done by taking blocks of consecutive data instead of single points to try to maintain the sample-time correlation of the data. There are many different

block bootstrapping methods, each with its advantages and selection of parameters (Lahiri 2003).

The general block bootstrap definition is derived from the definition of the IID bootstrap. By resampling blocks of data instead of individual samples, that is, the original sequence $X_0, \ldots, X_{M-1}$ is divided into N blocks of consecutive samples as

$$\mathbf{X} = \{\mathbf{B}_0, \mathbf{B}_1, \ldots, \mathbf{B}_{N-1}\}, \tag{3.4}$$

and

$$\mathbf{B}_j = \{X_{jL}, \ldots, X_{(j+1)L-1}\}. \tag{3.5}$$

for $0 \leq j < N$, where N is the number of blocks, and L is the block length. The different dependent data bootstrap methods are similar in principle, though the block selection scheme varies for each method. For now, it suffices to say that these blocks of data can be arranged in different ways yielding different results. Following this, a bootstrap sample becomes

$$\mathbf{X}' = \{\mathbf{B}'_0, \mathbf{B}'_1, \ldots \mathbf{B}'_{N-1}\}, \tag{3.6}$$

where $\mathbf{X}'$, in this case, is obtained by reassigning blocks of consecutive samples in $\mathbf{X}$ randomly with replacement, i.e., with probability

$$P(\mathbf{B}'_i = \mathbf{B}_j | \mathbf{X}) = \frac{1}{N}, \tag{3.7}$$

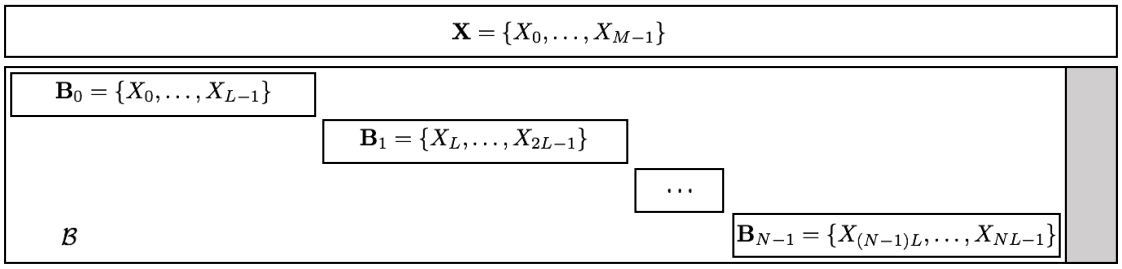

Figure 3.2: Non-overlapping block bootstrap block scheme. Adapted from Lahiri (2003).

for $0 \leq i, j \leq N-1$. It should be noted that for larger block lengths, these methods are less computationally expensive because of the reduced number of blocks per bootstrap sample. However, dividing the data into blocks reduces the degrees of freedom to do resampling.

The concept of dividing the time-series signals into blocks may be similar to Bartlett's and Welch's method of PSD estimation. In fact, two of the block bootstrap methods that will be described hereafter employ a non-overlapping as well as an overlapping block scheme like the aforementioned PSD estimators. However, neither of them resample the blocks in the way bootstrap does. Additionally, a circular and a stationary block bootstrap method will be presented. The former method allows the samples in the blocks to wrap around the data circularly, while the latter uses a dynamic block length.

3.1.2.1 Non-Overlapping Block Bootstrap (NBB)

This method was introduced by Carlstein (1986) and consists in dividing the signal into blocks that do not overlap. These blocks are then resampled with equal probability (Lahiri 2003).

By definition (Lahiri 2003),

$$\mathbf{X} = \{\mathbf{B}_0, \mathbf{B}_1, \ldots, \mathbf{B}_{N-1}, \ldots, X_{M-1}\} \tag{3.8}$$

$$\mathbf{B}_j = \{X_{jL}, \ldots, X_{(j+1)L-1}\} \tag{3.9}$$

$$\mathcal{B} = \{\mathbf{B}_0, \mathbf{B}_1, \ldots, \mathbf{B}_{N-1}\}, \tag{3.10}$$

where $\mathcal{B}$ defines all the possible blocks available for resampling (Figure 3.2). A bootstrap sample $\mathbf{X}'$ is obtained as

$$\mathbf{X}' = \{\mathbf{B}'_0, \mathbf{B}'_1, \ldots \mathbf{B}'_{N-1}\} \tag{3.11}$$

with

$$P(\mathbf{B}'_i = \mathbf{B}_j | \mathcal{B}) = \frac{1}{N} \tag{3.12}$$

$$N = \left\lfloor \frac{M}{L} \right\rfloor, \tag{3.13}$$

for $0 \leq i, j \leq N-1$, where M is the length of the signal, L is the block length, N is the number of blocks, and $\lfloor \cdot \rfloor$ is the floor function. If L is an integer multiple of M (i.e. $NL = M$), there will be exactly N blocks in $\mathbf{X}$. Otherwise, there will be N blocks of length L, and the remaining $M - NL$ samples of $\mathbf{X}$ will not have a block assigned. In this case, an extra block at index N is drawn and the resulting sequence is truncated to have exactly M data points (as the original sequence).

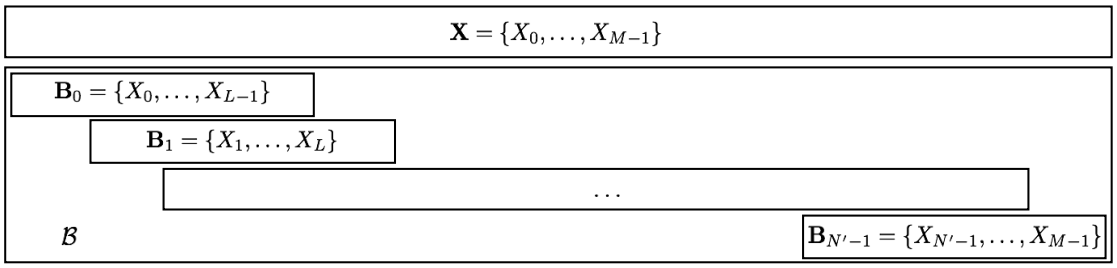

Figure 3.3: Moving block bootstrap block scheme. Adapted from Lahiri (2003).

3.1.2.2 Moving Block Bootstrap (MBB)

In the moving block bootstrap (MBB) (Künsch 1989; Liu and Singh 1992), unlike the NBB, the blocks are allowed to overlap as depicted in Figure 3.3. The blocks are then resampled with equal probability (Lahiri 2003).

By definition,

$$\mathbf{B}_j = \{X_j, \ldots, X_{j+L-1}\} \tag{3.14}$$

$$\mathcal{B} = \{\mathbf{B}_0, \mathbf{B}_1, \ldots, \mathbf{B}_{N'-1}\}, \tag{3.15}$$

for $0 \leq j \leq N' - 1$, where $N' = M - L + 1$ is the number of available blocks (Figure 3.3). A bootstrap sample $\mathbf{X}'$ is obtained as

$$\mathbf{X}' = \{\mathbf{B}'_0, \mathbf{B}'_1, \ldots \mathbf{B}'_{N-1}\} \tag{3.16}$$

$$P(\mathbf{B}'_i = \mathbf{B}_j | \mathcal{B}) = \frac{1}{N'} \tag{3.17}$$

$$N = \left\lceil \frac{M}{L} \right\rceil, \tag{3.18}$$

for $0 \leq i \leq N - 1$, where N is the number of blocks to be drawn from $\mathcal{B}$ for each bootstrap sample, L is the block length, and $\lceil \cdot \rceil$ is the ceiling function. As with

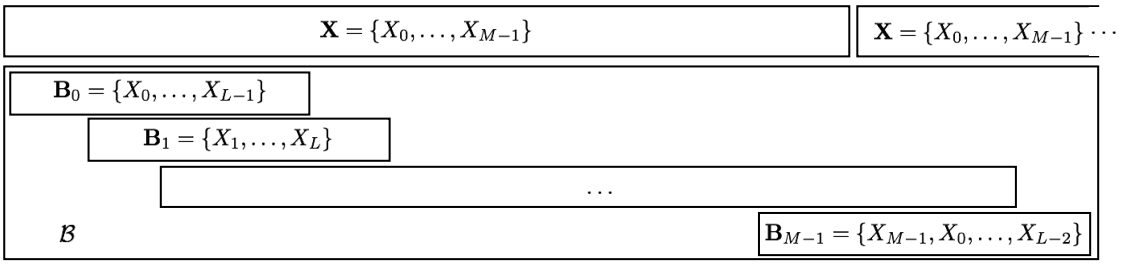

Figure 3.4: Circular block bootstrap block scheme.

the previous scheme, the bootstrap samples exceeding the length of the original sequence will be truncated to M.

3.1.2.3 Circular Block Bootstrap (CBB)

A variant of the MBB, which additionally allows the blocks to wrap around the data circularly, is the circular block bootstrap (CBB) (Lahiri 2003) depicted in Figure 3.4.

By definition,

$$\mathbf{B}_j = \{X_{\langle j \rangle_M}, \ldots, X_{\langle j+L-1 \rangle_M}\} \tag{3.19}$$

$$\mathcal{B} = \{\mathbf{B}_0, \mathbf{B}_1, \ldots, \mathbf{B}_{M-1}\}. \tag{3.20}$$

A bootstrap resample $\mathbf{X}'$ is obtained as

$$\mathbf{X}' = \{\mathbf{B}'_0, \mathbf{B}'_1, \ldots, \mathbf{B}'_{M-1}\} \tag{3.21}$$

$$P(\mathbf{B}'_i = \mathbf{B}_j | \mathcal{B}) = \frac{1}{M} \tag{3.22}$$

$$N = \left\lceil \frac{M}{L} \right\rceil, \tag{3.23}$$

for $0 \leq i \leq N-1$ and $0 \leq j \leq M-1$, where N is the number of blocks per bootstrap resample. The bootstrap samples exceeding the length of the original sequence will be truncated to M.

3.1.2.4 Stationary Block Bootstrap (SBB)

The stationary block bootstrap (SBB) (Politis and Romano 1994) makes the assumption of stationarity by dynamically varying the block lengths for each bootstrap sample (Lahiri 2003). The blocks, however, are not allowed to wrap around circularly. The length of each block is a random number with geometric distribution with parameter p. This allows for even higher variability and randomness than the previous methods. Let the bootstrap resample be drawn as

$$\mathbf{X}' = \{\mathbf{B}(i_0, j_0), \mathbf{B}(i_1, j_1), \ldots\} \tag{3.24}$$

$$\mathbf{B}(i, j) = \{X_i, \ldots, X_{i+j-1}\}, \tag{3.25}$$

where i defines the starting index of the block, and j defines the length of the block. Furthermore, i has an uniform distribution:

$$i \sim U(0, M-1), \tag{3.26}$$

and j has a geometric distribution with probability parameter p:

$$P(j = k) = p(1-p)^{k-1}. \tag{3.27}$$

For each bootstrap sample, blocks are continuously drawn until the length of the resample is greater than the original sequence. Then, the resulting sequence is truncated to have a length equal to M.

3.1.2.5 Other Methods

Bootstrapping can also be performed in the frequency domain rather than in the time domain. There are a variety of methods within this group of which the general procedure is to assume a spectral model and then to bootstrap the residuals, i.e., the difference between the model and the spectral estimate. This procedure yields bootstrapped PSDs directly, as opposed to bootstrapped time-series signals. Additionally, bootstrapped time-series signals may be obtained with the inverse Fourier transform of the bootstrapped PSD. Although they make no assumption on data dependence in the time domain, these methods rely on a good spectral model in order to be effective. Obviously, this is unsuitable for DPSD estimation since the model of the underlying phenomena is unknown, and hence will not be discussed in this work.

3.2 Bootstrapping I/Q Time-Series Signals

The diagram in Figure 3.5 illustrates the bootstrap process applied to I/Q time-series signals. After gathering the measurements for a dwell, instead of estimating the PSD as per the classical approach, bootstrap samples of the I/Q signals are generated and the PSD of the resamples are estimated. This yields K' spectra per dwell,

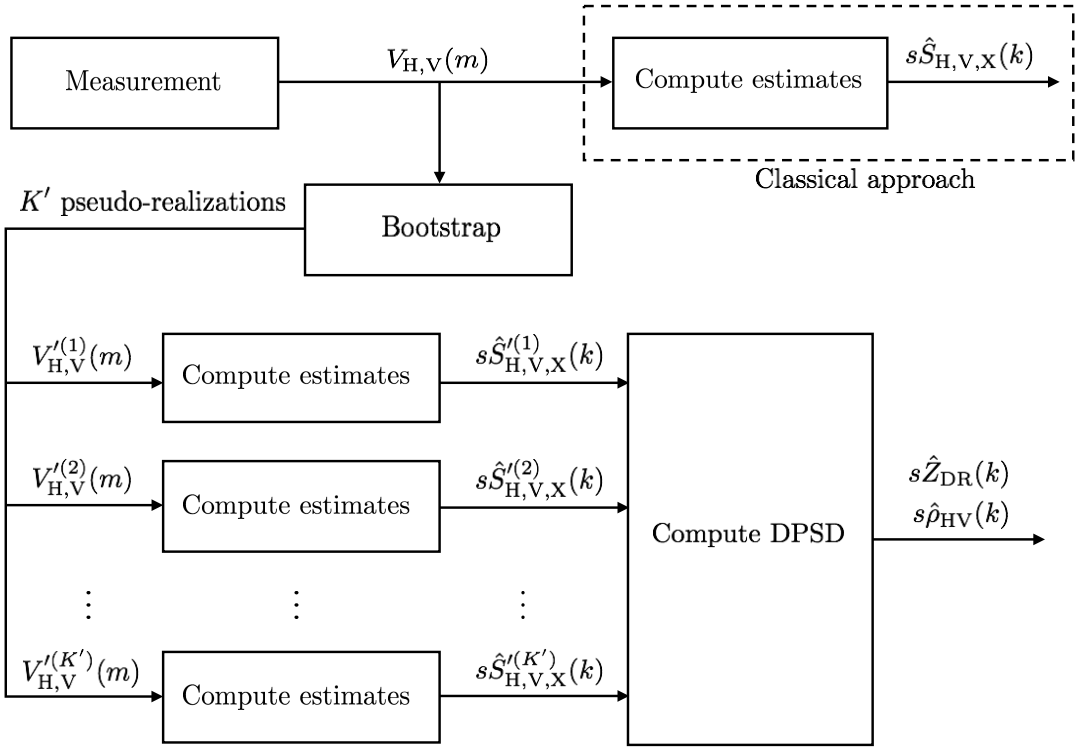

Figure 3.5: Diagram of the bootstrap. Adapted from Zoubir and Iskander (2004) for I/Q time-series signals.

which are averaged to compute the DPSD estimates. The process of averaging bootstrapped estimates is known as bootstrap aggregating (Breiman 1996). Hereafter, the bootstrap resamples of the I/Q signals shall be referred to as pseudo-realizations. For weather radar signals, although the samples of the I and Q components are uncorrelated with each other, the random processes controlling the changes in I and Q are correlated (Doviak and Zrnić 2006). Therefore, the structure of the pseudo-realizations must be similar to the original sequence in order to correctly convey the sample-time coherence. For this reason, it is evident that the IID bootstrap assumption is inadequate and cannot be applied to estimate the spectra of weather signals. The different block bootstrapping methods have a different selection of blocks available for resampling, which is why a preliminary assessment is necessary to determine the method that yields the best results for DPSD estimation. This section illustrates the block bootstrap methods applied to polarimetric weather radar I/Q time-series signals and the DPSD estimates obtained with each method. At the end of this section a summary of methods is presented.

3.2.1 IID Bootstrap

Given the I/Q signal for the H- and V- channels from Equation (2.7),

$$\mathbf{V}_{\mathrm{H,V}} = [V_{\mathrm{H,V}}(0), \ldots, V_{\mathrm{H,V}}(M-1)] \tag{3.28}$$

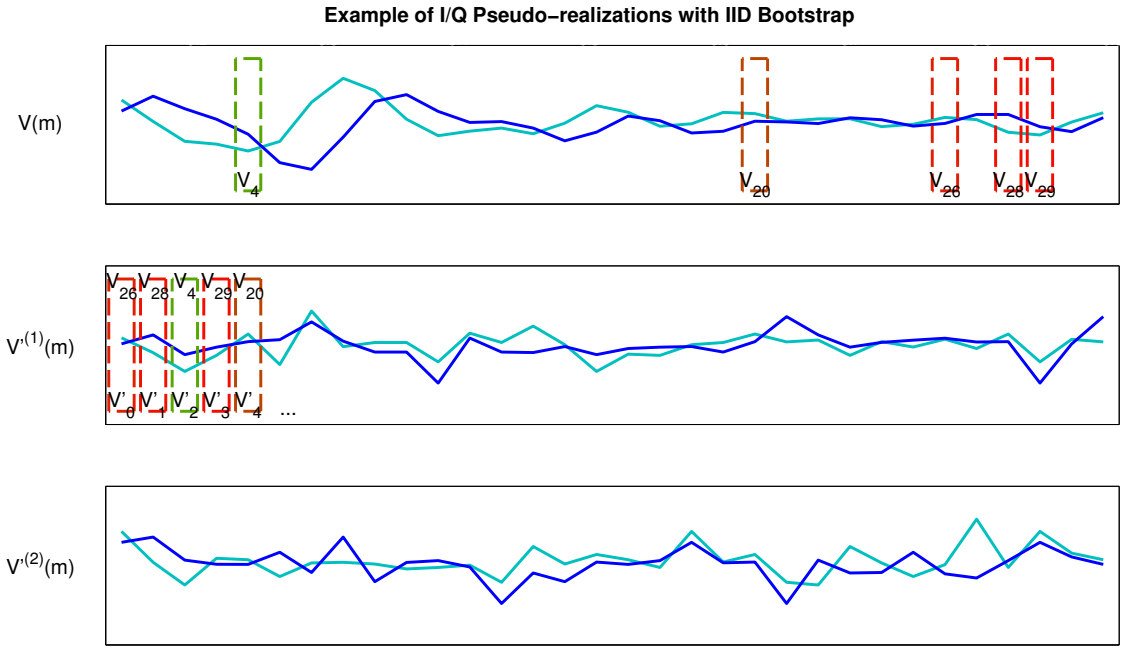

Figure 3.6: Obtaining I/Q pseudo-realizations with the IID bootstrap.

and the definitions in Equations (3.1-3.3), a pseudo-realization is obtained as

$$\mathbf{V}'_{\mathrm{H,V}} = [V'_{\mathrm{H,V}}(0), \ldots, V'_{\mathrm{H,V}}(M-1)], \tag{3.29}$$

where

$$P(V'_{\mathrm{H,V}}(m') = V_{\mathrm{H,V}}(m) | \mathbf{V}_{\mathrm{H,V}}) = \frac{1}{M}, \tag{3.30}$$

and $0 \leq m, m' \leq M-1$. In this sense, a pseudo-realization is obtained from $\mathbf{V}$ by resampling randomly with replacement, which means the data points are drawn with equal probability, and as such, they can be repeated in the sequence (Figure 3.6). The IID bootstrap is a particular case of a block bootstrap with unit block length.

To assess the quality of the spectral estimates obtained from each bootstrap method, simple simulations for a single signal are run. The simulation parameters

Parameter	Value
SNR	30 dB
$\bar{v}_r$	5 m/s
σ_v	2 m/s
Z_{DR}	1.5 dB
ρ_{HV}	0.9
M	100
K	1 independent spectrum
K'	100 pseudo-realizations
N_i	1000 iterations
v_a	15.7 m/s

Table 3.1: Simulation parameters for a simple single signal case.

of the bulk radar variables of the signal are summarized in Table 3.1. The parameters are chosen to resemble a realistic weather signal, while ρ_{HV} is arbitrarily set to a low value so that potential biases become more evident. N_i independent realizations of a signal are simulated and, for each of them, K' pseudo-realizations are bootstrapped. The PSD of the pseudo-realizations are estimated using the periodogram with a Blackman-Nuttall window, and then averaged to compute the DPSD assuming only one independent spectrum is available. Simply put, for each independent realization, the PSD is estimated using the average of K' bootstrapped spectra, and K independent spectra (in this case, $K = 1$) may be averaged to estimate the DPSD. The K independent spectra may be obtained from different sources (i.e., different azimuth, range or dwell, or generated from simulations), whereas the K' bootstrapped spectra are obtained from the same source. The N_i independent realizations are performed to assess the statistical characteristics of the DPSD. The weather-like I/Q time-series signals are simulated using the procedure described in Zrnić (1975), extended to dual-polarized signals with the procedure described by Galati and Pavan (1995), as presented in Torres and Zrnić (2003). This procedure

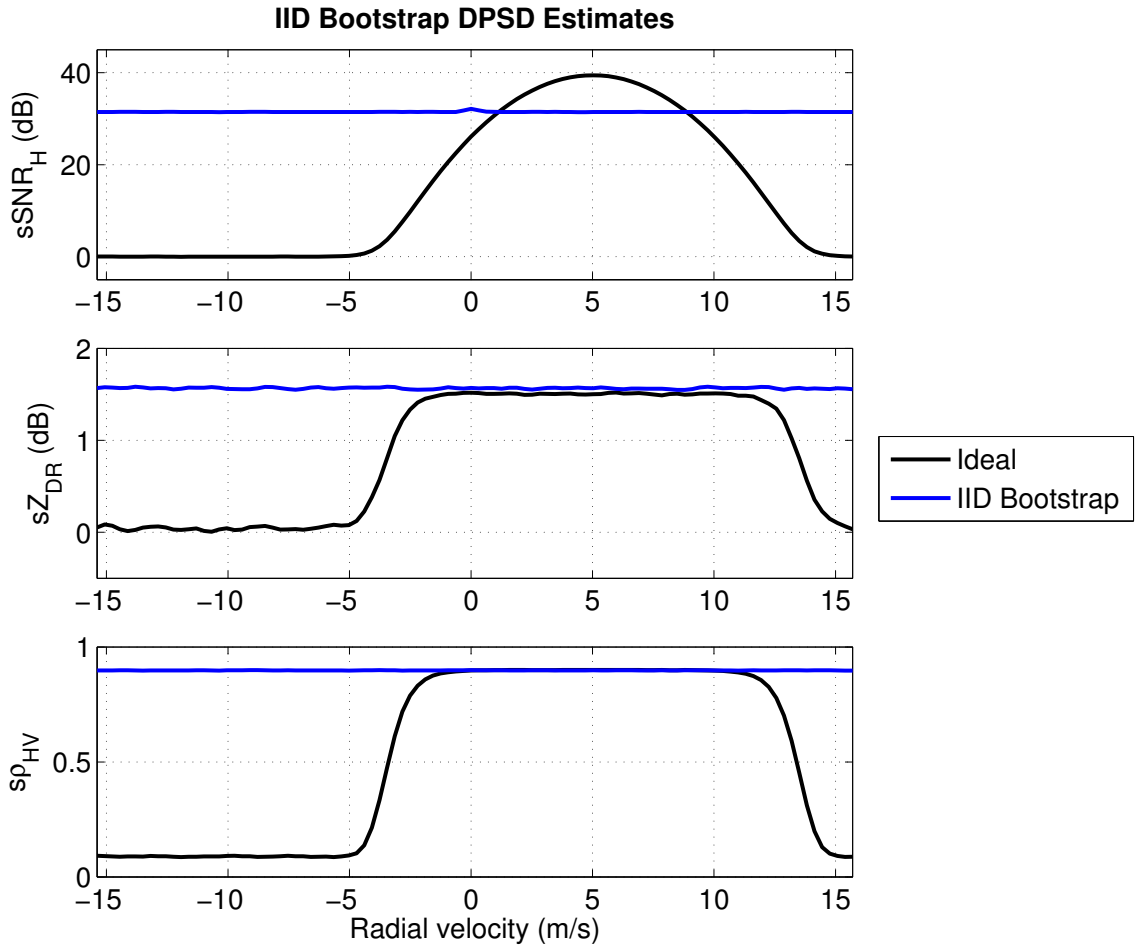

Figure 3.7: Mean of $N_i = 1000$ DPSD estimates obtained with IID bootstrap (blue) and the ideal estimates (black): $s\hat{\mathrm{SNR}}_{\mathrm{H}}$ (top), $s\hat{Z}_{\mathrm{DR}}$ (middle), and $s\hat{\rho}_{\mathrm{HV}}$ (bottom).

is the same for all the methods evaluated hereafter. The estimates using the IID bootstrap are shown in Figure 3.7. To assess the quality of the estimates, the bootstrap DPSD estimates are compared to ideal DPSD estimates obtained with a large number of independent spectra ($K = 100$). It can be seen that the mean of the spectral estimates of the IID bootstrap tend to the average radar variables. For this single signal case, the values of the DPSD for frequency components with high enough SNR should be approximately equivalent to the bulk radar variables. However, by assuming no data dependence in the time domain, the information about

the distribution of radial velocities cannot be captured. As previously mentioned, the underlying phenomena controlling the I/Q time-series signals are correlated, thus a dependent data bootstrap must be used.

3.2.2 Non-Overlapping Block Bootstrap (NBB)

The NBB was defined in Section 3.1.2.1, where the I/Q time-series signal can be expressed as,

$$\mathbf{V}_{\mathrm{H,V}} = \{\mathbf{B}_0, \mathbf{B}_1, \ldots, \mathbf{B}_{N-1}, \ldots, V_{\mathrm{H,V}}(M-1)\}, \tag{3.31}$$

where

$$\mathbf{B}_j = \{V_{\mathrm{H,V}}(jL), \ldots, V_{\mathrm{H,V}}[(j+1)L-1]\}, \tag{3.32}$$

and an I/Q pseudo-realization $\mathbf{V}'_{\mathrm{H,V}}$ is obtained as

$$\mathbf{V}'_{\mathrm{H,V}} = \{\mathbf{B}'_0, \mathbf{B}'_1, \ldots \mathbf{B}'_{N-1}\}, \tag{3.33}$$

with

$$P(\mathbf{B}'_i = \mathbf{B}_j | \mathcal{B}) = \frac{1}{N} \tag{3.34}$$

for $0 \leq i, j \leq N-1$. $\mathcal{B}$ is the set of all available blocks, M is the length of the signal, L is the block length, and $N = \left\lfloor \frac{M}{L} \right\rfloor$ is the number of blocks. Figure 3.8 illustrates this process. If $N = ML$, there will be exactly M samples in the pseudo-realization. Otherwise, the last $M - NL$ samples from $\mathbf{V}$ will not have a block assigned and therefore will not be part of any pseudo-realization. In this case, an additional block is drawn from $\mathcal{B}$ and the pseudo-realization is truncated to M samples.

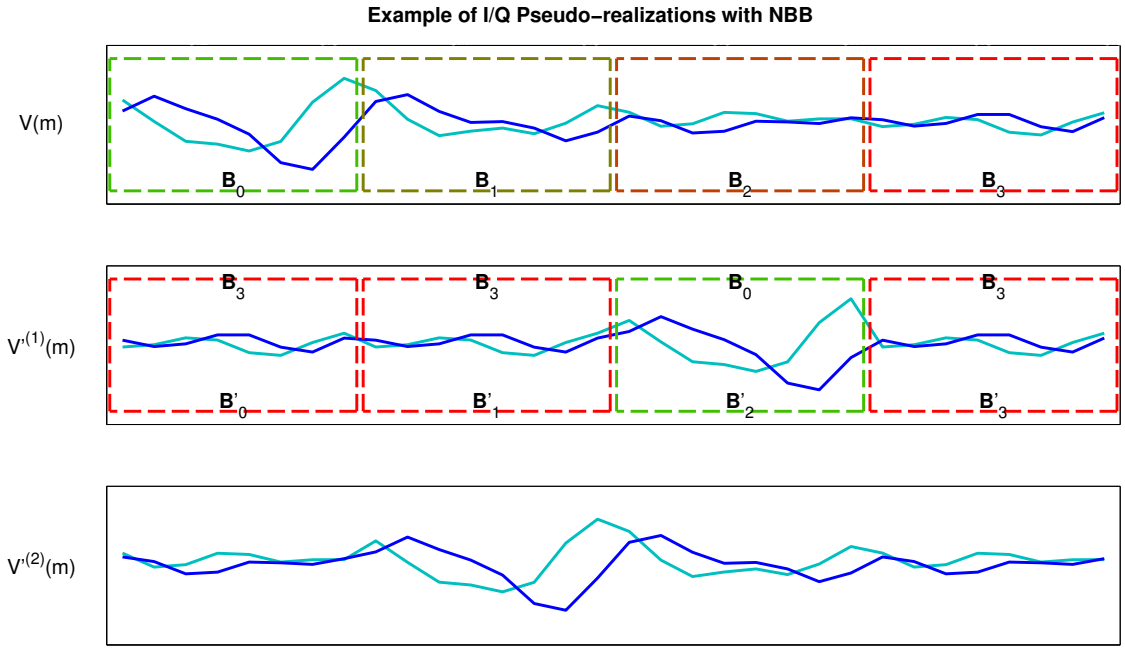

Figure 3.8: Obtaining I/Q pseudo-realizations with the NBB.

The DPSD is estimated using the same procedure mentioned in the previous section, but using the NBB scheme for different block lengths (Figure 3.9). The effect of spectral leakage can be seen in all estimates and it is such that even a very aggressive data window function as the Blackman-Nuttall (SLL -98 dB) is not enough to mitigate it. This example shows the tradeoff between the selection of the bootstrap block length and the spectral leakage introduced by disrupting the sample-time coherence. Methods to mitigate this effect will be discussed later, but for now, it is assumed that the discontinuities between blocks are not accounted for in any of the methods.

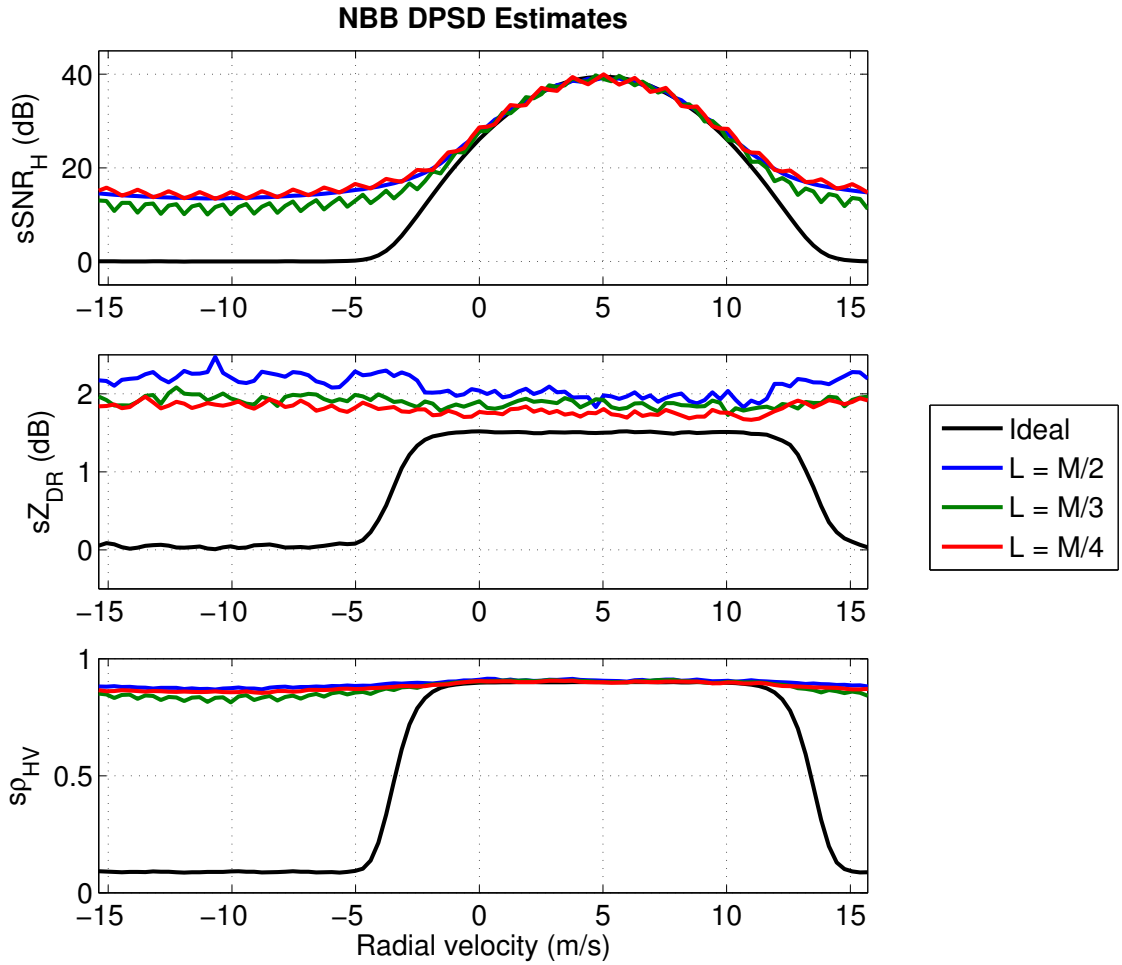

Figure 3.9: Mean of $N_i = 1000$ DPSD estimates obtained with NBB for $L = M/2$ (blue), $L = M/3$ (green), $L = M/4$ (red), and the ideal estimates (black): $s\hat{\mathrm{SNR}}_{\mathrm{H}}$ (top), $s\hat{Z}_{\mathrm{DR}}$ (middle), and $s\hat{\rho}_{\mathrm{HV}}$ (bottom).

3.2.3 Moving Block Bootstrap (MBB)

The definition of the MBB was presented in Section 3.1.2.2, and the implementation on the I/Q time-series signal is as follows. Let the set of available blocks for resampling be

$$\mathcal{B} = \{\mathbf{B}_0, \mathbf{B}_1, \ldots, \mathbf{B}_{N'-1}\}, \tag{3.35}$$

where each block is given by

$$\mathbf{B}_j = \{V_{\mathrm{H,V}}(j), \ldots, V_{\mathrm{H,V}}(j+L-1)\} \tag{3.36}$$

for $0 \leq j \leq N'-1$, where $N' = M - L + 1$ is the number of available blocks. An I/Q pseudo-realization $\mathbf{V}'_{\mathrm{H,V}}$ is obtained as

$$\mathbf{V}'_{\mathrm{H,V}} = \{\mathbf{B}'_0, \mathbf{B}'_1, \ldots \mathbf{B}'_{N-1}\}, \tag{3.37}$$

where

$$P(\mathbf{B}'_i = \mathbf{B}_j | \mathcal{B}) = \frac{1}{N'}, \tag{3.38}$$

for $0 \leq i \leq N-1$, where $N = \lceil \frac{M}{L} \rceil$ is the number of blocks to be drawn from $\mathcal{B}$ for each pseudo-realization, and L is the block length. Figure 3.8 illustrates this process.

The DPSD estimated using MBB for different block lengths is shown in Figure 3.11 For block lengths of $0.9M$ and $0.8M$ there is almost no spectral leakage, while it is noticeable for $0.7M$ and even higher for $0.6M$. However, for larger block lengths

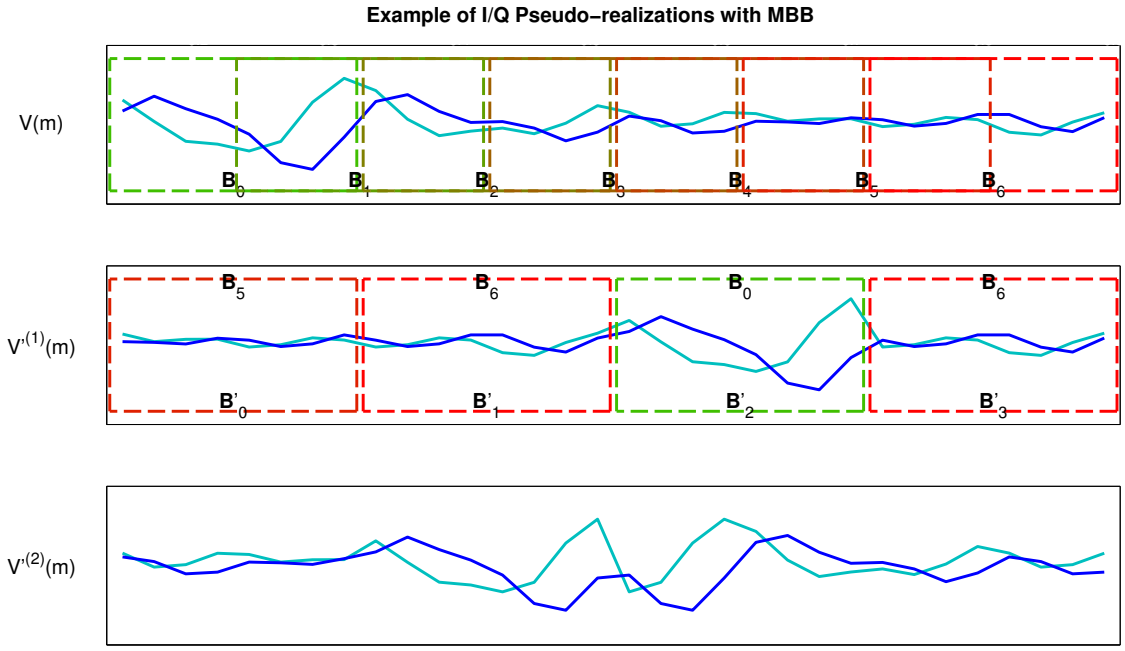

Figure 3.10: Obtaining I/Q pseudo-realizations with the MBB.

the DPSD estimates are significantly biased. The MBB estimates for block lengths of $0.8M$ seem to follow the shape of $s\rho_{\mathrm{HV}}$ better, but $s\hat{Z}_{\mathrm{DR}}$ still has large biases. As the block length is reduced, it can be seen that the error is also reduced. Moreover, in the limit where the estimates are unbiased, the block length is 1, which is the case of the IID bootstrap. The tradeoff between the block length and the quality of the estimates is thus evident.

3.2.4 Circular Block Bootstrap (CBB)

The CBB was defined in Section 3.1.2.3. The implementation on the I/Q time-series signal is similar to the MBB, though the blocks are now allowed to wrap data points circularly. With the CBB, an I/Q pseudo-realization $\mathbf{V}'_{\mathrm{H,V}}$ is obtained as

$$\mathbf{V}'_{\mathrm{H,V}} = \{\mathbf{B}'_0, \mathbf{B}'_1, \ldots \mathbf{B}'_{M-1}\}, \tag{3.39}$$

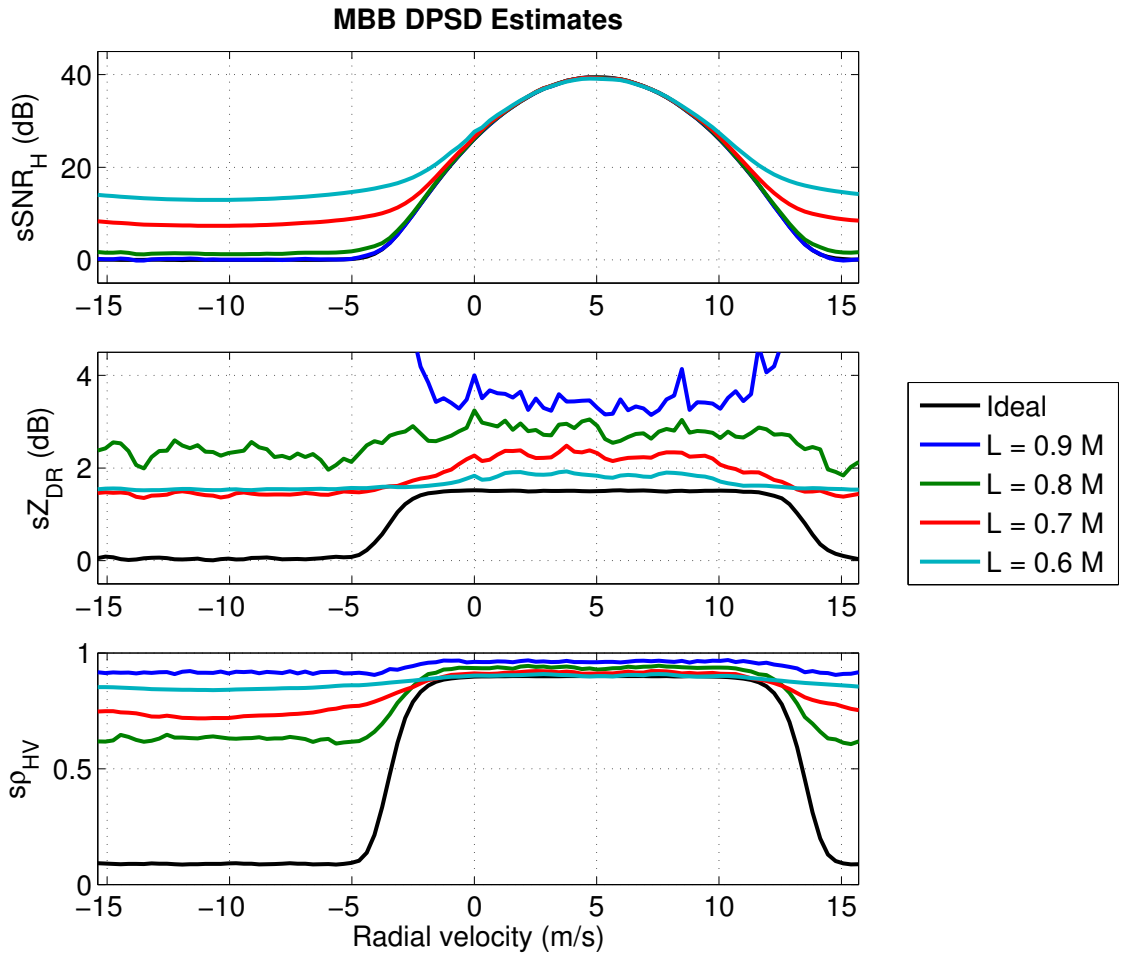

Figure 3.11: Mean of $N_i = 1000$ DPSD estimates obtained with MBB for $L = 0.9M$ (blue), $L = 0.8M$ (green), $L = 0.7M$ (red), $L = 0.6M$ (teal) and the ideal estimates (black): $s\hat{\mathrm{SNR}}_{\mathrm{H}}$ (top), $s\hat{Z}_{\mathrm{DR}}$ (middle), and $s\hat{\rho}_{\mathrm{HV}}$ (bottom).

where

$$P(\mathbf{B}'_i = \mathbf{B}_j|\mathcal{B}) = \frac{1}{M}, \tag{3.40}$$

for $0 \leq i \leq N-1$, where $N = \left\lceil \frac{M}{L} \right\rceil$ is the number of blocks to be drawn from $\mathcal{B}$ for each pseudo-realization, and L is the block length (Figure 3.12). The set of available blocks $\mathcal{B}$ is

$$\mathcal{B} = \{\mathbf{B}_0, \mathbf{B}_1, \ldots, \mathbf{B}_{M-1}\}, \tag{3.41}$$

with

$$\mathbf{B}_j = \{V_{\mathrm{H,V}}(\langle j \rangle_M), \ldots, V_{\mathrm{H,V}}(\langle j + L - 1 \rangle_M)\}, \tag{3.42}$$

for $0 \leq j \leq M-1$, and there are as many blocks available as M samples in the I/Q signal. The $\langle \cdot \rangle_x$ is the modulo-x operator.

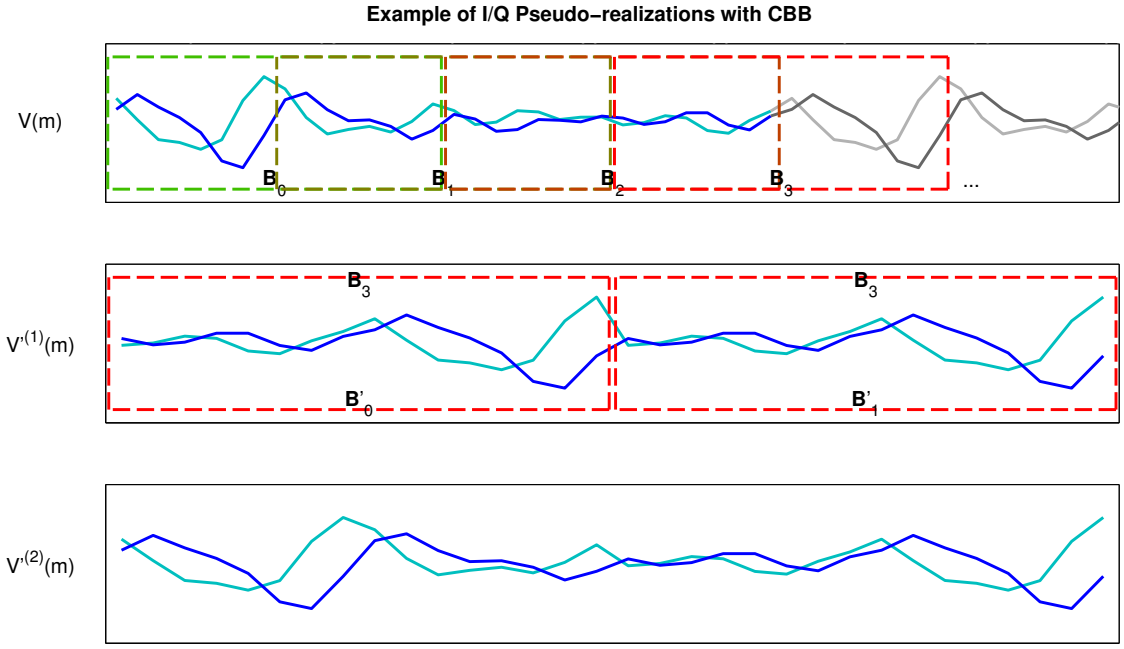

Figure 3.12: Obtaining I/Q pseudo-realizations with the CBB.

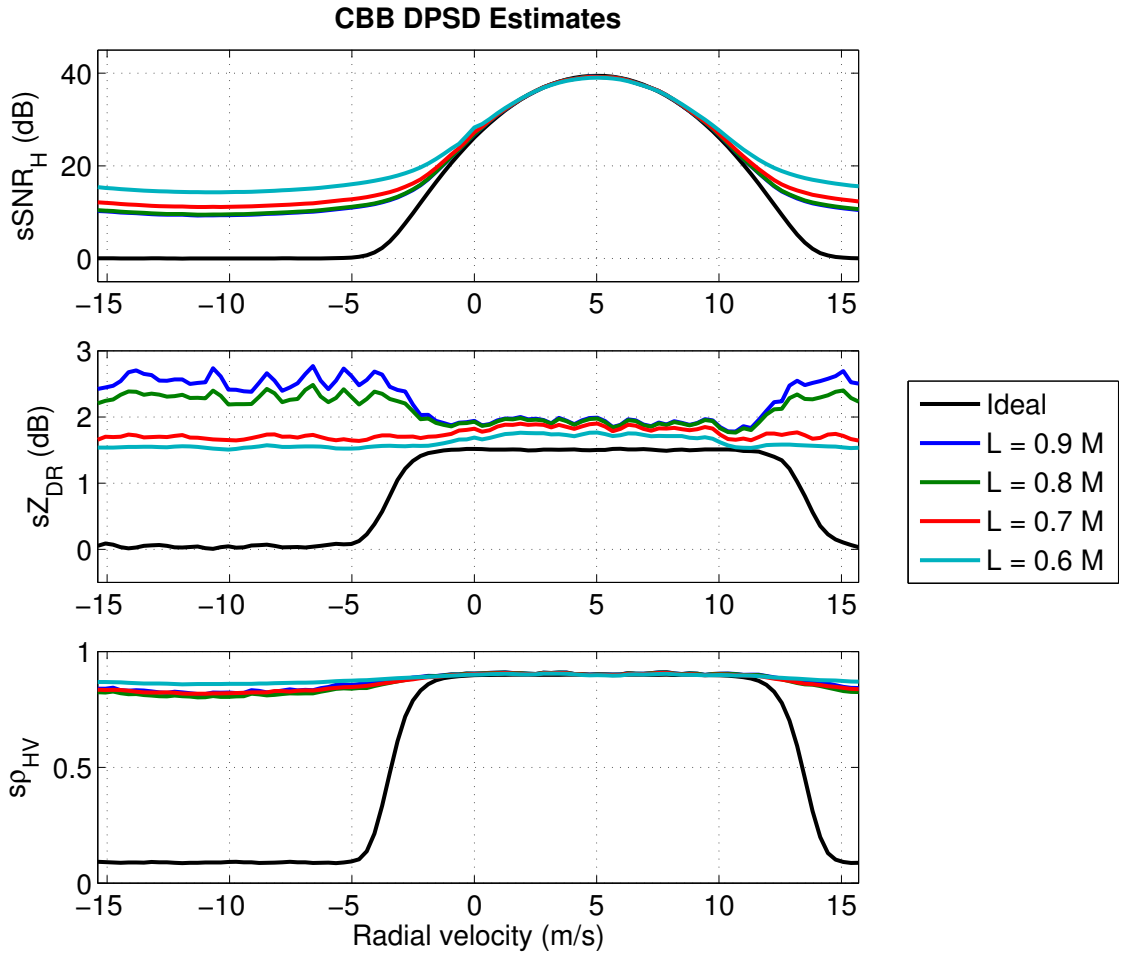

Figure 3.13: Mean of $N_i = 1000$ DPSD estimates obtained with CBB for $L = 0.9M$ (blue), $L = 0.8M$ (green), $L = 0.7M$ (red), $L = 0.6M$ (teal) and the ideal estimates (black): $s\hat{\mathrm{SNR}}_{\mathrm{H}}$ (top), $s\hat{Z}_{\mathrm{DR}}$ (middle), and $s\hat{\rho}_{\mathrm{HV}}$ (bottom).

With the CBB, results similar to those of the MBB are expected. However, because circular wrapping is allowed, higher spectral leakage is also introduced by the lack of coherence between the samples in blocks closer to the ends of the original sample set. The DPSD estimated using CBB for different block lengths is shown in Figure 3.13. Once again the counteracting effects of block length and spectral leakage can be seen. An advantage of the CBB is that it has a larger number of different blocks available to resample, which yields higher variability or "randomness" of the pseudo-realizations. Additionally, it is observed that when compared

to the MBB for a same block length, the biases for frequency components with high sSNR are lower for the CBB although the spectral leakage is higher, as expected. It is important to note that a very aggressive window is used for the analysis, yet the spectral leakage is significant. This leakage contaminates the frequency components of noise, and as such, there is a possibility to wrongfully conclude that there is significant signal where there is none.

3.2.5 Stationary Block Bootstrap (SBB)

Following the SBB scheme defined in Section 3.1.2.4, the pseudo-realizations are obtained as

$$\mathbf{V}'_{\mathrm{H,V}} = \{\mathbf{B}(i_0, j_0), \mathbf{B}(i_1, j_1), \ldots\}, \tag{3.43}$$

where

$$\mathbf{B}(i, j) = \{V_{\mathrm{H,V}}(i), \ldots, V_{\mathrm{H,V}}(i + j - 1)\}, \tag{3.44}$$

i is uniformly distributed in $U(0, j - 1)$ and defines the starting index of the block, and j has a geometric distribution with parameter p and defines the length of the block. For each pseudo-realization, blocks are continuously drawn until the length of the pseudo-realization is equal to or greater than the original sequence. Then, it is truncated to have a length equal to M. The estimates for values of $p = 0.1$, 0.01 and 0.01 are shown in Figure 3.14. The estimates show results similar to those obtained with the MBB and CBB. The biases for frequency components with high sSNR are lower compared to the MBB and CBB. However, due to the randomness

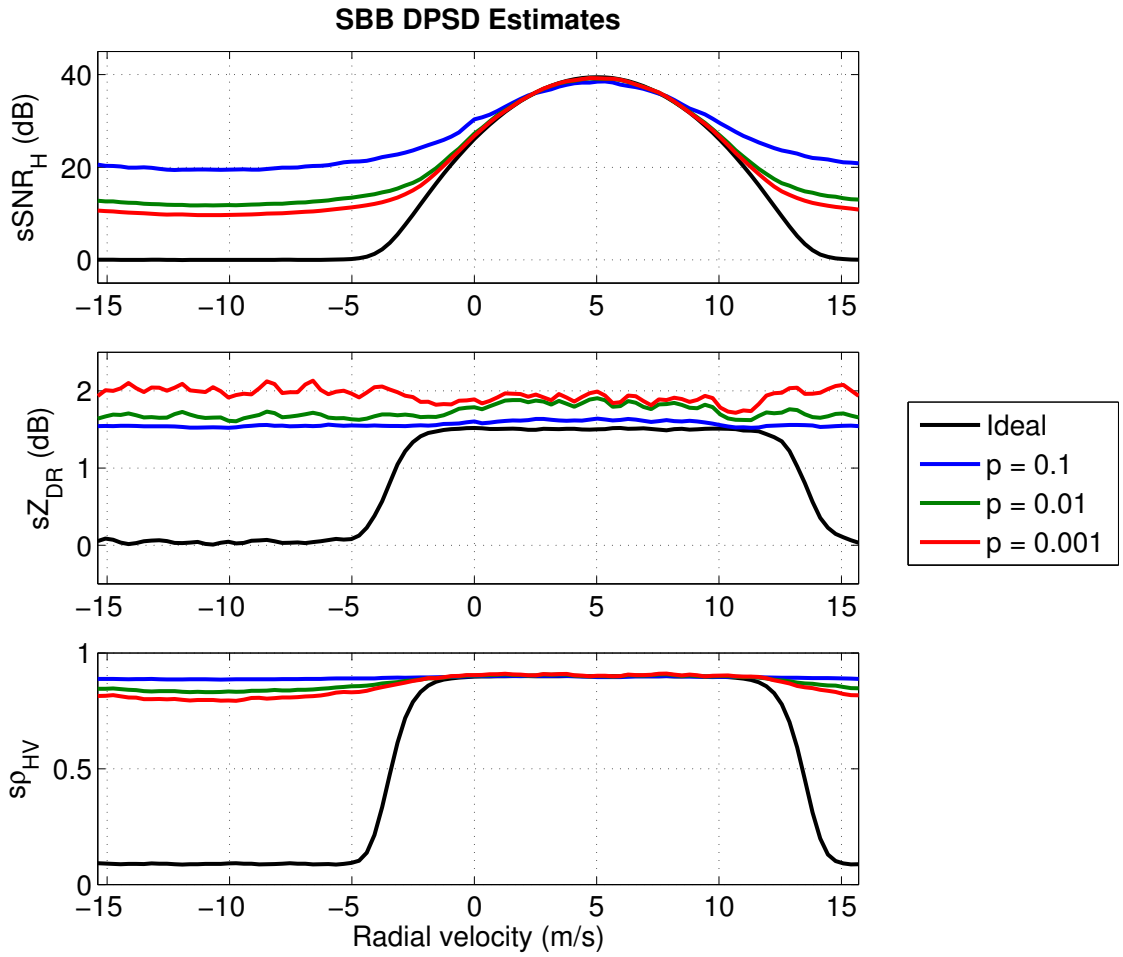

Figure 3.14: Mean of $N_i = 1000$ DPSD estimates obtained with CBB for $p = 0.1$ (blue), $p = 0.01$ (green), $p = 0.001$ (red), and the ideal estimates (black): $s\hat{\mathrm{SNR}}_{\mathrm{H}}$ (top), $s\hat{Z}_{\mathrm{DR}}$ (middle), and $s\hat{\rho}_{\mathrm{HV}}$ (bottom).

of the block length of each pseudo-realization, it is harder to control the spectral leakage on the estimates.

3.2.6 Summary of Block Bootstrap Methods

It has been observed that smaller block lengths can help increase the variability which in turn decreases the errors for the spectral coefficients corresponding to the significant components of the signal, but also decreases the sample-time coherence, which in turn increases the spectral leakage. Herein, the significant components of the signal are the spectral coefficients for which the sSNR is higher than 20 dB. The NBB has the lowest variability for any block length because the blocks are not allowed to overlap. This means that individual blocks from the NBB block population are less correlated. The MBB has a higher variability than the NBB, but lower than both the CBB and SBB. Due to this, the errors in the MBB estimates are higher, but the main advantage of the MBB is that its block population best preserves the signal coherence and thus has the lowest spectral leakage. The CBB has lower errors than the MBB, but higher spectral leakage due to the characteristics of its blocking scheme. The SBB has the lowest errors because of the high variability in the pseudo-realizations. However, it is also the worst at preserving signal coherence and the has highest spectral leakage. With this exercise, it has been understood that the spectral leakage and the error of the block bootstrap methods depend mainly on the block length L and the block arrangement. For the NBB, MBB and CBB methods, the block length L can be adjusted to obtain better estimator quality, while for the SBB this cannot be done. The NBB exhibits side-lobe contamination in the spectra

even with an aggressive window such as the Blackman-Nuttall window; therefore, it can be concluded that this method is not appropriate for spectral estimation of weather signals. The SBB performs poorly for detecting features in the spectra, so it is also discarded from the analysis. Ideally, the spectral leakage characteristics of the MBB and the error characteristics of the CBB would be desired characteristics of a useful block bootstrap method. Since the CBB is an extension of the MBB, the advantages of both methods can be exploited to obtain optimal results both in terms of spectral leakage and statistical errors. Such strategies and considerations are discussed in the following section.

3.3 Considerations in the Design of the Bootstrap DPSD Estimator

The selection of the best block bootstrap method is based on parameters that result in an "optimal" quality of the spectral estimates. The choice of such parameters is a compromise between a number of factors, such as spectral leakage, statistical errors of estimates, and computational cost. Before selecting the block bootstrap method and analyzing the performance with different parameters, the criteria to determine the quality of the DPSD estimates must be established.

3.3.1 Indicators of the Quality of Spectral Estimates

3.3.1.1 Spectral Leakage

As mentioned before, the random processes controlling the changes in the I and Q components are correlated. Provided that the pulse repetition time is small enough, the phasor of the I/Q signal follows a somewhat ordered path (Doviak and Zrnić 2006). Block bootstrap methods randomly resample blocks of data to generate a pseudo-realization, but by doing so the sample-time coherence is disrupted (i.e., discontinuities are added to the phasor's path) increasing spectral leakage. As mentioned previously, this leakage contaminates the frequency components of noise or other weaker signals, which can lead to the wrong conclusion when performing spectral analysis. Therefore, mitigating spectral leakage is important in terms of the quality of the spectral estimates.

Discontinuities The two main sources of spectral leakage for block bootstrapping are block discontinuities and circular discontinuities. A block discontinuity is a transition that occurs between the last (or first) sample of a block and the first (or last) sample of an adjacent block. Clearly, with an increasing number of blocks, there is also an increasing number of discontinuities. A circular discontinuity is a transition that occurs between the last (or first) sample of the original sequence and the first (or last) sample of the same sequence when the signal is extended periodically. Although these incoherencies added by the random resampling of blocks can provide additional variability, they should be kept to a minimum to reduce spectral leakage. To achieve this, it is important to keep the bootstrap block length as large as possible to have

the least amount of discontinuities in the signal while also keeping the population of different blocks as large as possible to have more variability. This tradeoff must be considered in the design to ensure estimates provide useful information with minimal errors.

Data Windowing The choice of the data windowing function to be applied to the original sequence as well as to the pseudo-realizations has an impact on spectral leakage. As shown by Harris (1978), the data windowing function smoothes a time-series signal as samples near the edges are attenuated, which improves the spectral estimates because the extraneous frequency components due to the discontinuity at the edges are attenuated. However, doing so decreases the ability to resolve different peaks in the spectra due to the "smearing" of the power of frequency components into adjacent components, i.e., the main-lobe of the spectral window is wider. If a proper windowing function is not applied to the signal, additional spectral leakage may occur. By de-emphasizing the incoherent pulses, the spectral leakage can be reduced.

3.3.1.2 Statistical Errors

In addition to the other indicators of quality of spectral estimates, the accuracy and precision of the estimates obtained with the block bootstrap methods must be assessed to select the method that produces the best estimates. As it was observed from the preliminary results of implementing the block bootstrap methods to estimate the DPSD, a major tradeoff between the statistical errors and the spectral

leakage is expected. Clearly, the aim is to develop an estimator with small errors and little spectral leakage. However, that is not feasible and a compromise between both must be reached. A reasonable compromise is to determine a block bootstrap method that results in minimal leakage while still providing acceptable error levels for practical purposes. For this, the quality of the estimates of the different block bootstrap methods is analyzed in terms of spectral leakage and statistical errors.

3.3.1.3 Computational Cost

Because the bootstrap methods inherently depend on generating a large number of pseudo-realizations from one measurement, their computational cost is also of interest since we would like the Bootstrap DPSD estimator to be viable in an operational environment (i.e., a real-time implementation should be feasible). This is especially important because there are typically hundreds of thousands of I/Q signals per radar scan, which can quickly increase the computational cost by a few orders of magnitude depending on the complexity of the blocking scheme and the number of pseudo-realizations generated. While this is noted, a proper analysis is beyond the scope of this work, though a discussion about the resampling scheme will be presented later.

3.3.2 Strategies to Improve the Quality of the Spectral Estimates

Although bootstrapping weather radar I/Q signals can enable spectral estimation when the available number of independent spectra is limited, improvements must be made to obtain the best possible results. The strategies described in this section

work independently to optimize the quality of the spectral estimates; thus, the core of the Bootstrap DPSD estimator is a combination of the best block bootstrap method and these pre-processing strategies.

3.3.2.1 Signal Coherency Correction

To mitigate the effects of discontinuities, coherency corrections can be applied to the blocks of a pseudo-realization. These corrections consist in multiplying an adjacent block in a pseudo-realization by a complex scalar. Borowska et al. (2016) presents a phase correction technique for phased array radar signals similar to the one presented in this work, though the strategy presented here is better suited for polarimetric radar I/Q time-series signals. In general, these correction factors have three degrees of freedom: the block used as reference, the polarimetric channel used as reference, and the type of correction.

The propagation of the correction factor can be either forward or backward depending on block used as a reference to compute the correction factor. That is

$$C_i = \begin{cases} \frac{B'_{i-1}(L-1)}{B'_i(0)} = C_i^+ & \text{for forward correction} \\ \frac{B'_{i+1}(0)}{B'_i(L-1)} = C_i^- & \text{for backward correction,} \end{cases} \tag{3.45}$$

where i indicates the index of the block (within the pseudo-realization) to be corrected. A superscript by the correction factor indicates whether it is a forward or backward correction, and the lack of a superscript indicates that the propagation direction is irrelevant. The first element of the block has an index of 0, while the

last element of the block has an index of $L-1$. The propagation of the correction indicates whether the i-th block is corrected using the last element of the previous block (forward propagation), or the first element of the next block (backward propagation). When applying a forward (or backward) correction, the blocks must be drawn with an additional data point (i.e., a block length of $L+1$) because the first (or last) pulse in the corrected block will be equal to the last (or first) pulse of the contiguous block and, as such, should be eliminated. Because the I/Q signals are random processes, the choice of forward or backward correction should provide similar results since the correction factors are random. However, from our experience, it is best to keep an uncorrected block around the center of the signal as the reference to correct the other blocks because the data windowing functions have maximum weight around $M/2$. In such case, if the center block is the i-th block, the blocks with indices greater than i should be corrected using forward correction, and those with indices lesser than i should be corrected using backward correction.

The type of correction could be based on magnitude, phase, or both. The corrected pseudo-realization then becomes

$$\mathbf{V}' = \left\{C_0'\mathbf{B}_0', C_1'\mathbf{B}_1', \ldots, C_{N-1}'\mathbf{B}_{N-1}'\right\} = \{C_i'\mathbf{B}_i'\} \tag{3.46}$$

$$C_i' = \begin{cases} |C_i| & \text{for magnitude correction} \\ e^{j\arg(C_i)} & \text{for phase correction} \\ C_i & \text{for magnitude and phase correction,} \end{cases} \tag{3.47}$$

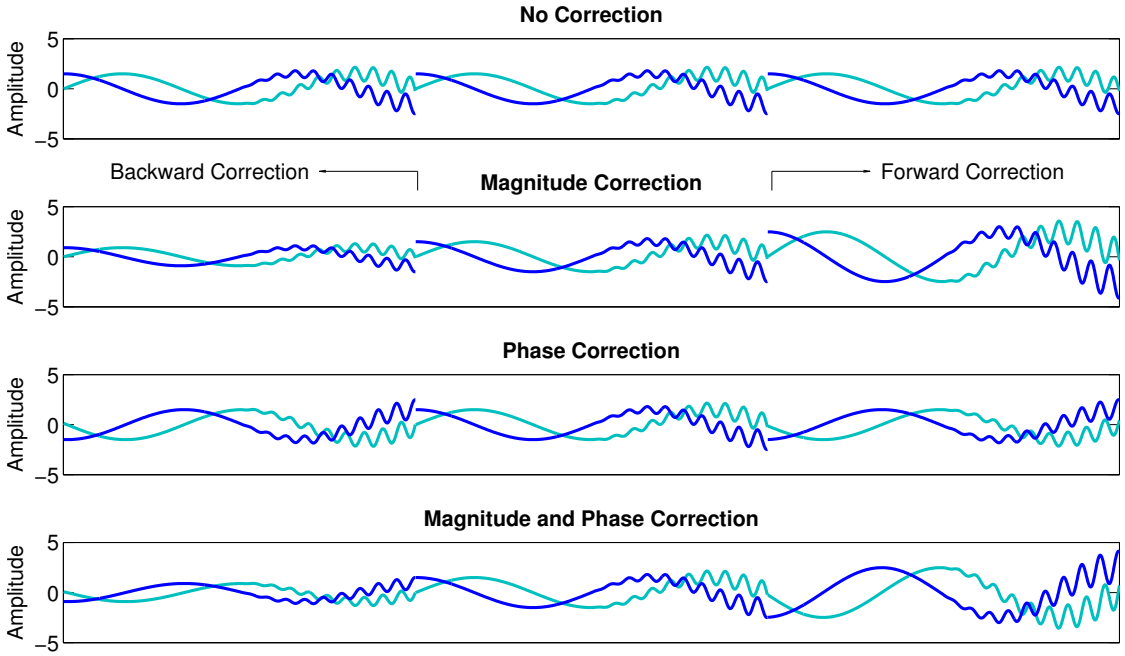

Figure 3.15: Correcting sample-time coherency on a periodically extended complex sinusoid using different methods.

Figure 3.15 shows the propagation and the complex constant correction methods that can be applied to a signal. Here, the signal used to illustrate this concept is a sum of complex sinusoids of different frequencies. The block of the uncorrected signal is in the center, while the signal is periodically extended to the left and to the right. The first row shows the extended signal with no corrections, the second row is corrected by magnitude, the third row is corrected by phase, and the last row is corrected by magnitude and phase. Additionally, the blocks on the left side are backward-corrected, whereas the blocks on the right side are forward-corrected. Clearly, the magnitude-and-phase-corrected signal appears to have a smoother transition for both its real and imaginary parts while the magnitude- and phase-corrected signals are inferior in correcting the discontinuities. It can be

inferred that the magnitude and phase correction provides the best discontinuity mitigation, and thus, is the preferred type of correction.

Although it is not explicitly stated in the formulas, the correction factors depend on other correction factors applied to other blocks prior to the correction of the i-th block. For example, consider the case where all blocks of a particular pseudo-realization are corrected with forward correction in magnitude and phase. If $\tilde{\mathbf{B}}'_1 = C'_1\mathbf{B}'_1$ is the first block of the pseudo-realization after a coherency correction, the second block should be computed as $\tilde{\mathbf{B}}'_2 = C'_1C'_2\mathbf{B}'_2$. This is done to consistently propagate the coherence throughout the blocks, otherwise there would still exist discontinuities in the sequence. From this, it should be clear that the corrections are propagated along the pseudo-realization, which is one reason why it is important to keep the number of blocks as small as possible when corrections are applied.

So far, two degrees of freedom of the correction factor have been presented. The last one deals with which polarimetric channels are used as a reference to apply the corrections. That is, the correction factor may be applied to both channels based on the H- or V-channel, to each channel individually, or to both channels simultaneously using a combined correction factor. A correction based on the H-channel is

$$\begin{aligned}\mathbf{V}'_{\mathrm{H}} &= \left\{C'_{\mathrm{H},0}\mathbf{B}'_{\mathrm{H},0}, C'_{\mathrm{H},1}\mathbf{B}'_{\mathrm{H},1}, \ldots, C'_{\mathrm{H},N-1}\mathbf{B}'_{\mathrm{H},N-1}\right\} = \{C'_{\mathrm{H},i}\mathbf{B}'_{\mathrm{H},i}\} \\ \mathbf{V}'_{\mathrm{V}} &= \left\{C'_{\mathrm{H},0}\mathbf{B}'_{\mathrm{V},0}, C'_{\mathrm{H},1}\mathbf{B}'_{\mathrm{V},1}, \ldots, C'_{\mathrm{H},N-1}\mathbf{B}'_{\mathrm{V},N-1}\right\} = \{C'_{\mathrm{H},i}\mathbf{B}'_{\mathrm{V},i}\},\end{aligned} \tag{3.48}$$

where the $C'_{\mathrm{H},i}$ are correction factors based on blocks of the H-channel. Similarly, a correction based on the V-channel is

$$\begin{aligned}\mathbf{V}'_{\mathrm{H}} &= \left\{C'_{\mathrm{V},0}\mathbf{B}'_{\mathrm{H},0}, C'_{\mathrm{V},1}\mathbf{B}'_{\mathrm{H},1}, \ldots, C'_{\mathrm{V},N-1}\mathbf{B}'_{\mathrm{H},N-1}\right\} = \{C'_{\mathrm{V},i}\mathbf{B}'_{\mathrm{H},i}\} \\ \mathbf{V}'_{\mathrm{V}} &= \left\{C'_{\mathrm{V},0}\mathbf{B}'_{\mathrm{V},0}, C'_{\mathrm{V},1}\mathbf{B}'_{\mathrm{V},1}, \ldots, C'_{\mathrm{V},N-1}\mathbf{B}'_{\mathrm{V},N-1}\right\} = \{C'_{\mathrm{V},i}\mathbf{B}'_{\mathrm{V},i}\},\end{aligned} \tag{3.49}$$

where the $C'_{\mathrm{V},i}$ are correction factors based on blocks of the V-channel. The choice of either the H- or V-channel based correction should yield similar results for the DPSD, although the spectral leakage will be lower for H-channel if using the H-channel based correction, and vice versa. The individual correction for each channel is

$$\begin{aligned}\mathbf{V}'_{\mathrm{H}} &= \left\{C'_{\mathrm{H},0}\mathbf{B}'_{\mathrm{H},0}, C'_{\mathrm{H},1}\mathbf{B}'_{\mathrm{H},1}, \ldots, C'_{\mathrm{H},N-1}\mathbf{B}'_{\mathrm{H},N-1}\right\} = \{C'_{\mathrm{H},i}\mathbf{B}'_{\mathrm{H},i}\} \\ \mathbf{V}'_{\mathrm{V}} &= \left\{C'_{\mathrm{V},0}\mathbf{B}'_{\mathrm{V},0}, C'_{\mathrm{V},1}\mathbf{B}'_{\mathrm{V},1}, \ldots, C'_{\mathrm{V},N-1}\mathbf{B}'_{\mathrm{V},N-1}\right\} = \{C'_{\mathrm{V},i}\mathbf{B}'_{\mathrm{V},i}\}.\end{aligned} \tag{3.50}$$

And the combined correction is

$$\begin{aligned}\mathbf{V}'_{\mathrm{H}} &= \left\{C'_{\mathrm{X},0}\mathbf{B}'_{\mathrm{H},0}, C'_{\mathrm{X},1}\mathbf{B}'_{\mathrm{H},1}, \ldots, C'_{\mathrm{X},N-1}\mathbf{B}'_{\mathrm{H},N-1}\right\} = \{C'_{\mathrm{X},i}\mathbf{B}'_{\mathrm{H},i}\} \\ \mathbf{V}'_{\mathrm{V}} &= \left\{C'_{\mathrm{X},0}\mathbf{B}'_{\mathrm{V},0}, C'_{\mathrm{X},1}\mathbf{B}'_{\mathrm{V},1}, \ldots, C'_{\mathrm{X},N-1}\mathbf{B}'_{\mathrm{V},N-1}\right\} = \{C'_{\mathrm{X},i}\mathbf{B}'_{\mathrm{V},i}\}\end{aligned} \tag{3.51}$$

Two variants of the combined correction were considered:

$$C_{\mathrm{X},i} = \begin{cases} \frac{B'_{\mathrm{H},i-1}(L-1)+B'_{\mathrm{V},i-1}(L-1)}{B'_{\mathrm{H},i}(0)+B'_{\mathrm{V},i}(0)} = C^{+}_{\mathrm{X},i} & \text{for forward correction} \\ \frac{B'_{\mathrm{H},i+1}(0)+B'_{\mathrm{V},i+1}(0)}{B'_{\mathrm{H},i}(L-1)+B'_{\mathrm{V},i}(L-1)} = C^{-}_{\mathrm{X},i} & \text{for backward correction,} \end{cases} \tag{3.52}$$

and

$$C_{\mathrm{X},i} = \begin{cases} \frac{1}{2}\left[\frac{B'_{\mathrm{H},i-1}(L-1)}{B'_{\mathrm{H},i}(0)} + \frac{B'_{\mathrm{V},i-1}(L-1)}{B'_{\mathrm{V},i}(0)}\right] = C^{+}_{\mathrm{X},i} & \text{for forward correction} \\ \frac{1}{2}\left[\frac{B'_{\mathrm{H},i+1}(0)}{B'_{\mathrm{H},i}(L-1)} + \frac{B'_{\mathrm{V},i+1}(0)}{B'_{\mathrm{V},i}(L-1)}\right] = C^{-}_{\mathrm{X},i} & \text{for backward correction.} \end{cases} \tag{3.53}$$

However, the latter variant is selected because it is more robust for a wide range of ϕ_{DP} values (e.g., the denominator in 3.52 would become small or tend to zero as the value of ϕ_{DP} gets close to 180°, which can produce unexpected results). It should be noted that the selection of the channel used for the correction is independent of the choice of the type or propagation. Figure 3.16 is provided to illustrate how the different correction factors can be applied to the H- and V-channel signals.

To summarize the correction methods, the following set of expressions are provided for a clearer interpretation on how these corrections are applied. The general form of the corrected signal becomes

$$\begin{aligned} \mathbf{V}'_{\mathrm{H}} &= \{C''_{\mathrm{H},i}\mathbf{B}'_{\mathrm{H},i}\} \\ \mathbf{V}'_{\mathrm{V}} &= \{C''_{\mathrm{V},i}\mathbf{B}'_{\mathrm{V},i}\}, \end{aligned} \tag{3.54}$$

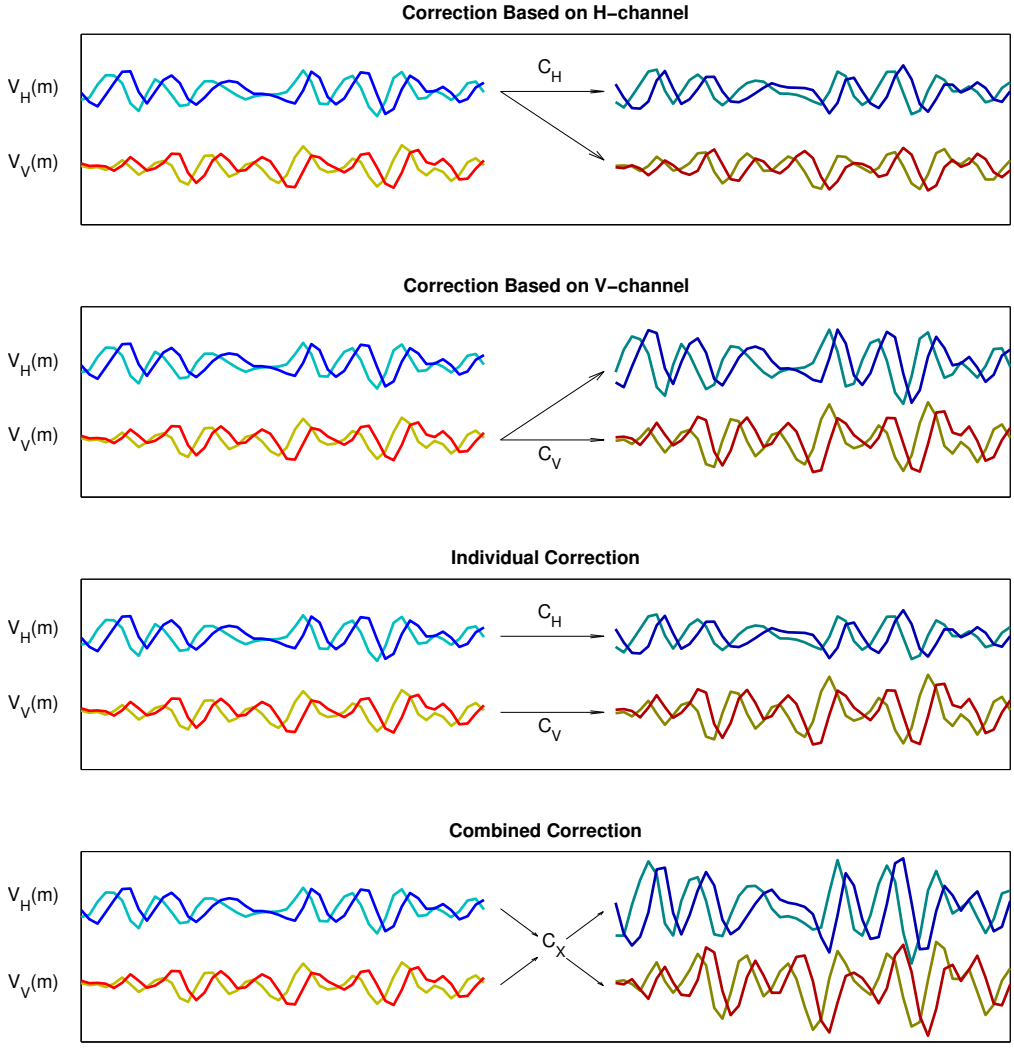

Figure 3.16: Methods to apply the correction factors on the H- and V-channel signals.

for $0 \leq i \leq N-1$, where i is the block index within the pseudo-realization, N is the number of blocks in the pseudo-realization, and the correction factors $C''_{\mathrm{H},i}$ and $C''_{\mathrm{V},i}$ depend on how the channels are corrected as

$$C''_{\mathrm{H},i}, C''_{\mathrm{V},i} = \begin{cases} C'_{\mathrm{H},i}, C'_{\mathrm{H},i} & \text{for H-channel based correction} \\ C'_{\mathrm{V},i}, C'_{\mathrm{V},i} & \text{for V-channel based correction} \\ C'_{\mathrm{H},i}, C'_{\mathrm{V},i} & \text{for individual correction} \\ C'_{\mathrm{X},i}, C'_{\mathrm{X},i} & \text{for combined correction.} \end{cases} \tag{3.55}$$

Then, the factors $C'_{\mathrm{H},i}$, $C'_{\mathrm{V},i}$, and $C'_{\mathrm{X},i}$ depend on the complex constant as

$$C'_{x,i} = \begin{cases} |C_{x,i}| & \text{for magnitude correction} \\ e^{j \arg(C_{x,i})} & \text{for phase correction} \\ C_{x,i} & \text{for magnitude and phase correction,} \end{cases} \tag{3.56}$$

for x = H,V or X, and where the $C_{x,i}$ factors depend on whether the previous or next block is used as a reference, as

$$C_{\mathrm{H},i} = \begin{cases} \frac{B'_{\mathrm{H},i-1}(L-1)}{B'_{\mathrm{H},i}(0)} = C^{+}_{\mathrm{H},i} & \text{for forward correction} \\ \frac{B'_{\mathrm{H},i+1}(0)}{B'_{\mathrm{H},i}(L-1)} = C^{-}_{\mathrm{H},i} & \text{for backward correction,} \end{cases}$$

$$C_{\mathrm{V},i} = \begin{cases} \frac{B'_{\mathrm{V},i-1}(L-1)}{B'_{\mathrm{V},i}(0)} = C^{+}_{\mathrm{V},i} & \text{for forward correction} \\ \frac{B'_{\mathrm{V},i+1}(0)}{B'_{\mathrm{V},i}(L-1)} = C^{-}_{\mathrm{V},i} & \text{for backward correction,} \end{cases} \tag{3.57}$$

$$C_{\mathrm{X},i} = \begin{cases} \frac{1}{2}\left[\frac{B'_{\mathrm{H},i-1}(L-1)}{B'_{\mathrm{H},i}(0)} + \frac{B'_{\mathrm{V},i-1}(L-1)}{B'_{\mathrm{V},i}(0)}\right] = C^{+}_{\mathrm{X},i} & \text{for forward correction} \\ \frac{1}{2}\left[\frac{B'_{\mathrm{H},i+1}(0)}{B'_{\mathrm{H},i}(L-1)} + \frac{B'_{\mathrm{V},i+1}(0)}{B'_{\mathrm{V},i}(L-1)}\right] = C^{-}_{\mathrm{X},i} & \text{for backward correction.} \end{cases}$$

Because some concepts need to be introduced in order to simplify the analysis, the selection of the best channel correction method will be deferred to later.

3.3.2.2 Extended Signal

Although the corrected data provides an added variability to the pseudo-realizations, it is desired to keep the number of original (uncorrected) samples as high as possible, regardless of the coherence correction method used, so that the estimated spectra are as close to the true spectra as possible. The MBB is suited for this task because it introduces fewer discontinuities when the block length is large. However, by doing so, the block population available for resampling gets reduced significantly. The CBB can overcome this limitation since it allows large blocks and has good variability, but the spectral leakage is very high. In the limit when the block length

is M (i.e., same as the original sequence), the signal is as coherent as possible. Though by assigning blocks of length M, the MBB would only have one block in the population. However, the CBB has exactly M blocks of length M available because the signal is extended periodically. If the samples of the periodically extended signal were coherent, the CBB would have the best performance of all methods. Thus, the coherence correction can be applied to the periodic extensions of the original sequence to improve the quality of the estimates. Therefore, to benefit from both methods, an extended I/Q signal with coherency corrections is proposed. With this idea, the extended signal is kept as coherent as possible by applying the correction to the periodic extension, while also keeping the original signal unaltered. To create this extended signal (Figure 3.17), three instances of the signal $\mathbf{V}$ are concatenated. Then, the left extension is backward-corrected and the right extension is forward-corrected. That is,

$$\mathbf{X}_{\mathrm{H,V}} = \{\mathbf{V}^{\mathrm{L}}_{\mathrm{H,V}}, \mathbf{V}_{\mathrm{H,V}}, \mathbf{V}^{\mathrm{R}}_{\mathrm{H,V}}\}, \tag{3.58}$$

where

$$\begin{aligned} \mathbf{V}^{\mathrm{L}}_{\mathrm{H,V}} &= C''^{-}_{\mathrm{H,V}}\{V_{\mathrm{H,V}}(0), \ldots, V_{\mathrm{H,V}}(M-2)\}, \\ \mathbf{V}^{\mathrm{R}}_{\mathrm{H,V}} &= C''^{+}_{\mathrm{H,V}}\{V_{\mathrm{H,V}}(1), \ldots, V_{\mathrm{H,V}}(M-1)\}, \end{aligned} \tag{3.59}$$

and the correction factors $C''^{-}_{\mathrm{H,V}}$ and $C''^{+}_{\mathrm{H,V}}$ can be obtained with (3.55)-(3.57) depending on the type of correction. Here, the superscripts indicate backward and forward corrections specifically, while the type of correction and the polarimetric channel(s) used as reference(s) are unspecified. It should also be noted that the extensions are of length $M-1$ due to the fact that, with the correction, the first (or last) element

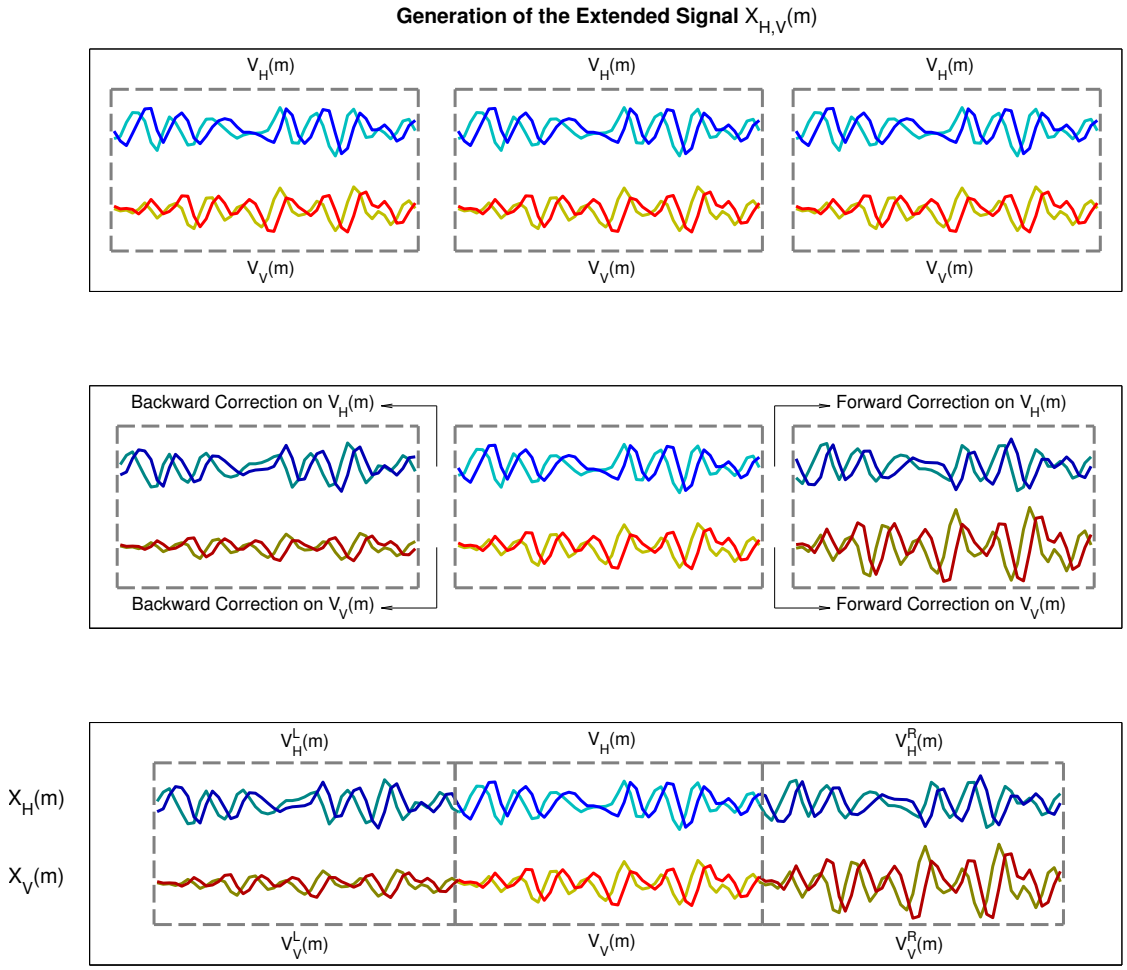

Figure 3.17: Generation of the extended signal $X_{\mathrm{H,V}}(m)$. The left and right extensions of the original sequence are denoted by the superscripts L and R, respectively; while the channel of polarization is indicated by the H and V subscripts, for horizontal and vertical channels, respectively.

of a block is matched to the last (or first) element of the adjacent block. The length of the extended signal then becomes $M' = 3M - 2$, and the block population for the extended signal is defined as

$$\mathcal{B} = \{\mathbf{B}_0, \mathbf{B}_1, \ldots, \mathbf{B}_{N'-1}\}, \tag{3.60}$$

where

$$\mathbf{B}_j = \{X_{\mathrm{H,V}}(j), \ldots, X_{\mathrm{H,V}}(j + M - 1)\}. \tag{3.61}$$

With the use of an extended signal, the block population increases to $N' = 2M - 2$, where the block length is now M. However, a pseudo-realization obtained by resampling from this set of blocks is still prone to spectral leakage, albeit lesser than the case with no coherency correction applied.

3.3.2.3 Ratio of Original Samples

To further improve the quality of the bootstrapped estimates, a careful selection of the blocks can be made. As mentioned previously, by keeping a larger number of original samples in a pseudo-realization, it is guaranteed that the spectral estimates will be less biased. Logically, pseudo-realizations with more discontinuities (corrected or not) are more likely to contain more spectral leakage. Hence, instead of using all the blocks of the extended signal, it is possible to select the set of blocks

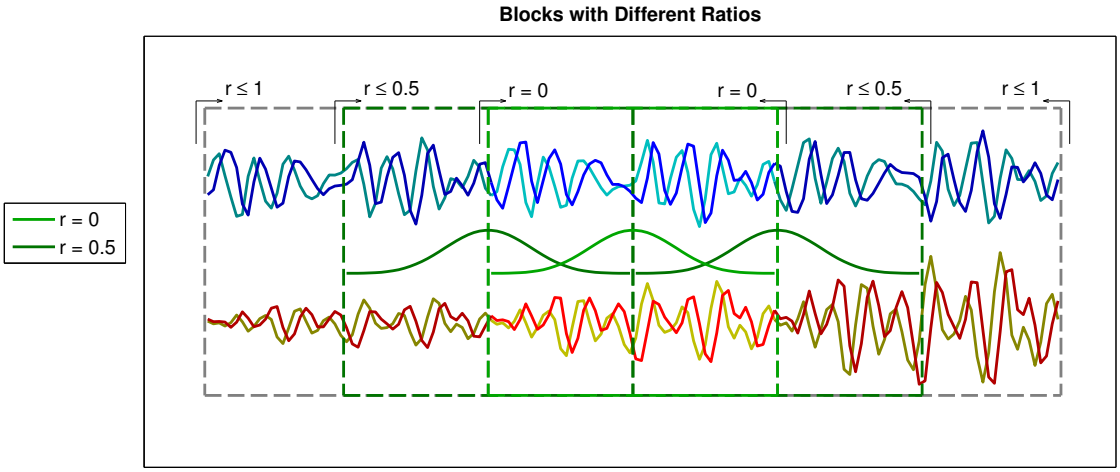

Figure 3.18: Applying data windows on blocks with different ratio.

that contain more original samples than corrected samples. The concept of the ratio of corrected samples in a block (or pseudo-realization) is introduced as

$$r = \frac{N_{\text{corrected}}}{M}, \tag{3.62}$$

where $N_{\text{corrected}}$ is the number of corrected samples in the block (or pseudo-realization). In this sense, the original sequence has a ratio $r = 0$, while the $(M/2)$ and $(3M/2)$-th blocks have a ratio close to $r = 0.5$, and the first and the last blocks have a ratio close to $r = 1$. For example, by establishing a threshold for blocks that have a maximum ratio of $r = 0.5$, it can be guaranteed that all the blocks in the reduced population will have at least 50% of the original samples (Figure 3.18). Clearly, this strategy can additionally reduce the spectral leakage due to the incoherencies remaining in the periodic extension of the original signal.

While the selection of r can be made arbitrarily with tradeoffs in spectral leakage and error statistics, its automatic determination is more convenient. Due to

how the blocks are arranged, r depends on the data windowing function used. The spectral leakage is reduced with this strategy mainly because the data points near the discontinuities are de-emphasized, while more weight is placed on the original samples. Essentially, it is comparable to applying a sliding data window on a signal, while allowing the signal to be periodically extended. A similar approach is presented by Barbé et al. (2010), where Welch's method is extended by allowing segments to overlap circularly. The segments that overlap circularly use windows of different length to deal with the circular discontinuities. However, this method still loses frequency resolution if the length of the segments is not equal to the number of samples. Moreover, the use of different windows for the segments results in poor SLL for spectral estimation. Another approach where different data windows are used is with the Thomson's multi-taper method (MTM) for PSD estimation (Thomson 1982). In this method, a discrete number of orthogonal windows are used to capture different characteristics of the spectra, then the partial PSD estimates are averaged together. However, this method is not suitable for the spectral analysis of weather signals because there is no control over the SLL, and therefore estimates show can be severely biased. The use of an extended signal along with a maximum ratio of corrected samples allows extracting spectral information from data points that are attenuated by the data windowing function without introducing additional biases in terms of both spectral leakage and statistical errors. As mentioned before, the ratio that maximizes the amount of information depends on the data windowing function

used in the analysis. A good compromise between spectral leakage and statistical errors is obtained by limiting the selection to blocks with a maximum ratio of:

$$r = \frac{1 - \sqrt{\frac{1}{M}\sum_{m=0}^{M-1} |d(m)|^2}}{2} = \frac{1 - \sqrt{\alpha}}{2}, \tag{3.63}$$

where α is the mean power of the data windowing function, and the amplitude $\sqrt{\alpha}/2$ is related to the number of points in the data window that contribute the most to the spectral estimate. It is assumed that the data windows are normalized to a maximum amplitude of 1. With this definition, r is bounded between 0.5, where half of the samples are corrected, and 0, where none of the samples are corrected. It can be easily seen that more aggressive windows have a lower window power, thus leading to higher maximum ratio and vice versa. For example, if only the original sequence is used to estimate the PSD, with the use of a data window, part of the information is lost due to the end samples being severely attenuated. The setting of a maximum ratio threshold for the resampling of blocks can be thought of as if a data window is shifted and applied on the extended signal to recover information that was attenuated by the conventional application of the data window. Less aggressive windows allow more power from the corrected samples, therefore their corresponding maximum ratio is lower than for more aggressive windows. In other words, the amplitude of the data windowing function determines the number of corrected samples, as weighted by the window, that can be present on either end of a sequence before the spectral leakage becomes significant.

3.3.2.4 Power Correction

An additional step is taken to correct the power of the I/Q pseudo-realizations. Since the coherence correction factors scale both magnitude and phase of corrected samples, a power correction must be applied to preserve the power of the original signal. Let $\hat{P}_{\mathrm{H,V}}$ be the estimated average power of the H- and V-channels of the original signal, and $\hat{P}'_{\mathrm{H,V}}$ be the average power of the H- and V-channels of a I/Q pseudo-realization. The average power of each pseudo-realization is matched to the average power of the original signal; mathematically,

$$V''_{\mathrm{H,V}}(m) = \sqrt{\frac{\hat{P}_{\mathrm{H,V}}}{\hat{P}'_{\mathrm{H,V}}}} V'_{\mathrm{H,V}}(m), \tag{3.64}$$

so that

$$\hat{P}''_{\mathrm{H,V}} = \hat{P}_{\mathrm{H,V}}. \tag{3.65}$$

3.3.2.5 Bias Correction

In general, the expected value of the DPSD estimate and the true value are related by

$$E[s\hat{Z}_{\mathrm{dr}}(k)] = sZ_{\mathrm{dr}}(k) + \mathrm{bias}[s\hat{Z}_{\mathrm{dr}}](k), \tag{3.66}$$

and

$$E[s\hat{\rho}_{\mathrm{HV}}(k)] = s\rho_{\mathrm{HV}}(k) + \mathrm{bias}[s\hat{\rho}_{\mathrm{HV}}](k), \tag{3.67}$$

where sZ_{dr} is the linear spectral differential reflectivity (i.e., $sZ_{\mathrm{DR}} = 10 \log sZ_{\mathrm{dr}}$). The analytical expressions of the statistical errors of $s\hat{Z}_{\mathrm{DR}}$ and $s\hat{\rho}_{\mathrm{HV}}$ were determined

in Yu et al. (2012). The biases of the DPSD depend on the number of independent spectra K, the spectral SNR of the H- and V-channels, $s\mathrm{SNR}_{\mathrm{H,V}}$, and the real spectral correlation coefficient, $s\rho_{\mathrm{HV}}$. The bias expressions derived from Yu et al. (2012) are:

$$\frac{\mathrm{bias}[s\hat{Z}_{\mathrm{dr}}](k)}{s\hat{Z}_{\mathrm{dr}}(k)} = \frac{1}{\beta K}\left[1 - s\hat{\rho}^2_{\mathrm{HV}}(k)\right] \tag{3.68}$$

$$\frac{\mathrm{bias}[s\hat{\rho}_{\mathrm{HV}}](k)}{s\hat{\rho}_{\mathrm{HV}}(k)} = \frac{1}{\beta K}\left\{\frac{[1 - s\hat{\rho}^2_{\mathrm{HV}}(k)]^2}{4s\hat{\rho}^2_{\mathrm{HV}}(k)}\right\}, \tag{3.69}$$

where β is introduced in this work as a error scaling factor accounting for the changes in the quality of bootstrapped estimates prior to the bias correction, and the estimates of the DPSDs are used rather than the true DPSDs. The sSNR terms are neglected because it is assumed that the SNR of the signal of interest is high (more than 20 dB). The factor β is determined by fitting different values of r such that the error is minimized for all K, as

$$\beta = \begin{cases} (1-r)^{-3.3} - 2(1-r)^{1.1} & \text{for } K = 1 \\ (1-r)^{-4.5} - (1-r)^{-2.1} & \text{for } K > 1, \end{cases} \tag{3.70}$$

where r is the maximum ratio defined by (3.63), and K the number of independent spectra. By replacing (3.68) and (3.69) in (3.67), the following expressions are obtained

$$s\tilde{Z}_{\mathrm{dr}}(k) = s\hat{Z}_{\mathrm{dr}}(k)\left\{1 - \frac{1}{\beta K}[1 - s\hat{\rho}^2_{\mathrm{HV}}(k)]\right\} \tag{3.71}$$

$$s\tilde{\rho}_{\mathrm{HV}}(k) = s\hat{\rho}_{\mathrm{HV}}(k)\left\{1 - \frac{1}{\beta K}\left\{\frac{[1 - s\hat{\rho}^2_{\mathrm{HV}}(k)]^2}{4s\hat{\rho}^2_{\mathrm{HV}}(k)}\right\}\right\}, \tag{3.72}$$

where the tilde denotes the bias corrected estimate to distinguish it from the true DPSD.

3.4 Analysis and Optimal Selection of Strategies

While some parameters have already been selected, there are others that still need further analysis before a final selection can be done. So far it has been established that neither the MBB nor the CBB were by themselves the best block bootstrap methods, which is why the periodic extension of the signal and the maximum ratio strategies have been proposed. In this sense, the block bootstrap method of choice is essentially the MBB because the blocks are not allowed to wrap around circularly on the extended signal. However, the periodic extension idea was inspired by the CBB, even though the method is not a CBB under the formal definition because of the coherency corrections. A more appropriate description is as a hybrid between the MBB and the CBB. Hereafter, the proposed method is referred to as the hybrid block bootstrap (or HBB). The parameters that give useful DPSD estimates under this method have been found to be $L = M$ (i.e., blocks of the same size as the original I/Q signal), while an optimal value for K' is yet to be determined (and will be analyzed later in this section). Moreover, with $L = M$ and also the limitation set by a maximum value of r, the block population $\mathcal{B}$ is further reduced to a point in which it is useful to compare a deterministic resampling scheme, as opposed to a random resampling scheme, i.e., using all or a subset of the possible pseudo-realizations in a systematic order, versus randomly selecting the pseudo-realizations.

The maximum ratio of corrected samples establishes a limit on the block population to control the leakage that is introduced in the spectral coefficients. The selection of the maximum ratio can be made arbitrarily, although the value that maximizes the information in the set of pseudo-realizations can be computed and it depends on the data windowing function.

The parameter β for correcting the biases of the DPSD estimates is dependent on the maximum ratio. While simpler expressions for β have been studied, the current form, which was obtained empirically (as explained in the previous section), gives satisfactory results. Additionally, it can be automatically obtained for different data windows and number of independent spectra, which could further improve the quality of the Bootstrap DPSD estimates.

By having selected most parameters, the dimension of the problem is simplified. A statistical assessment of the quality of the estimates using different polarimetric channel correction methods was mentioned previously and will be analyzed next, followed by a comparison of bootstrap and deterministic resampling schemes.

3.4.1 Performance of Channel Correction Methods

Two of the three aspects of the correction factor have been analyzed in previous sections. An analysis of the polarization channel correction must be made to determine which one yields the best results. Since it is difficult to objectively assess the performance of each channel correction method, the statistical quality of the estimates obtained with each variant must be analyzed (Figure 3.19). To estimate the DPSD, the HBB is performed, as indicated earlier. The simulation parameters

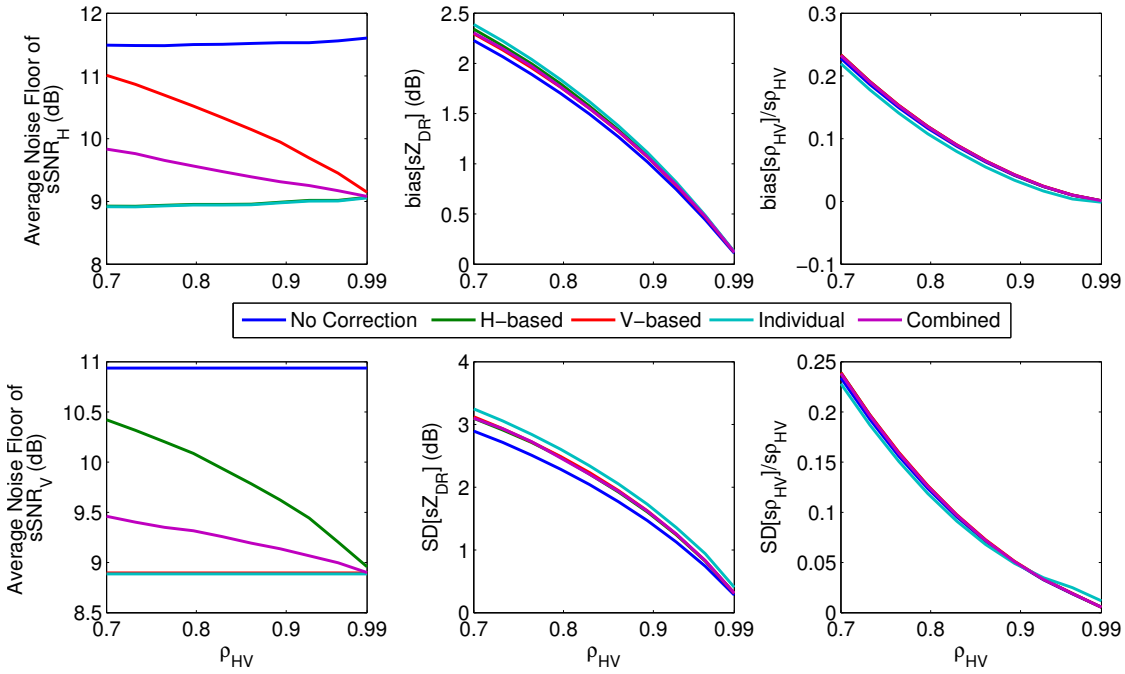

Figure 3.19: Statistics of the estimator quality for different channel correction methods as a function of the correlation coefficient ($s\rho_{\mathrm{HV}}$). The average noise floor as a measure of spectral leakage (left), the bias and stabdard deviation (SD) of $s\hat{Z}_{\mathrm{DR}}$ (center), and the bias and standard deviation of $s\hat{\rho}_{\mathrm{HV}}$ (right) are shown. The simulation parameters are shown in Table 3.1, but with SNR = 40 dB and a von Hann window.

used for this analysis are similar to those in Table 3.1, though the SNR is set to 40 dB, and the data window used in the analysis is a von Hann window. This is done in order to emphasize the spectral leakage as a quality indicator, since the errors (bias and standard deviation) are expected to be similar for all cases. The spectral leakage is measured by the average noise floor in the PSD of both channels, while the accuracy and precision are measured by the statistical errors of the DPSD. A proper description on how these statistical analyses are performed will be presented in Chapter 4. For now, it suffices to say that the average noise floor is computed as the average SNR of frequency components with $s\hat{\mathrm{SNR}} < 20$ dB over all independent realizations, while the bias and standard deviation are computed as the averages for frequency components with $s\hat{\mathrm{SNR}} \geq 20$ dB based on to the modeled value of Z_{DR} and ρ_{HV}, and over all independent realizations. The ρ_{HV} of the signal is varied to highlight the effects of the different polarization channel correction methods. For high ρ_{HV}, all methods should have comparable performance given that the H- and V-channel signals are very similar, and thus the correction factors based on any method should be roughly the same. For lower ρ_{HV}, the correction factors can no longer appropriately correct both channels simultaneously. If the correction is based on either the H- or V-channel, either the V- or H-channel, respectively, will not be completely matched and will be affected with higher spectral leakage, as can be seen in the green curve of the top-left panel and red curve of the bottom-left panel of Figure 3.19. If both channels are corrected individually, the lowest joint effect of leakage is observed. However, this negatively affects $s\hat{Z}_{\mathrm{DR}}$ because the correction factors are not necessarily equivalent, and also affects $s\hat{\rho}_{\mathrm{HV}}$ because it adds

an artificial modification to the correlation coefficient. Therefore, the method that reasonably corrects the spectral leakage for both channels while keeping good error statistics is the combined correction method.

3.4.2 Bootstrap versus Deterministic Resampling

Since many constraints have been put on the bootstrap resampling mechanism and the block population in order to obtain estimates of good quality, an analysis of the performance of bootstrap as compared to a deterministic resampling scheme is appropriate. A deterministic resampling scheme consists in selecting all or a subset of the available pseudo-realizations in a systematic order in order to obtain averaged estimate. If the block population is small, it would be beneficial to implement this type of scheme because all of the available information would be used. Figure 3.20 shows the quality indicators as a function of the number of pseudo-realizations generated. The same simulation procedure as in the previous analysis is maintained. The difference between the two estimates is the way the blocks are resampled. The bootstrapped estimates are shown in blue, while estimates with deterministic sampling are shown in green. The deterministic resampling scheme used for this case takes contiguous blocks with increasing ratio as the number of pseudo-realizations increases. It can be observed that with this scheme, while the deterministic sampling starts with a lower leakage, its errors are very high. In the limit where the maximum number of different blocks has been sampled (i.e., around $K' = 40$ for this particular data window), the deterministic resampling scheme converges with the bootstrap in error statistics. However, it should be noted that bootstrap resampling

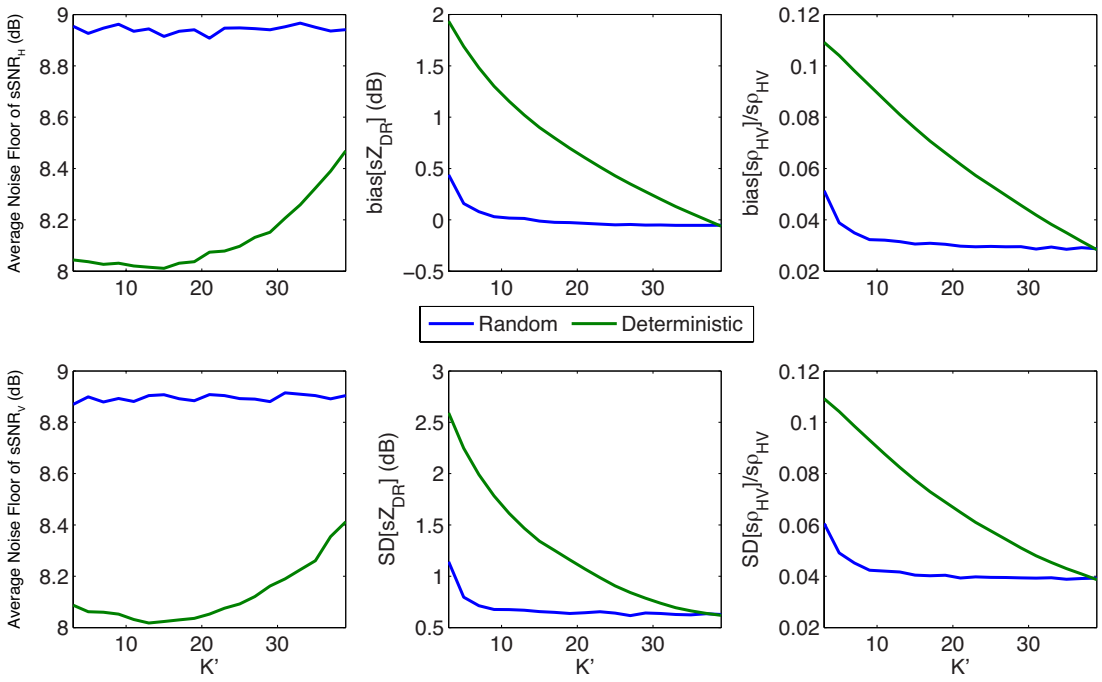

Figure 3.20: Estimator statistics for bootstrap and deterministic resampling schemes as a function of the number of pseudo-realizations (K'). The average noise floor as a measure of spectral leakage (left), the bias and SD of $s\hat{Z}_{\mathrm{DR}}$ (center), and the bias and SD of $s\hat{\rho}_{\mathrm{HV}}$ (right) are shown. The deterministic resampling scheme in this scenario takes contiguous blocks with increasing ratio as the number of pseudo-realizations increases.

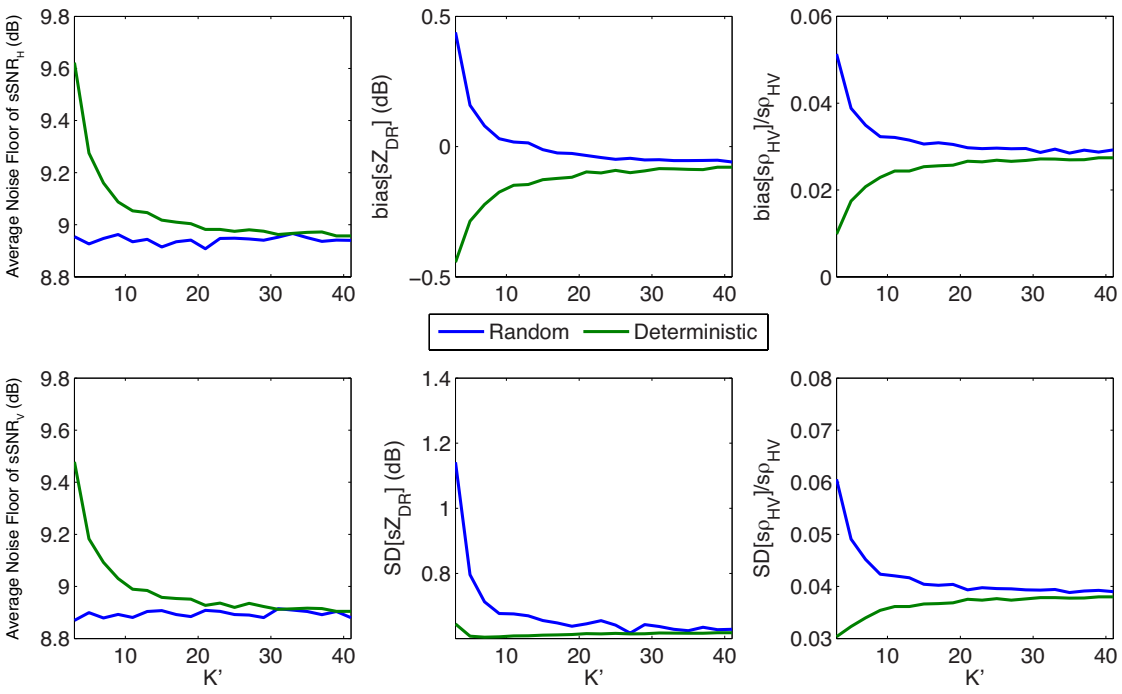

Figure 3.21: Estimator statistics for bootstrap and deterministic resampling as a function of the number of pseudo-realizations (K'). A modified deterministic resampling scheme is used. The blocks with $r = 0.5$ are sampled first, and successive blocks are taken as the mid-point ratio of the previously sampled blocks.

achieves these error levels for smaller values of K'. Assuming 10 pseudo-realizations are good enough, the difference with a deterministic sampling scheme is four-fold. The number of computations can rapidly increase for a large number of radar bins in an operational setting, though a more thorough analysis is required to estimate the actual difference in computational cost.

A different deterministic sampling scheme is analyzed next. In this scheme, the blocks with $r = 0$ and $r = 0.5$ are sampled first, and successive blocks are taken as the mid-point ratio of the previously sampled blocks, i.e. $r = 0.25$ then $r = 0.125$ and $r = 0.375$, and so on. With this modification, faster convergence is expected for the deterministic scheme. In this case, it is observed that the modified deterministic resampling scheme converges faster to the bootstrap, though a higher noise floor

is present because the pseudo-realizations with $r \simeq 0.5$ have the least sample-time coherence from the population. The standard deviation of estimates is lower, but the spectral leakage is higher (indicated by the average noise floor of $s\mathrm{SNR}_\mathrm{H}$ and $s\mathrm{SNR}_\mathrm{V}$ in Figure 3.21). Moreover, the $s\hat{Z}_\mathrm{DR}$ bias is negative and higher than the bootstrap in absolute value. It may be possible that a deterministic resampling scheme may be vulnerable to artifacts in the signal or sampling biases, and also depending on the scheme, systematic biases may be introduced (e.g., by choosing pseudo-realizations with $r \simeq 0.5$, as mentioned previously). The bootstrap appears to be superior in both cases. The statistical errors have a marginal improvement with increasing number of pseudo-realizations starting from approximately $K' = 10$. At this point, it would be a reasonable compromise to keep a lower number of pseudo-realizations to save computational cost.

3.5 The Bootstrap DPSD Estimator

All of the strategies and design considerations as well as the selection of parameters have been taken into account to develop the Bootstrap DPSD estimator. The concepts employed in the design of the Bootstrap DPSD estimator are explained with the necessary details in Sections 3.2, 3.3, and 3.4. Here, a concise description of the estimator is given.

The Bootstrap DPSD estimator is the result of the combining the bootstrap method with the DPSD estimator using averaged periodogram estimates. The basic idea is to generate bootstrap samples of the weather radar I/Q time-series signals, in

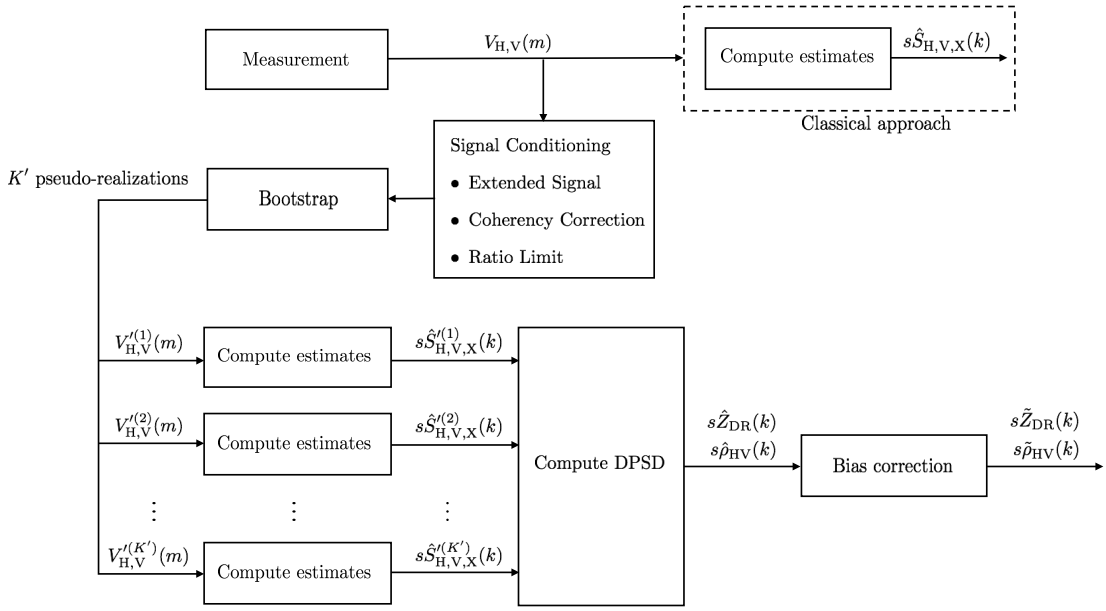

Figure 3.22: Diagram of the Bootstrap DPSD estimator.

order to construct a bootstrap aggregate of the PSD of the I/Q pseudo-realizations from which a DPSD estimate can be obtained. The signals of the H- and V-channels are bootstrapped as a pair in order to preserve the correlation between channels. Since the processes controlling the I/Q time series signals are correlated, the signals must be conditioned prior to the generation of bootstrapped pseudo-realizations, such that additional information can be extracted from each signal without degrading the quality of the estimates. A block bootstrap method is then employed to generate a suitable number of pseudo-realizations from which the PSD are computed. These are then input to the DPSD estimator which averages the PSDs to obtain a DPSD estimate. Finally, a bias correction technique is applied to the DPSD estimate to obtain the Bootstrap DPSD estimate. A diagram of the Bootstrap DPSD estimator is shown in Figure 3.22.

The steps taken by the Bootstrap DPSD estimator are summarized as follows:

1. Construct the periodic extension of the time series signal $X_{\mathrm{H,V}}(m)$ as in (3.58) and (3.59), using the magnitude and phase correction, and the combined correction.

2. Compute the maximum ratio of corrected samples $r_{\max}$ as in (3.63) for the selected data windowing function.

3. Generate $K' = 20$ pseudo-realizations of length M from $X_{\mathrm{H,V}}(m)$ limiting the blocks to those with $r \leq r_{\max}$.

4. Apply the power correction to each pseudo-realization as in (3.64).

5. Compute the PSD estimates using (2.41) and (2.42).

6. Average the PSD estimates obtained and compute the biased DPSD estimate using (2.43) and (2.44).

7. Compute the corrected DPSD estimates with (3.71) and (3.72) and the results from the previous step.

The statistical performance of the Bootstrap DPSD estimator in various scenarios will be compared to conventional DPSD estimators and to the ideal DPSD in the next chapter.

3.6 Summary

The bootstrap as a tool to measure the accuracy of statistical estimates was introduced. Such methods are useful to make inferences about the unknown underlying

distribution when the sample size is relatively small. Different methods to bootstrap dependent data (e.g., correlated data) have been presented. These methods are known as block bootstrap methods, and they may be applied to weather radar I/Q time-series signals, provided that the signals are conditioned in a way that additional information can be extracted from each pseudo-realization without degrading the quality of the estimates. These considerations and strategies are at the core of the Bootstrap DPSD estimator. Moreover, the appropriate selection of the parameters and methods plays a big role in the quality of the estimates. With objective analyses of the most important parameters, the optimal set of values was defined for the Bootstrap DPSD estimator, which was summarized in algorithmic terms. In the following chapter, the statistical performance of the proposed Bootstrap DPSD estimator will be analyzed under different scenarios.

Chapter 4

Performance of the Bootstrap Dual-Polarimetric Spectral Density Estimator

To properly demonstrate the advantages of the Bootstrap DPSD estimator, the statistical performance under different conditions must be analyzed. First of all, the methodology is explained thoroughly, from the simulation of dual-polarized weather radar signals to the computation of the statistical errors. Also, the relationship between the bulk and spectral polarimetric radar variables is studied. Next, the ideal DPSD estimator is analyzed in terms of statistical errors and their dependence with relevant parameters. Then, the analysis of the performance of the Bootstrap DPSD estimator is presented in three different categories: single signal single dwell, single signal multiple dwells, and dual signal. Finally, an overview of the error performance of the Bootstrap DPSD estimator is presented at the end of the chapter.

4.1 Methodology

4.1.1 Synthetic I/Q Time-Series Weather-Signal Simulator

A dual polarimetric version of the weather-like signal simulator (Zrnić 1975) is used, as presented in Torres and Zrnić (2003) and Yu et al. (2012). Let $V_{\mathrm{H}}(m)$ and $V_{\mathrm{V}}(m)$ be the I/Q time-series signals of the H and V channels, respectively. As shown in

Torres and Zrnić (2003), and by following the procedure in Galati and Pavan (1995), these can be obtained as:

$$\begin{aligned} V_{\mathrm{H}}(m) &= \sqrt{S_{\mathrm{H}}}X(m) + N_{\mathrm{H}}(m), \\ V_{\mathrm{V}}(m) &= \sqrt{S_{\mathrm{V}}}\Big[\rho_{\mathrm{HV}}X(m) + \sqrt{1-\rho_{\mathrm{HV}}^2}Y(m)\Big]e^{-j\phi_{\mathrm{DP}}} + N_{\mathrm{V}}(m), \end{aligned} \tag{4.1}$$

where S_{H}, S_{V}, ρ_{HV} and ϕ_{DP} are the true values of the bulk radar variables, $N_{\mathrm{H}}(m)$ and $N_{\mathrm{V}}(m)$ are additive white Gaussian noise (AWGN), and $X(m)$ and $Y(m)$ are unit power, independent time-series signals obtained as (Zrnić 1975):

$$X(m) = \mathcal{F}^{-1}\{\sqrt{-sS(k)\ln u(k)}e^{j\theta(k)}\}, \tag{4.2}$$

where $sS(k)$ is the Gaussian PSD model of the weather signal, $u(k)$ is an independent and identically distributed (IID) random variable with uniform distribution between 0 and 1, and $\theta(k)$ is also an IID random variable but with uniform distribution between $-\pi$ and π. $Y(m)$ is obtained similarly from (4.2) but using independently generated $u(k)$ and $\theta(k)$. With this procedure, the signal parameters that can be modified are: mean radial velocity ($\bar{v}_{\mathrm{r}}$) and spectrum width (σ_v) of the Gaussian PSD model, the bulk radar variables in terms of signal power (S_{H} or S_{V}), signal-to-noise ratio ($\mathrm{SNR_H}$ or $\mathrm{SNR_V}$), differential reflectivity ($Z_{\mathrm{DR}} = S_{\mathrm{H}}/S_{\mathrm{V}}$), correlation coefficient (ρ_{HV}) and differential phase (ϕ_{DP}). Additionally, radar acquisition parameters can also be modified, which include maximum unambiguous velocity (v_{a}) and number of samples per dwell (M). Multiple realizations can be produced to get K independent spectra, and statistical properties of the estimator

are computed running N iterations in the simulation. With (4.1), the coefficients of the DPSDs corresponding to the signal follow a constant value which agrees with the true value of the bulk polarimetric radar variable. However, the DPSDs of weather radar signals are not necessarily constant for all radial velocities. To simulate different profiles of DPSDs as a function of radial velocity, the method described in Yu et al. (2012) is more appropriate, as it allows the DPSDs to follow a model for each spectral coefficient. Physically, the presence of turbulent winds may produce signals with constant spectral polarimetric variables (Yanovsky 2011). Nevertheless, the assumption that the DPSDs are constant in the spectrum is sufficient to analyze the statistical performance of the DPSD estimates. This type of synthetic simulation allows generation of virtually any desired signal or composite signal under different scenarios, making it a powerful tool to study the statistical properties of any estimator. However, the challenge in simulating a realistic signal using this method is that while it is possible to modify the simulation parameters to match actual observations, the mechanisms that drive the underlying phenomena may not be emulated. Further discussion on this type of physical simulators is presented in Chapter 5. Throughout this chapter, the signal parameters were selected to resemble typical observations. The SNR is arbitrarily set high (20 dB) such that the noise contamination is minimal. While a Gaussian assumption for the simulated signals may not be the most realistic case, it provides a simple model that can capture features of the signal such that quantitative performance analyses can be conducted.

4.1.2 Statistical Error Calculation

Assuming the signal originates from a single group of uniform scatterers, for each set of independent estimates ($s\hat{Z}_{\mathrm{DR}}$ and $s\hat{\rho}_{\mathrm{HV}}$), the spectral coefficients above a SNR threshold are used to compute the average spectral errors. Herein, the bulk radar variables are used as the true value to compute the errors because the signal is modeled as such. If we used a more complex model as described above, the errors would become a function of the spectral coefficient and the statistical analysis would unnecessarily become more complicated. The average value of the SNR-thresholded spectral coefficients represents the strong signal components with minimal noise. These are obtained as

$$\overline{s\hat{Z}_{\mathrm{dr}}} = \langle s\hat{Z}_{\mathrm{dr}}(k')\rangle, \tag{4.3}$$

$$\overline{s\hat{\rho}_{\mathrm{HV}}} = \langle s\hat{\rho}_{\mathrm{HV}}(k')\rangle, \tag{4.4}$$

where k' are the spectral coefficients for which $s\hat{\mathrm{SNR}}_{\mathrm{H}}$ and $s\hat{\mathrm{SNR}}_{\mathrm{V}}$ are greater than 20 dB, and $\langle\cdot\rangle$ indicates averaging in the frequency domain. The bias of $s\hat{Z}_{\mathrm{DR}}$ is then obtained as

$$\mathrm{bias}(s\hat{Z}_{\mathrm{dr}}) = E\left[\overline{s\hat{Z}_{\mathrm{dr}}} - Z_{\mathrm{dr}}\right] \simeq \frac{1}{N}\sum_{n=0}^{N-1}\left(\overline{s\hat{Z}_{\mathrm{dr},n}} - Z_{\mathrm{dr}}\right), \tag{4.5}$$

$$\mathrm{bias}(s\hat{Z}_{\mathrm{DR}}) \simeq 10\log\left[1 + \frac{\mathrm{bias}(s\hat{Z}_{\mathrm{dr}})}{Z_{\mathrm{dr}}}\right]\mathrm{(dB)}, \tag{4.6}$$

where N is the number of independent DPSDs used to study the statistical variability of the spectral estimates, not to be confused with the K independent spectra used to compute the DPSDs. The standard deviation (SD) of $s\hat{Z}_{\rm DR}$ is computed as

$$\mathrm{SD}(s\hat{Z}_{\rm dr}) = \sqrt{E\left[\left(\overline{s\hat{Z}_{\rm dr}} - Z_{\rm dr}\right)^2\right]} \simeq \sqrt{\frac{1}{N}\sum_{n=0}^{N-1}\left(\overline{s\hat{Z}_{{\rm dr},n}} - Z_{\rm dr}\right)^2}, \tag{4.7}$$

$$\mathrm{SD}(s\hat{Z}_{\rm DR}) \simeq 10\log_{10}\left[1 + \frac{\mathrm{SD}(s\hat{Z}_{\rm dr})}{Z_{\rm dr}}\right] (\mathrm{dB}). \tag{4.8}$$

The normalized bias and SD of $s\hat{\rho}_{\rm HV}$ are

$$\frac{\mathrm{bias}(s\hat{\rho}_{\rm HV})}{\rho_{\rm HV}} = \frac{E\left[\overline{s\hat{\rho}_{\rm HV}} - \rho_{\rm HV}\right]}{\rho_{\rm HV}} \simeq \frac{\frac{1}{N}\sum_{n=0}^{N-1}\left(\overline{s\hat{\rho}_{{\rm HV},n}} - \rho_{\rm HV}\right)}{\rho_{\rm HV}}, \tag{4.9}$$

$$\frac{\mathrm{SD}(s\hat{\rho}_{\rm HV})}{\rho_{\rm HV}} = \frac{\sqrt{E\left[\left(\overline{s\hat{\rho}_{\rm HV}} - \rho_{\rm HV}\right)^2\right]}}{\rho_{\rm HV}} \simeq \frac{\sqrt{\frac{1}{N}\sum_{n=0}^{N-1}\left(\overline{s\hat{\rho}_{{\rm HV},n}} - \rho_{\rm HV}\right)^2}}{\rho_{\rm HV}}. \tag{4.10}$$

Equations (4.5)-(4.10) will be used later to quantify the dependence on the different parameters under analysis.

4.1.3 Relationship between Bulk and Spectral Radar Variables

As presented by Yu et al. (2012), the values of the bulk polarimetric variables may be obtained from the spectra as:

$$Z_{\rm dr} = \frac{1}{P_{\rm V}}\int_{-\infty}^{\infty} sZ_{\rm dr}(f)sS_{\rm V}(f)df, \tag{4.11}$$

$$\rho_{\mathrm{HV}} = \frac{1}{\sqrt{P_{\mathrm{H}} P_{\mathrm{V}}}} \left| \int_{-\infty}^{\infty} sS_{\mathrm{X}}(f) df \right|, \tag{4.12}$$

where sS_{X} is related to $s\rho_{\mathrm{HV}}$ by

$$s\rho_{\mathrm{HV}}(f) = \frac{|sS_{\mathrm{X}}(f)|}{\sqrt{sS_{\mathrm{H}}(f) sS_{\mathrm{V}}(f)}}. \tag{4.13}$$

In other words, the bulk variables are obtained by integrating power-weighted DPSDs. While bulk variables provide a good insight about the underlying phenomena for single signals, it is clear that they can be biased when there is more than one signal in the spectra. The spectral polarimetric variables add another dimension (of velocity) to the bulk polarimetric variables, and display additional information about the scatterers in a resolution volume that is not depicted in bulk variables. Furthermore, the average of the thresholded coefficients is arguably a better way to obtain bulk estimates, provided that the statistical error of the DPSDs are better than those of bulk estimates, since the noise spectral coefficients can be ignored altogether.

Additionally, the errors for bulk and spectral variables have a different parameter dependence. An extensive analysis on the errors of bulk polarimetric variables was done by Melnikov and Zrnić (2004) and the analytical expressions for the errors were obtained with the perturbation method as:

$$\mathrm{bias}(\hat{Z}_{\mathrm{DR}}) = \frac{10}{M \ln 10} \left[\frac{1 + 2\mathrm{SNR}_{\mathrm{V}}}{\mathrm{SNR}_{\mathrm{V}}^2} + \frac{0.56(1 - \rho_{\mathrm{HV}}^2)}{\sigma_{vn}} \right], \tag{4.14}$$

$$\mathrm{SD}(\hat{Z}_{\mathrm{DR}}) = \frac{10}{\sqrt{M} \ln 10} \sqrt{\frac{1 + 2\mathrm{SNR}_{\mathrm{H}}}{\mathrm{SNR}_{\mathrm{H}}^2} + \frac{1 + 2\mathrm{SNR}_{\mathrm{V}}}{\mathrm{SNR}_{\mathrm{V}}^2} + \frac{1.13(1 - \rho_{\mathrm{HV}}^2)}{\sigma_{vn}}}, \tag{4.15}$$

$$\frac{\mathrm{bias}(\hat{\rho}_{\mathrm{HV}})}{\rho_{\mathrm{HV}}} = \frac{1}{M}\left[\frac{2\mathrm{SNR_H}+3}{8\mathrm{SNR_H^2}} + \frac{2\mathrm{SNR_V}+3}{8\mathrm{SNR_V^2}} + \frac{\mathrm{SNR_H}+\mathrm{SNR_V}+1}{4\mathrm{SNR_H}\mathrm{SNR_V}\rho_{\mathrm{HV}}^2} + \frac{0.14(1-\rho_{\mathrm{HV}}^2)^2}{\sigma_{vn}\rho_{\mathrm{HV}}^2}\right], \tag{4.16}$$

$$\frac{\mathrm{SD}(\hat{\rho}_{\mathrm{HV}})}{\rho_{\mathrm{HV}}} = \sqrt{\frac{1}{M}\left[\frac{1-2\mathrm{SNR_H}}{4\mathrm{SNR_H^2}} + \frac{1-2\mathrm{SNR_V}}{4\mathrm{SNR_V^2}} + \frac{\mathrm{SNR_H}+\mathrm{SNR_V}+1}{2\mathrm{SNR_H}\mathrm{SNR_V}\rho_{\mathrm{HV}}^2} + \frac{0.28(1-\rho_{\mathrm{HV}}^2)^2}{\sigma_{vn}\rho_{\mathrm{HV}}^2}\right]}, \tag{4.17}$$

where σ_{vn} is the normalized spectrum width. Likewise, Yu et al. (2012) studied the spectral polarimetric variables and obtained the analytical expressions for the errors as:

$$\mathrm{bias}(s\hat{Z}_{\mathrm{DR}}) = \frac{10}{K\ln 10}\left[\frac{1+2s\mathrm{SNR_V}}{s\mathrm{SNR_V^2}} + (1-s\rho_{\mathrm{HV}}^2)\right], \tag{4.18}$$

$$\mathrm{SD}(s\hat{Z}_{\mathrm{DR}}) = \frac{10}{\sqrt{K}\ln 10}\sqrt{\frac{1+2s\mathrm{SNR_H}}{s\mathrm{SNR_H^2}} + \frac{1+2s\mathrm{SNR_V}}{s\mathrm{SNR_V^2}} + 2(1-s\rho_{\mathrm{HV}}^2)}, \tag{4.19}$$

$$\frac{\mathrm{bias}(s\hat{\rho}_{\mathrm{HV}})}{s\rho_{\mathrm{HV}}} = \frac{1}{K}\left[\frac{2s\mathrm{SNR_H}+3}{8s\mathrm{SNR_H^2}} + \frac{2s\mathrm{SNR_V}+3}{8s\mathrm{SNR_V^2}} + \frac{s\mathrm{SNR_H}+s\mathrm{SNR_V}+1}{4s\mathrm{SNR_H}s\mathrm{SNR_V}s\rho_{\mathrm{HV}}^2} + \frac{(1-s\rho_{\mathrm{HV}}^2)^2}{4s\rho_{\mathrm{HV}}^2}\right], \tag{4.20}$$

$$\frac{\mathrm{SD}(s\hat{\rho}_{\mathrm{HV}})}{s\rho_{\mathrm{HV}}} = \sqrt{\frac{1}{K}\left[\frac{1-2s\mathrm{SNR_H}}{4s\mathrm{SNR_H^2}} + \frac{1-2s\mathrm{SNR_V}}{4s\mathrm{SNR_V^2}} + \frac{s\mathrm{SNR_H}+s\mathrm{SNR_V}+1}{2s\mathrm{SNR_H}s\mathrm{SNR_V}s\rho_{\mathrm{HV}}^2} + \frac{(1-s\rho_{\mathrm{HV}}^2)^2}{2s\rho_{\mathrm{HV}}^2}\right]}. \tag{4.21}$$

A simple comparison of these expressions shows the differences in variable dependence for bulk and spectral variables. For these analyses the SNR in both channels is assumed to be high, and thus, the terms with $\mathrm{SNR_{H,V}}$ and $s\mathrm{SNR_{H,V}}$ can be neglected. Consequently, in the absence of noise, the errors do not depend on Z_{DR} (Melnikov and Zrnić 2004) or sZ_{DR}, but show a dependence on ρ_{HV}, M and σ_v for bulk variables, and $s\rho_{\mathrm{HV}}$, and K for spectral variables. Although the spectral variables do not explicitly show dependence with M and σ_v in the analytical expressions, the thresholded spectral coefficients are averaged. Thus, a smaller dependence

in the spectral variables is expected because the number of thresholded coefficients depends on M and σ_v. In the next section, the errors of the spectral variables are analyzed for different parameters to illustrate the error behavior of spectral variables in detail.

4.2 Analysis of the Ideal Estimator

As described in Chapter 2, with the use of the periodogram PSD estimator and by averaging independent spectra, DPSDs with better precision can be obtained. It is expected that the errors will be higher for spectral variables because they mostly depend on K, whereas the bulk variables depend on M (generally, M is larger than K). Ideally, the number of independent spectra to obtain estimates with acceptable error levels must be large. It was determined by Yu et al. (2012) that $K \geq 20$ yields good error levels. Hereafter, the periodogram DPSD estimator is the one that averages K independent periodogram PSD estimates; and the ideal DPSD estimator becomes the periodogram DPSD estimator with $K = 20$. It is important to recall that it is not operationally possible to obtain estimates with a large number of independent spectra. In this section, the errors of the periodogram DPSD estimator for different values of K as functions of relevant parameters are analyzed, so that a standard for comparison for further performance analyses can be established. The signal parameters that have a potential impact in the quality of the spectral estimates are SNR, M, σ_v, Z_{DR}, ρ_{HV}, and K. Since studying the effect of each parameter on the error quality over a wide range of values for all

Simulation parameter	Value
M	64
N	5000
$\bar{v}_{\mathrm{r}}$	5 m/s
σ_v	2 m/s
$\mathrm{SNR_V}$	30 dB
Z_{DR}	1.5 dB
ρ_{HV}	0.90
v_{a}	15.7 m/s

Table 4.1: Simulation parameters for the analysis of the errors.

DPSD estimators under consideration would be cumbersome, the analysis of the ideal estimator can help determine the parameters with higher impact on the errors. Thus, by focusing on these parameters, the complexity of further analyses are greatly simplified. The signal parameters are summarized in Table 4.1. Each point in the error curves are computed using (4.5)-(4.10) with a total of NK independent signals per step in the x-axis.

4.2.1 Dependence with SNR

The behavior of the errors as a function of the SNR is analyzed using the parameters listed in Table 4.1, but by varying $\mathrm{SNR_V}$ between 14 and 30 dB. In bulk variables, for a fixed M, higher SNR yields smaller errors (Melnikov and Zrnić 2004). In spectral variables, higher SNR will cause more spectral leakage if data windows with insufficient SLL are used. When spectral leakage occurs, the effective number of samples above the SNR threshold can unrealistically increase, and it may potentially affect the interpretation of the errors of estimates. Ideally, for higher SNR, it is expected that the errors are smaller and independent of the SNR values because the thresholded spectral coefficients already have minimal noise contamination. Additionally,

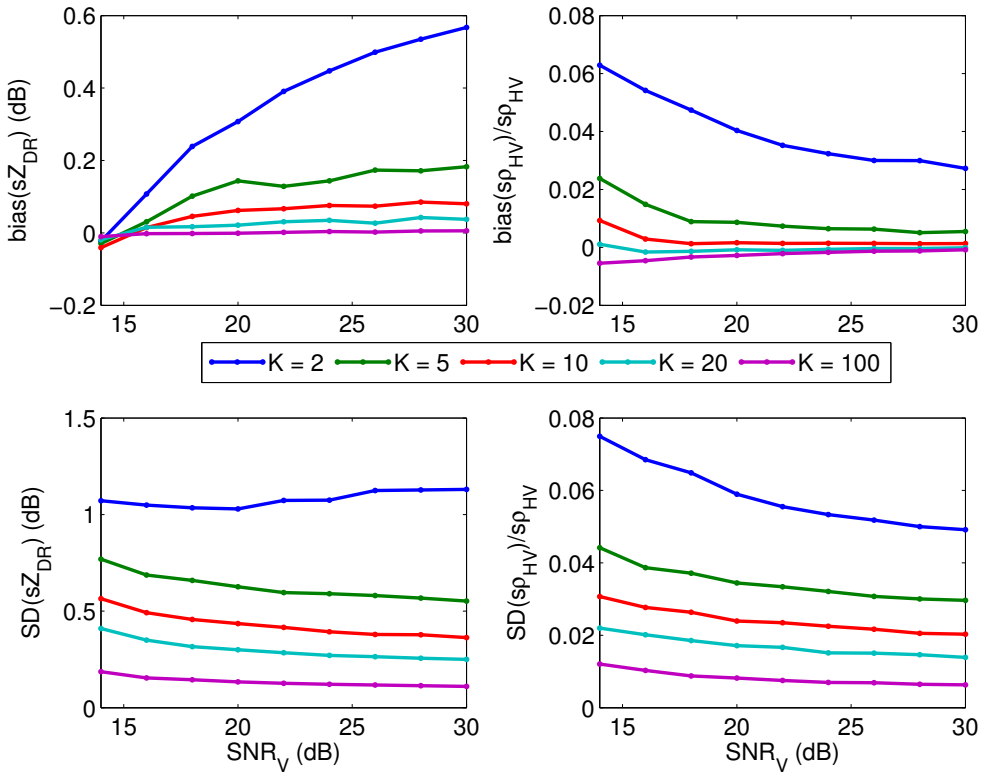

Figure 4.1: Errors of the spectral polarimetric variables as function of the true V-channel SNR for the periodogram DPSD estimator and different values of K. Bias (top left) and SD (bottom left) of $s\hat{Z}_{\rm DR}$, normalized bias (top right) and SD (bottom right) of $s\hat{\rho}_{\rm HV}$ for $K = 2$ (blue), $K = 5$ (green), $K = 10$ (red), $K = 20$ (cyan), and $K = 100$ (magenta). Herein, the periodogram DPSD with $K = 20$ is considered to be the "ideal" DPSD estimator.

the dependence on SNR for bulk variables is stronger because all M samples are used to compute the estimates and errors, as opposed to using averaged thresholded spectral coefficients. The bias and standard deviation (SD) of $s\hat{Z}_{\rm DR}$ and $s\hat{\rho}_{\rm HV}$ as a function of $\mathrm{SNR_V}$ are shown in Figure 4.1. Since the noise components in the spectra have $sZ_{\rm DR} = 0$ dB and the signal components have $sZ_{\rm DR} = 1.5$ dB, the errors in $sZ_{\rm DR}$ for the cases corresponding to bulk $\mathrm{SNR_V} < 20$ dB are more biased towards the noise DPSD values, which explains the unusual behavior (smaller biases for smaller SNR). In other words, the bias of $s\hat{Z}_{\rm DR}$ for this estimator is inherently

positive and large, and lower SNR values "help" reduce the bias, though this effect is a function of the bulk Z_{DR} chosen. For example, if a negative Z_{DR} is selected, the bias of sZ_{DR} will decrease with increasing SNR, as expected. Likewise, the noise components have $s\rho_{\mathrm{HV}} = 0$, while the signal components have $s\rho_{\mathrm{HV}} = 0.90$; it can be seen that $s\rho_{\mathrm{HV}}$ is overestimated for lower K, while it shows the expected behavior for the curves corresponding to higher K. The bias and SD of $s\hat{Z}_{\mathrm{DR}}$ and $s\hat{\rho}_{\mathrm{HV}}$ as a function of $\mathrm{SNR_V}$ are almost constant for the curves corresponding to $K = 5, 10, 20$ and 100, for $\mathrm{SNR_V} \geq 20$. Clearly, this exercise shows that the estimates with $K = 2$ are not reliable even for signals with high SNR; and with higher K, the errors become increasingly independent of the SNR (for $\mathrm{SNR} \geq 20$) and gradually smaller. Higher bulk SNR translates into more spectral coefficients that meet or exceed the SNR threshold ($\mathrm{SNR_{H,V}} \geq 20$ dB); and thus, the SD of the estimates is reduced (higher number of averaged samples), while the biases tend to an asymptotic value. The rest of the analysis is conducted for an SNR of 30 dB to ensure minimal noise contamination in the spectral coefficients of the signal.

4.2.2 Dependence with M

In bulk variables, the errors have a strong dependence with M, while a weaker dependence is expected for spectral variables. The errors as a function of the number of samples (M) are shown for different number of independent spectra (K) in Figure 4.2. The signal parameters are shown in Table 4.1, except different values of M are analyzed. As usual, it is desired to have small errors in the estimates, and once again it can be seen how the errors improve for higher K. Increasing M increases the

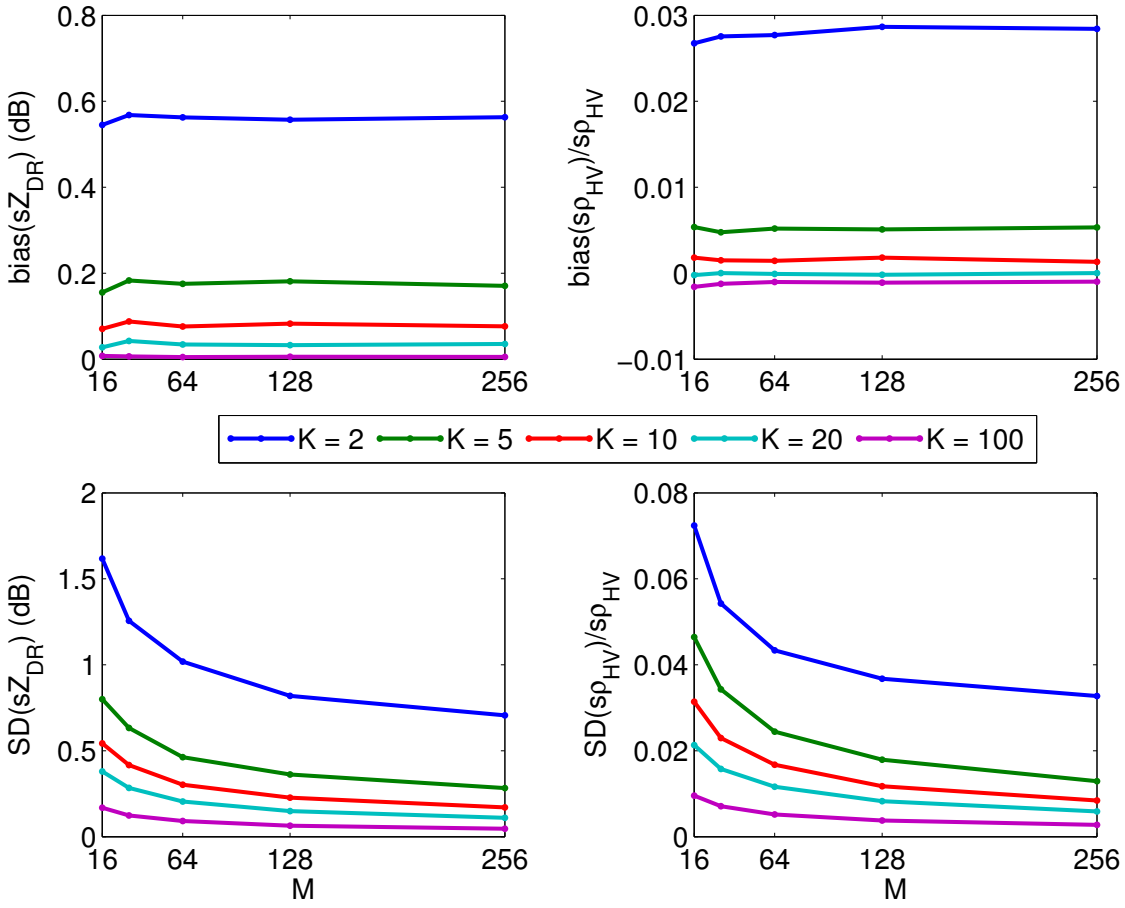

Figure 4.2: Same as Figure 4.1, but as a function of the number of samples (M) for different values of K.

frequency resolution and translates into having more sample points in the spectral estimates. Although the choice of M does not necessarily affect the accuracy of the DPSD estimates, averaging SNR-thresholded spectral coefficients does depend on M. Logically, by increasing M, the number of spectral coefficients above the SNR threshold also increases. A small dependence of the errors and M can be observed for small M, where the number of samples above the SNR threshold is insufficient to produce good estimates, and a bias towards the noise value of 0 dB can be observed (similar to the case with small SNR). Furthermore, for $M \geq 32$, the biases are approximately constant, while an improvement in the SDs can be seen. Hereafter, the number of samples for the analyses is set to $M = 64$ to resemble operational settings.

4.2.3 Dependence with σ_v

The signal parameters used in this analysis are those of Table 4.1, but for different values of σ_v from 0.5 to 3 m/s. In bulk variables, as seen in (4.14)-(4.17), the errors have a term that depends on the spectrum width; however, spectral variables do not strongly depend on the spectrum width. As with the previous analysis for M, the actual value of σ_v does not affect the accuracy of the DPSD estimates, but it does affect the averaging of SNR-thresholded spectral coefficients. Thus, a small dependence with σ_v is expected. For spectral variables, the dependence of the errors with the spectrum width is similar to that with M (Figure 4.3), though slightly stronger because the number of samples above the threshold increases at a higher rate for increasing σ_v than for increasing M. The biases of the DPSD estimates have

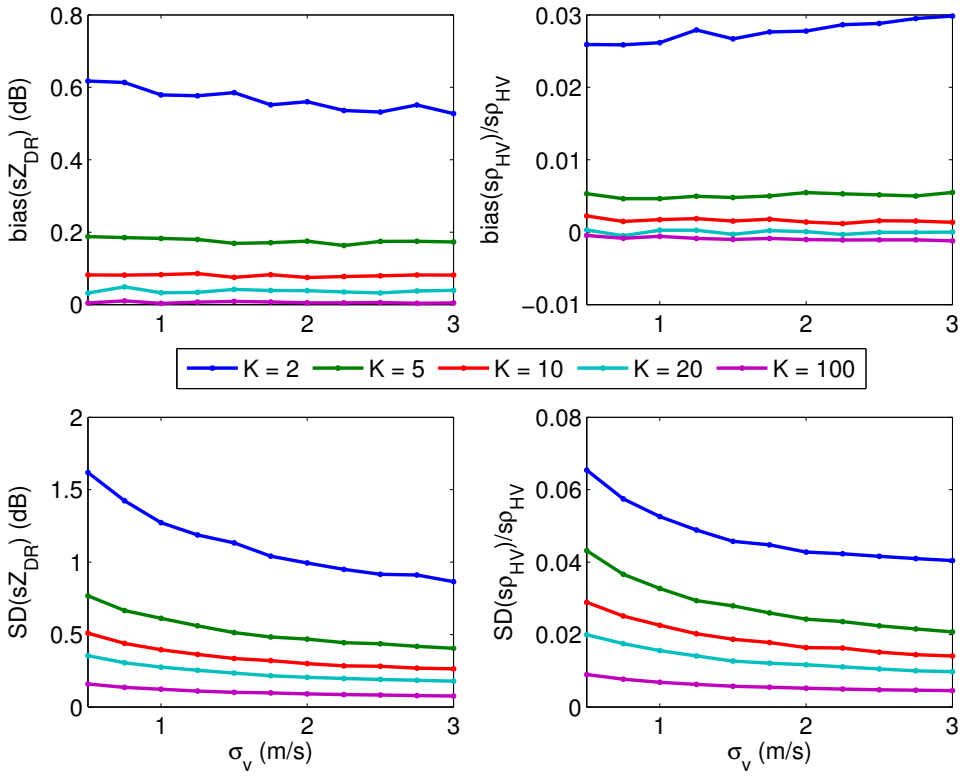

Figure 4.3: Same as Figure 4.1, but as a function of the true spectrum width (σ_v) for different values of K.

stronger dependence with σ_v for smaller K, as seen in the blue curves corresponding to $K = 2$, while for higher K, the biases become almost independent of σ_v. For all K, the SDs decrease with increasing σ_v as expected, because of the increased number of samples above the SNR threshold. The spectrum width for the simulations is selected to match typical raindrop signals with $\sigma_v = 2$ m/s (Fang et al. 2004).

4.2.4 Dependence with Z_{DR}

As previously mentioned, in the absence of noise, it is expected that the errors do not show a dependence with Z_{DR} (Melnikov and Zrnić 2004). The simulation parameters are listed in Table 4.1 with the Z_{DR} varied from -2.5 to 2.5 dB (Figure 4.4). For the curves corresponding to $K > 2$, it is observed that the errors remain almost constant as a function of Z_{DR}, as expected. However, it can be seen that $K = 2$ is insufficient to yield good estimates, as the bias in $s\hat{Z}_{\mathrm{DR}}$ is weakly dependent on the true value of Z_{DR}. In other words, the estimates are influenced by the Z_{DR} of the noise (0 dB). For further analyses, a Z_{DR} of 1.5 dB is used to resemble slightly larger raindrops of about 2.70 mm (Bringi and Chandrasekar 2001).

4.2.5 Dependence with ρ_{HV}

The correlation coefficient is varied from 0.70 to 0.99 to obtain the curves for Figure 4.5. Both bulk and spectral variables have a similar, strong dependence with ρ_{HV}. It is observed that for higher ρ_{HV}, the errors become smaller. Additionally, the dependence with ρ_{HV} can be interpreted as a measure of signal consistency, as the estimates for high true ρ_{HV} values are less dispersed, both in bias and variance;

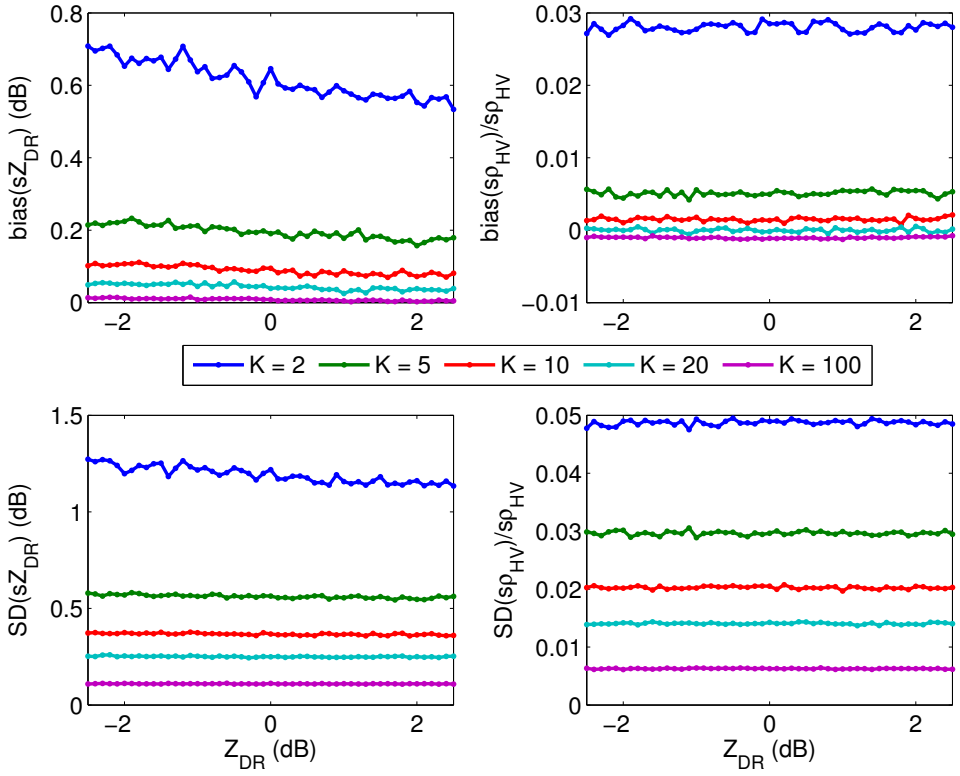

Figure 4.4: Same as Figure 4.1, but as a function of the true differential reflectivity (Z_{DR}) for different values of K.

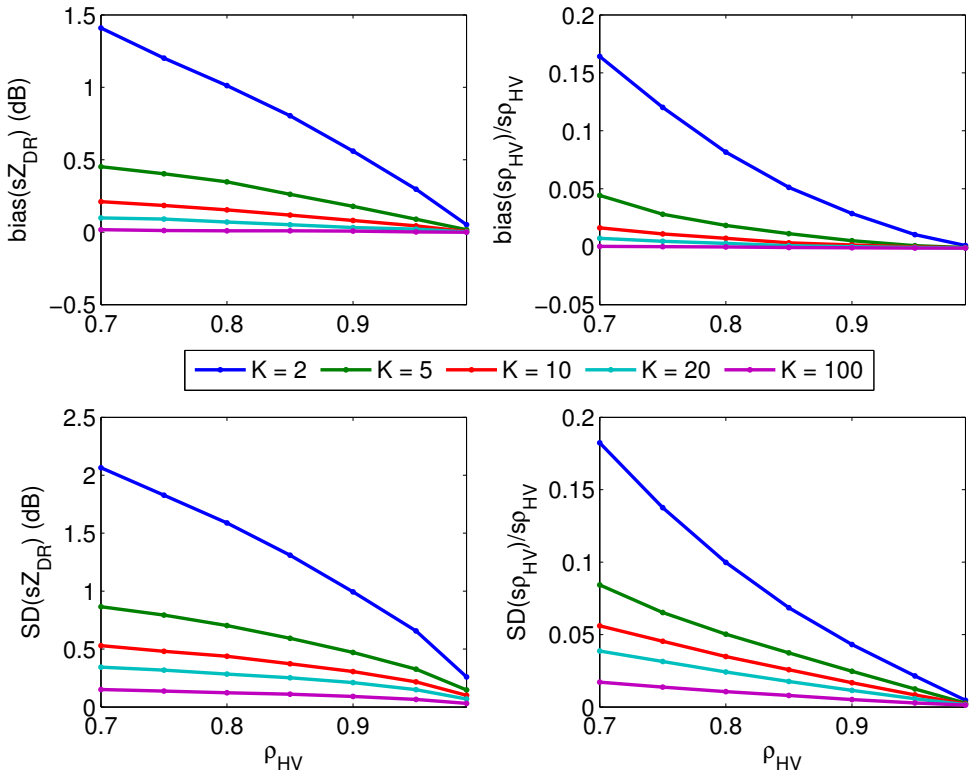

Figure 4.5: Same as Figure 4.1, but as a function of the true correlation coefficient (ρ_{HV}) for different values of K.

while the estimates for lower true ρ_{HV} values are highly dispersed and inaccurate. Although most hydrometeors exhibit high correlation coefficient (i.e., $\rho_{\mathrm{HV}} > 0.98$), the value of $\rho_{\mathrm{HV}} = 0.90$ was used in most simulations (unless otherwise stated) to reveal potential biases in the DPSDs.

4.2.6 Dependence with K

So far, it was shown that for spectral variables, errors show weak to no dependence on most parameters, with the exception of ρ_{HV}, and the remaining parameter to be analyzed is K. The errors as a function of K, are presented for different values of ρ_{HV} in Figure 4.6. Again, the simulation values are those shown in Table 4.1, with K ranging from 2 to 30, and for ρ_{HV} values of 0.80, 0.90, 0.95, and 0.99. For $K > 20$, the improvement in the errors is marginal, while for $K < 10$ the quality of the estimates can be significantly degraded.

4.3 Analysis of the Single-Dwell Estimator for the Single-Signal Case

It is understood that a large number of independent spectra for DPSD estimation is not feasible in practice. The Bootstrap DPSD estimator presented in Chapter 3 was developed to overcome this limitation by allowing the estimation of DPSDs from a single dwell ($K = 1$), with minimal resolution loss. Moreover, there are conventional estimators that are also capable of producing DPSD estimates from a single dwell. In this section, the performance of the conventional and Bootstrap

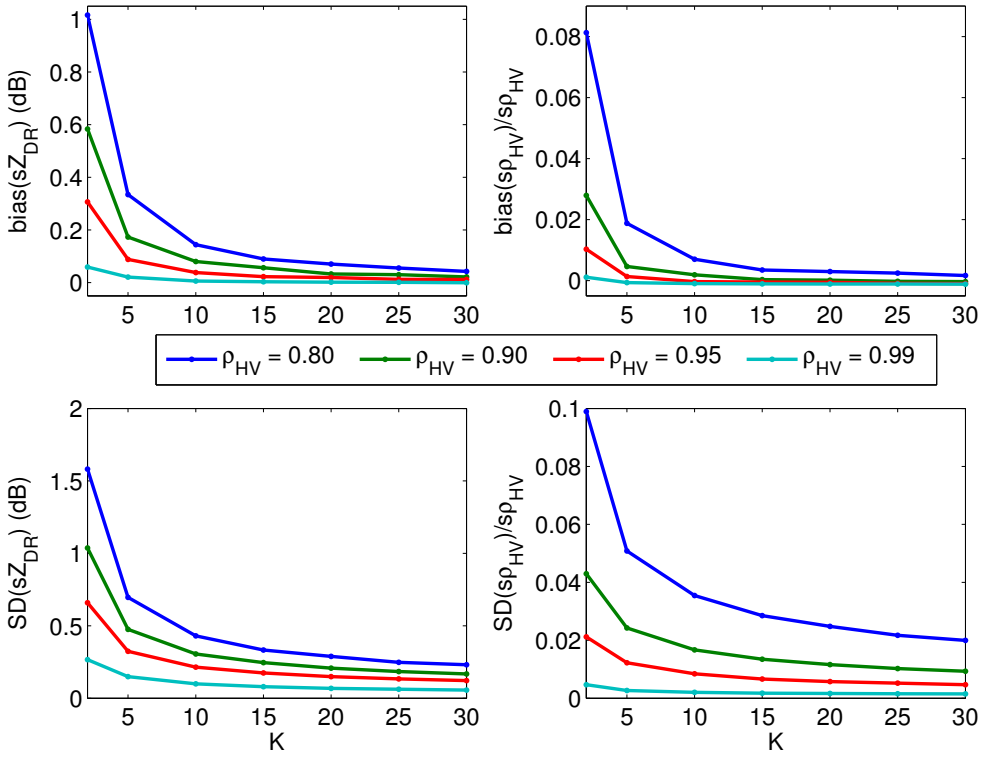

Figure 4.6: Errors of the spectral polarimetric variables as function of the number of independent spectra (K) of the periodogram DPSD estimator for different values of ρ_{HV}. Bias (top left) and SD (bottom left) of $s\hat{Z}_{\mathrm{DR}}$, normalized bias (top right) and SD (bottom right) of $s\hat{\rho}_{\mathrm{HV}}$ for $\rho_{\mathrm{HV}} = 0.80$ (blue), $\rho_{\mathrm{HV}} = 0.90$ (green), $\rho_{\mathrm{HV}} = 0.95$ (red), and $\rho_{\mathrm{HV}} = 0.99$ (cyan).

DPSD estimators is studied for a single signal, and the ideal estimator with $K = 20$ is selected as a standard for comparison. Additionally, the analysis focuses on the errors as a function of ρ_{HV} as justified by the previous analysis.

For a fair comparison between the different DPSD estimators, the parameters for the conventional methods are selected such that there is minimal frequency resolution loss and spectral smearing. That is, for Welch's estimator, the segment length is set to $L = M - 1$ with maximum overlap; and for Daniell's estimator, a 3-point moving average filter ($p = 1$) is used for PSD smoothing. Bartlett's estimator is not analyzed because its frequency resolution is degraded by at least a factor of 2. The Bootstrap DPSD estimates are obtained using $K' = 20$ pseudo-realizations. The analysis parameters are listed in Table 4.1, with ρ_{HV} varying from 0.85 to 0.99. The data window for the analysis is a Blackman-Nuttall window, though it should be noted that other windows with sufficient SLL yield similar results. The performance of the estimators in terms of the statistical errors as a function of the true correlation coefficient is shown in Figure 4.7. The errors for Welch estimates (red) with the best possible frequency resolution are very high and useless for practical purposes. It can be observed that the Bootstrap DPSD estimates (blue) are better than Daniell estimates (red) for all cases. For $s\hat{Z}_{\mathrm{DR}}$, and $\rho_{\mathrm{HV}} = 0.90$, the Daniell estimator has a bias of 0.708 dB, while the biases of the Bootstrap estimator and the ideal estimator are of 0.057 dB and 0.029 dB, respectively. The SDs are 1.187, 0.686, and 0.1662 dB, for the Daniell, Bootstrap, and ideal estimators, respectively. For the same $\rho_{\mathrm{HV}} = 0.90$, the normalized biases of $s\hat{\rho}_{\mathrm{HV}}$ are 0.0344, 0.0177, and 0.0006; and the normalized SDs are 0.0476, 0.0377,

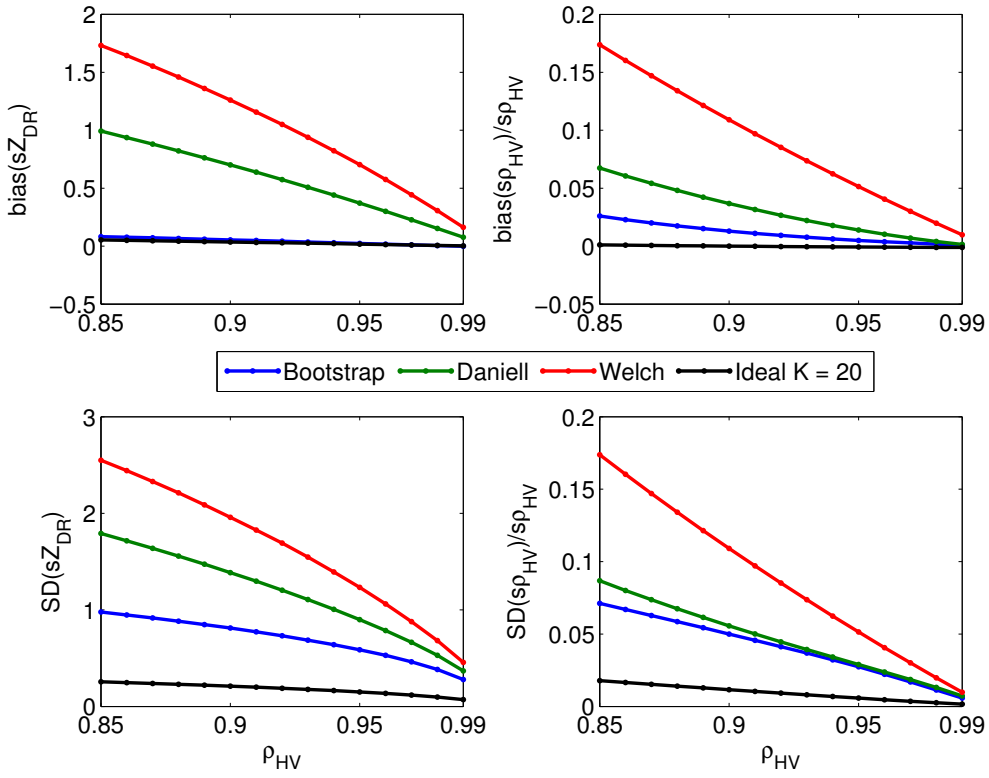

Figure 4.7: Errors of the spectral polarimetric variables as function of the true ρ_{HV} values. Bias (top left) and SD (bottom left) of $s\hat{Z}_{\mathrm{DR}}$, normalized bias (top right) and SD (bottom right) of $s\hat{\rho}_{\mathrm{HV}}$ for $Z_{\mathrm{DR}} = 1.5$ dB. The Bootstrap DPSD (blue), Daniell (green), Welch (red), and ideal with $K = 20$ (black) estimates are compared.

and 0.0089, for the Daniell, Bootstrap, and ideal estimators, respectively. A clear improvement in the quality of the DPSD estimates can be seen for the Bootstrap estimator over conventional methods, especially for the $s\hat{Z}_{\mathrm{DR}}$ bias. It is important to note that for higher ρ_{HV}, the errors of the Bootstrap estimates are closer to the error levels of the ideal estimator. However, for less coherent signals (i.e., lower ρ_{HV}), the quality of the estimates is degraded. Therefore, in practice, with single-dwell DPSD estimates using the Bootstrap DPSD estimator, a good qualitative analysis can be performed but the error levels may not be sufficient for a reliable quantitative analysis. Nonetheless, the following section will show that the errors can be improved by using multiple dwells.

4.4 Analysis of the Multiple-Dwell Estimator for the Single-Signal Case

The results of the conventional and Bootstrap DPSD estimators using a single dwell were shown in the previous section. However, it is possible to obtain better error levels by averaging multiple spectra for DPSD estimation (i.e., $K \geq 2$) with the estimators under analysis. As mentioned in Chapter 2, more spectra can be obtained from different range gates, azimuths, or dwells, and it is important to keep the averaging in any of these dimensions to a minimum in order to avoid degrading the resolution if the results. For this analysis, the statistical errors of conventional and Bootstrap DPSD estimators for $K \geq 2$ are compared to the ideal estimator as depicted in Figure 4.8 (same simulation parameters as before). For $\rho_{\mathrm{HV}} = 0.90$, the

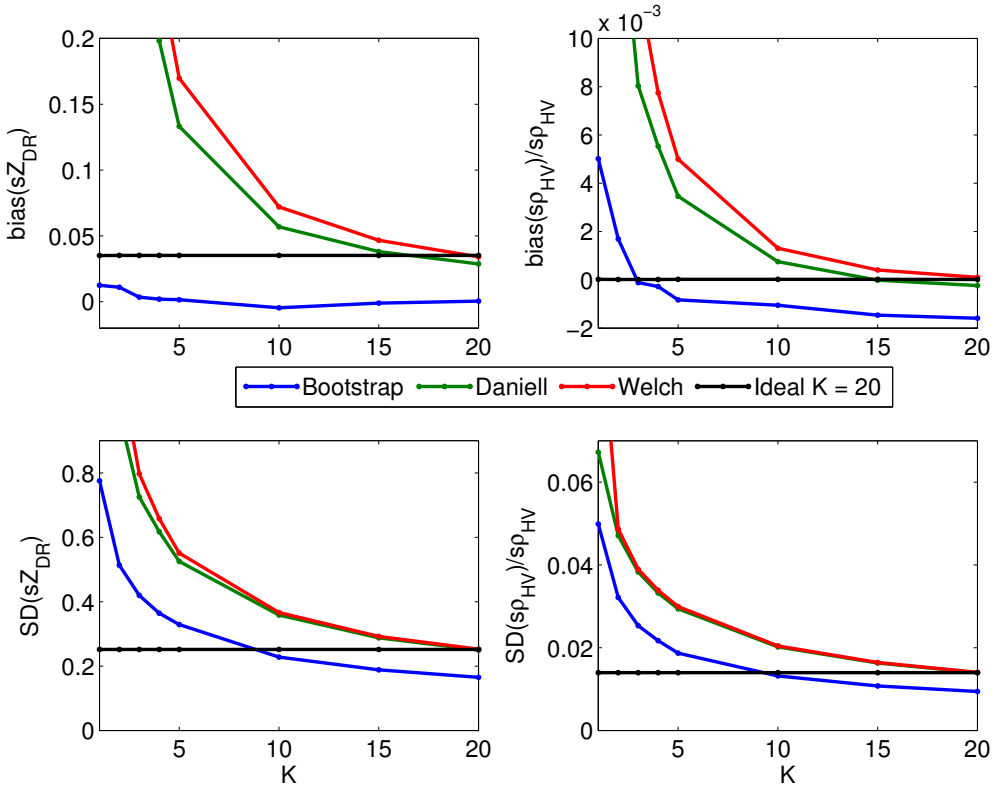

Figure 4.8: Errors of the spectral polarimetric variables as functions of the number of independent dwells K for $\rho_{\mathrm{HV}} = 0.90$. Bias (top left) and SD (bottom left) of $s\hat{Z}_{\mathrm{DR}}$, normalized bias (top right) and SD (bottom right) of $s\hat{\rho}_{\mathrm{HV}}$. The Bootstrap (blue), Daniell (green), Welch (red), and ideal (black) estimators are shown for comparison.

biases of the ideal estimator are equivalent to the Daniell estimator with $K \simeq 16$, and the Bootstrap estimator with $K \simeq 3$. The Bootstrap DPSD estimator shows a significant improvement in the biases and in the reduction of the number of independent spectra needed. However, to meet the SD of the ideal estimates, a considerable number of independent spectra is still needed. The SDs for the ideal estimator are equivalent to the Daniell estimator with $K \simeq 20$, and the Bootstrap estimator with $K \simeq 9$. For the Daniell estimator, a marginal improvement is observed, while the Bootstrap estimator shows overall better performance. When $K > 20$, the Welch estimator converges with the ideal estimator, while the Daniell estimator performs marginally better, and the Bootstrap estimator exceeds the performance of the ideal estimator. One important drawback of the Bootstrap DPSD estimator is the inherent loss of coherence associated with the application of correction strategies, depicted in the negative biases of $s\hat{\rho}_{\mathrm{HV}}$ for larger K. Still, the normalized bias of $s\hat{\rho}_{\mathrm{HV}}$ is within 0.002 for $K \geq 2$ and for $\rho_{\mathrm{HV}} = 0.90$, which is within the error level recommended by Melnikov and Zrnić (2004). While this limitation is noted, the Bootstrap DPSD estimator can generally achieve better quality estimates (for a given number of independent spectra) than other estimators. A more in-depth analysis of the impact of this effect is beyond the scope of this work. Additionally, it should be indicated that while the spectra in this analysis are independent, in practice, the spectra could be correlated depending on where the additional spectra come from (e.g., different scans vs. adjacent range gates).

4.5 Analysis of the Single-Dwell Estimator for the Dual-Signal Case

4.5.1 Signal Interaction

In order to discriminate signals in the spectra, the interaction of different signals in a composite weather radar I/Q signal must be understood. A signal becomes dominant in the spectrum whenever its power relative to the powers of other signals is large (e.g., $>$ 20 dB), and for these spectral coefficients, the characteristics in the DPSDs become predominantly those of the stronger signal. The single-signal case is essentially composed of two spectral signatures: the simulated signal and the white noise. As such, the spectra in the single-signal analysis can be separated into three regions: dominant signal, dominant noise, and the transition where neither is dominant. That is, if the PSD can be represented as:

$$sS(k) = sS_0(k) + sS_1(k), \tag{4.22}$$

where sS_1 is the PSD of the signal without noise, and sS_0 is the PSD of noise; then the DPSDs become:

$$sZ_{\mathrm{dr}}(k) \simeq \frac{sS_0(k)sZ_{\mathrm{dr},0}(k) + sS_1(k)sZ_{\mathrm{dr},1}(k)}{sS(k)}, \tag{4.23}$$

and

$$s\rho_{\mathrm{HV}}(k) \simeq \frac{sS_0(k)s\rho_{\mathrm{HV},0}(k) + sS_1(k)s\rho_{\mathrm{HV},1}(k)}{sS(k)}. \tag{4.24}$$

Based on this, when $sS_1 \gg sS_0$, the signal is dominant and $sZ_{\mathrm{dr}} \simeq sZ_{\mathrm{dr},1}$, $s\rho_{\mathrm{HV}} \simeq s\rho_{\mathrm{HV},1}$; and when $sS_1 \ll sS_0$, noise is dominant and $sZ_{\mathrm{dr}} \simeq sZ_{\mathrm{dr},0}$, $s\rho_{\mathrm{HV}} \simeq s\rho_{\mathrm{HV},0}$. For spectral coefficients where neither the signal nor the noise is dominant, the DPSDs are a weighted average of the DPSDs of the individual signals; i.e., they are neither the DPSDs of the signal nor the noise.

A similar behavior is expected when an additional signal is present in the spectra. The purpose of this dual-signal analysis is to study the effects of having an additional signal in the spectra, both in terms of statistical errors and in terms of the ability to discriminate the different signals. With two signals and noise, (4.22)-(4.24) become:

$$sS(k) = sS_0(k) + sS_1(k) + sS_2(k), \tag{4.25}$$

where sS_2 is the PSD of the additional signal; and the DPSDs become:

$$sZ_{\mathrm{dr}}(k) \simeq \frac{sS_0(k)sZ_{\mathrm{dr},0}(k) + sS_1(k)sZ_{\mathrm{dr},1}(k) + sS_2(k)sZ_{\mathrm{dr},2}(k)}{sS(k)}, \tag{4.26}$$

$$s\rho_{\mathrm{HV}}(k) \simeq \frac{sS_0(k)s\rho_{\mathrm{HV},0}(k) + sS_1(k)s\rho_{\mathrm{HV},1}(k) + sS_2(k)s\rho_{\mathrm{HV},2}(k)}{sS(k)}. \tag{4.27}$$

To demonstrate this, the ideal DPSDs for each signal are estimated individually and the power-weighted average of the DPSDs is then computed. This is compared with the ideal DPSDs estimated from the composite I/Q signal, as shown in Figure 4.9, for a unimodal and a bimodal case. The blue and green lines are the averaged ideal estimates as obtained from the individual I/Q signals. The continuous black line represents the averaged ideal estimate of the composite signal (i.e., the I/Q signal

Parameter	Signal 1	Signal 2
SNR	20 dB	40 dB
$\hat{v}_{\mathrm{r}}$	0 m/s	0 m/s
σ_v	3.5 m/s	1 m/s
Z_{DR}	1.5 dB	−1.5 dB
ρ_{HV}	0.99	0.90

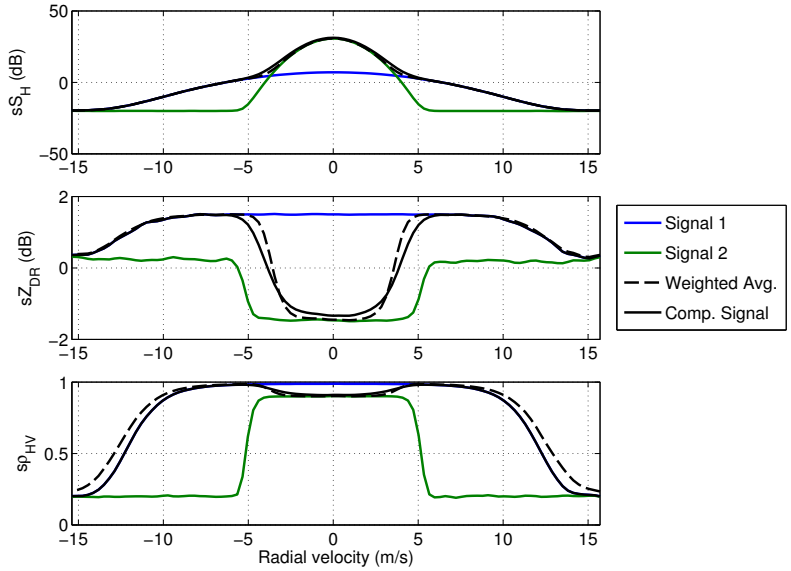

(a)

Parameter	Signal 1	Signal 2
SNR	20 dB	35 dB
$\hat{v}_{\mathrm{r}}$	−3 m/s	3 m/s
σ_v	2.5 m/s	0.75 m/s
Z_{DR}	0.5 dB	2 dB
ρ_{HV}	0.99	0.85

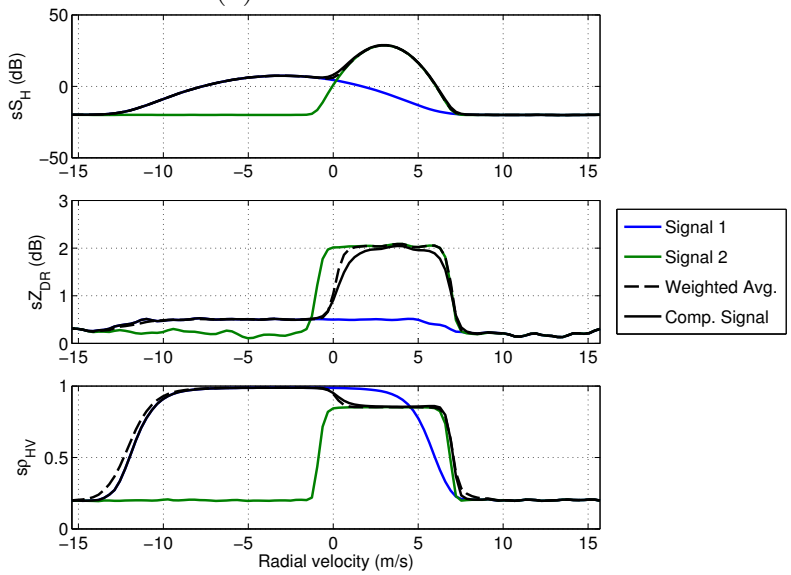

(b)

Figure 4.9: Dual-signal spectral coefficient interaction and composite effect on the DPSD for (a) unimodal case, and (b) bimodal case. The mean of the ideal estimates of signal 1 (blue) and signal 2 (green) are computed separately. The mean ideal estimate of the composite signal (continuous black) is compared to the power-weighted average of the DPSDs of signals 1 and 2 (dashed black).

composed of signals 1 and 2 plus noise). The dashed black line is computed as the power-weighted average of the DPSDs of signals 1 and 2 (the noise is negligible in this case). When the two signal powers are comparable, the DPSDs do not exactly follow one signal or the other. Instead, they show characteristics that fall in between the two signals, and as the power of one signal increases, it gradually becomes dominant. The unimodal case shows how two signals may appear as one, even though the spectrum width is exaggerated for clarity. Here, the DPSDs provide evidence that a narrower signal is overlaid on top of a wider signal, and that these two have different polarimetric characteristics. In the bimodal case, the two different signals show a difference in velocity, which makes them somewhat easier to identify. Once again, both signals show different polarimetric characteristics which can be used to classify them accordingly. While the power-weighted average of the DPSDs does not exactly follow the composite signal's DPSDs for regions with comparable SNR, both curves are similar for higher SNR. Thus, qualitatively, it can be seen assumed that the DPSDs are a power-weighted average of the DPSDs of each signal. Moreover, this suggests the possibility for discriminating signals that are overlapped by identifying distinct polarimetric signatures in the spectra. A few representative examples will be presented next.

4.5.2 Case Studies

There are various signal parameters that affect the ability to separate different spectral signatures; some of them are the difference between the mean radial velocities,

Case	Signal 1					Signal 2				
	SNR (dB)	$\bar{v}_r$ (m/s)	σ_v (m/s)	Z_{DR} (dB)	ρ_{HV}	SNR (dB)	$\bar{v}_r$ (m/s)	σ_v (m/s)	Z_{DR} (dB)	ρ_{HV}
0	25	-6	2	1.5	0.995	40	9	1	-1.5	0.97
1	25	-6	2	1.5	0.995	40	-6	1	-1.5	0.97
2							-4			
3							-2			
4							0			
5	25	-6	2	1.5	0.995	25	-6	1	-1.5	0.97
6							-4			
7							-2			
8							0			
9	40	-6	2	1.5	0.995	25	-6	1	-1.5	0.97
10							-4			
11							-2			
12							0			

Table 4.2: Signal parameters for dual-signal analysis cases.

the spectrum widths, the difference between the SNRs, and the polarimetric characteristics. The parameters for the signals used hereafter are summarized in Table 4.2, with $N = 1000$ iterations. Signal 1 is assumed to be a highly coherent signal with values resembling those of typical raindrops, while signal 2 is less coherent with negative Z_{DR} resembling hypothetical tornadic debris. Although a Gaussian assumption for debris signals is not realistic, it serves to illustrate the presence of signals with different polarimetric characteristics in the spectra, as will be shown in the following cases.

4.5.2.1 Case 0

When the spectra of the signals do not overlap (i.e., the difference in mean radial velocities is sufficiently large and the spectrum widths are not too wide), the signals can be easily separated by their velocities, and by assessing their spectral polarimetric variables, it may be possible to classify them accordingly (Figure 4.10). The average of $N = 1000$ DPSD estimates of the signals is shown in Figure 4.10a, for

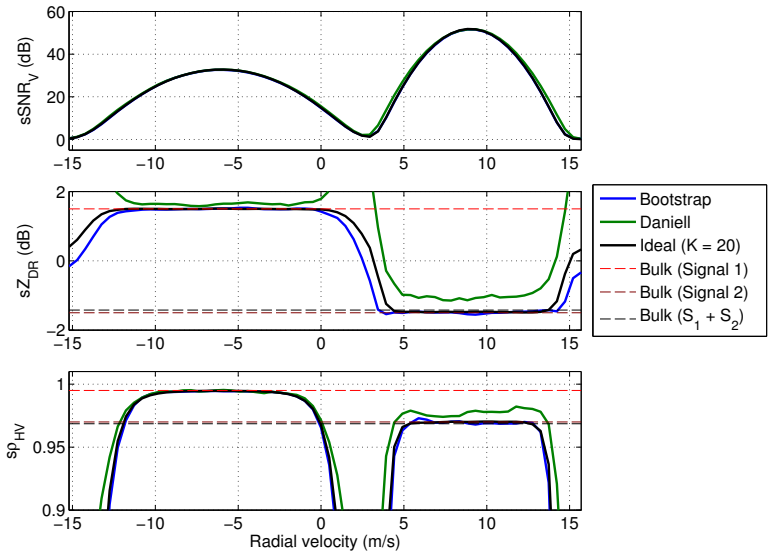

(a)

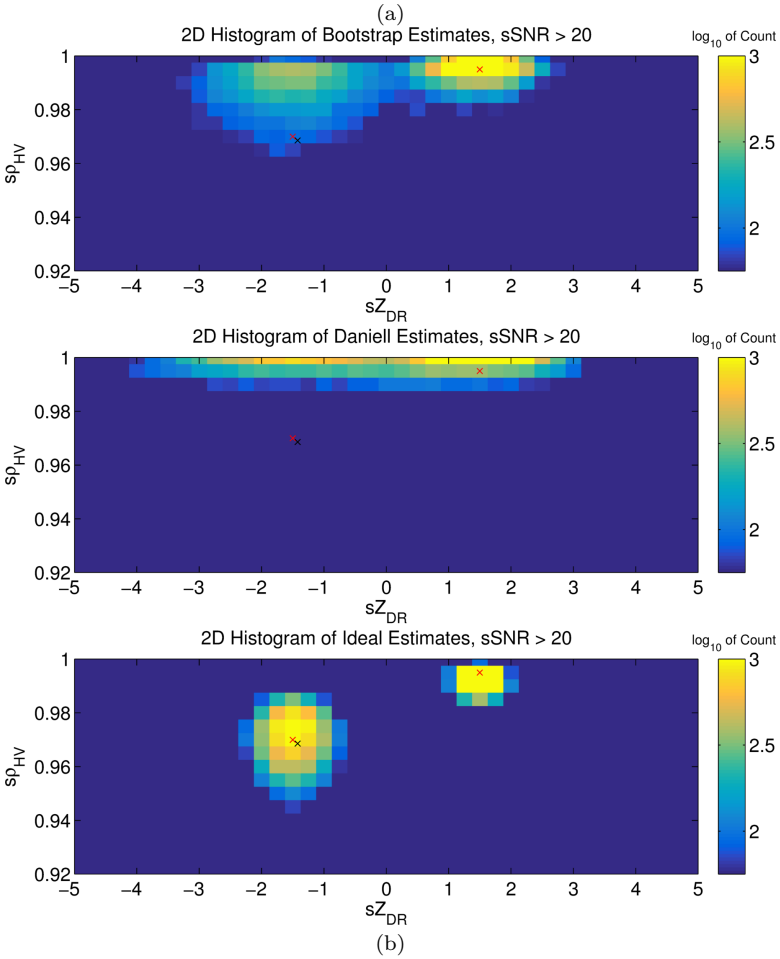

(b)

Figure 4.10: Dual-signal analysis, case 0. (a) The mean of the DPSD estimates of Bootstrap (blue), Daniell (green), and ideal (black) estimates, and the true bulk polarimetric variables of signal 1 (dashed red) and signal 2 (dashed dark red) are shown. (b) A 2D histogram of $s\hat{\rho}_{\mathrm{HV}}$ and $s\hat{Z}_{\mathrm{DR}}$ for thresholded spectral coefficients in logarithmic ($\log_{10}$) scale, of Bootstrap (top), Daniell (middle), and ideal (bottom) estimates, with $\times$ indicating the bulk estimates of the composite (black) and individual (red) signals.

the Bootstrap ($K = 1$), Daniell ($K = 1$), and ideal ($K = 20$) estimators. Additionally, the values for the true bulk polarimetric variables for the signals are plotted in dashed lines. Whenever the difference in radial velocity is large enough, there is no ambiguity in determining the presence of different signals, and with the DPSDs, the polarimetric characteristics of the signals can be obtained. In Figure 4.10b, a 2D histogram (hereafter, histogram) of $s\hat{\rho}_{\mathrm{HV}}$ and $s\hat{Z}_{\mathrm{DR}}$ is computed for the thresholded spectral coefficients, over $N = 1000$ iterations, in logarithmic ($\log_{10}$) scale. The red marker indicates the true values of the signals, while the black marker indicates the bulk estimate of the composite signal. For this and upcoming cases, it is important to note that the distributions are skewed towards high $s\rho_{\mathrm{HV}}$, but the mean values depicted in the DPSD estimates (e.g., in Figure 4.10a) are in fact closer to the markers (e.g., in Figure 4.10b) than it appears. The logarithmic scale was chosen to emphasize the distributions of the polarimetric characteristics of the SNR-thresholded spectral coefficients, since the mean values of the DPSD estimates may not always correctly represent important differences between the estimators under analysis. Comparing the estimators, the effect of increasing K in the ideal estimator can be seen to reduce the errors. Additionally, in the Bootstrap estimates, the difference between the values of the signals is clearer than with the Daniell estimates, showing a better performance for the Bootstrap DPSD estimator. While the Bootstrap estimates are slightly more dispersed when compared to the ideal estimates, it should be noted that the Bootstrap estimates are obtained using $K = 1$, while the ideal estimates are obtained with $K = 20$, which is a significant difference. The actual values of the SNR, the mean radial velocities, or the spectrum widths of the

signals are irrelevant in this case (assuming the signals are not "leaking" into one another), since the separation between the signals is evident. The error statistics for each individual signal are equivalent to those of the single-signal analysis.

The spectrum widths and the difference between the mean radial velocities of the signals determine the degree to which the spectral coefficients of one signal are "leaking" into the spectral coefficients of other signals. Now that it is better understood how different signals interact to yield the DPSDs, it can be inferred from the SNR which spectral coefficients are more relevant. Additionally, certain patterns in $s\hat{Z}_{\mathrm{DR}}$ and $s\hat{\rho}_{\mathrm{HV}}$ can aid in determining characteristics of dominant (or non-dominant) signals in the spectra. In practice, however, it would be impossible to determine the amount of overlap to perform a one-to-one classification of the polarimetric variables for each spectral coefficient. Nevertheless, even if the presence of two or more different signals is not readily apparent in the spectra, it is possible to obtain a meaningful qualitative inference of the underlying phenomena with the DPSDs.

4.5.2.2 Cases 1-4

For this set of cases, the hypothetical debris signal is assumed to be higher in power. The mean radial velocity of the debris signal is varied such that the difference in radial velocity with the hypothetical raindrop signal is 0 for case 1, $\sigma_{v,1}$ for case 2, $2\sigma_{v,1}$ for case 3, and $3\sigma_{v,1}$ for case 4. Case 1 (Figure 4.11a) shows a complete overlap of the debris spectral signature on the raindrop spectral signature, which yields a unimodal PSD. An analysis based on the PSD alone would not provide any useful

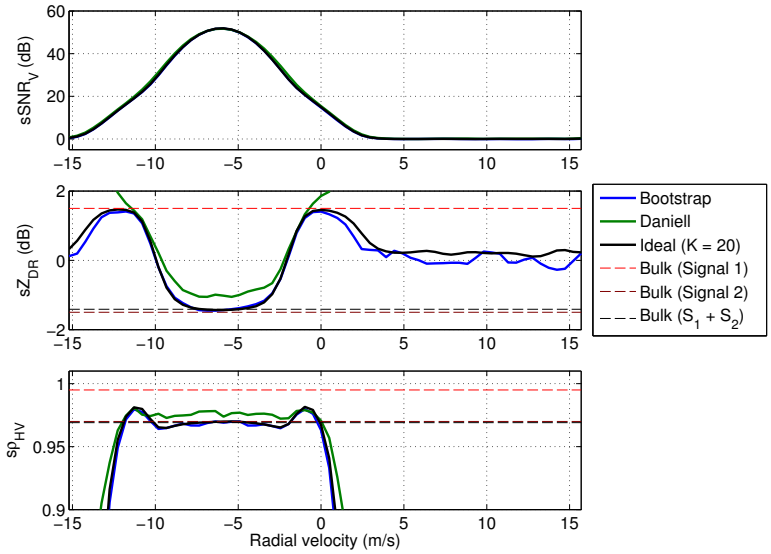

(a)

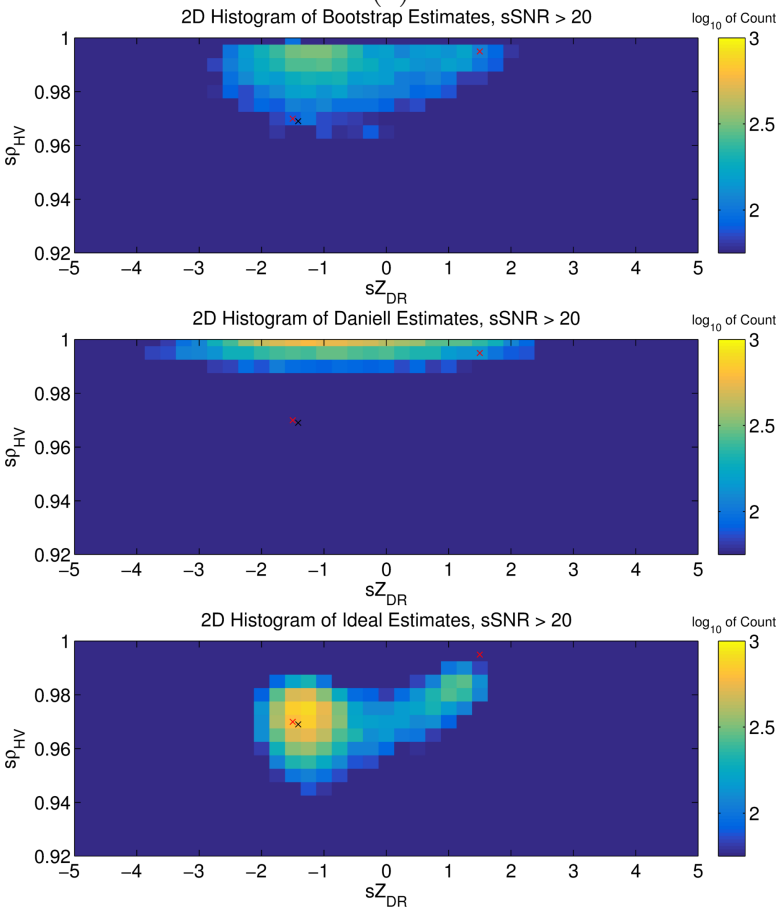

(b)

Figure 4.11: Same as Figure 4.10, but for case 1.

information about the additional signal. However, the spectral signatures of Z_{DR} and ρ_{HV} show evidence of different polarimetric characteristics. Spectral techniques to extract information from the DPSDs could be developed for various applications, though this is beyond the scope of this work. In Figure 4.11b, the histograms of the ideal estimates show two distinct regions distributed near the true values of the signals. The Bootstrap estimates are also able to produce these two regions, though the errors are visibly higher than the ideal estimates (higher bias and variance). With the Daniell estimates, the values are distributed across a wider range of Z_{DR} and mostly high ρ_{HV} values. The distinction between the values of the two different signals is not apparent, and thus it fails to produce distinctive signatures in the DPSDs.

The subsequent cases show bimodal spectra (Figures 4.12a-4.14a), with the difference in mean radial velocities increased to $\sigma_{v,1}$, $2\sigma_{v,1}$, and $3\sigma_{v,1}$ for cases 2, 3, and 4, respectively. With the increasing separation between the signals' mean radial velocities, it becomes easier to identify the different spectral signatures based on the PSD. With the aid of the DPSDs, the influence of the debris signal can be detected and the raindrop signal can be extracted to obtain more accurate measurements of its properties. Additionally, the histograms (Figures 4.12b-4.14b) of the Bootstrap and ideal estimates indicate the presence of two distinct signals, with the separation becoming clearer with increasing difference in the mean radial velocities. The Daniell estimates, while they show a weak separation for higher $s\hat{\rho}_{\mathrm{HV}}$ values, are not able to properly capture the less coherent signal.

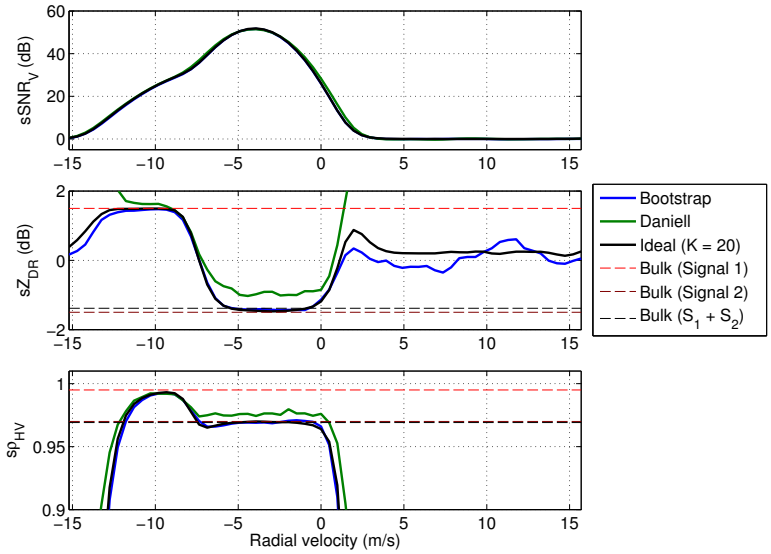

(a)

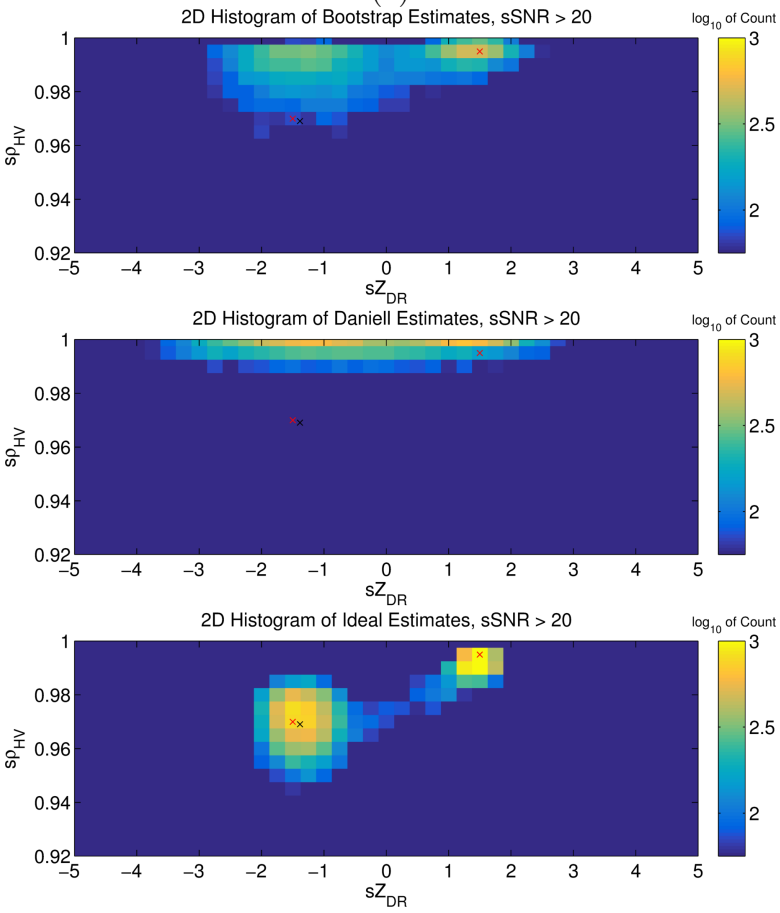

(b)

Figure 4.12: Same as Figure 4.10, but for case 2.

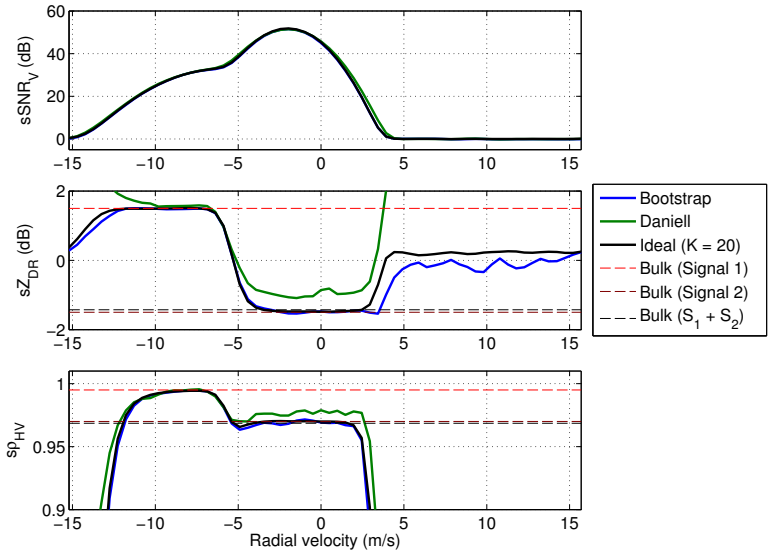

(a)

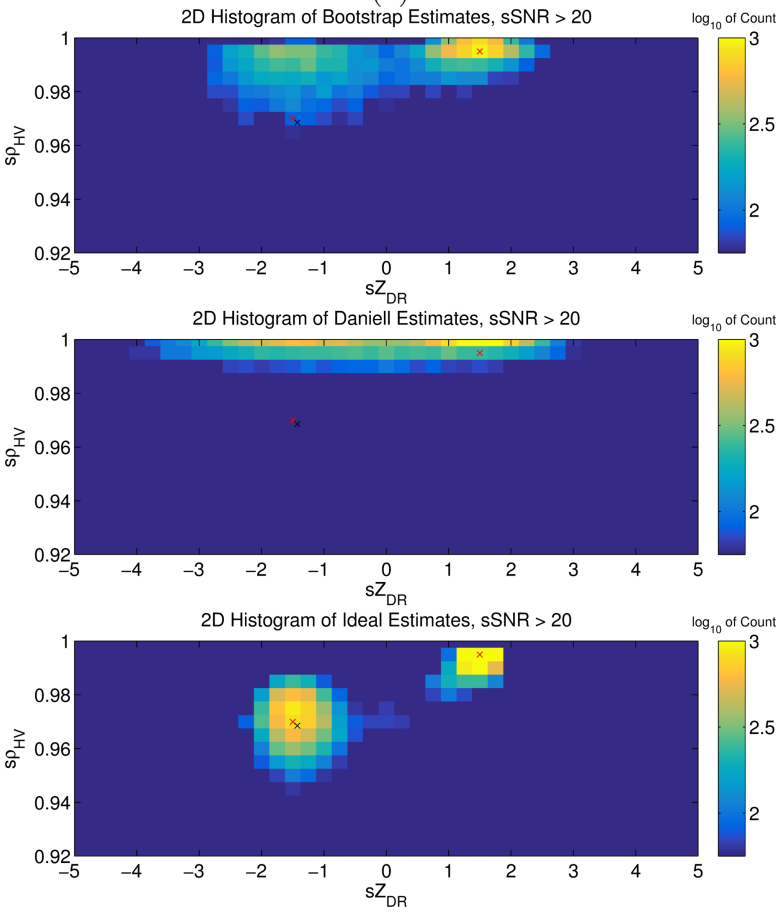

(b)

Figure 4.13: Same as Figure 4.10, but for case 3.

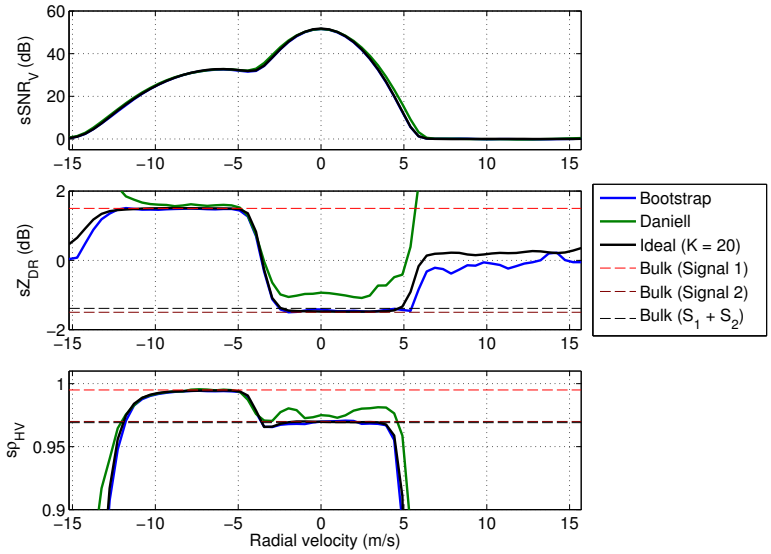

(a)

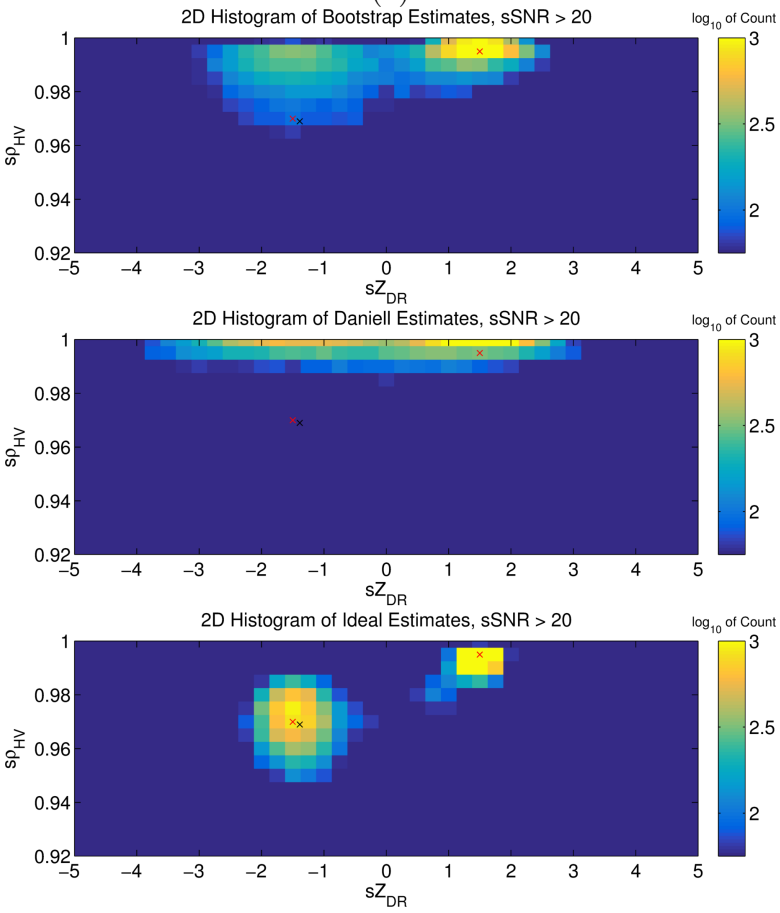

(b)

Figure 4.14: Same as Figure 4.10, but for case 4.

4.5.2.3 Cases 5-8

This set of cases assume the raindrop and the debris signals are comparable in power. Similar to the previous set, the mean radial velocity of the debris signal is varied such that the difference in radial velocities is: 0 for case 5, $\sigma_{v,1}$ for case 6, $2\sigma_{v,1}$ for case 7, and $3\sigma_{v,1}$ for case 8. A unimodal spectrum is observed for case 5 (Figure 4.15a). Here, since the signals are comparable in power, neither signal is dominant across the width of the debris signal. As such, the spectral polarimetric variables show $s\hat{Z}_{\mathrm{DR}}$ values in between $Z_{\mathrm{DR},1}$ and $Z_{\mathrm{DR},2}$, while $s\hat{\rho}_{\mathrm{HV}}$ is slightly less coherent due to the mixing of signals of different nature. Outside this range, the raindrop signal, which is wider, becomes slightly more dominant and the DPSDs tend to its true bulk polarimetric variable values. Although it is not possible to quantitatively retrieve accurate estimates of the debris signal, the raindrop signal may be reconstructed based on the most accurate information available. Thus, it would be possible to obtain more accurate estimates of the raindrop signal properties; e.g., for retrieval of bulk polarimetric estimates. While the histogram of the ideal estimator (Figure 4.15b, bottom) shows the values spread close to the true values, the debris signal is not dominant for any spectral coefficients and the likely value of $s\hat{Z}_{\mathrm{DR},2}$ and $s\hat{\rho}_{\mathrm{HV},2}$ is shifted towards $Z_{\mathrm{DR},1}$ and $\rho_{\mathrm{HV},1}$. Likewise, the Bootstrap histogram (Figure 4.15b, top) does not show a clear separation of two signals, but the presence of the dominant signal given by $s\hat{Z}_{\mathrm{DR}} \approx s\hat{Z}_{\mathrm{DR},1}$, and $s\hat{\rho}_{\mathrm{HV}} \approx s\hat{\rho}_{\mathrm{HV},1}$ is evident. Additionally, the Daniell histogram values (Figure 4.15b, middle) are inaccurate even to determine the properties of the dominant signal.

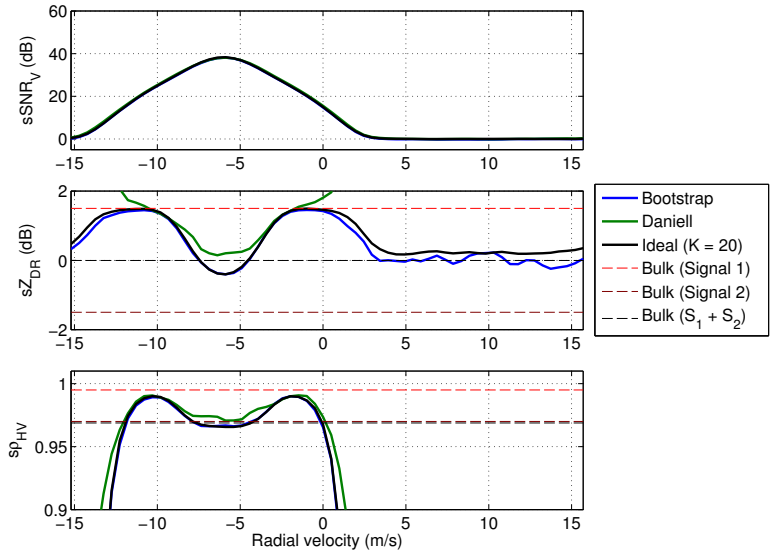

(a)

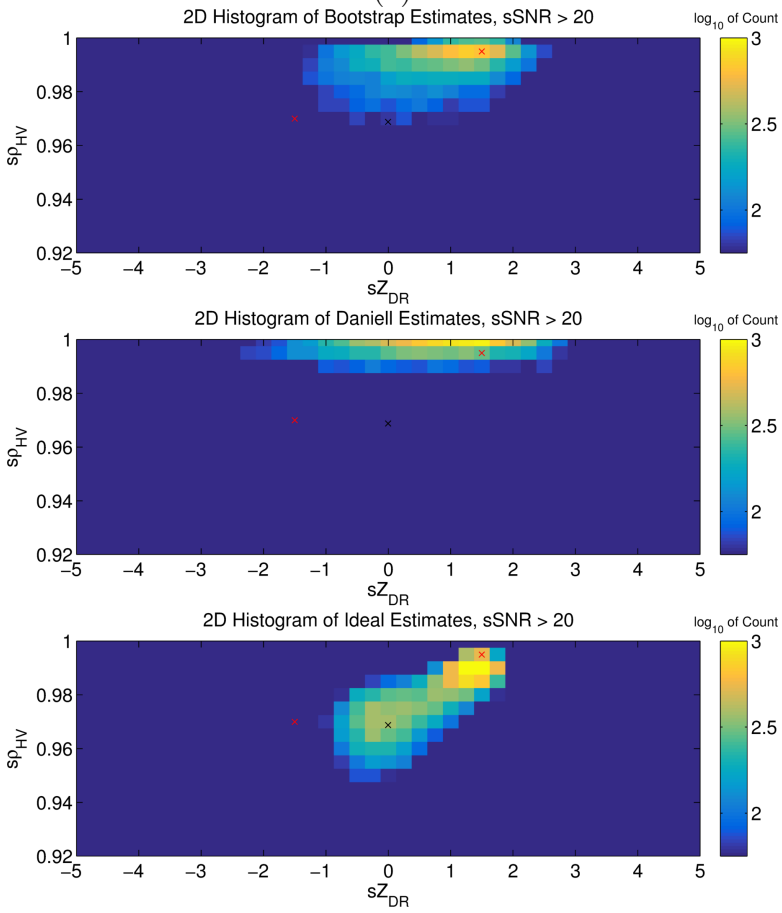

(b)

Figure 4.15: Same as Figure 4.10, but for case 5.

With a mean radial velocity difference of $\sigma_{v,1}$ (case 6, Figure 4.16), a minimal discrimination improvement in the histograms can be seen, though a clear separation of the signals is still not detectable for the Bootstrap estimates. Additionally, the PSD is still somewhat unimodal, but the DPSDs show evidence of different polarimetric characteristics in the spectra. The previous analysis for case 5 still holds true. It is possible to filter out the non-dominant signal to obtain a better estimate of the dominant signal (which, in this case, is the raindrop signal).

In cases 7 and 8, the difference in mean radial velocities are $2\sigma_{v,1}$ and $3\sigma_{v,1}$, respectively (Figures 4.17 and 4.18). The bimodal spectra become more evident and the histograms of the Bootstrap and ideal estimates show a separation closer to the actual values of the signals. Even the Daniell estimates show a weak separation in the $s\hat{Z}_{\mathrm{DR}}$ range, but they are unable to accurately represent the $s\hat{\rho}_{\mathrm{HV}}$ of less coherent signals, as previously mentioned.

4.5.2.4 Cases 9-12

In these cases, it is assumed the raindrop signal has higher power. For cases 9 and 10 (Figures 4.19 and 4.20), the PSDs are unimodal because the raindrop signal, which is wider and stronger, masks the debris signal. The information about the debris signal is completely obscured in the histograms, and even the ideal estimator fails in these cases. There are subtle signatures in the DPSDs that another signal is obscured by this stronger signal; they are characterized by a slight loss in $s\hat{\rho}_{\mathrm{HV}}$ and a variation in $s\hat{Z}_{\mathrm{DR}}$ towards the true value of the debris signal. Despite this, any meaningful qualitative information about the masked signal is lost. In a practical

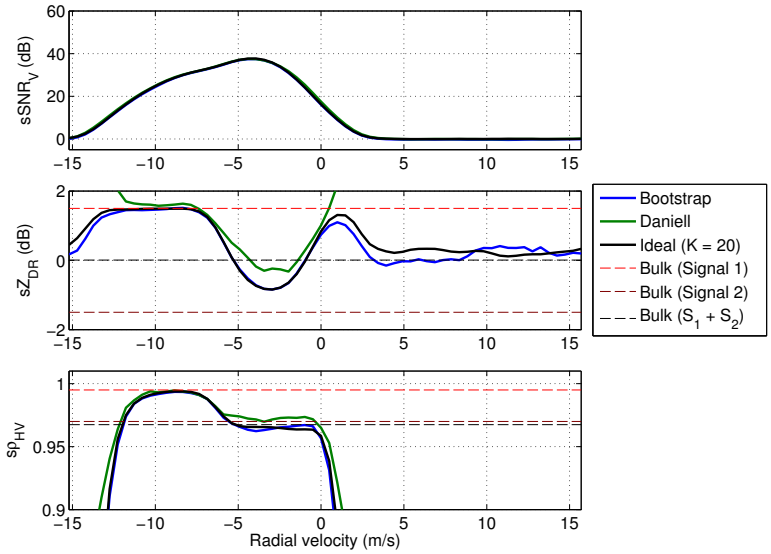

(a)

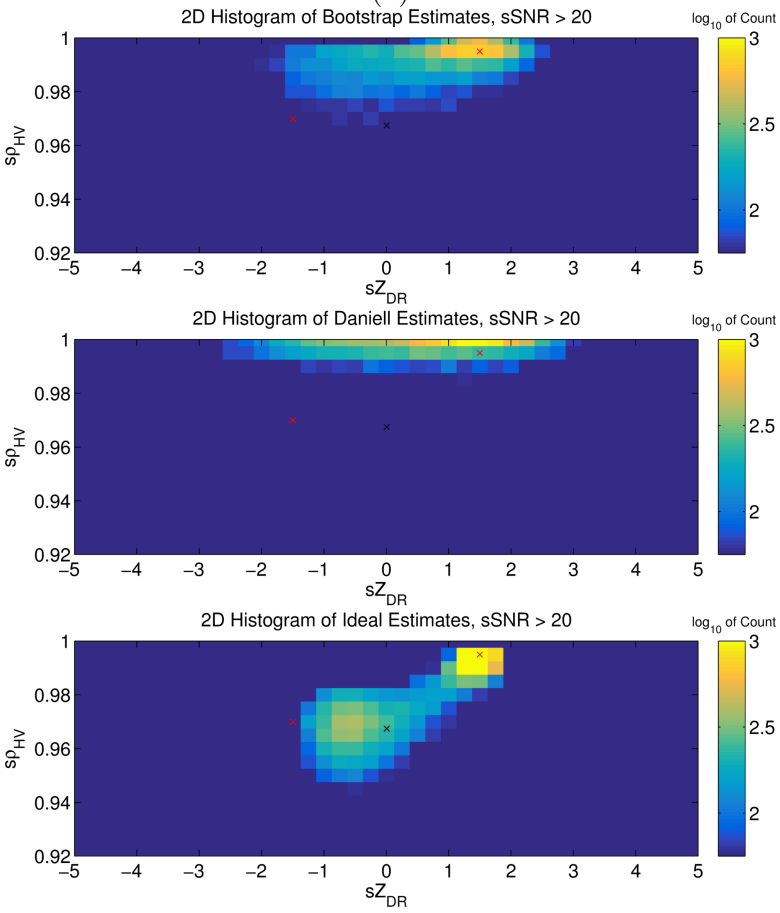

(b)

Figure 4.16: Same as Figure 4.10, but for case 6.

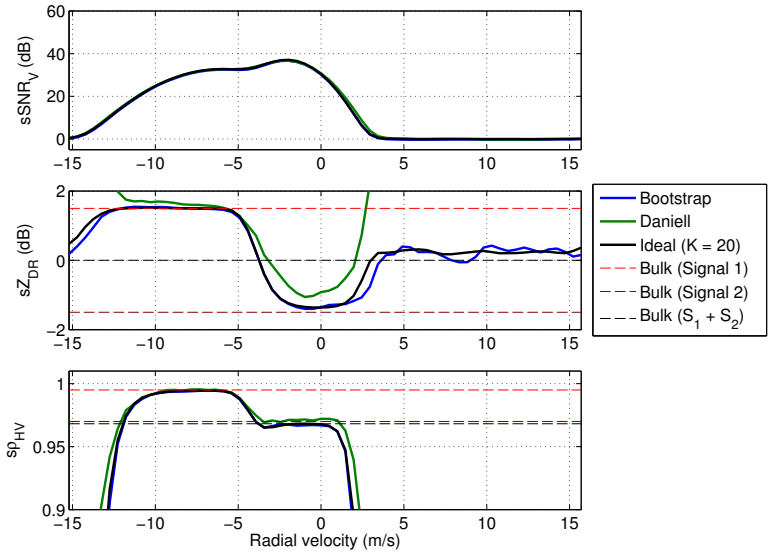

(a)

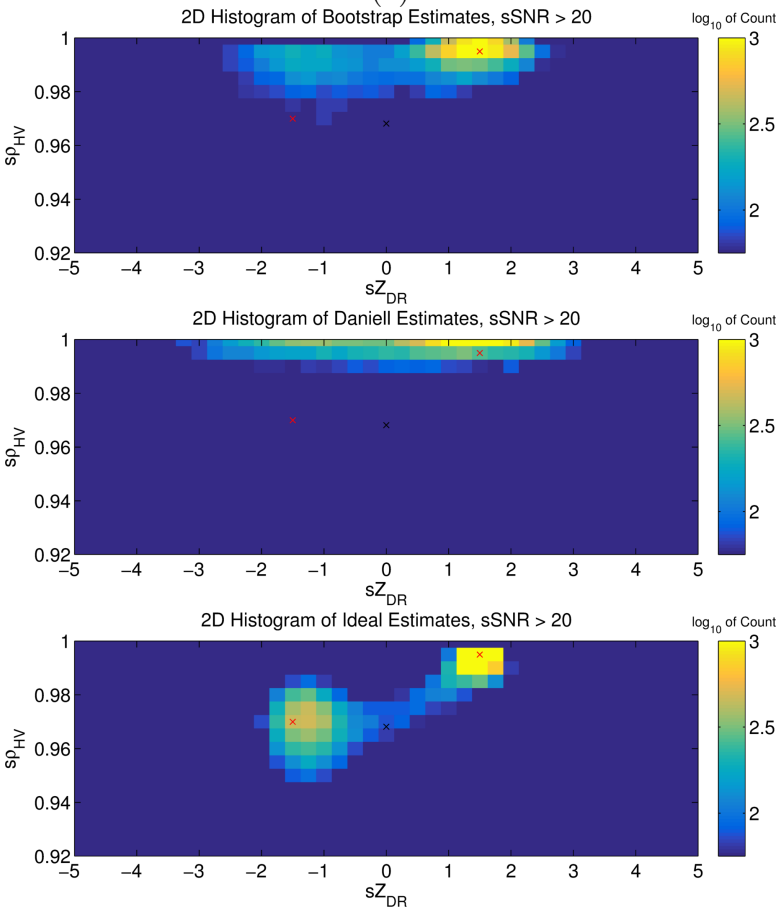

(b)

Figure 4.17: Same as Figure 4.10, but for case 7.

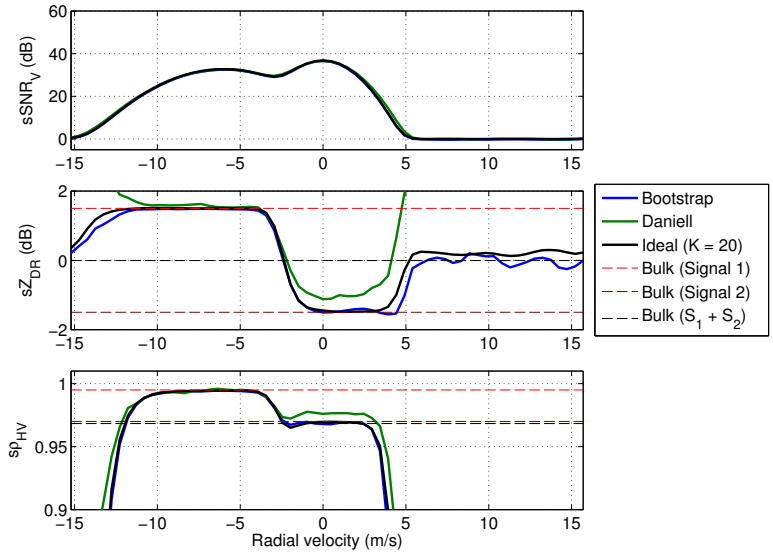

(a)

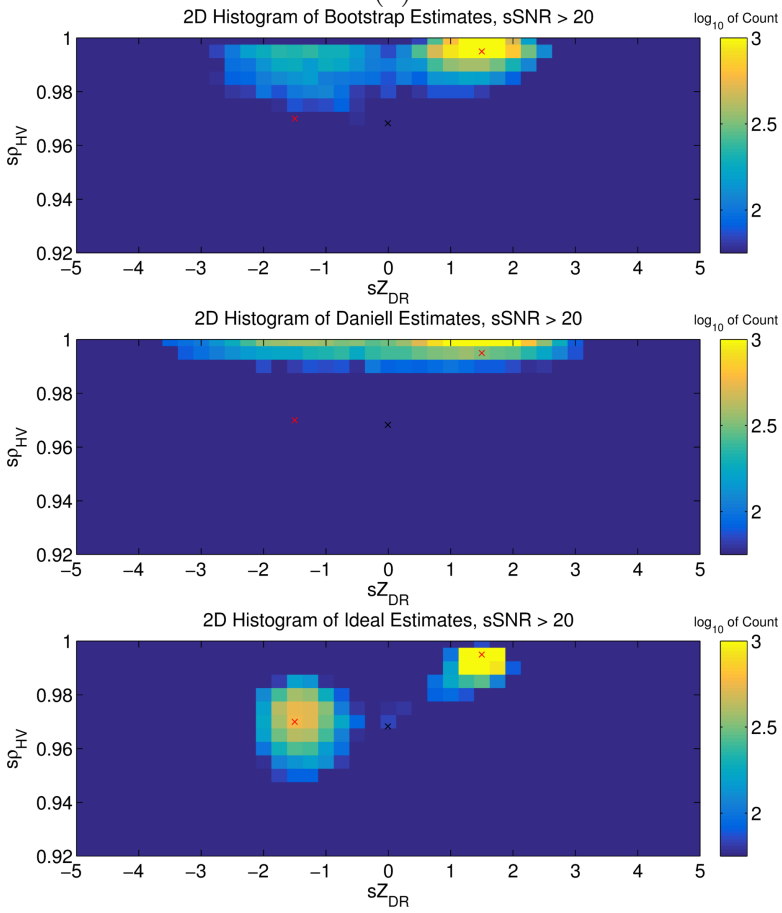

(b)

Figure 4.18: Same as Figure 4.10, but for case 8.

weather radar situation, if a hydrometeor signal is completely dominant, that would not constitute a problem. However, if the dominant signal is of non-hydrometeor nature, the weather information would be irretrievable.

For case 11 (Figure 4.21), the signals are simulated with a difference in mean radial velocities of $2\sigma_{v,1}$, but with the raindrop signal being higher in power, the PSD still appears to be unimodal. However, the DPSDs show a more noticeable variation as the raindrop signal weakens and the influence of debris signal becomes stronger. The histogram of the ideal estimates show a distribution around the true value of the dominant signal, and also around the weighted values where neither signal is dominant. As previously mentioned, this shifted distribution can be attributed to the presence of a different signal, albeit not quantitatively meaningful due to the poor accuracy. The performance of the Bootstrap estimates in detecting this additional signal is inferior as the distribution in the histogram is mostly around the true value of the raindrop signal. Nevertheless, with the information provided by the DPSDs, it is possible to filter out spectral coefficients with different polarimetric characteristics and focus on the dominant characteristics; e.g., to get better bulk estimates of the polarimetric variables. Once again, Daniell estimates have high variance on $s\hat{Z}_{\mathrm{DR}}$ and are skewed towards higher $s\hat{\rho}_{\mathrm{HV}}$, and thus, are unreliable.

The mean radial velocity difference is set to $3\sigma_{v,1}$ for Case 12 (Figure 4.22). Note that the signals are sufficiently apart in velocity such that the PSD is somewhat bimodal and the DPSDs are closer to their respective true values. This can be detected in the histograms as the values are more closely distributed around the true values of the signals. While both the ideal and the Bootstrap estimates show

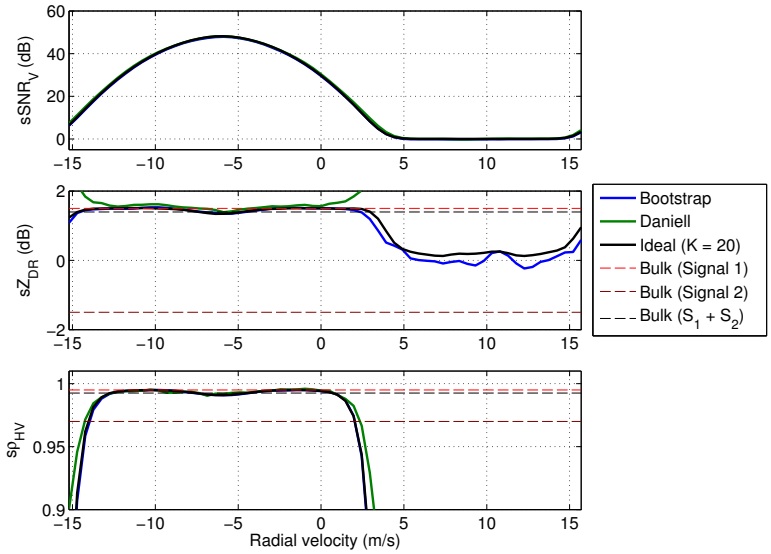

(a)

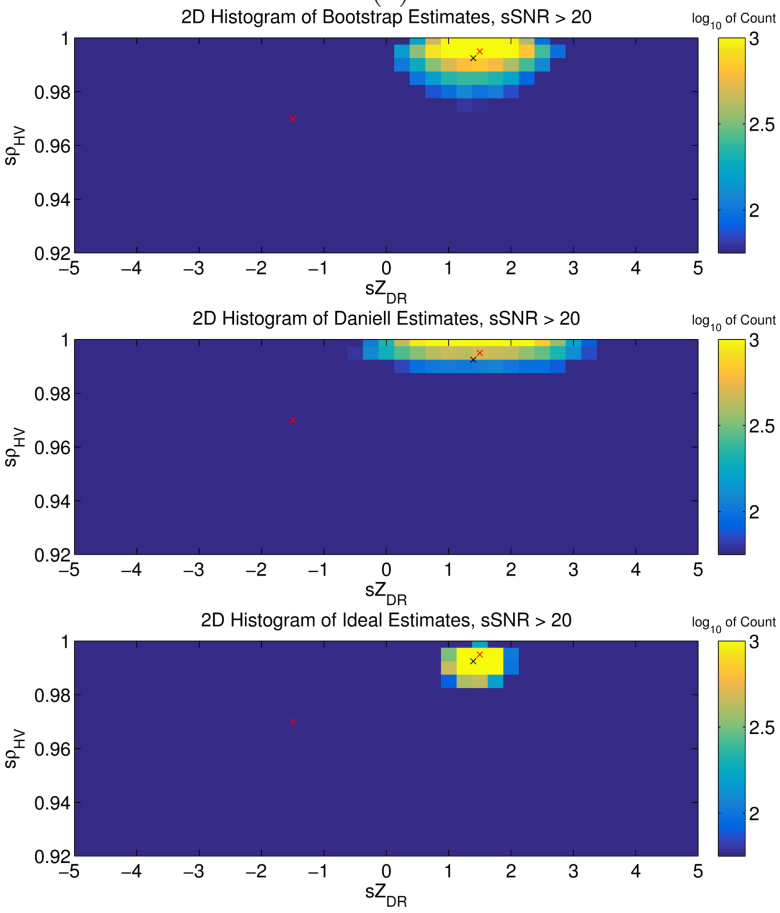

(b)

Figure 4.19: Same as Figure 4.10, but for case 9.

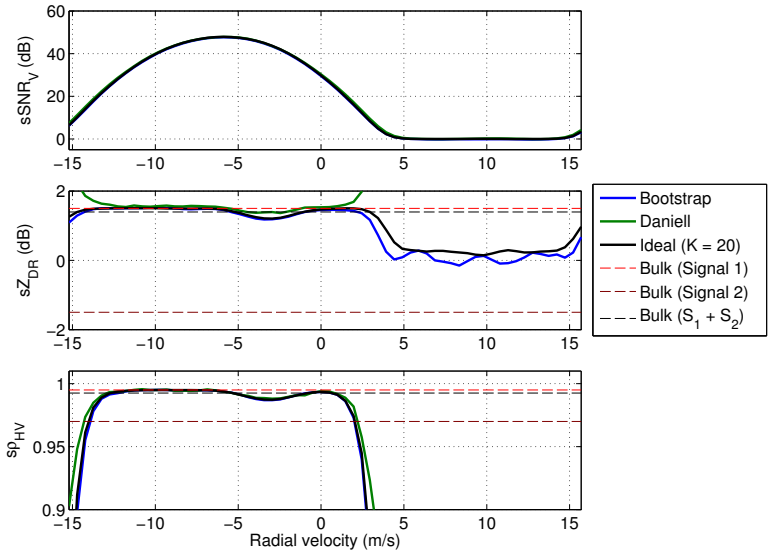

(a)

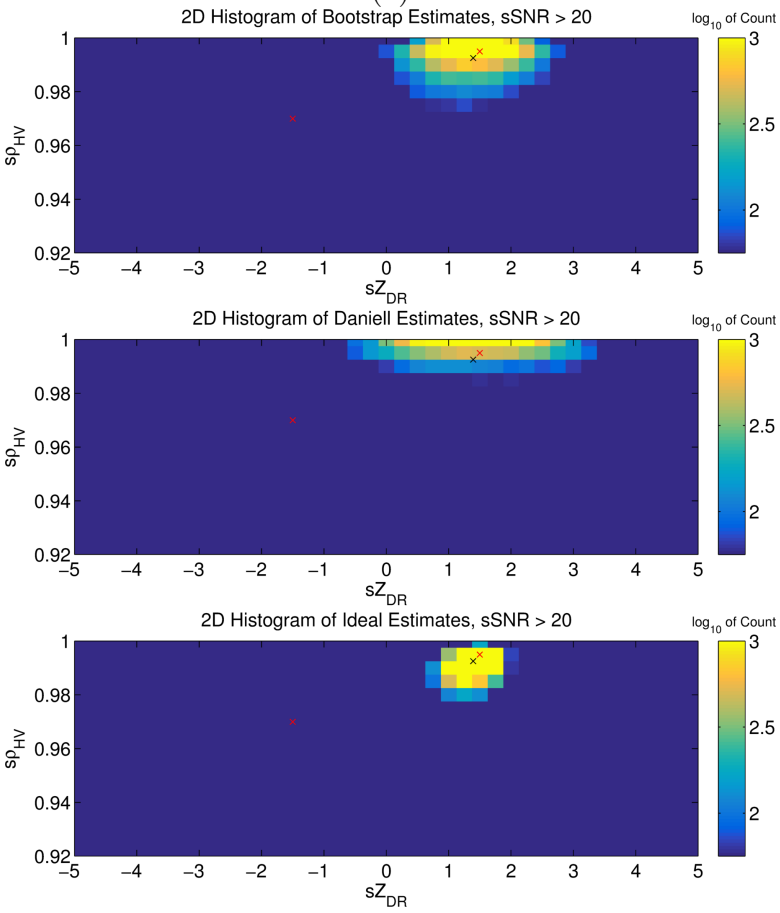

(b)

Figure 4.20: Same as Figure 4.10, but for case 10.

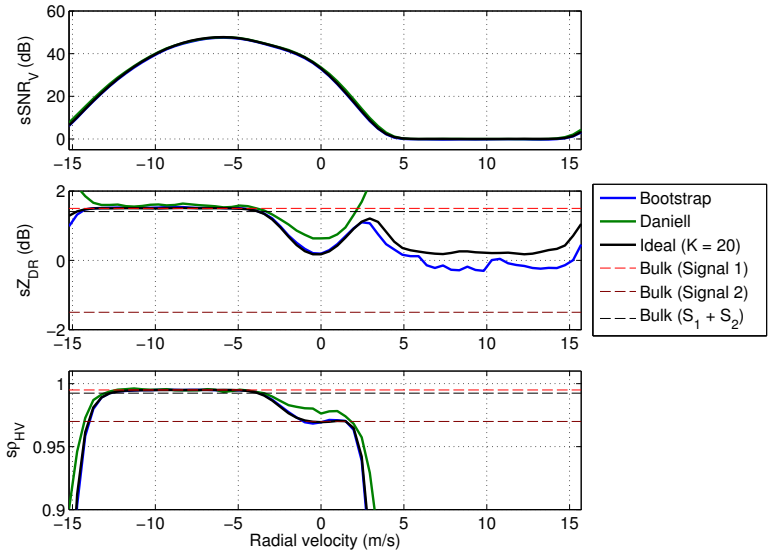

(a)

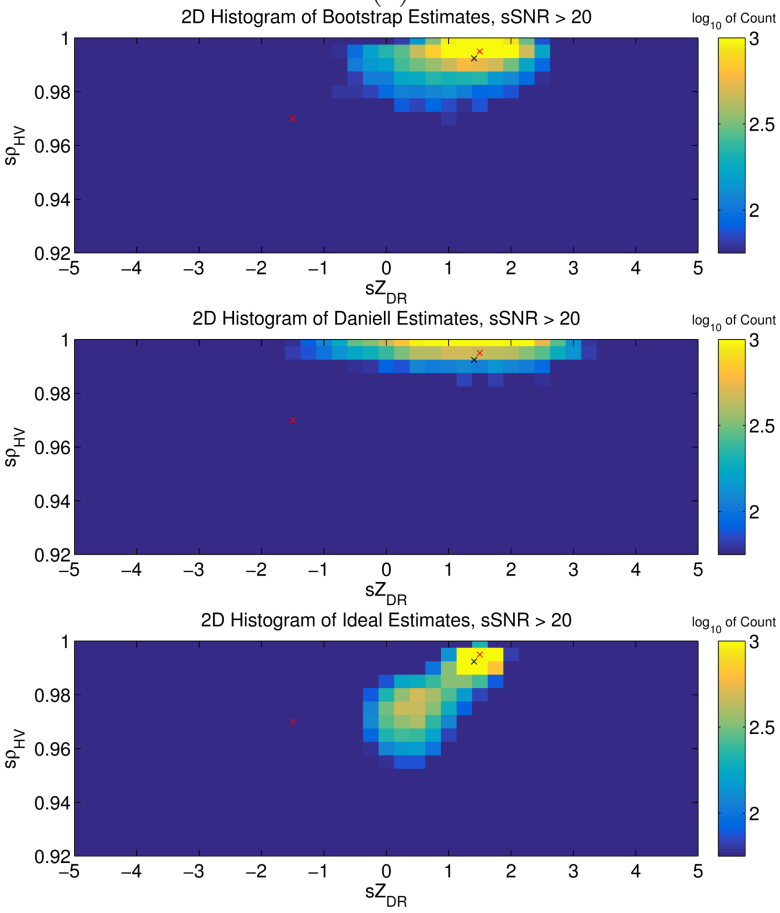

(b)

Figure 4.21: Same as Figure 4.10, but for case 11.

Methods	Cases				
	1, 5, 9 ($\lvert\Delta\bar{v}_r\rvert = 0$)	2, 6, 10 ($\lvert\Delta\bar{v}_r\rvert = \sigma_{v,1}$)	3, 7, 11 ($\lvert\Delta\bar{v}_r\rvert = 2\sigma_{v,1}$)	4, 8, 12 ($\lvert\Delta\bar{v}_r\rvert = 3\sigma_{v,1}$)	0 ($\lvert\Delta\bar{v}_r\rvert > 3\sigma_{v,1}$)
Daniell	None	None	1 out of 3 (sZ_{DR} only)	1 out of 3 (sZ_{DR} only)	All
Bootstrap	1 out of 3	1 out of 3	2 out of 3	All	All
Ideal	2 out of 3	2 out of 3	All	All	All

Table 4.3: Ability to distinguish signal constituents.

two distinct signals (with the Bootstrap estimates being less accurate), the Daniell estimates are still inferior to the Bootstrap estimates.

4.5.2.5 Recap of All Cases

It was clear from the previous analysis that the Daniell estimates performed the worst, mainly due to the inability to correctly estimate the DPSDs of less coherent signals (the $s\hat{\rho}_{\mathrm{HV}}$ distributions were particularly skewed). As summarized in Table 4.3, in 8 out of the 13 cases under analysis, the histogram of Bootstrap estimates showed distinct distributions near the true Z_{DR} values of the signals, though with a somewhat skewed distribution in $s\hat{\rho}_{\mathrm{HV}}$, with a mean bias similar to the values from the single signal single dwell analysis. A successful separation in the histogram means that the polarimetric characteristics of two distinct signals were properly identified for these cases (in a qualitative manner). Likewise, the ideal estimates were slightly more successful, with 11 out of 13 cases, and obviously with less errors. However, it should be emphasized that the ideal estimates used $K = 20$ independent spectra, whereas Daniell and Bootstrap estimates were obtained using only one independent spectrum ($K = 1$). Additionally, the cases included unimodal and bimodal spectra. In the three cases where the Bootstrap estimates performed poorly, it was shown that there was evidence of dispersion in the distribution. In these situations,

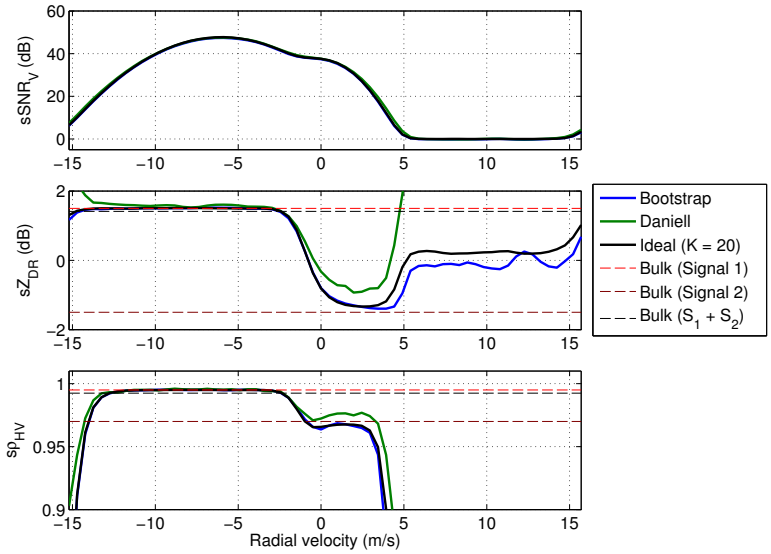

(a)

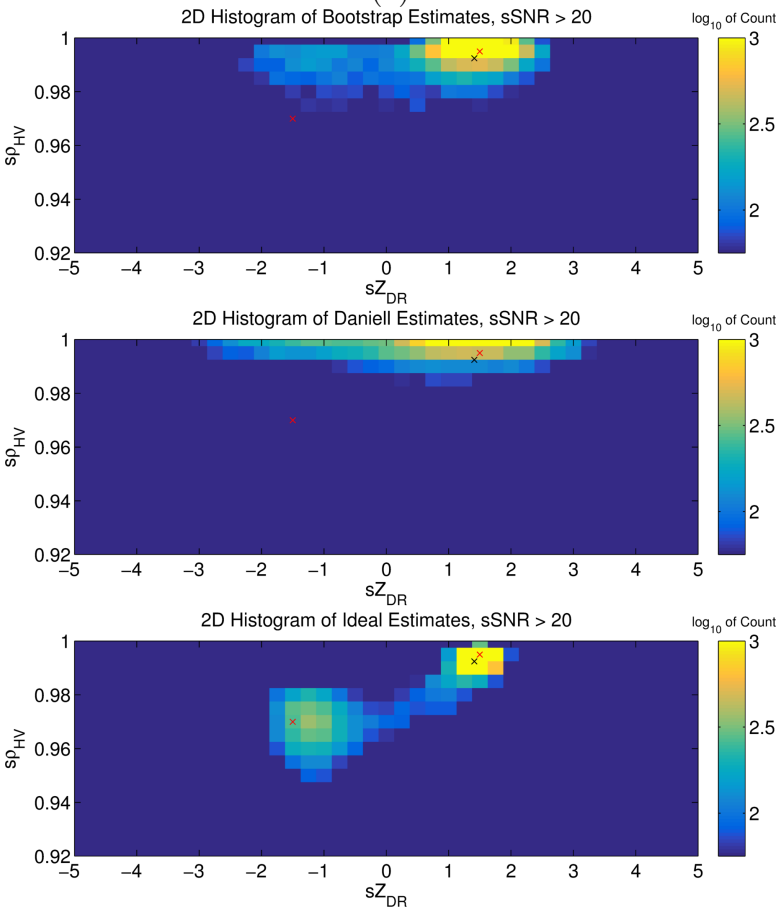

(b)

Figure 4.22: Same as Figure 4.10, but for case 12.

techniques such as filtering of non-desired signals could be used to further improve the estimation of the properties of the desired signal. Furthermore, in two cases where a wider and stronger signal was completely dominating the weaker signal, not even the ideal estimates were able to identify the distinct spectral signatures. It should be noted that there are many cases in which the identification may not be at all possible even with an ideal DPSD estimator; e.g., wide high-power signal completely masking a narrow weaker signal, signals of similar widths and mean radial velocities, signals with similar polarimetric characteristics and mean radial velocities, etc.

4.6 Summary

The Bootstrap DPSD estimator shows superior error statistics when compared to conventional DPSD estimators under similar conditions (i.e., minimal frequency resolution loss). Moreover, it allows estimation of DPSDs with better quality using a single dwell ($K = 1$), without resorting to averaging PSDs in time, range, azimuth or frequency. However, if it is acceptable to compromise the resolution in any of those dimensions, the Bootstrap DPSD estimates with just a few dwells produce accurate results with better performance than the conventional DPSD estimators. In such cases, the bias levels of the ideal DPSD estimator ($K = 20$) are equivalent to the Bootstrap DPSD estimator with $K = 5$; and the variance levels are equivalent to the Bootstrap DPSD estimator with $K = 13$. These numbers show a significant reduction in the number of independent spectra needed to achieve desirable error

levels (and to consequently produce accurate quantitative spectral analyses), though they may still be somewhat elevated to be operationally feasible. The dual-signal analysis showed that the single-dwell Bootstrap DPSD estimates still yield useful results for meaningful qualitative spectral analysis, and is superior than the conventional DPSD estimator. For bimodal (or multimodal) spectra, the Bootstrap DPSD estimates are able to identify distinct spectral signatures, regardless of the difference in mean radial velocities, as long as the polarimetric characteristics of the signals are not too similar. Additionally, even with certain unimodal spectra composed of different signals, the Bootstrap DPSD estimator is able to identify distinct spectral features, though not as good as (and with more errors than) the ideal estimates. The next chapter discusses the results of applying the Bootstrap DPSD estimator on data from a simulated environment and from real observations.

Chapter 5

Results on Observations and Simulations

When non-hydrometeor scatterers are dominant (e.g., in TDS), the desired weather information, which is given by the non-dominant scatterers, may be lost in bulk radar estimates. It was mentioned previously that a major limitation with the conventional polarimetric spectral analysis techniques was the requirement of a large number of independent spectra in order to obtain accurate estimates. Averaging spectra from different range gates, azimuths, dwells, or even by smoothing in the frequency domain, are different methods used in the past to estimate the DPSDs. However, the associated resolution loss could obscure important details of the underlying phenomena, especially if it is evolving fast in time and in a small spatial extent. The Bootstrap DPSD estimator provides a means to obtain better quality dual-polarimetric spectra based on a single dwell. This chapter illustrates the performance of the Bootstrap DPSD estimator when applied to real and simulated data. The first section presents examples of polarimetric spectral signatures observed in four different datasets obtained with different radars for two tornado cases, with the goal of illustrating the advantages of the Bootstrap DPSD estimator over conventional DPSD estimators, and over range-, azimuth-, scan-, or frequency-averaged

DPSDs. The next section shows examples of DPSDs obtained from a radar simulator, based on raindrops and debris in a tornadic vortex, to assess the impact of tornado dynamics on radar measurements from a spectral polarimetric perspective.

5.1 Real Observations

The following analyses use I/Q time-series data collected with the KOUN, OU-PRIME, and PX-1000 radars during the 10 May 2010 Moore-Norman, OK, and the 20 May 2013 Moore, OK tornadoes. A brief description of the radar systems is presented hereafter next and a summary of the characteristics of the radar systems is presented in Table 5.1. KOUN is an S-band polarimetric radar with a 0.9° 3-dB beamwidth, range sampling of 250 m, and a peak transmit power of 750 kW; on these dates, it operated with a maximum unambiguous velocity of 27.5 m/s. OU-PRIME is a C-band polarimetric radar with a 0.45° 3-dB beamwidth, a range sampling of up to 60 m, and a peak transmit power of 1 MW. During the acquisition of the data, it operated with a range sampling of 125 m and a maximum unambiguous velocity of 16 m/s. PX-1000 is a transportable, X-band polarimetric radar, with a 1.8° 3-dB beamwidth, a range sampling of up to 30 m, and two identical and independent solid state transmitters with total peak power of 200 W (at the time of data collection). Data under analysis were collected with a maximum unambiguous velocity of 15.7 m/s and a range sampling of up to 30 m.

Detailed technical specifications on OU-PRIME can be found in Palmer et al. (2011), and on PX-1000 in Cheong et al. (2013). Data were collected with KOUN

Transmitter			
	KOUN	OU-PRIME	PX-1000
Operating frequency	2705 MHz	5510 MHz	9550 MHz
Wavelength	11.1 cm	5.44 cm	3.14 cm
Peak transmitter power	750 kW	1000 kW	0.2 kW SSPA*
Polarization	STSR**	STSR**	STSR**
Pulse lengths	1.57 or 4.7 μs	0.4 to 2.0 μs	1 to 70 μs
Antenna			
	KOUN	OU-PRIME	PX-1000
Diameter	8.5 m	8.5 m	1.2 m
Beamwidth (-3 dB)	0.9°	0.45°	1.8°
Gain	44.5 dB	50 dB	38.5 dB
First SLL	Better than -27 dB	Better than -27 dB	Better than -26 dB
Cross-polar isolation	Better than -35 dB	Better than -35 dB	Better than -26 dB
Rotation rate	36°/s max	30°/s max	50°/s max
Receiver			
	KOUN	OU-PRIME	PX-1000
A/D converter bits	16 bit	16 bit	14 bit
Gate spacing	250 m	25-500 m	30 m

* Solid State Power Amplifier.
** Simultaneous Transmission - Simultaneous Reception.

Table 5.1: Characteristics of the KOUN, OU-PRIME, and PX-1000 radar systems.

05/10/2010 data sets	KOUN	OU-PRIME
Time (UTC)	22:21:33-22:58:28	22:00:47-22:59:12
Scanning strategy	PPI	PPI
Elevation angles (°)	0.5, 0.9, 1.4, 1.9, 2.4, 3.2, 4.0, 5.1, 6.4, 8.0, 10.0, 12.5, 15.6, 19.5	0.2, 1.0, 2.0, 3.0, 4.0, 5.0, 6.5, 9.0
Update time	∼4'20"	∼2'30"
Wavelength	11.1 cm	5.44 cm
PRF	1000 Hz	1176.5 Hz
Maximum unambiguous velocity	27.5 m/s	16 m/s
Range sampling	250 m	125 m
05/20/2013 data sets	**KOUN**	**PX-1000**
Time (UTC)	19:46:29-20:42:31	19:44:49-20:39:51
Scanning strategy	PPI	PPI
Elevation angles (°)	0.5, 1.0, 2.0, 3.0, 4.0, 5.0, 6.0, 8.0, 10.0	2.6
Update time	∼4'20"	∼20"
Wavelength	11.1 cm	3.14 cm
PRF	1000 Hz	2000 Hz
Maximum unambiguous velocity	27.5 m/s	15.7 m/s
Range sampling	250 m	30 m

Table 5.2: Operational settings and acquisition parameters for the four cases under analysis.

and OU-PRIME radars for the 10 May 2010 case, and with KOUN and PX-1000 for the 20 May 2013 case. The operational settings corresponding to the available data are summarized in Table 5.2.

Brief descriptions of the two weather events are presented next. The first case took part in the second largest tornado outbreak documented in Oklahoma, which affected a large part of northern, central, and southern portions of the state. According to NWS Weather Forecast Office Norman (2010), during the late afternoon and early evening hours of May 10, 2010, thirteen different storms produced tornadoes, spawning a total of 36 tornadoes in the NWS Norman forecast area alone, and also producing significant structural damage over many areas with estimated losses in excess of $595 million, three fatalities and over 450 injuries. It is indicated

that due to the potent combination of atmospherical conditions, the storms that developed quickly became tornadic after initiation, with typical storm motions of 50 to 60 mph. Reports indicate that between 22:33 and 22:59 UTC, three to five tornadoes were occurring simultaneously every minute, which includes two EF-4 tornadoes (the Moore and Norman tornadoes), and two other EF-3 tornadoes. Additionally, very large hail was reported in several locations with sizes up to 4.25" in diameter (softball size). A detailed report of this event can be found in NWS Weather Forecast Office Norman (2010).

The second case was part of another tornado outbreak, which took place in parts of the midwest and the Great Plains from May 18-20, 2013. According to NWS Weather Forecast Office Norman (2013), where the most relevant aspects are summarized, during the afternoon and evening hours of May 20, 2013, several supercell thunderstorms developed along a dryline in central Oklahoma. It is indicated that one of these storms developed and rapidly intensified, producing a tornado to the west of Newcastle. The tornado, which touched down at 19:56 UTC, quickly became violent with an east-northeastward direction, across Moore and parts of south Oklahoma City causing catastrophic damage in these areas for about 40 minutes before finally dissipating. The reported losses due to the tornado were over billions of dollars in damage, 24 fatalities, and over 200 injuries. It was given a maximum rating of EF-5, making it the deadliest and most devastating tornado of the year in the United States. In addition to the tornadoes, large hail and damaging winds caused significant damage in many areas. A detailed report of this event can be found in NWS Weather Forecast Office Norman (2013).

In-depth analyses based on weather radar observations of the 10 May 2010 case can be found in Bodine et al. (2011), and of the 20 May 2013 case in Kurdzo et al. (2015). Hence, no discussions about the spatial and temporal evolution or characteristics of the storm will be given in this work. The following sections will provide some examples of polarimetric spectral signatures estimated with the Bootstrap DPSD estimator that are not captured by the bulk polarimetric variables.

5.1.1 Case 1: 10 May 2010, OU-PRIME and KOUN

To make a fair comparison between the datasets corresponding to different radars, it is important that the spatial and temporal characteristics of the event are matched as closely as possible. In this example, the KOUN set corresponding to 22:22:38 UTC with an elevation angle of 1.36°, and the OU-PRIME set corresponding to 22:23:22 with an elevation angle of 0.96° were selected, which are approximately one minute apart. The PPIs for the selected scans for each radar are shown in Figure 5.1. KOUN data were grouped into 2.0° radials with a 0.5° azimuthal spacing, yielding approximately 79 pulses per radial. OU-PRIME data were grouped into 1.0° radials with a 0.5° azimuthal spacing, yielding approximately 70 pulses per radial. Range-Doppler plots are useful for spectral analyses, as they illustrate spectral variables as a function of range and radial velocity, with the intensity representing the particular spectral variable. Each row in the y-axis of the range-Doppler plots represents the spectrum for a given range gate, and the x-axis represents the radial velocity. With the aid of range-Doppler plots, it is possible to observe the spatial distribution and radar-relative motion of the scatterers in a particular radial; and

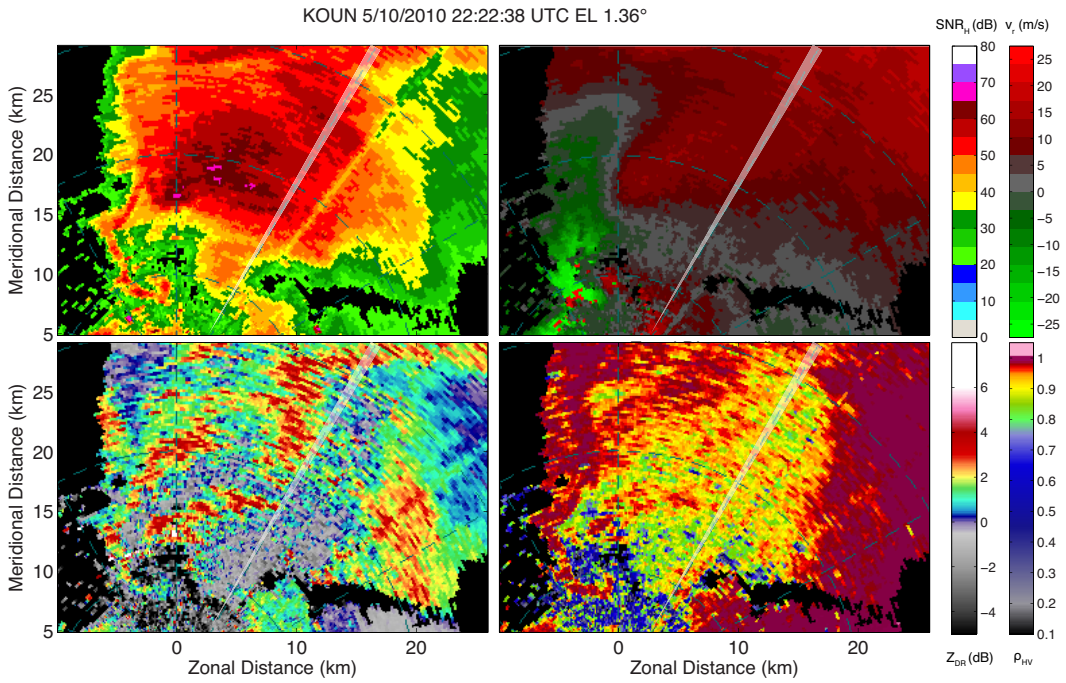

(a)

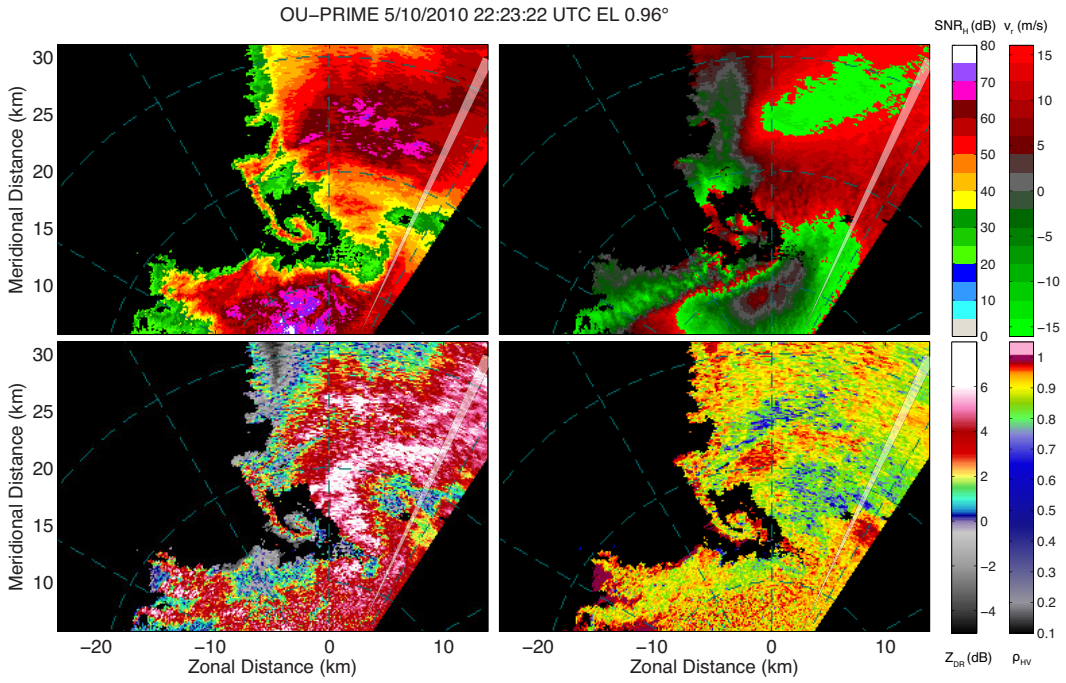

(b)

Figure 5.1: PPI plots corresponding to (a) KOUN data at 22:22:38 UTC, and elevation $\phi = 1.36°$ with azimuth $\theta = 30°$ highlighted, and (b) OU-PRIME data at 22:23:22 UTC, and elevation $\phi = 0.96°$ with azimuth $\theta = 25°$ highlighted: $\mathrm{SNR_H}$ (top left), $\bar{v}_r$ (top right), Z_{DR} (bottom left), and ρ_{HV} (bottom right). Grid lines are 30° and 10 km apart.

with the DPSDs, it is also possible to detect any significantly different scatterer signatures for given radar resolution volumes. First, the differences between the different DPSD estimators will be illustrated. By computing the DPSD estimates, distinct spectral signatures can be found near azimuth $\theta = 30^\circ$ in KOUN data, and $\theta = 25^\circ$ in OU-PRIME data, as depicted in Figures 5.2-5.4. The DPSDs were estimated with a Blackman window (-58 dB SLL), with no zero-padding for the DFT. Furthermore, a 20-dB SNR threshold is used to censor low-SNR spectral coefficients. For a single dwell (i.e., $K = 1$), both Bootstrap and Daniell DPSD estimators provide qualitatively meaningful results, while the periodogram estimator fails to yield useful results. For an easier interpretation, the velocities were manually de-aliased (i.e., x-axis from 0 to $+2v_{\mathrm{a}}$) with information about the storm motion, illustrating the peak of the stronger signal moving at similar radial velocities from both radar measurements. Additionally, estimates with $K = 3$ averaged spectra from adjacent radials are included for clarity. Each spectrum corresponds to a coverage of approximately 4° for the KOUN dataset and 2.5° for the OU-PRIME dataset (Figures 5.5-5.7). It can be observed that the spectral signatures are similar in both cases (using $K = 1$ and $K = 3$), although the single-dwell estimates are noisier. As it has been mentioned in previous chapters, it is desirable to minimize the averaging in any dimension to avoid masking spectral features that may be present. Upon a quick examination, the Daniell estimates are qualitatively similar to the Bootstrap estimates as previously shown. However, the Daniell estimator smoothes the spectra in frequency, and it also does not take into account additional signal information obtainable with bootstrapping. Hence, the $s\rho_{\mathrm{HV}}$ tends to be higher for higher SNR

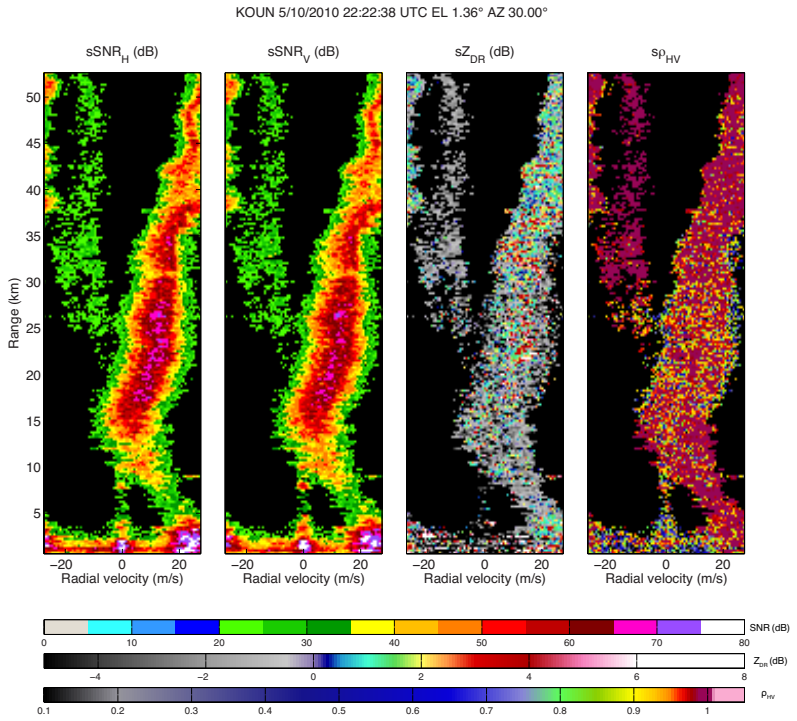

(a)

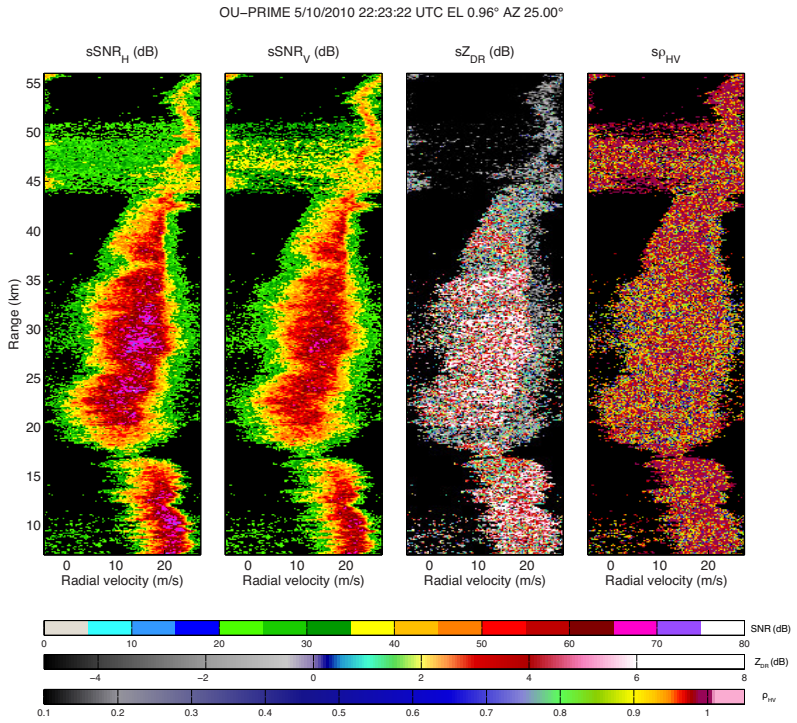

(b)

Figure 5.2: Range-Doppler plots of single-dwell Bootstrap DPSD estimates corresponding to: (a) KOUN data at 22:22:38 UTC, elevation $\phi = 1.36°$, and azimuth $\theta = 30°$, and (b) OU-PRIME data at 22:23:22 UTC, elevation $\phi = 0.96°$, and azimuth $\theta = 25°$ (after velocity dealiasing).

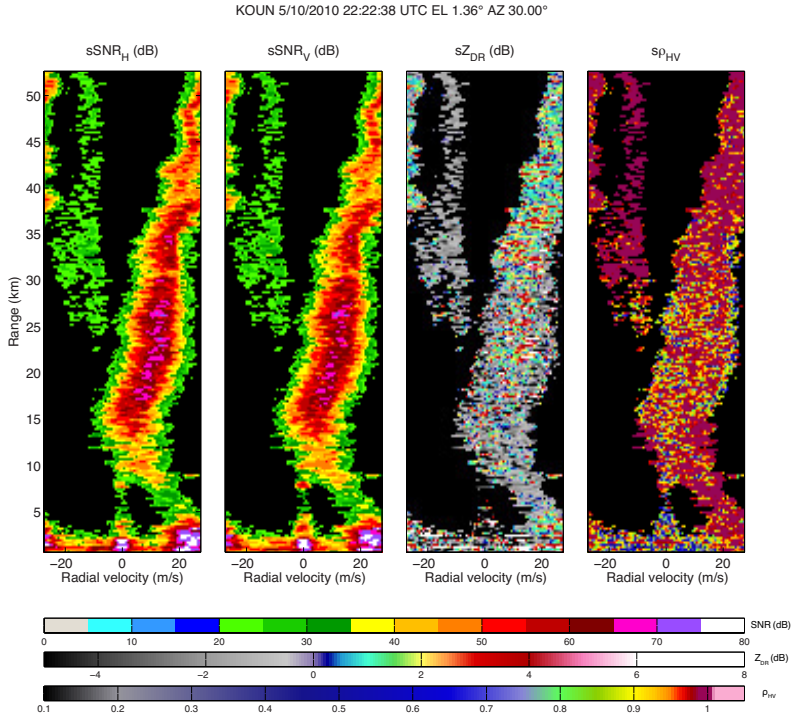

(a)

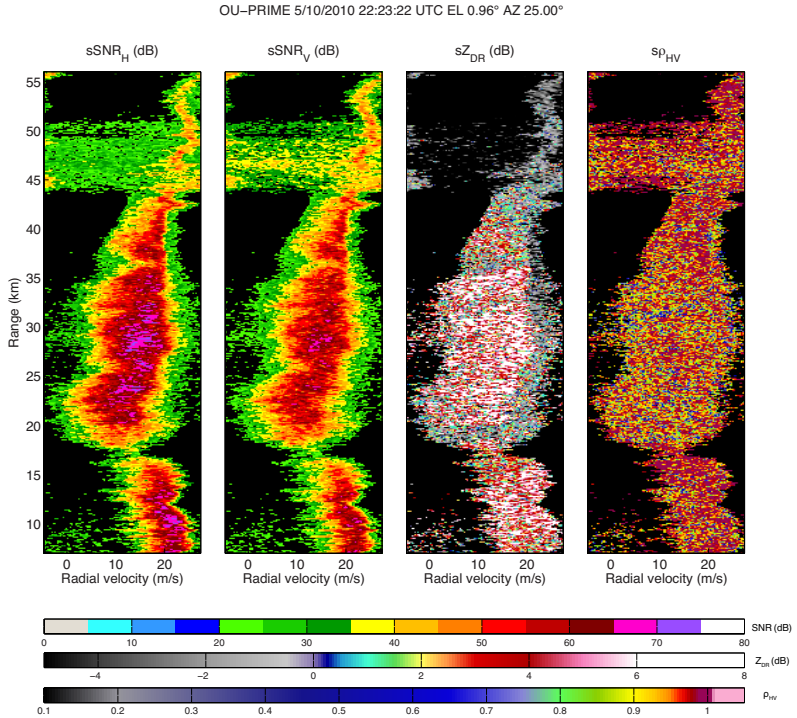

(b)

Figure 5.3: Same as Figure 5.2, but for Daniell DPSD estimates.

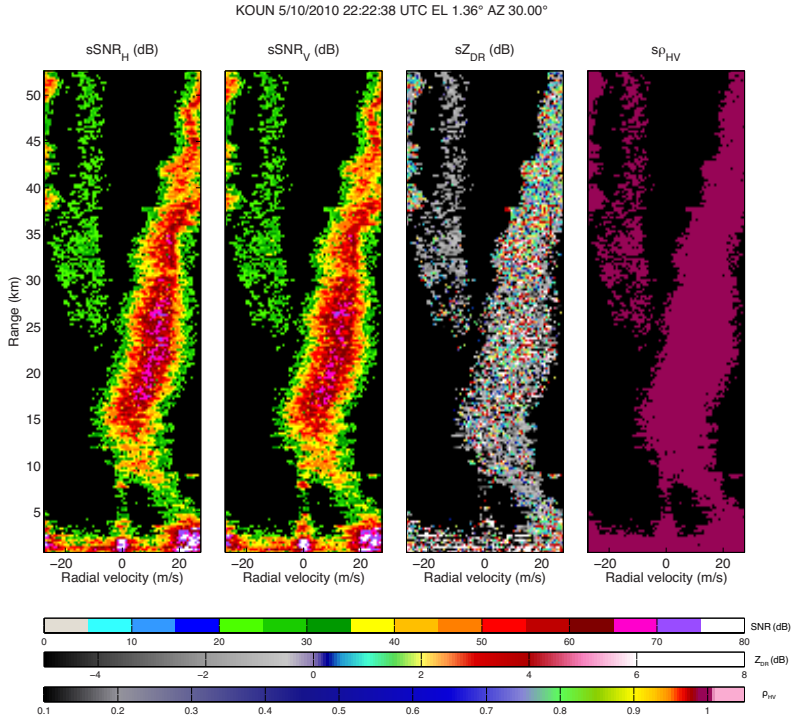

(a)

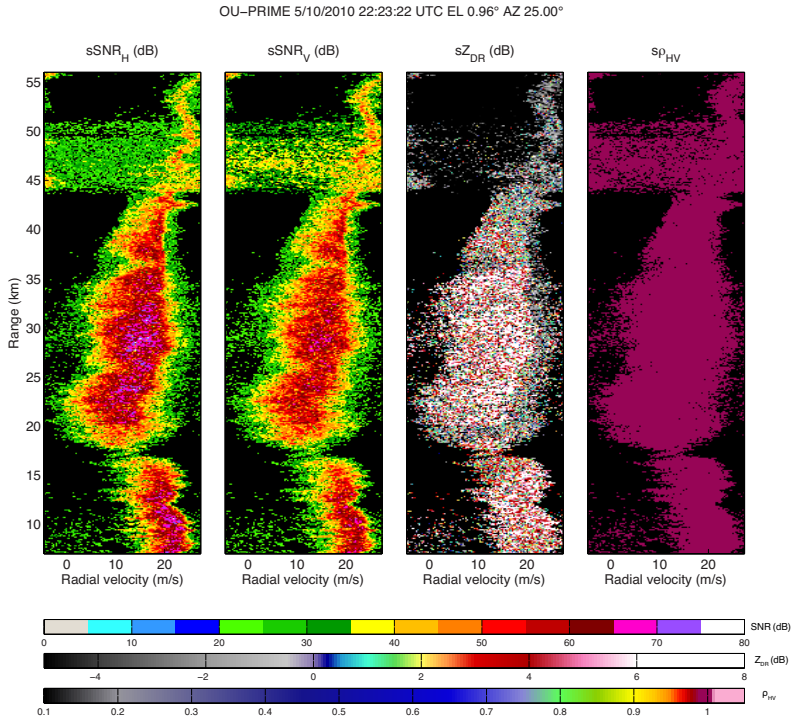

(b)

Figure 5.4: Same as Figure 5.2, but for periodogram DPSD estimates.

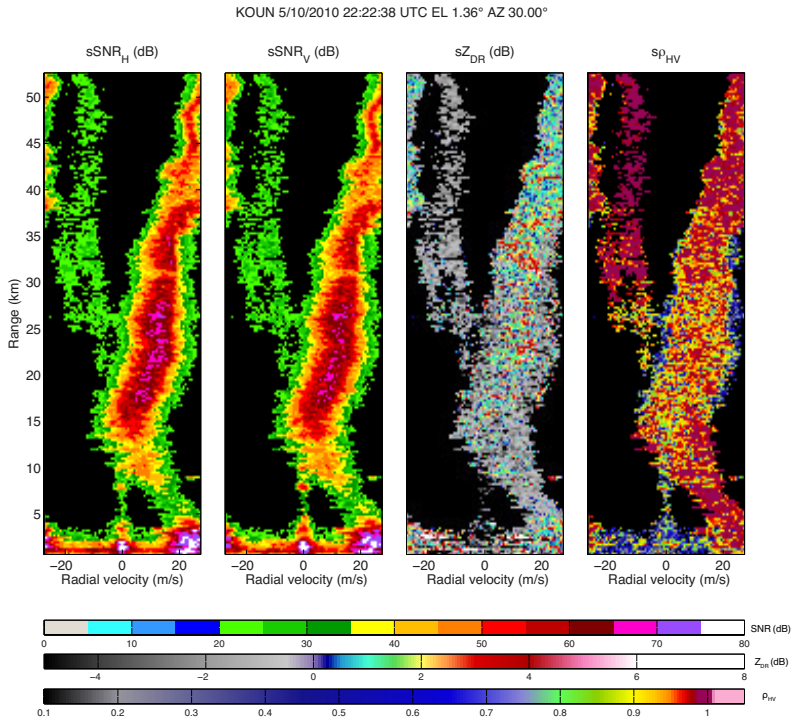

(a)

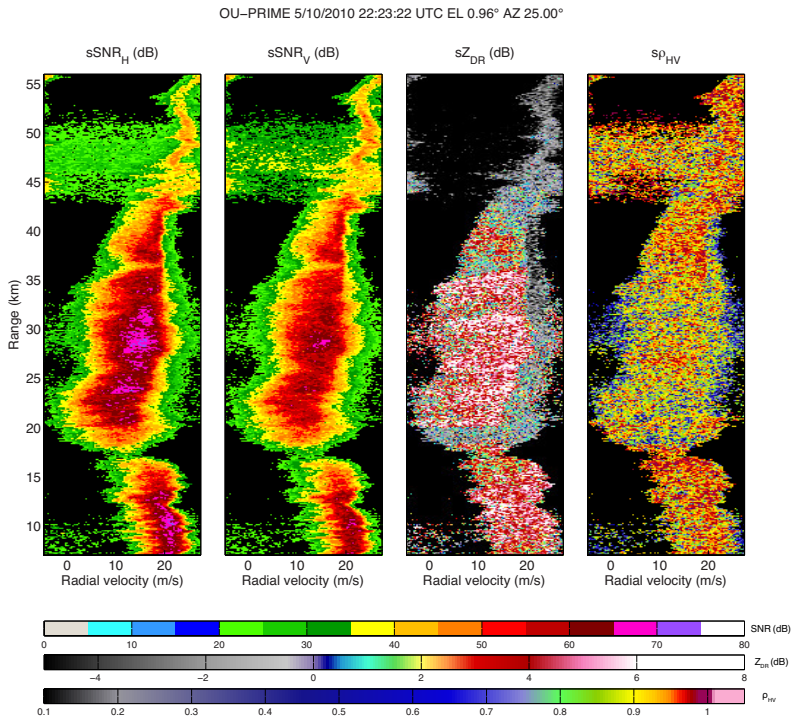

(b)

Figure 5.5: Range-Doppler plots of $K = 3$ averaged Bootstrap DPSD estimates corresponding to: (a) KOUN data at 22:22:38 UTC, elevation $\phi = 1.36°$, and azimuth $\theta = 30°$, and (b) OU-PRIME data at 22:23:22 UTC, elevation $\phi = 0.96°$, and azimuth $\theta = 25°$.

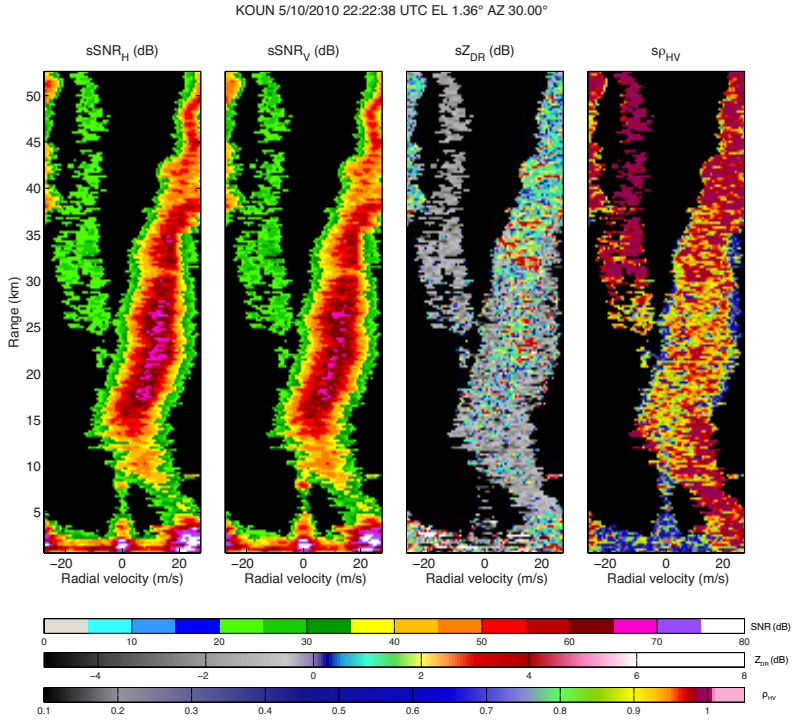

(a)

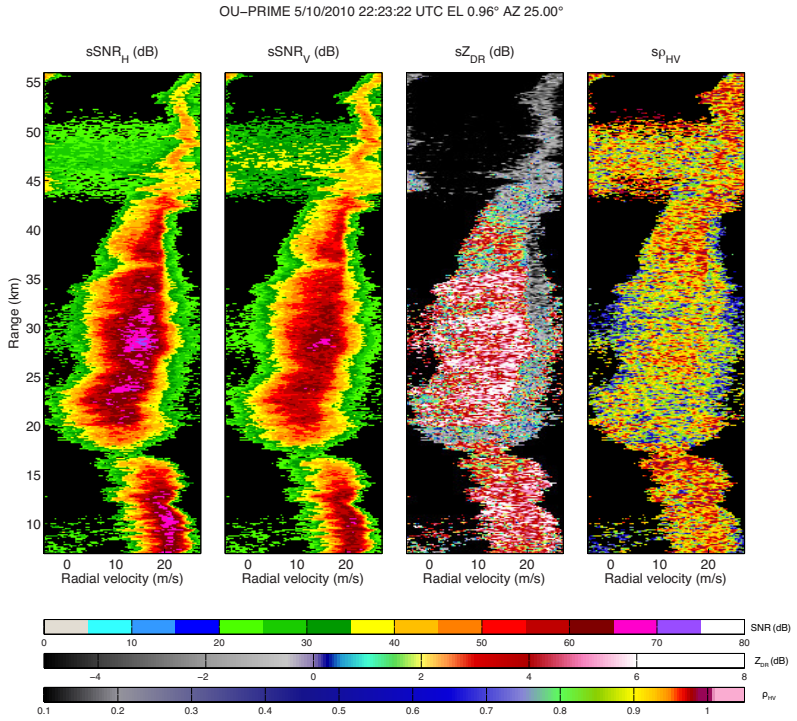

(b)

Figure 5.6: Same as Figure 5.5, but for Daniell DPSD estimates.

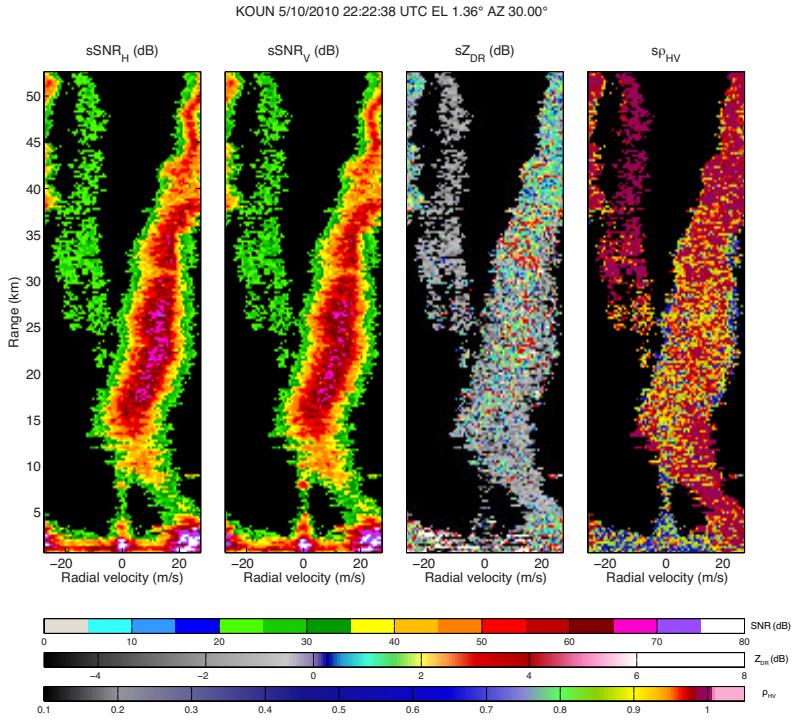

(a)

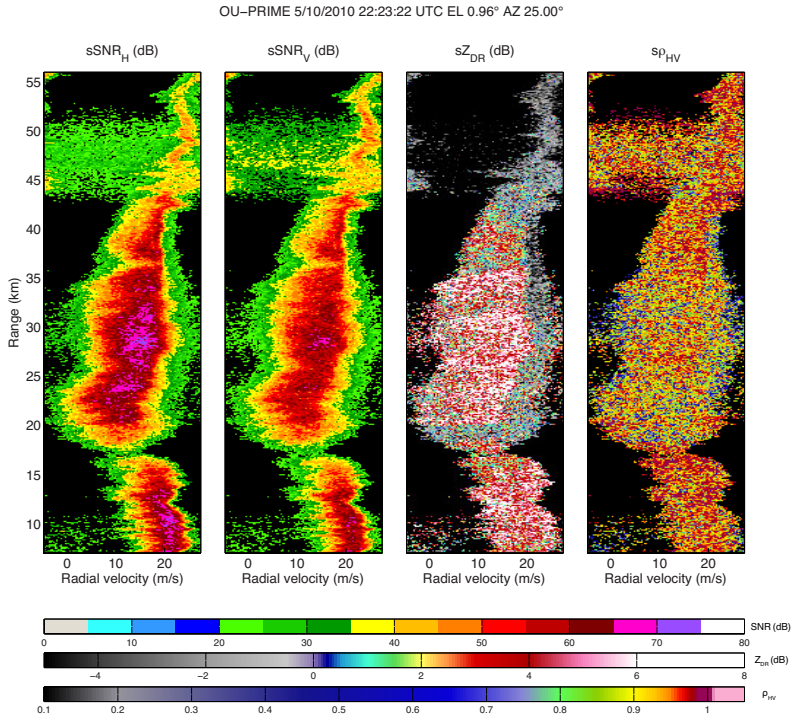

(b)

Figure 5.7: Same as Figure 5.5, but for periodogram DPSD estimates.

spectral coefficients and lower where the spectral coefficients are more affected by the smearing. Moreover, it can be demonstrated that the quality of the Daniell estimates are significantly degraded in cases with lower frequency resolution; i.e., for lower number of samples per dwell. By arbitrarily reducing the azimuthal extent of a radial to 0.5°, and keeping an azimuthal spacing of 0.5° for the KOUN dataset at the same azimuth of $\theta = 25°$, the number of pulses per radial is approximately 20. Figure 5.8 shows the estimated DPSDs, where the spectral broadening due to averaging in frequency of the Daniell estimates is more evident. Additionally, the region around 31.5 km in range is continuously high in $s\rho_{\mathrm{HV}}$, which could be interpreted as one signal with a wide spectrum width, depicted in Figure 5.9.

Moving on to a more interpretative analysis of the estimates, typical features such as unimodal weather signal, bimodal weather, and ground clutter are readily apparent in the range-Doppler plots. Examples of these typical DPSDs are shown in Figure 5.10. Other interesting signatures are the unimodal signal with markedly different polarimetric characteristics for different radial velocities spanning from approximately 20 km to 40 km in range in the OU-PRIME observation, the bimodal signal spanning from approximately 20 km to over 50 km in range in the KOUN observation, and a multimodal signal composed of weather, ground clutter, and an isolated peak at ∼8 km in the KOUN observation. The DPSDs of these signatures are shown in Figure 5.11. While it is difficult to provide a precise explanation for these observations, some hypotheses can be elaborated. The unimodal signal with differences in sZ_{DR} (Figure 5.5b, between approximately 20 and 42.5 km in range) may be attributed to smaller raindrops being centrifuged or size sorting,

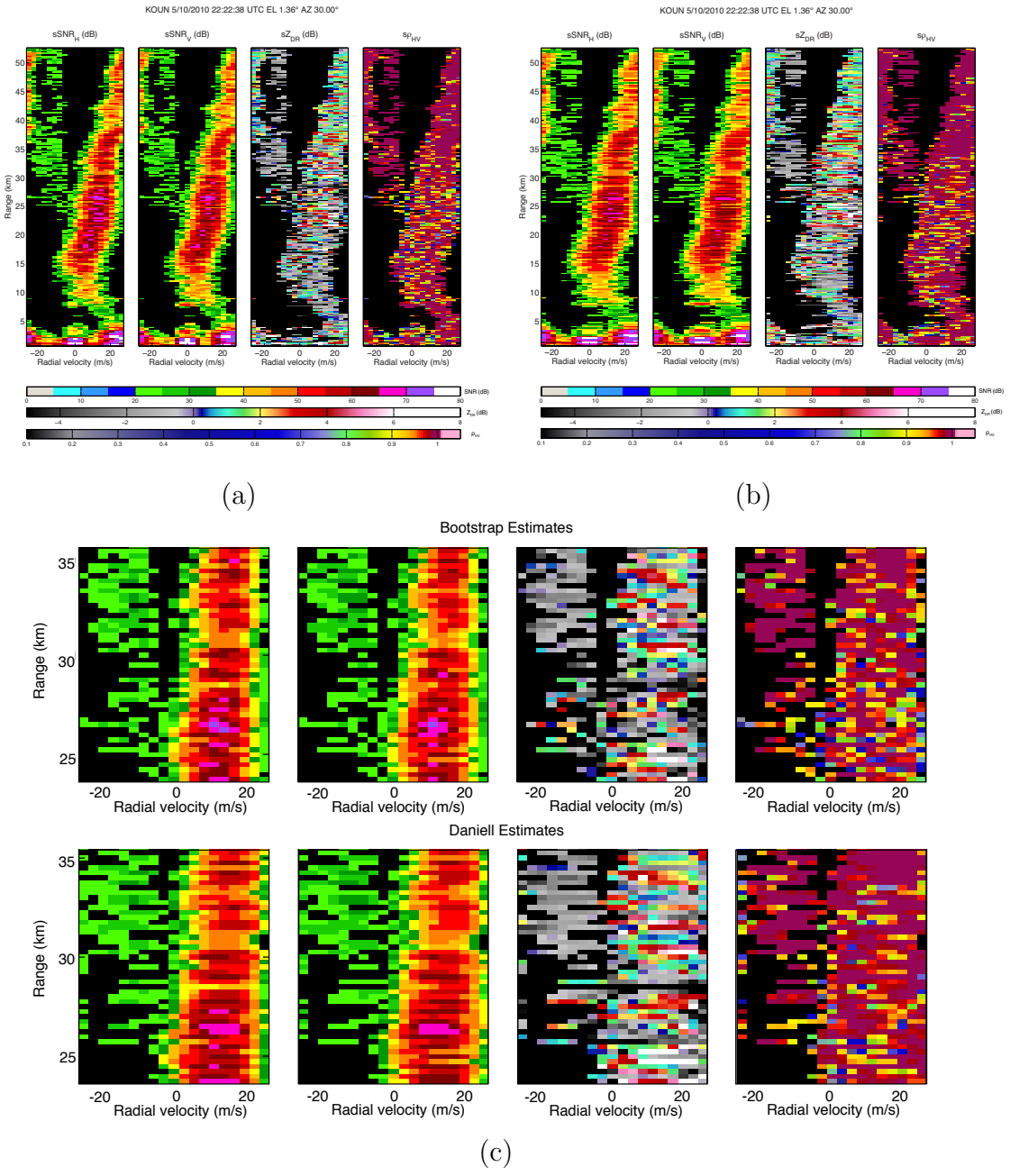

Figure 5.8: Range-Doppler plots of single-dwell DPSD estimates corresponding to KOUN data at 22:22:38 UTC, elevation $\phi = 1.36°$, azimuth $\theta = 30°$ and 0.5° radials with an average of 20 pulses per radial, for (a) Bootstrap estimator, (b) Daniell estimator, and (c) zoomed comparison of both estimates.

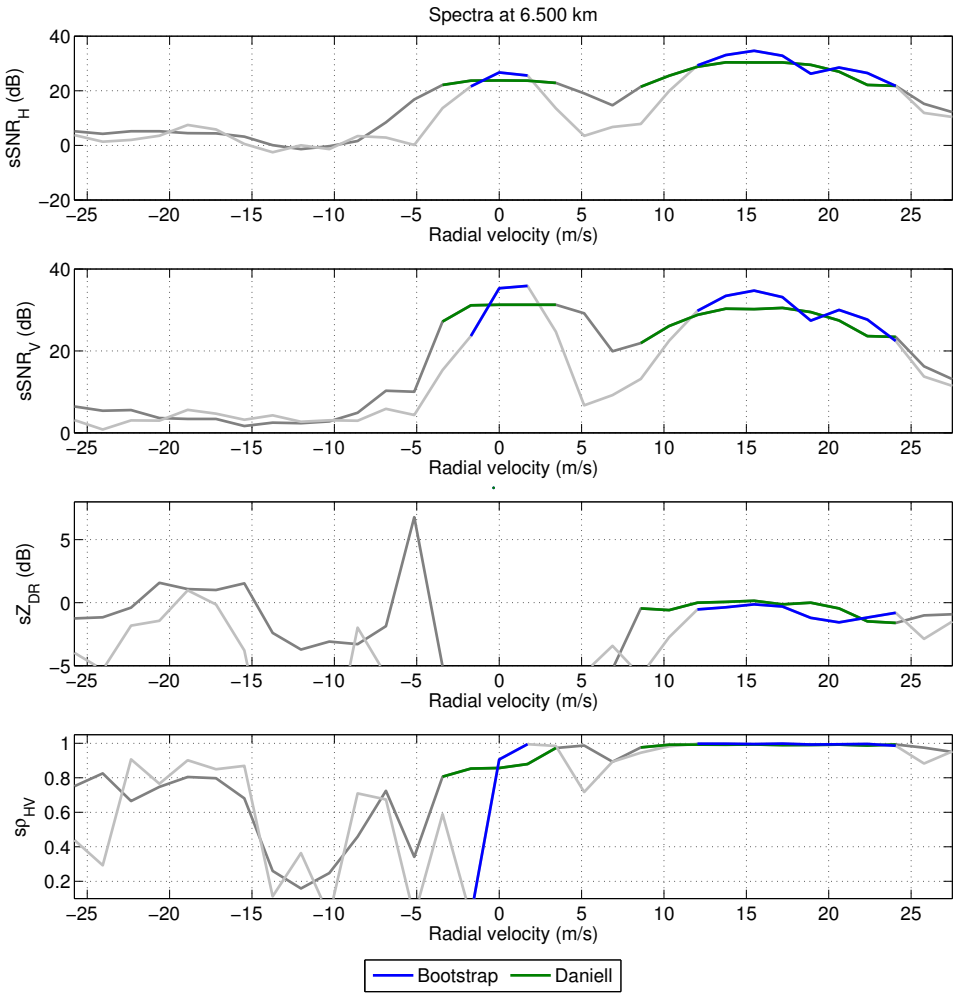

Figure 5.9: Line spectra at 31.5 km for the range-Doppler plots of Figure 5.8. Bootstrap (blue) and Daniell (green) estimates illustrating the effects of degraded frequency resolution.

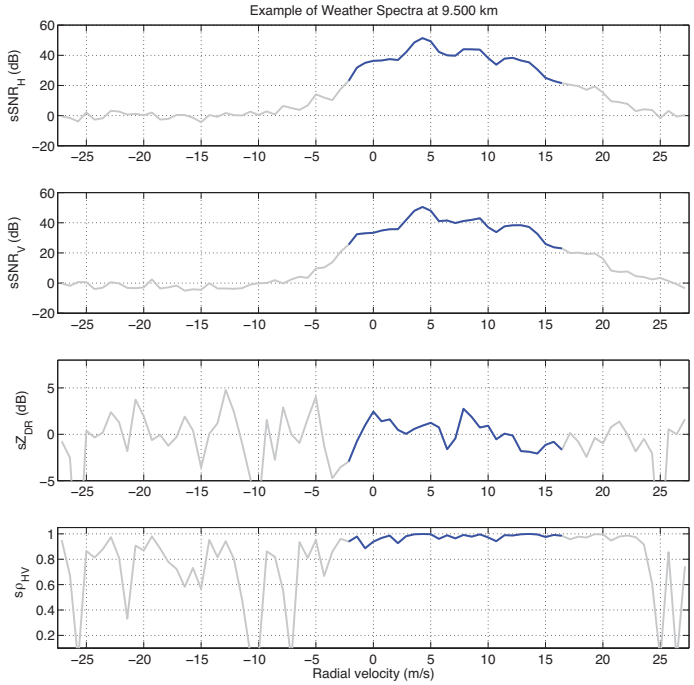

(a)

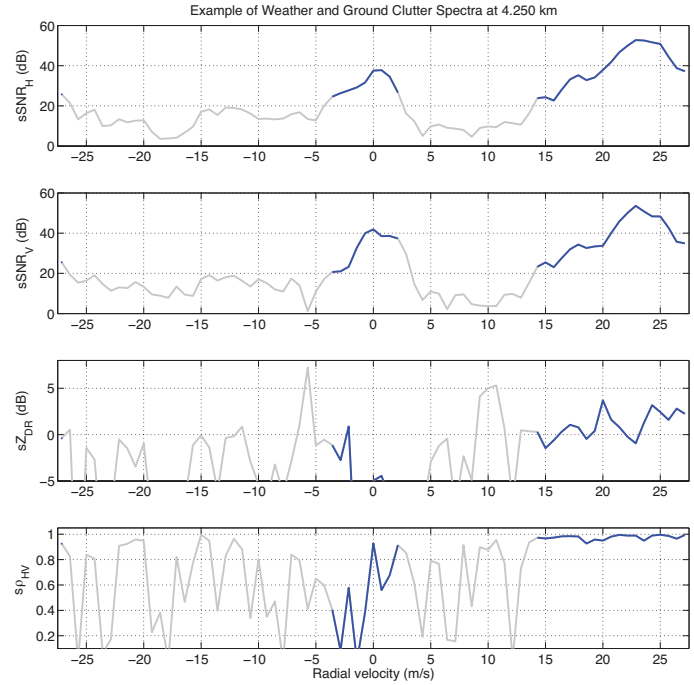

(b)

Figure 5.10: Plots of Bootstrap DPSD estimates corresponding to KOUN data at 22:22:38 UTC, elevation $\phi = 1.36°$, and azimuth $\theta = 30°$: (a) weather signature at 9.5 km, and (b) weather and ground clutter signature at 4.25 km.

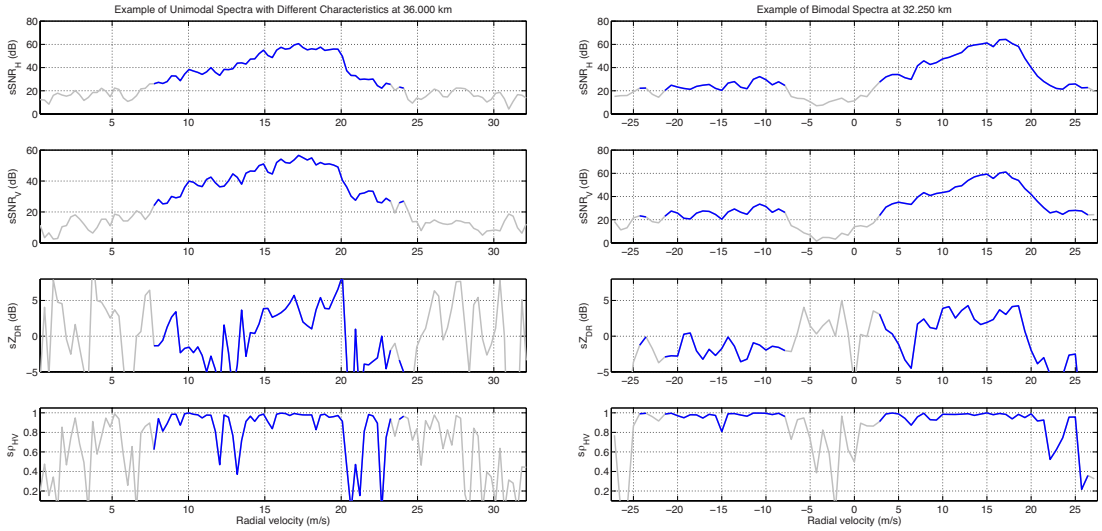

(a) (b)

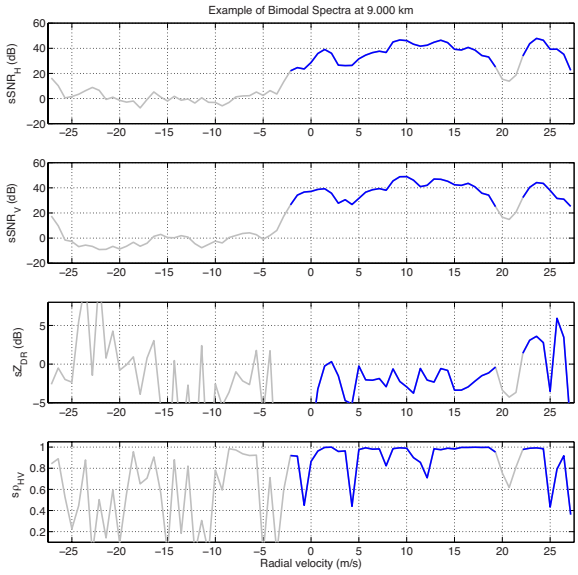

(c)

Figure 5.11: Plots of Bootstrap DPSD estimates corresponding to: (a) unimodal spectra with different polarimetric characteristics at 36 km, (OU-PRIME) (b) bimodal spectra at 32.25 km (KOUN), and (c) multimodal spectra at 9 km (KOUN).

while the decreasing values in range would possibly be due to attenuation. However, collocated with these sZ_{DR} values are really low $s\rho_{\mathrm{HV}}$ values, which might be an indication of non-meteorological scatterers. An example of the spectra at a range gate of 36 km is depicted in Figure 5.11a. Additionally, since OU-PRIME operates at C-band, it might be more susceptible to non-Rayleigh scattering from scatterers relatively larger than hydrometeors. Also, another indication that supports the hypothesis of non-meteorological scatterers lies farther ahead in range, where a wide distribution of lower sSNR with negative sZ_{DR} and low $s\rho_{\mathrm{HV}}$ is surrounding the weather signal. The KOUN spectral data also shows a weaker signal of low sZ_{DR} that is not apparent in the OU-PRIME spectral data. This weaker signal is observed within a bimodal spectrum (Figure 5.11b), along with a stronger weather signal with varying sZ_{DR} values, and relatively high $s\rho_{\mathrm{HV}}$ values. Although the weaker signal has high $s\rho_{\mathrm{HV}}$ values in the KOUN data, this may be due to the fact that these presumably non-hydrometeor scatterers might be small in size such that the scattering is mostly homogeneous. Another plausible explanation is that the weaker signal corresponds to a range-folded echo, as evidence of range folding was observed in the vicinity of the radial under analysis in later PPI scans for the same dataset. If such were the case, the range-folded echoes could be mitigated with polarimetric spectral analysis, showing another important potential application of the Bootstrap DPSD estimator. Finally, a signal with multiple peaks in the spectrum (Figure 5.11c) can be observed in range gates near 8 km in the KOUN range-Doppler plots. The peak at approximately 2 m/s corresponds to weather, with sZ_{DR} values close to 0 (small raindrops) and high $s\rho_{\mathrm{HV}}$. A wider signal with negative sZ_{DR} and

varying values of $s\rho_{\mathrm{HV}}$ can be seen with a mean radial velocity of approximately 14 m/s. The polarimetric characteristics of this spectral signature are similar to those of debris. And also, an isolated peak of a scatterer with high sZ_{DR} and high $s\rho_{\mathrm{HV}}$ with a motion of over 20 m/s can be seen in the spectra. This unknown scatterer could be a single large piece of debris being lofted in the air, and a hypothesis for the velocity being higher than the surrounding wind could be explained if the object was ejected radially in the direction of the radar beam with a higher tangential velocity. Alternatively, since ground clutter contamination is still affecting at this elevation angle and range, the echo could correspond to a vehicle. It is important to note that these characteristics can be appreciated even with single dwell DPSDs, showing the potential of the Bootstrap DPSD estimator in different spectral analysis applications.

5.1.2 Case 2: 20 May 2013, KOUN and PX-1000

A PPI of the selected elevation angle and time is shown in Figure 5.12. For the PX-1000 dataset, the update time is 20 seconds, the range gate spacing is 30 m with a resolution of 112 m, while the azimuthal spacing is 0.5° with a resolution of 1.8°. Since range is oversampled, it is possible to compute range-averaged DPSDs without significantly compromising the amount of information. Additionally, with faster update times, it would also be reasonable to obtain dwell-averaged DPSDs, as long as the underlying phenomenon is not evolving too rapidly. A comparison of DPSDs computed by averaging in different dimensions is possible with this dataset, which will be discussed next. The single-dwell Bootstrap DPSD estimate with $K = 1$ (first

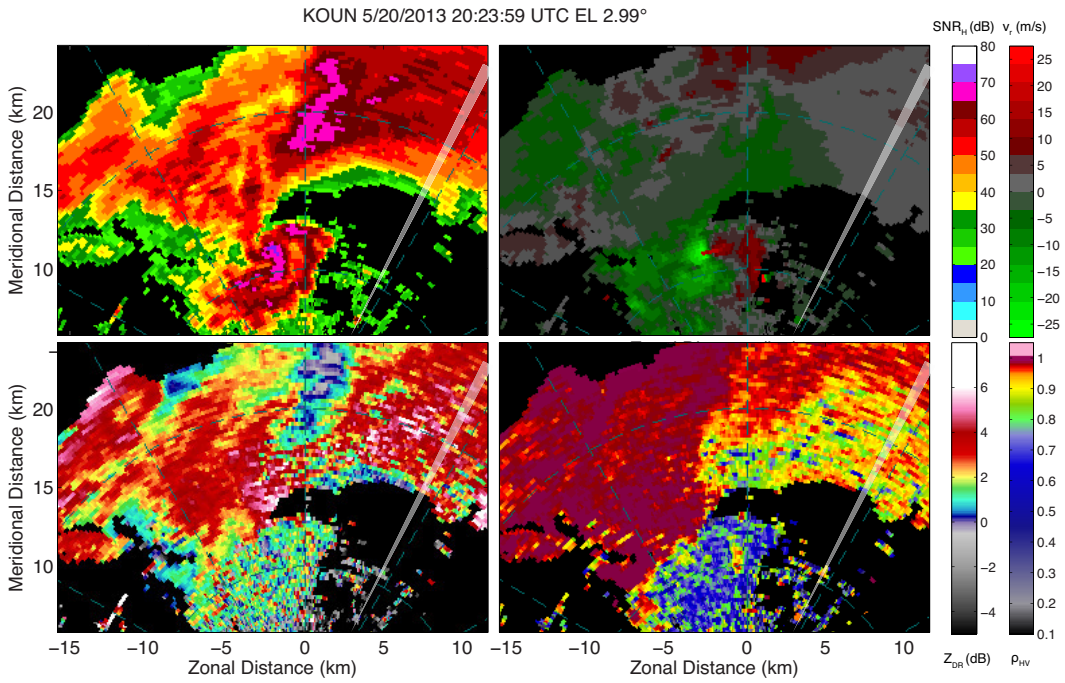

(a)

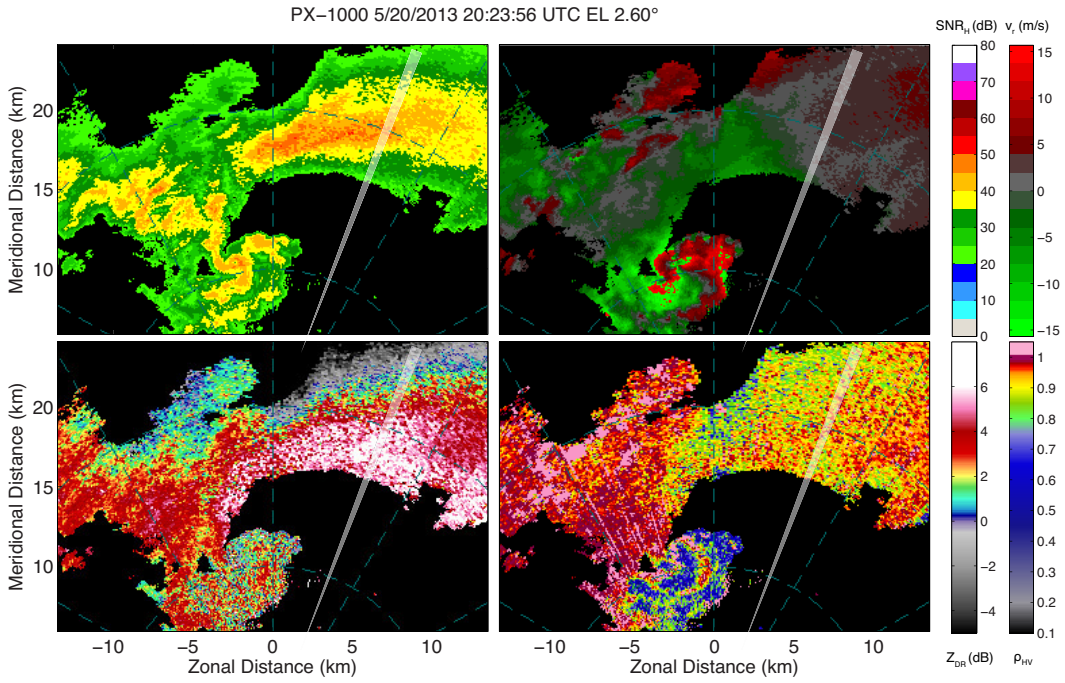

(b)

Figure 5.12: PPI plots corresponding to (a) KOUN data at 20:23:59 UTC, and elevation $\phi = 2.99°$ with azimuth $\theta = 27°$ highlighted, and (b) PX-1000 data at 20:23:56 UTC, and elevation $\phi = 2.6°$ with azimuth $\theta = 21°$ highlighted: $\mathrm{SNR_H}$ (top left), $\bar{v}_r$ (top right), Z_{DR} (bottom left), and ρ_{HV} (bottom right). Grid lines are 30° and 10 km apart.

column, Figure 5.13) is compared to those that resulted from the Daniell estimator with a three-point moving average (second column, Figure 5.13), and by averaging three gates in range (third column, Figure 5.13), three radials in azimuth (fourth column, Figure 5.13), and three scans in time (last column, Figure 5.13).

With range averaging, some information in range may be obscured, though if range is oversampled, the impact on the quality of DPSD estimates should be minimal. The azimuth-averaged DPSDs exhibit spectral leakage, mainly due to discontinuities in azimuth during the data acquisition. Spectral products are vulnerable to these artifacts, and in such a case, averaging in another dimension would be more appropriate. Additionally, scan-to-scan-averaging does not reduce the resolution in range or azimuth, but it is sensitive to the time between scans. By averaging three dwells that are 20 seconds apart, it yields an effective observation time of approximately 1 minute. If the phenomena is evolving fast in time, extraneous information may be gathered by averaging in time; e.g., the signature with high $s\rho_{\mathrm{HV}}$ with mean velocities close to 12.5 m/s is absent from all other DPSD estimates.

Similar spectral signatures as those found in previous examples can also be observed in the KOUN dataset for the 20 May 2013 case. Using a single spectrum for DPSD estimation ($K = 1$) and at an azimuth of $\theta = 27°$, a unimodal spectra with marked polarimetric characteristics can be observed (Figure 5.14). The weaker signal is collocated with low sZ_{DR}, while the stronger signal has small sZ_{DR}. The $s\rho_{\mathrm{HV}}$ behaves differently for both signals as their power ratio varies in range. From ranges 32 to 34 km, the dominant signal has high sZ_{DR}, and as the dominant signal power weakens for higher positive radial velocity (i.e., the right edge of the spectral

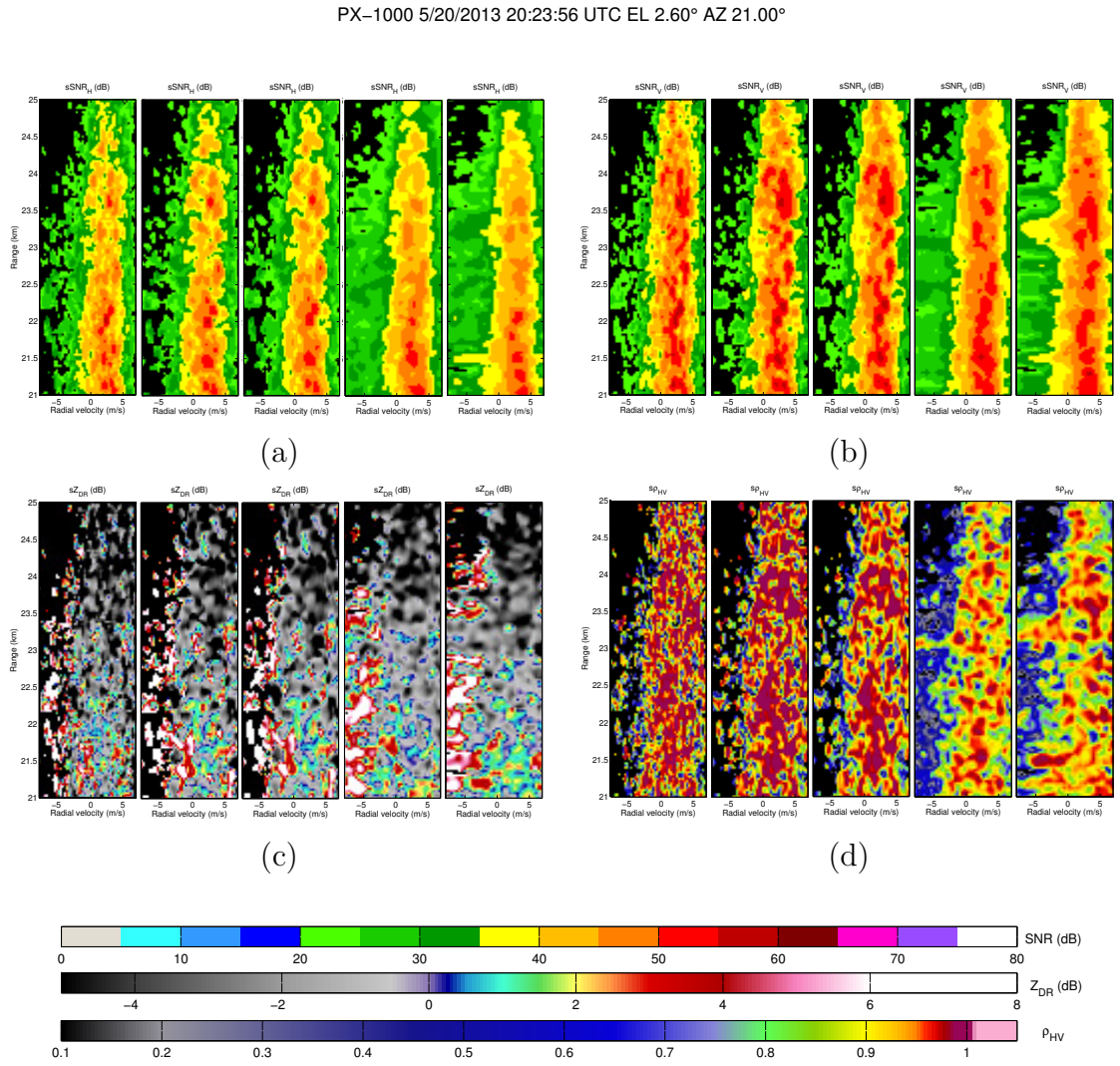

Figure 5.13: Comparison of different averaging methods. PX-1000 data at 20:23:56 UTC, elevation $\phi = 2.6°$ and azimuth $\theta = 21°$, estimated with the Bootstrap DPSD estimator using a single dwell (first column), with the Daniell three-point single-dwell estimator (second column), range averaging estimator (third column), azimuth averaging estimator (fourth column), and scan-to-scan averaging estimator (fifth column), for: (a) $s\mathrm{SNR_H}$, (b) $s\mathrm{SNR_V}$, (c) sZ_{DR}, and (d) $s\rho_{\mathrm{HV}}$.

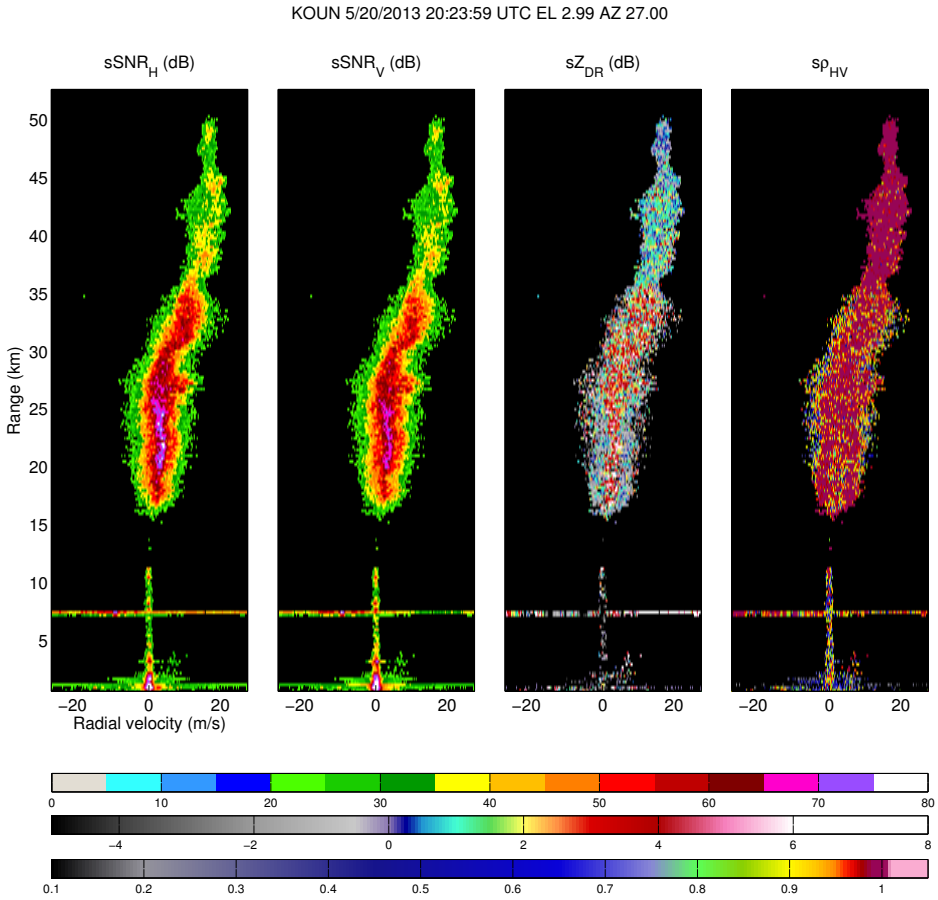

Figure 5.14: Range-Doppler plots of KOUN data at 20:23:59 UTC, elevation $\phi = 2.99°$ and azimuth $\theta = 27°$, estimated with the Bootstrap DPSD single-dwell estimator ($K = 1$).

signature), the mixing is stronger such that none of the signals are dominant, thus exhibiting a lower $s\rho_{\mathrm{HV}}$ (Figure 5.15a). From ranges 25 to 31 km, a similar effect is observed but the dominant signal is weaker for lower radial velocities; i.e., left side of the spectrum (Figure 5.15b). From ranges 22 to 24 km, the low sZ_{DR} signal is wider and less dominant, while the high sZ_{DR} signal is narrower and likely moving at about the same mean radial velocity as the less dominant signal; these marked differences in the unimodal spectra are more evident in sZ_{DR} (Figure 5.16a). From ranges 19 to 21 km, an overall decrease in $s\rho_{\mathrm{HV}}$ is evident, which could be explained by no signal being completely dominant over the other in the spectra (Figure 5.16b). And finally, from ranges 18 km and below, the power of the high sZ_{DR} signal starts weakening as the wider, low sZ_{DR} signal starts exhibiting higher $s\rho_{\mathrm{HV}}$ (Figure 5.17a). Another spectral signature featured in this radial is the helicopter at about 7 km in range (Figure 5.17b). It is known that this particular scatterer is a helicopter because it exhibits (in PPI plots, not shown) spatially isolated, unusually high returned power, rapid movement as a function of time, mean radial velocities that do not follow the surrounding winds, and non-homogeneous scattering (low ρ_{HV}). One last example of a spectral signature of a TDS range gate is shown in Figure 5.18. The range gate corresponds to KOUN data at 20:14:16 UTC, elevation $\phi = 1.98°$, azimuth $\theta = -29°$, and range 9.5 km, with a $\hat{Z}_{\mathrm{DR}}$ of -2.83 dB and a $\hat{\rho}_{\mathrm{HV}}$ of 0.50, which is consistent with a typical TDS. The spectra is multimodal and it exhibits different spectral polarimetric signatures collocated with different peaks in radial velocity, though it is unlikely that they are associated with typical weather signals due to the difference in polarimetric characteristics. Additionally, an isolated peak at 15 m/s

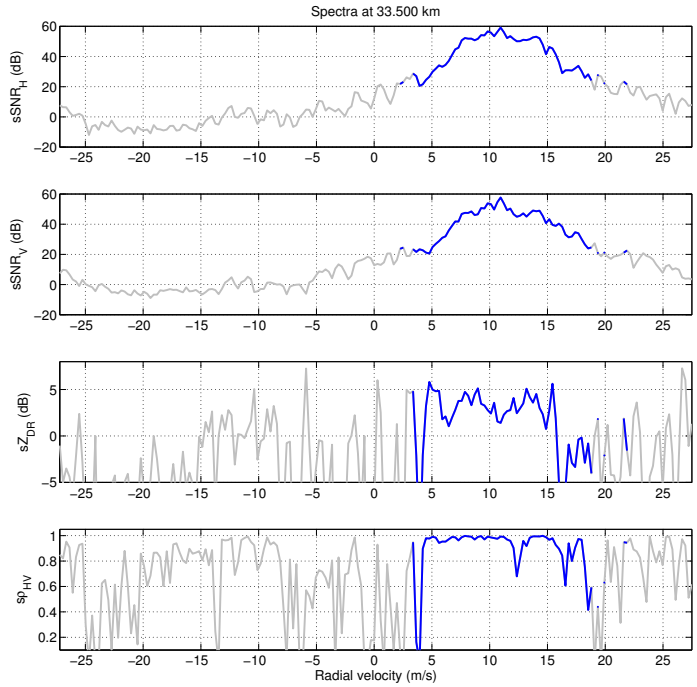

(a)

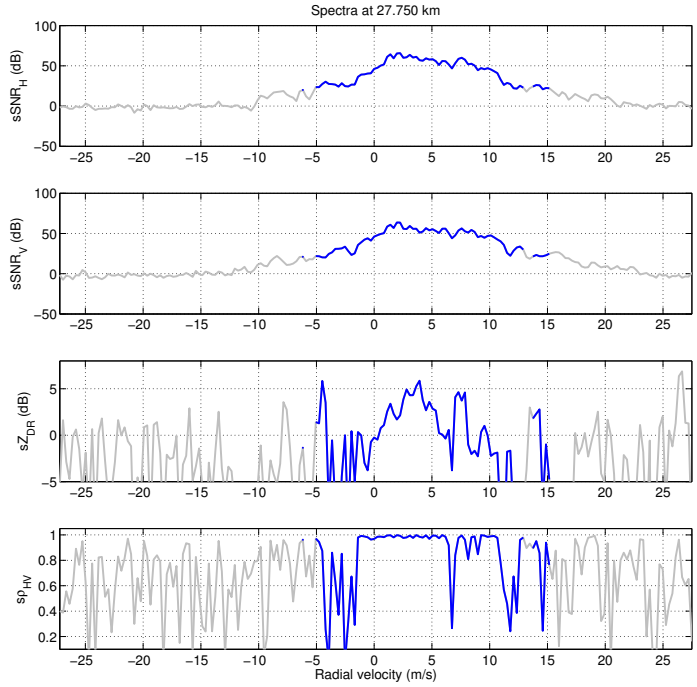

(b)

Figure 5.15: Plots of Bootstrap DPSD estimates corresponding to KOUN data at 20:23:59 UTC, elevation $\phi = 2.99°$, and azimuth $\theta = 27°$. Signatures at: (a) 33.5 km, and (b) 27.75 km.

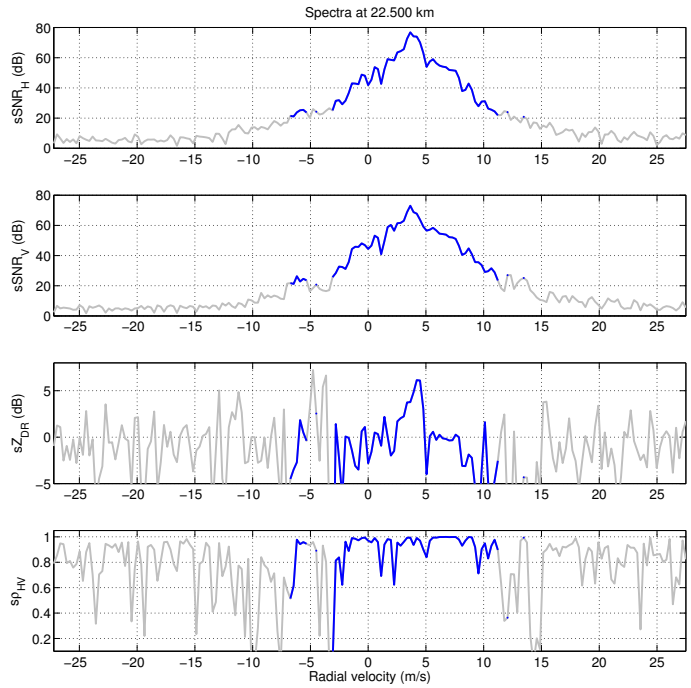

(a)

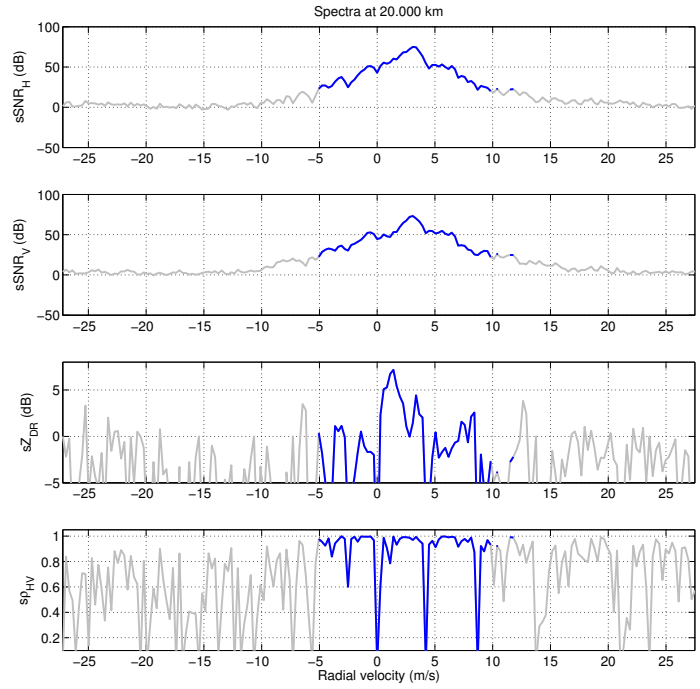

(b)

Figure 5.16: Same as Figure 5.15 but for signatures at: (a) 22.5 km, and (b) 20 km.

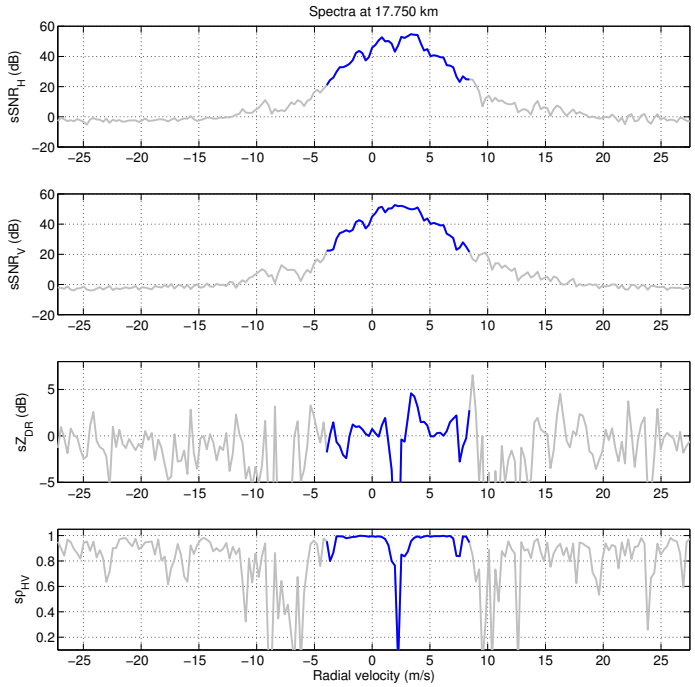

(a)

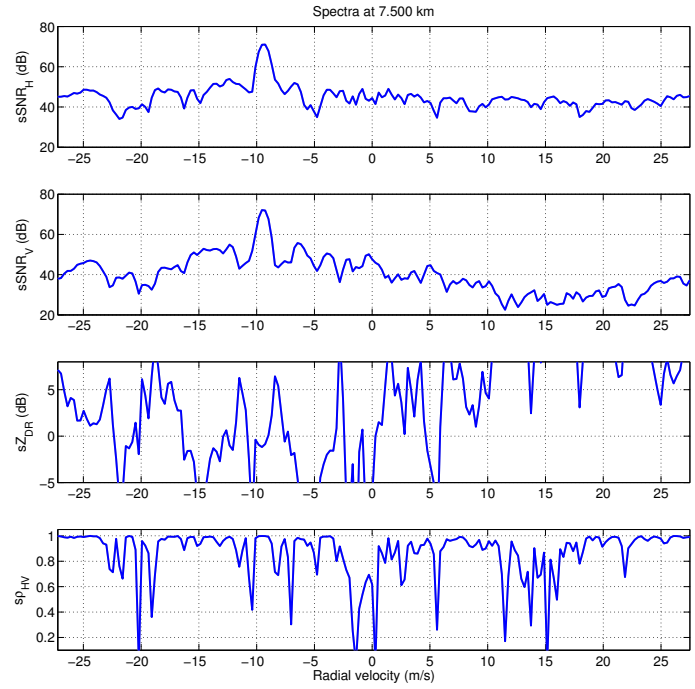

(b)

Figure 5.17: Same as Figure 5.15 but for signatures at: (a) 17.75 km, and (b) 7.5 km.

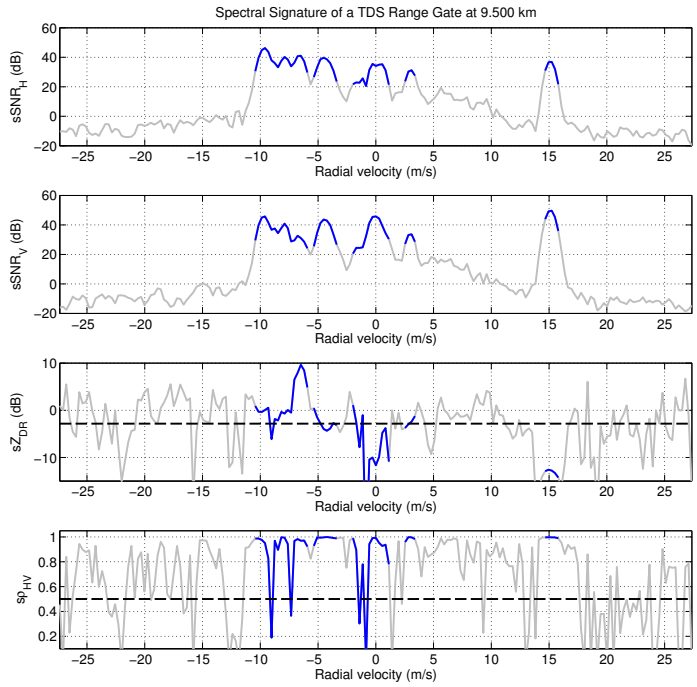

Figure 5.18: Plots of Bootstrap DPSD estimates corresponding to KOUN data at 20:14:16 UTC, elevation $\phi = 1.98°$, azimuth $\theta = -29°$, and range $r = 9.5$ km. The dashed black lines in $s\hat{Z}_{\mathrm{DR}}$ and $s\hat{\rho}_{\mathrm{HV}}$ indicate the values of the bulk estimates.

can be observed with $s\hat{Z}_{\mathrm{DR}} < -10$ dB, which may be debris that is being ejected from the vortex.

In summary, a few examples of the Bootstrap DPSD estimator applied to real data have been shown. Additionally, it has been demonstrated that the Bootstrap DPSD estimates show more details compared to the conventional estimators. Also, it was possible to identify spectral signatures using single-dwell estimates, in contrast to averaging in range, azimuth, scan, or frequency, where the resolution is degraded. The following section presents results of the Bootstrap DPSD estimator applied to data from a physically based simulator.

5.2 Simulated Observations

To generate realistic I/Q weather radar signals in a tornadic environment, a polarimetric radar time-series simulator (Cheong et al. 2015), SimRadar, is used (Figure 5.19). Briefly, this physical simulator synthesizes radar returns based on the position, velocity, orientation, and radar cross section (RCS) of scatterers, which include both raindrops and debris. It ingests large-eddy-simulation (LES) models for tornado-vortex wind fields and trajectories of the scatterers. The tumbling behavior of non-spherical objects and the drag forces are calculated based on a 6DOF model (Maruyama and Noda 2012; Richards 2012) and LES-meteorological-background wind vectors. For the RCS of hydrometeors, the electrical scattering model of an oblate raindrop is used (Bringi and Chandrasekar 2001), and for debris, the RCS

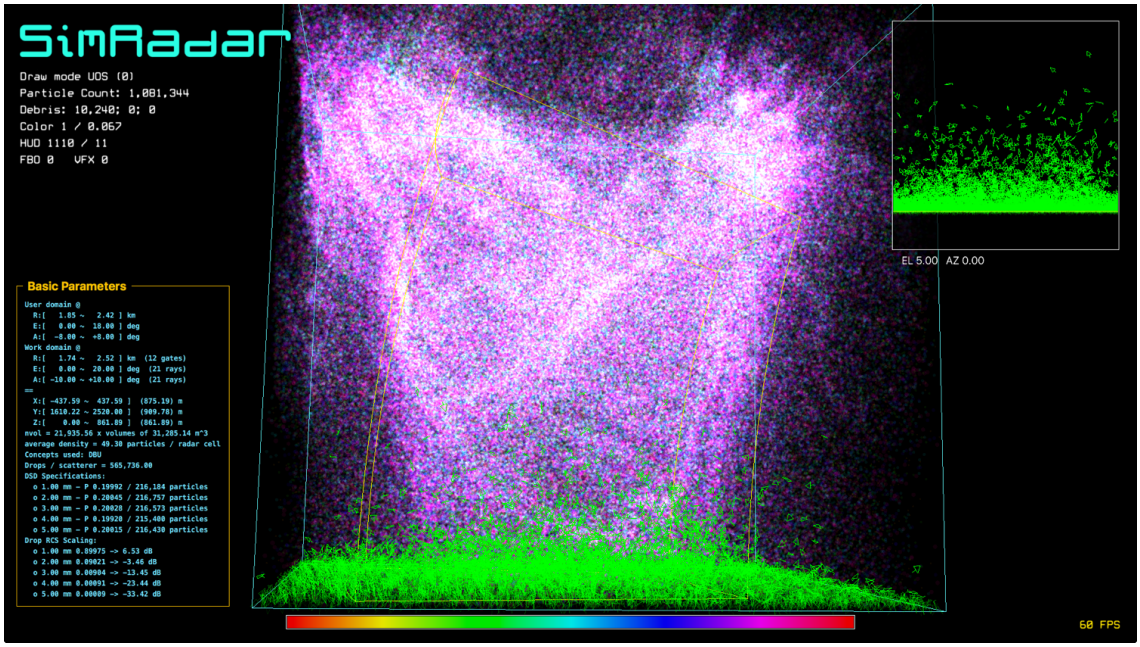

Figure 5.19: User interface of the polarimetric radar time-series simulator (SimRadar).

measurements of a leaf at different orientations are ingested into the radar simulator. The body of the leaf is modeled by a rectangular plate of 6-cm wide by 8-cm long; the stem is modeled as a cylinder of 12-cm long attached to the body. The DSD of the raindrops is modeled with a Marshall-Palmer distribution. Finally, the contribution of each scatterer is weighted by its radial and angular position relative to the radar beam. To produce the simulated I/Q time-series signals, contributions from all scatterers are coherently summed after updating the physical properties of the scene at each time step. Detailed technical specifications on the simulation framework can be found in Cheong et al. (2015). Thanks to the versatility of the simulator, many scenarios with different radar acquisition and simulation scene parameters can be generated, making it an incredibly powerful and useful tool to

tackle the scientific questions regarding tornado dynamics and interaction with debris. While the goal here is not to answer these scientific questions, a few examples of the Bootstrap DPSD estimates of simulated data are presented next to illustrate the potential utility of spectral-analysis tools in the study of tornado dynamics.

5.2.1 Simulation Case 1: Weather Only

The radar parameters (Table 5.3) are similar to typical WSR-88D values, though the PRT is arbitrarily modified to ensure there is no aliasing in velocity, and the range resolution is 30 m with a gate spacing of 15 m. The scene is populated with 1.024×10^6 raindrops with 5 different diameters for the weather-only case, and 1.024×10^6 leaves for the debris-only case. In both cases, there are about 240 scatterers per cell in both cases. The rest of the simulation parameters are listed in Table 5.3. The PPI plots of the simulation with weather-only scenes are shown in Figure 5.20. Briefly, the weather-only case shows the tornado vortex structure in the SNR field and a TVS in the velocity field. Also, the Z_{DR} plot shows that moderately-sized raindrops with Z_{DR} of approximately 2 dB are moving at a distance of $\sim$200 m in radius and with smaller sized raindrops in the core of the vortex, resembling what appears to be a ring in the SNR and Z_{DR} fields. The ρ_{HV} is also consistently high, as expected, since the simulation domain is only populated with raindrops. Spectral analysis shows unimodal weather spectra for most parts of the domain. As an example, a range-Doppler plot of a radial corresponding to an azimuth of $\theta = -10^\circ$ depicts this signature (Figure 5.21). Moreover, some signatures of possible size sorting due to the drag forces can be observed as larger drops (larger sZ_{DR})

Radar parameters	
PRT	0.2 ms
Wavelength	10 cm
Peak transmit power	50 kW
Antenna gain	50 dBi
Beamwidth	1.0°
Pulse width	0.2 μs
Range resolution	30 m
Gate spacing	15 m
Samples per dwell	100
Azimuthal sampling	0.5°
Maximum unambiguous velocity	82.5 m/s

Simulation domain		
Scatterer type	Raindrops	Debris (Leaf)
Number of scatterers	1.024×10^6	1.024×10^6
Density	$\sim$ 470 particles per cell	
DSD	Marshall-Palmer	
Number of diameter classes	5 (1, 2, 3, 4, 5 mm)	
LES model	Suction vortices	
Size of simulation domain	864.77 m x 738.81 m x 217.02 m	

Table 5.3: Radar acquisition and simulation domain parameters.

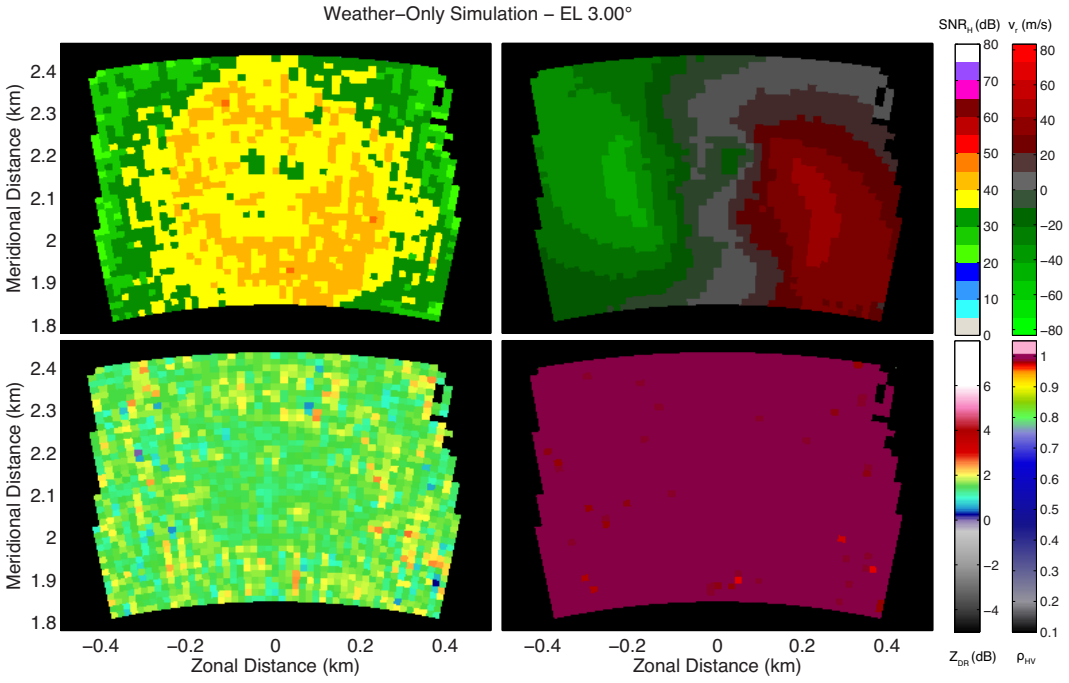

Figure 5.20: PPI plots of simulated weather-only data at elevation $\phi = 3.00°$: $\mathrm{SNR_H}$ (top left), $\bar{v}_\mathrm{r}$ (top right), Z_DR (bottom left), and ρ_HV (bottom right).

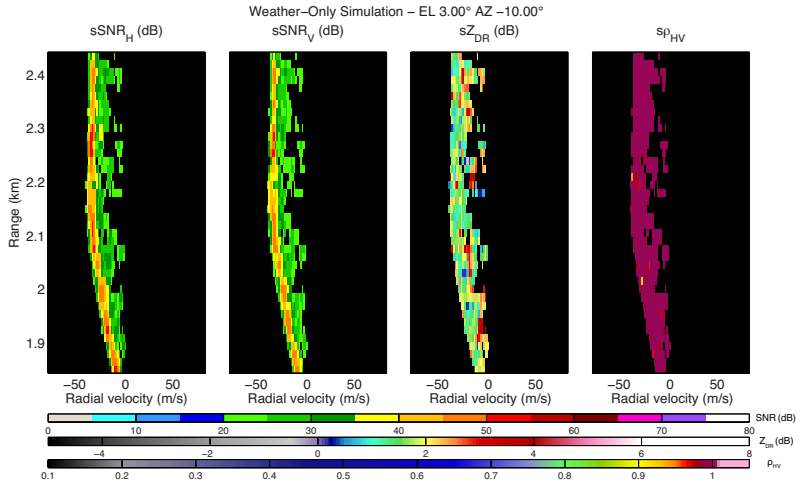

Figure 5.21: Range-Doppler plots of simulated weather data at elevation $\phi = 3.00°$ and azimuth $\theta = -10°$.

are collocated with smaller radial velocities than smaller raindrops (smaller sZ_{DR}). Again, the correlation coefficient, indicates high values owing to the homogeneity of the scatterers in motion. The DPSDs of a particular range gate exhibiting this behavior are shown in Figure 5.22.

5.2.2 Simulation Case 2: Debris Only

A more interesting case is the one with the debris signals only (Figure 5.23), where a ring can be appreciated in the SNR and Z_{DR} fields, while ρ_{HV} exhibits a low value region collocated near the core of the tornado vortex. The low to negative values of Z_{DR} could be explained by some degree of common alignment of the leaves, which is also supported by the fact that the ρ_{HV} in the annular region is also high (i.e., common alignment results in more homogeneous scattering). A range-Doppler plot of a radial across the core (azimuth $\theta = 1.5°$, Figure 5.24) shows multimodal spectra in power, as well as a wide range of sZ_{DR} values, while the $s\rho_{\mathrm{HV}}$ suggests

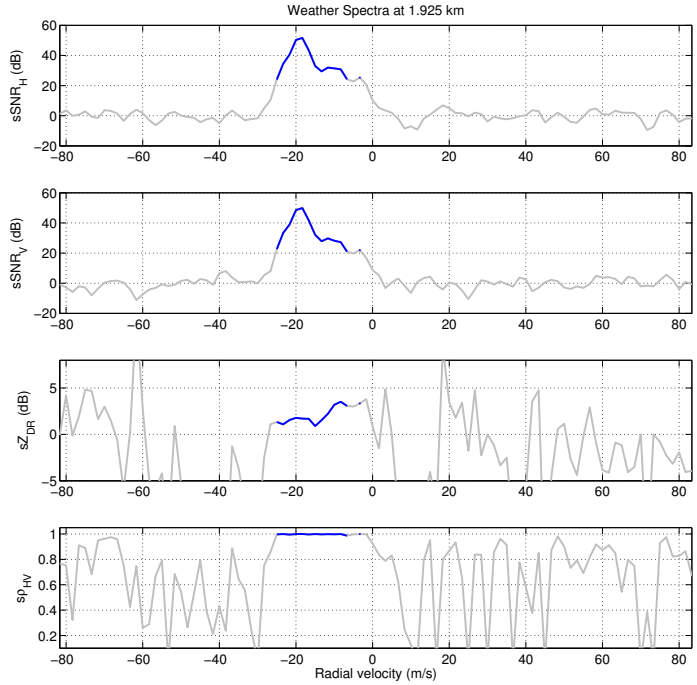

Figure 5.22: Bootstrap DPSD estimates of simulated weather data at elevation $\phi = 3.00°$, azimuth $\theta = -10°$ and $r = 1.925$ km.

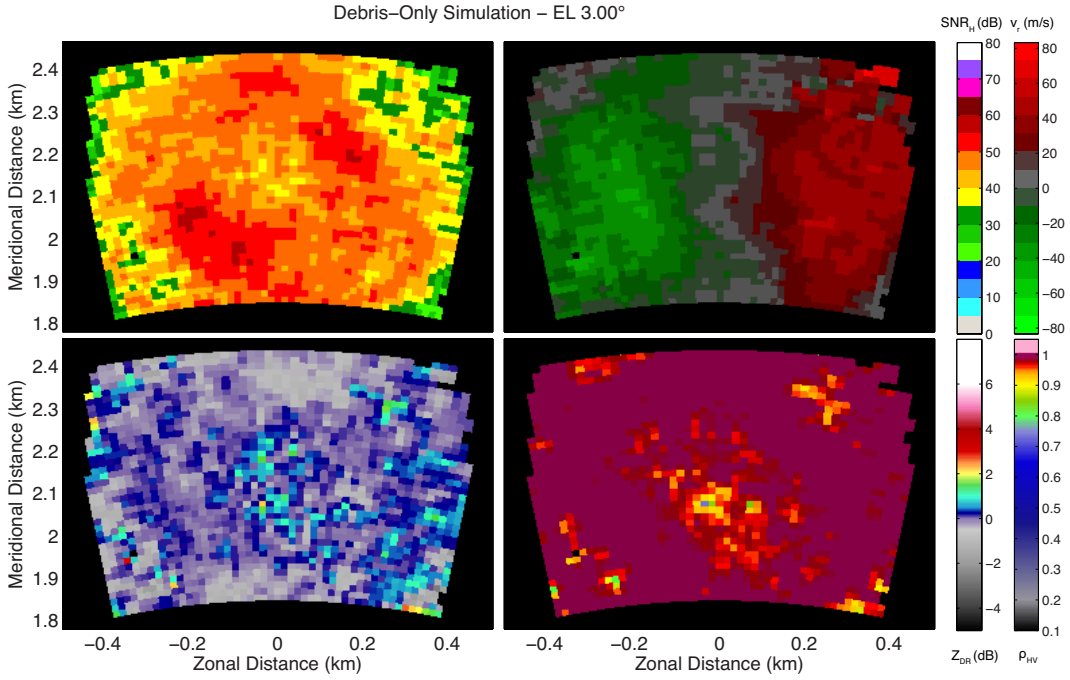

Figure 5.23: PPI plots of simulated debris-only data at elevation $\phi = 3.00°$: $\mathrm{SNR_H}$ (top left), $\bar{v}_\mathrm{r}$ (top right), Z_DR (bottom left), and ρ_HV (bottom right).

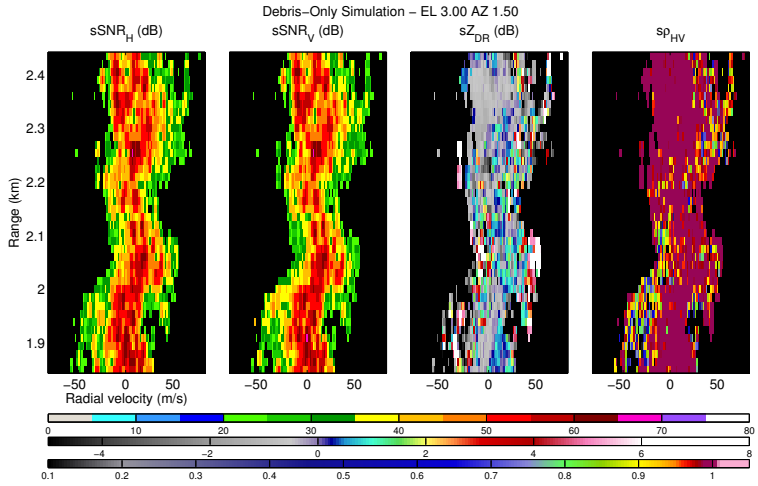

Figure 5.24: Range-Doppler plots of simulated debris data at elevation $\phi = 3.00°$ and azimuth $\theta = 1.5°$.

centrifuging of debris. With the radar beam pointing approximately perpendicular to the vortex-relative wind direction, a reasonable assumption is that most leaves that are carried by the wind will have a mean radial velocity close to zero. This observation is clearer between ranges 1.85 and 2.05 km, and between 2.25 and 2.4 km. Additionally, the high $s\rho_{\text{HV}}$ values collocated with the mean radial velocities suggest higher homogeneity of the scatterers, which in turn supports the hypothesis of commonly aligned debris. Finally, another interesting signature observed in these range-Doppler plots is how a few of the non-dominant peaks in the spectra exhibit higher motion towards (away from) the radar for the southern (northern) region of the vortex, as if these debris were being ejected radially outwards from the core (Figures 5.25a and 5.25b). They are also collocated with low $s\rho_{\text{HV}}$ values, suggesting these leaves are tumbling rapidly and are not commonly aligned with the wind motion.

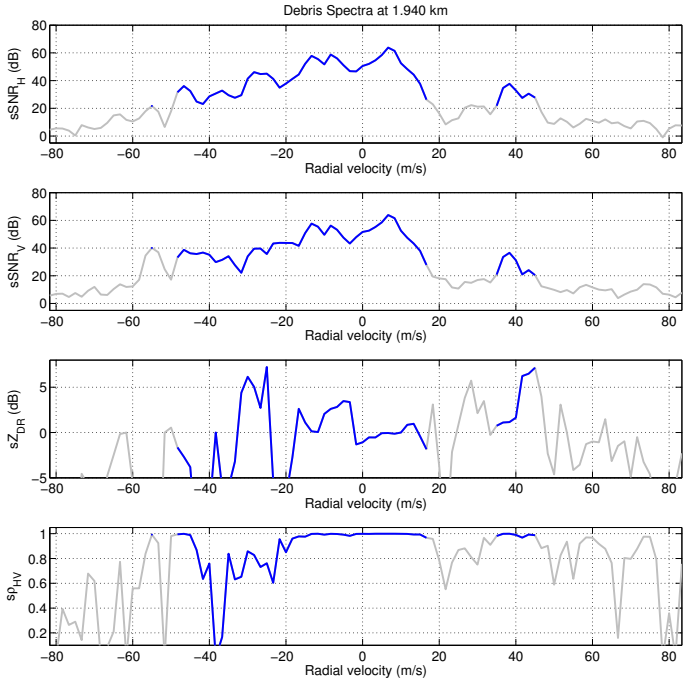

(a)

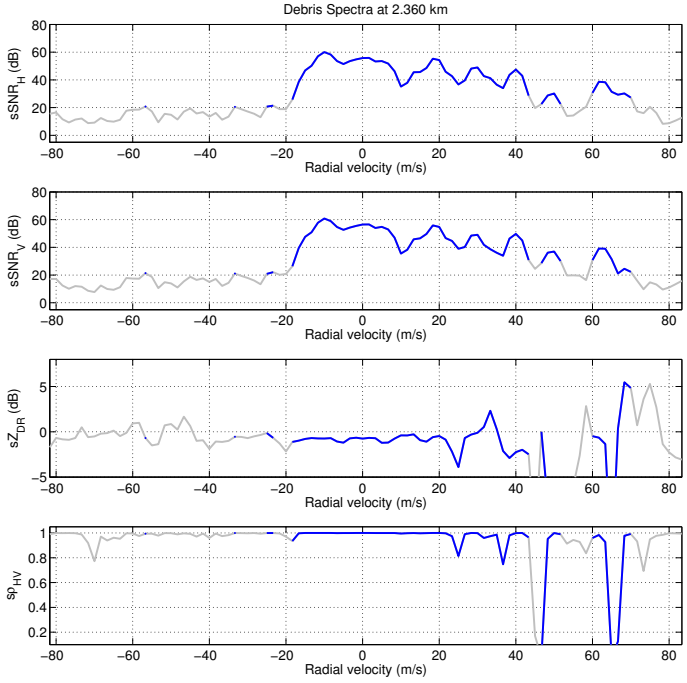

(b)

Figure 5.25: Bootstrap DPSD estimates simulated debris data at elevation $\phi = 3.00°$ and azimuth $\theta = 1.5°$ at: (a) 1.94 km, and (b) 2.36 km.

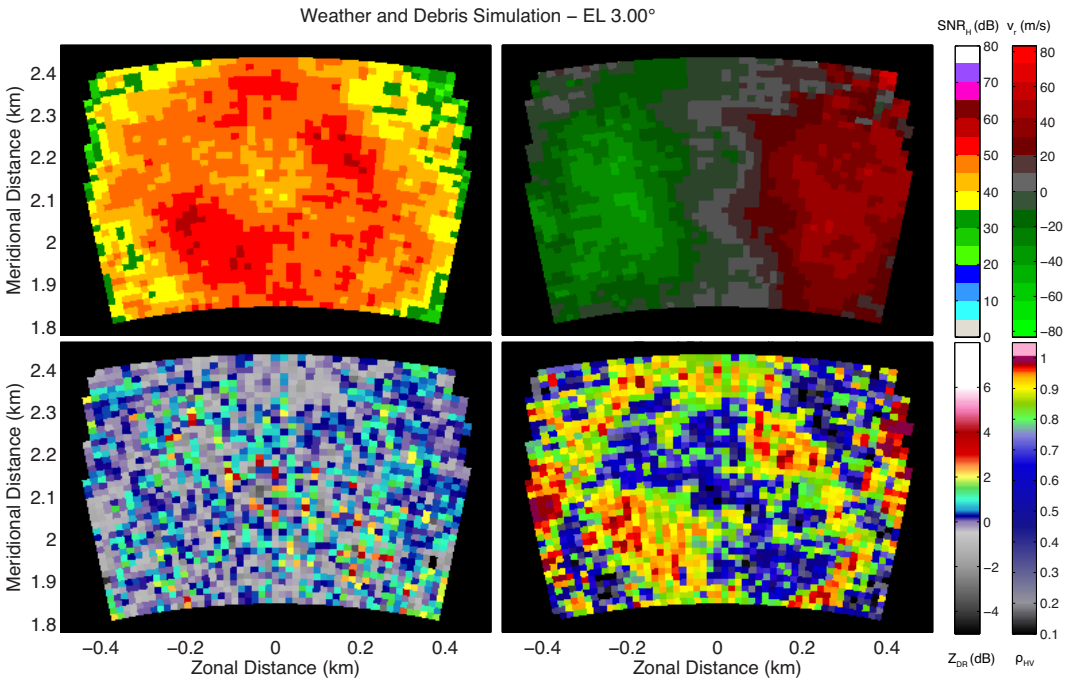

Figure 5.26: PPI plots of simulated weather and debris data at elevation $\phi = 3.00°$: $\mathrm{SNR_H}$ (top left), $\bar{v}_\mathrm{r}$ (top right), Z_DR (bottom left), and ρ_HV (bottom right).

5.2.3 Simulation Case 3: Weather and Debris Mix

The next simulated scenario is composed of weather and debris (Figure 5.26), each with a count of 1.024×16^6, totaling 2.048×10^6 particles with a density of approximately 470 particles per radar resolution volume, and with the same radar acquisition parameters. It is possible to analyze each signal and the composite signal separately, with the goal of testing hypotheses regarding velocity biasing. In a raindrops-only scenario, the differential velocity (i.e., the difference between the velocities estimated from the H and V channels) is expected to be minimal, provided that the raindrops are small, since the velocities estimated from each channel should be approximately equal. This hypothesis is tested with the weather-only signal (Figure 5.27), and the results are as expected. Following a similar logic, the

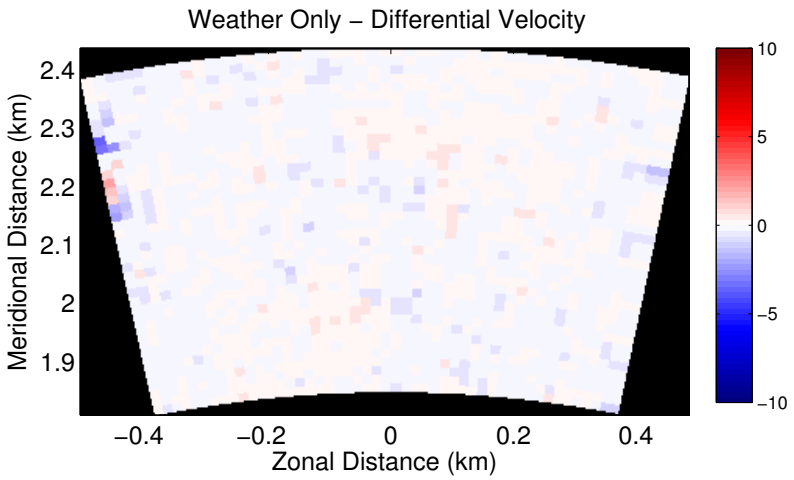

Figure 5.27: PPI plot of differential velocity for weather only at elevation $\phi = 3.00°$.

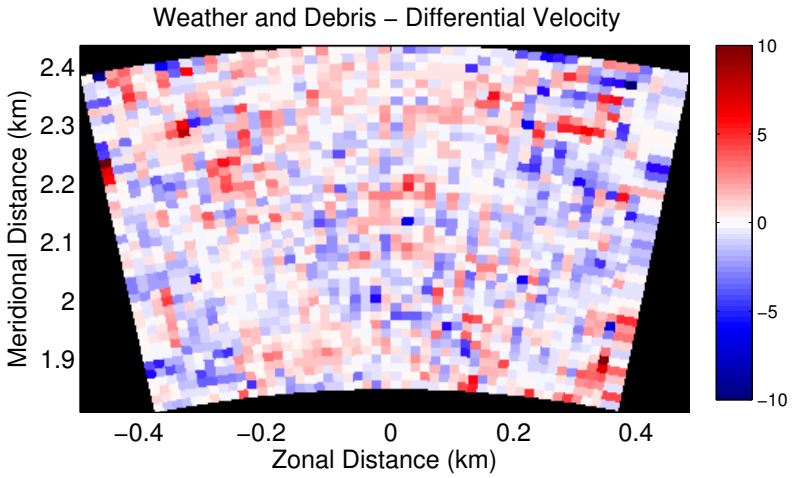

Figure 5.28: PPI plot of differential velocity for weather and debris at elevation $\phi = 3.00°$.

differential velocity for the composite weather-and-debris signal is expected to have a higher dispersion since the radial velocities estimated from either channel are more vulnerable to biases owing to the possibility that one signal could be more dominant than the other for a given polarization, and vice versa. The differential velocity of the weather-and-debris scenario is shown in Figure 5.28. Furthermore, the weather and weather-and-debris cases can be compared closely as they correspond to the same simulation scene, allowing the subtraction of the true wind motion from the

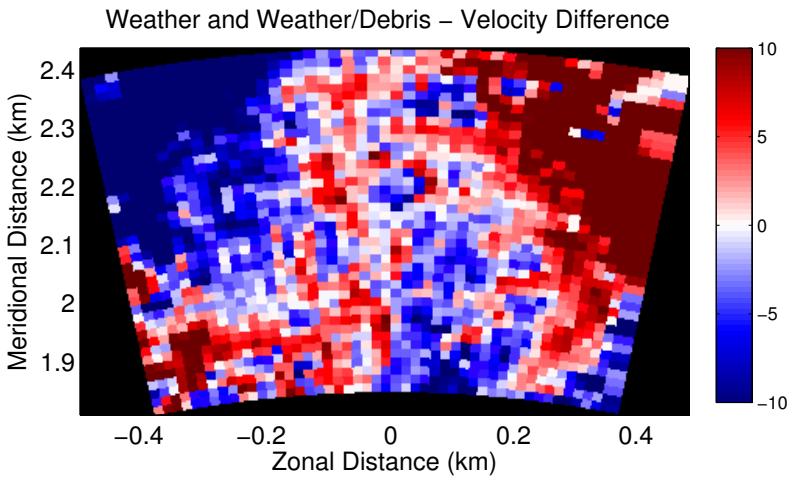

Figure 5.29: PPI plot of difference in mean radial velocities between weather and debris, and weather at elevation $\phi = 3.00°$.

composite case in order to assess the biases introduced by the presence of debris. This difference in velocity (Figure 5.29), i.e., the mean velocity of weather and debris minus the mean velocity of only weather, provides an insight into the measurement bias in the mean radial velocities. A difference close to zero can be interpreted as the wind velocity in the weather-and-debris case following the true wind motion accurately, while a negative difference means the wind motion is underestimated, and a positive difference represents overestimation. In a similar analysis, the difference in velocity between the debris-only case and the composite case is compared in Figure 5.30, where the values close to zero indicate that the radar is likely measuring debris motion rather than wind motion. Upon closer inspection of the northwestern quadrant where the wind motion seems to be underestimated, spectral analysis shows that the spectra is mostly dominated by debris ($\theta = 0.5°$, Figure 5.31a), as the signatures in power are very similar to those of the debris-only case (Figure 5.31b). Clearly, the biases in the mean radial velocities are due to the high-power returns from debris. However, even when the weather signal is dominated to some degree by

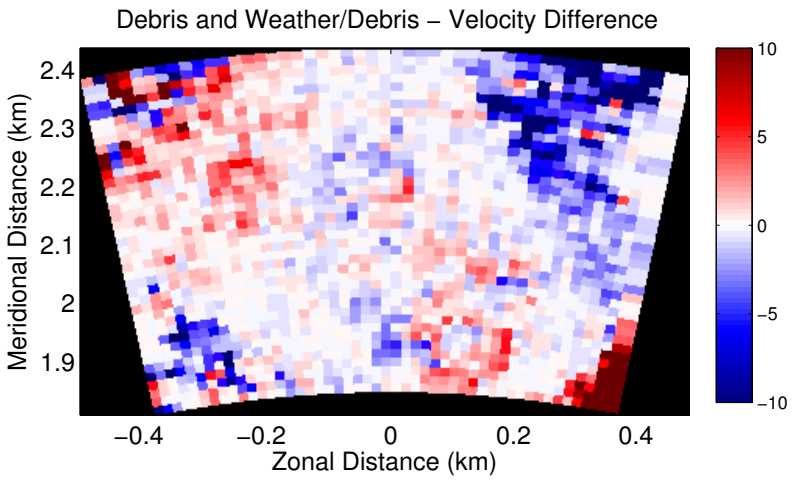

Figure 5.30: PPI plot of difference in mean radial velocities between weather and debris, and debris at elevation $\phi = 3.00°$.

debris, some signatures can be observed in the spectral correlation coefficient. As it was mentioned in Section 4.5, depending on the difference in power of the signals that are mixed in the composite signal, certain features remain possible to be identified. By comparing the range-Doppler plots of the three cases (weather, debris, and weather and debris), it is evident that a line of low $s\rho_{\mathrm{HV}}$ is embedded in the weather-and-debris spectral signature, and it is collocated mostly with the peak of the weather spectral signature (Figure 5.31). Additionally, the decrease in $s\rho_{\mathrm{HV}}$ can be attributed to the individual signals being comparable in power (i.e., within 20 dB of each other), such that none of them are dominant in that particular spectral coefficient, hence decreasing the homogeneity of the scattered signal. Finally, focus is directed to the northeastern quadrant, where the velocity is overestimated. At a radial in the $\theta = 7.5°$ direction, the mixing of both signals is more widespread, and at farther ranges, the debris spectral signatures start diverging more rapidly from the mean wind motion (Figure 5.32). This might be an indication of debris ejection,

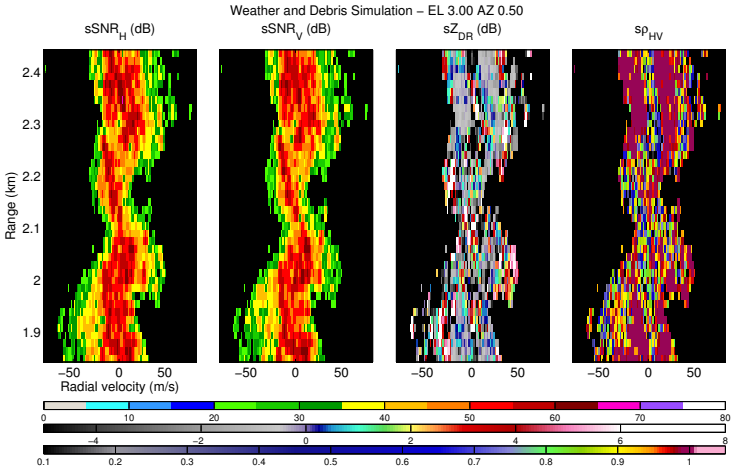

(a)

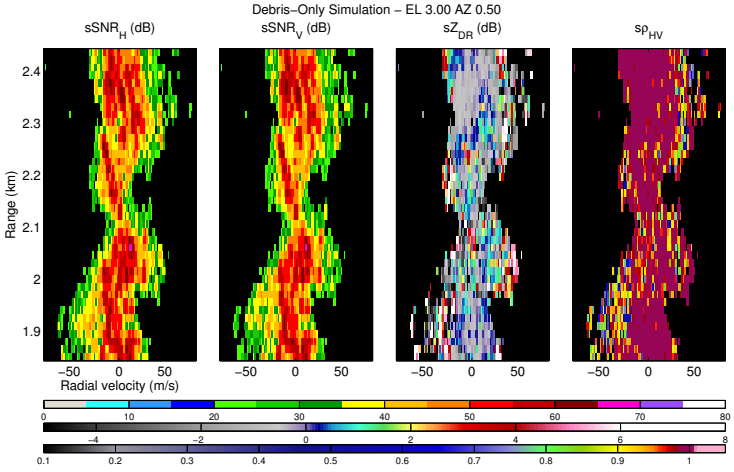

(b)

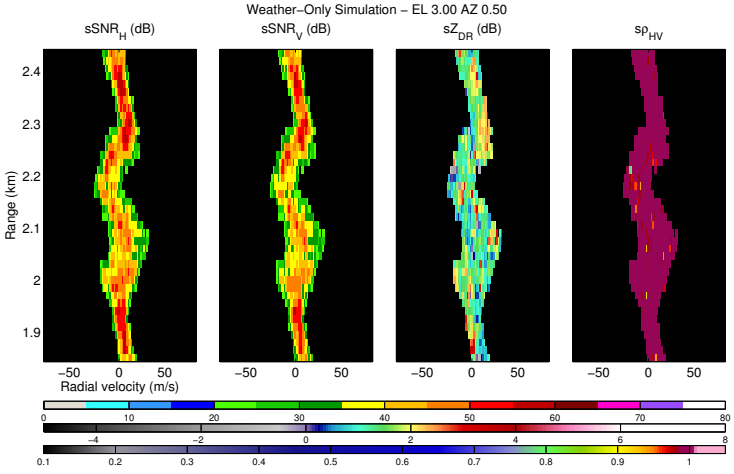

(c)

Figure 5.31: Range-Doppler plots of Bootstrap DPSD estimates at elevation $\phi = 3.00°$, and azimuth $\theta = 0.5°$, for: (a) weather and debris, (b) debris only, and (c) weather only.

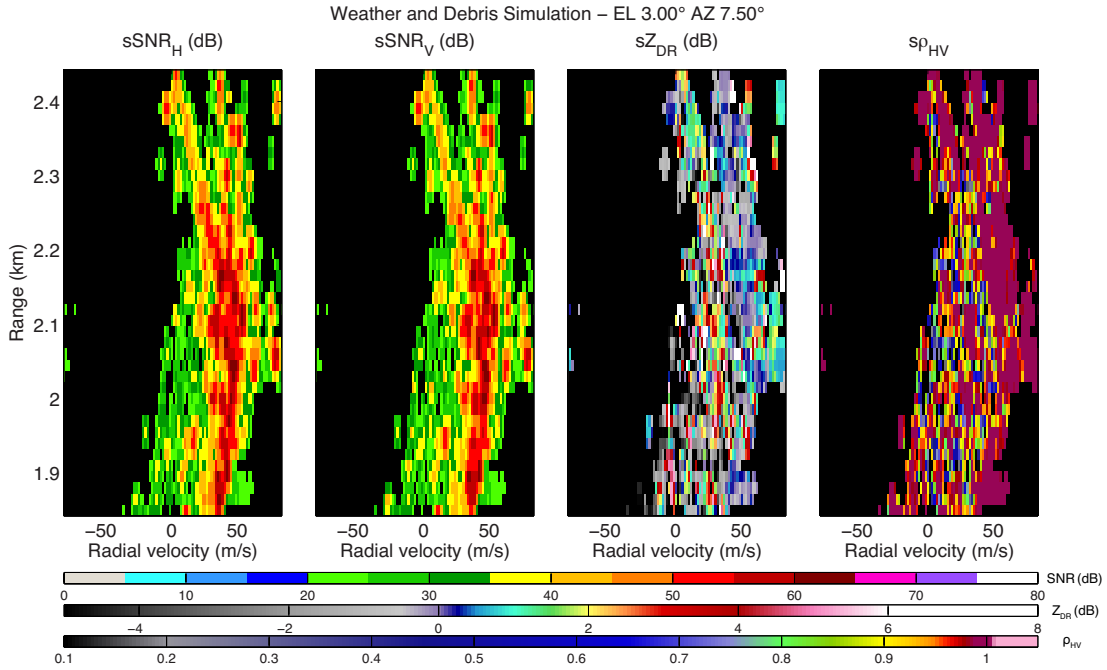

Figure 5.32: Range-Doppler plots of Bootstrap DPSD estimates for weather and debris at elevation $\phi = 3.00°$, and azimuth $\theta = 7.5°$.

since the fastest moving object appears to have a radial velocity close to the maximum radial velocity observed tangential to the vortex. The bulk radar estimates mask the velocities of all underlying groups of scatterers that are depicted in the DPSDs. Through visual analysis and statistical study of the simulation scene, it would be possible to determine the positions, velocities and orientations of the scatterers, in order to validate the results of the polarimetric spectral analysis. However, such study is beyond the scope of this work.

5.3 Summary

The advantages of using the Bootstrap DPSD estimator over conventional DPSD estimators were shown for single- and multiple-dwell cases. Also, it has been demonstrated that spectral signatures and qualitative features of the spectra can be identified with a single dwell estimate, without the resolution losses associated with range-, azimuth-, scan-, or frequency-averaged DPSDs. Polarimetric spectral analysis can unveil additional information masked in bulk estimates, and a few representative spectral signatures have been presented as examples to illustrate this. While a few interpretations for the observations have been provided, a validation of these is beyond the scope of this work. It is deemed appropriate to perform more in-depth studies with the simulator and the Bootstrap DPSD estimator to confirm the hypotheses discussed herein. Such work would entail exploiting many of the advantages provided by such a powerful simulation tool in its many possible configurations, in conjunction with the dual-polarimetric spectral analysis capabilities provided by the Bootstrap DPSD estimator. It is believed that the results of such studies will provide a better understanding of tornado dynamics and its connection to weather radar measurements, as well as to answer the scientific questions that motivated this work. In the next chapter, the conclusion for this work and discussions for future work will be presented.

Chapter 6

Conclusions and Future Work

In this chapter, the conclusions of this work are presented, and a few applications and recommendations for future work using the Bootstrap DPSD estimator are discussed. The primary objective of this work was the development of the Bootstrap DPSD estimator, which is capable of obtaining accurate dual-polarimetric spectral density estimates from a single dwell. A summary of the key aspects of each chapter is provided next. The fundamentals of weather radar signal processing and spectral analysis were presented in Chapter 2, along with a brief description of the TDS and how important weather information could be masked in bulk radar estimates. Typical non-polarimetric spectra were presented to demonstrate cases where the PSD alone would not be sufficient to determine the nature of the scatterers; and a hypothetical depiction of a spectral signature of tornadic debris was used as an example to demonstrate how the DPSDs could reveal additional spectral information that would aid in discriminating groups of scatterers of different nature moving at different radial velocities in a radar volume. The advantages and disadvantages of the periodogram, Bartlett, Welch, and Daniell non-parametric PSD estimation methods were evaluated to be used for DPSD estimation. While Bartlett, Welch, and Daniell PSD estimates can be used to obtain single-dwell DPSD estimates, the periodogram fails to yield useful single-dwell estimates. However, it was shown that

these degrade the frequency resolution considerably. Conventional DPSD estimation methods average in frequency or use PSDs from multiple dwells that are averaged in range, azimuth, scan; however, the resolution in the averaged dimension can get significantly degraded. This preliminary study helped in understanding the context of the problem, and showed the importance of having more accurate DPSD estimates for polarimetric spectral analyses. In Chapter 3, the Bootstrap DPSD estimator was introduced. First, the bootstrap resampling concept was presented, and the different block bootstrapping methods were evaluated taking into account their applicability to weather radar I/Q time-series signals. Next, the design considerations of the Bootstrap DPSD estimator were presented. In this context, a few indicators of the quality of the DPSD estimates, such as spectral leakage, statistical errors, and computational cost, were defined to establish comparison standards for selecting the optimal parameters in the design process of the Bootstrap DPSD estimator. Additionally, signal pre-processing strategies such as signal extension, coherency correction, ratio of original samples and power correction, and post-processing strategies such as the bias correction were explained in detail. In accordance with the quality indicators, performance analyses for the block bootstrap methods as well as for different configurations of the design strategies were conducted to obtain the optimal set of parameters that define the Bootstrap DPSD estimator. Finally, a summary of the algorithm of the Bootstrap DPSD estimator was provided. Chapter 4 began by describing the simulation methodology, and the calculation of the statistical errors. Also, the relationship between bulk and spectral radar variables, and their differences in error dependence was discussed. An analysis of error dependence on

radar acquisition and signal parameters for the ideal estimator was presented, which helped simplify the complexity of subsequent performance analyses. Additionally, the effects in the spectral estimates of the interaction of two signals were briefly explained. These preliminary analyses were important for a better interpretation of the results presented in the following chapter. A statistical error performance of the DPSD estimators was then presented in single-signal single-dwell, single-signal multiple-dwell, and dual-signal analyses, providing an objective evaluation of the advantages and limitations of the Bootstrap DPSD estimator. A few representative examples of the application of the Bootstrap DPSD estimator to real data and data obtained from a physical simulator were presented in Chapter 5. The examples of real data focused more on the differences between the Bootstrap DPSD estimator and conventional DPSD estimators, and on the effects of averaging spectra in different dimensions, while the examples of simulated data focused on information that is masked by the bulk radar estimates, and that can be revealed with polarimetric spectral analyses. These examples featured dual-polarimetric signatures of hydrometeor and non-hydrometeor scatterers in the same radar volume, which demonstrated the ability of the Bootstrap DPSD estimator to identify signals with different spectral characteristics.

From a broader perspective, this work can be summarized as follows. The bulk radar estimates depict useful information about the characteristics and motion of meteorological phenomena, though these measurements are susceptible to biases when the signal of interest is contaminated by other types of scatterers in the radar volume. The dual-polarimetric spectral densities may unveil additional information

for groups of scatterers moving at different Doppler velocities, which can potentially aid in the characterization of distinct scatterer types. Identification of different polarimetric spectral signatures is important for many applications. For example, by discriminating hydrometeors in spectra, it should be possible to obtain more accurate wind velocity measurements, which is very important for tornado intensity and damage potential estimation. Previous estimation methods required averaging $K \geq 20$ spectra to get DPSD estimates of desirable error levels, which could be obtained from different range gates, radials, scans. A smaller number of spectra could be averaged, though the quality of the estimates is usually insufficient for quantitative spectral analyses. Good resolution is required in all dimensions in order to capture important features of meteorological phenomena that evolve relatively fast in time, in a small spatial extent, and with scatterers moving at different velocities within the radar volume (e.g., tornadoes). The Bootstrap DPSD estimator was introduced as a means to compute the DPSDs from a single dwell with minimal resolution loss. It employs the bootstrap resampling concept, which is a useful method to measure statistical properties of estimators when the available sample size is small. Briefly, the estimator pre-processes and then bootstraps the conditioned I/Q time-series signals to obtain I/Q pseudo-realizations, which are in turn used to obtain bootstrapped PSD estimates. The DPSDs are then computed by averaging the bootstrapped estimates, and a bias correction is applied to obtain the final estimates. The pre- and post-processing strategies, as well as the appropriate selection of parameters are at the core in the design of the Bootstrap DPSD estimator. The Bootstrap DPSD estimator shows superior error statistics when compared

to conventional DPSD estimators for single-dwell as well as for multiple-dwell estimates, and it was shown that it meets the performance of the ideal estimator with about half the number of averaged independent spectra. However, the Bootstrap DPSD estimator has a particular limitation in that, by attempting to correct the signal coherency, it could introduce an incoherence that adds a minimal bias into the spectral correlation coefficient estimates. Further analyses of the impacts of this limitation are needed. Additionally, the Bootstrap DPSD estimator shows better performance than the conventional DPSD estimators when discriminating polarimetric signatures of signals corresponding to different groups of scatterers moving at different radial velocities in the radar volume. However, the ideal estimator still outperforms the single-dwell Bootstrap DPSD estimator in the dual-signal analysis. Though a multiple-dwell dual-signal analysis was not conducted, it is expected that the Bootstrap DPSD estimator will have superior performance compared to conventional and the ideal DPSD estimators. The potential of the Bootstrap DPSD estimator was demonstrated with a few representative examples using data from real tornado cases and from a physically-based simulator. It was illustrated in the examples how polarimetric spectral analyses can unveil additional information obscured by bulk estimates. It is expected that spectral analysis can provide more insight to better understand tornado dynamics and their connection to weather radar measurements. However, to validate the observations from a physical point of view and to answer the scientific questions that motivated this work, more in-depth analyses are required. Such studies are beyond the scope of this work and a few recommendations for future work are proposed next.

By identifying the spectral coefficients that correspond to hydrometeors using the DPSDs, it is possible to obtain better estimates of the weather components, and to consequently improve the bulk radar estimates for the signal of interest. A simple spectral-based algorithm would entail thresholding the spectra for components with high SNR (e.g., $s\mathrm{SNR_H} > 20$ and $s\mathrm{SNR_V} > 20$ dB), and to perform a Gaussian fit on the PSD, though algorithms of higher complexity can be implemented. Based on the PSD, multiple Gaussian fits could determine the number of signals in the spectra, their power distribution, mean radial velocities and spectrum widths. The polarimetric characteristics of each signal could be discriminated with the DPSDs, by analyzing the distribution of sZ_{DR} and $s\rho_{\mathrm{HV}}$ that correspond to the spectral coefficients of the fitted curves. Such additional information of the scatterers in a radar resolution volume could be exploited for many different applications. Velocity bias correction should be possible by filtering out the signals that are more likely to be of non-hydrometeor nature, and by recalculating the spectra (if more than one signal is tagged as weather after filtering), or by simply using the fitted curve of the weather signal (if only one signal is left after filtering). Another important application is a spectral-based hydrometeor classification algorithm (HCA). Since evidence of unimodal spectra with different polarimetric characteristics has been found, it is possible to extend the HCA to work with spectral coefficients, as to provide a distribution of hydrometeors for a given radar resolution volume. Moreover, as it was suggested in an example in Chapter 5, the contribution from range-folded echoes may be mitigated from bulk radar estimates, provided that their spectral signature is different. Additionally, the Bootstrap DPSD estimator can be

used to improve already existing analysis techniques. The performance of previous DSD retrieval algorithms using spectral analysis may be improved by using Bootstrap DPSD estimates. Also, clutter mitigation techniques can now be based on the spectral polarimetric variables to more accurately discriminate moving clutter and zero-mean radial velocity weather signals.

Polarimetric spectral signatures that are tagged as coming from non-hydrometeors can be useful in other applications. From a qualitative point of view, the Bootstrap DPSD estimator is an important tool of analysis in quest to answer some of the science questions that motivated this work. As it was presented in Chapter 5, identification of non-hydrometeor scatterers may provide more insight into debris ejection and loading dynamics, as well as for common alignment of debris in tornadic flows. Such hypotheses can be validated by cross-referencing the polarimetric spectral signatures obtained with the Bootstrap DPSD, with visual outputs and statistical studies of the positions, velocities and orientations of the debris particles in the physically-simulated scene. Additionally, the connection between different physical and electrical debris characteristics with radar variables can be tested and characterized. This includes the dependence of spectral differential reflectivity, spectral correlation coefficient, and differential velocity with different debris characteristics, including size, shape, material, concentration, orientation, etc. Also, hypotheses about the differences in radar data (both bulk and spectral estimates) for different radar wavelengths can also be validated with the aid of the physically-based simulator.

While the bootstrap term derives from the phrase: "to pull oneself up from one's bootstrap", the Bootstrap DPSD estimator is not magical. The general idea of the estimator is that it rearranges its limited, yet available data, in a way that additional information (which is otherwise lost with other estimators) can be extracted. It is expected that weather radar researchers could use this work to gain some insight into the interpretation of polarimetric spectral signatures. Additionally, further work to improve the current state of the Bootstrap DPSD estimator, and the understanding of spectral polarimetry, in general, is encouraged.

Bibliography

Alku, L., Moisseev, D. N., Aittomäki, T. and Chandrasekar, V. (2015), 'Identification and Suppression of Nonmeteorological Echoes Using Spectral Polarimetric Processing', *IEEE Transactions on Geoscience and Remote Sensing* **53**(7), 3628–3638.

Bachmann, S. M. and Zrnić, D. S. (2007), 'Spectral Density of Polarimetric Variables Separating Biological Scatterers in the VAD Display', *Journal of Atmospheric and Oceanic Technology* **24**(7), 1186–1198.

Barbé, K., Pintelon, R. and Schoukens, J. (2010), 'Welch Method Revisited: Nonparametric Power Spectrum Estimation Via Circular Overlap', *IEEE Transactions on Signal Processing* **58**(2), 553–565.

Bartlett, M. S. (1950), 'Periodogram Analysis and Continuous Spectra', *Biometrika* **37**(1), 1–16.

Bluestein, H. B., French, M. M., Tanamachi, R. L., Frasier, S., Hardwick, K., Junyent, F. and Pazmany, A. L. (2007), 'Close-Range Observations of Tornadoes in Supercells Made with a Dual-Polarization, X-Band, Mobile Doppler Radar', *Monthly Weather Review* **135**(4), 1522–1543.

Bodine, D. J. (2014), Polarimetric Radar Observations and Numerical Simulations of Tornadic Debris, PhD thesis, School of Meteorology, University of Oklahoma, 264 pp.

Bodine, D. J., Kumjian, M. R., Palmer, R. D., Heinselman, P. L. and Ryzhkov, A. V. (2013), 'Tornado Damage Estimation Using Polarimetric Radar', *Weather and Forecasting* **28**, 139–158.

Bodine, D. J., Kumjian, M. R., Smith, A. J., Palmer, R. D., Ryzhkov, A. V. and Heinselman, P. L. (2011), High Resolution Polarimetric Observations of an EF-4 Tornado on 10 May 2010 from OU-PRIME, *in* '35th Conference on Radar Meteorology', American Meteororological Society, Pittsburgh, PA.

Bodine, D. J., Palmer, R. D. and Zhang, G. (2014), 'Dual-Wavelength Polarimetric Radar Analyses of Tornadic Debris Signatures', *Journal of Applied Meteorology and Climatology* **53**, 242–261.

Bohonos, J. J. and Hogan, D. E. (1999), 'The Medical Impact of Tornadoes in North America', *Journal of Emergency Medicine* **17**(1), 67–73.

Borowska, L., Zhang, G. and Zrnić, D. S. (2016), 'Spectral Processing for Step Scanning Phased-Array Radars', *IEEE Transactions on Geoscience and Remote Sensing* **54**(8), 4534–4543.

Breiman, L. (1996), 'Bagging Predictors', *Machine Learning* **24**, 123–140.

Bringi, V. N. and Chandrasekar, V. (2001), *Polarimetric Doppler Weather Radar: Principles and Applications*, Cambridge University Press.

Bringi, V. N. and Seliga, T. A. (1977), 'Scattering from Non-Spherical Hydrometeors', *Annales des Télécommunications* **32**(11-12), 392–397.

Brown, R. A., Lemon, L. R. and Burgess, D. W. (1978), 'Tornado Detection by Pulsed Doppler Radar', *Monthly Weather Review* **106**(1), 29–38.

Cao, Q., Zhang, G., Palmer, R. D., Knight, M., May, R. and Stafford, R. J. (2012), 'Spectrum-Time Estimation and Processing (STEP) for Improving Weather Radar Data Quality', *IEEE Transactions on Geoscience and Remote Sensing* **50**(11), 4670–4683.

Carlstein, E. (1986), 'The Use of Subseries Values for Estimating the Variance of a General Statistic from a Stationary Sequence', *The Annals of Statistics* **14**, 1171–1179.

Cheong, B. L., Bodine, D. J., Zhu, Y., Fulton, C. J., Torres, S. M., Maruyama, T. and Palmer, R. D. (2015), Understanding Tornadic Debris Echoes using a Radar Time-Series Emulator, *in* 'IEEE Radar Conference (RadarCon)', IEEE, pp. 0912–0917.

Cheong, B. L., Kelley, R., Palmer, R. D., Zhang, Y., Yeary, M. B. and Yu, T.-Y. (2013), 'PX-1000: A Solid-State Polarimetric X-Band Weather Radar and Time-Frequency Multiplexed Waveform for Blind Range Mitigation', *IEEE Transactions on Instrumentation and Measurement* **62**(11), 3064–3072.

Crum, T. D. and Alberty, R. L. (1993), 'The WSR-88D and the WSR-88D Operational Support Facility', *Bulletin of the American Meteorological Society* **74**(9), 1669–1687.

Daniell, P. J. (1946), 'Discussion on Symposium on Autocorrelation in Time Series', *Supplement to Journal of the Royal Statistical Society* **8**, 88–90.

Doviak, R. J., Bringi, V. N., Ryzhkov, A. V., Zahrai, A. and Zrnić, D. S. (2000), 'Considerations for Polarimetric Upgrades to Operational WSR-88D Radars', *Journal of Atmospheric and Oceanic Technology* **17**(3), 257–278.

Doviak, R. J. and Zrnić, D. S. (2006), *Doppler Radar and Weather Observations*, 2nd edn, Dover Publications.

Dowell, D. C., Alexander, C. R., Wurman, J. M. and Wicker, L. J. (2005), 'Centrifuging of Hydrometeors and Debris in Tornadoes: Radar-Reflectivity Patterns and Wind-Measurement Errors', *Monthly Weather Review* **133**(6), 1501–1524.

Dufournet, Y. (2010), Ice Crystal Properties Retrieval Using Radar Spectral Polarimetric Measurements Within Ice/Mixed-Phase Clouds, PhD thesis, Delft University of Technology.

Efron, B. (1979), 'Bootstrap Methods: Another Look at the Jackknife', *Annals of Statistics* **7**(1), 1–26.

Efron, B. and Tibshirani, R. J. (1994), *An Introduction to the Bootstrap*, CRC press.

Fang, M., Doviak, R. J. and Melnikov, V. M. (2004), 'Spectrum Width Measured by WSR-88D: Error Sources and Statistics of Various Weather Phenomena', *Journal of Atmospheric and Oceanic Technology* **21**(6), 888–904.

Galati, G. and Pavan, G. (1995), 'Computer Simulation of Weather Radar Signals', *Simulation Practice and Theory* **3**(1), 17–44.

Hall, P. (1992), *The Bootstrap and Edgeworth Expansion*, Springer Science & Business Media.

Harris, F. J. (1978), 'On the Use of Windows for Harmonic Analysis with the Discrete Fourier Transform', *Proceedings of the IEEE* **66**(1), 51–83.

Hayes, M. H. (1996), *Statistical Digital Signal Processing and Modeling*, John Wiley & Sons.

Janssen, L. H. and Van Der Spek, G. A. (1985), 'The Shape of Doppler Spectra from Precipitation', *IEEE Transactions on Aerospace and Electronic Systems* **AES-21**(2), 208–219.

Kingfield, D. M. and LaDue, J. G. (2015), 'The Relationship between Automated Low-Level Velocity Calculations from the WSR-88D and Maximum Tornado Intensity Determined from Damage Surveys', *Weather and Forecasting* **30**(5), 1125–1139.

Kumjian, M. R. (2013), 'Principles and Applications of Dual-Polarization Weather Radar. Part I: Description of the Polarimetric Radar Variables', *Electronic Journal of Operational Meteorology* **1**(19), 226–242.

Kumjian, M. R. and Ryzhkov, A. V. (2008), 'Polarimetric Signatures in Supercell Thunderstorms', *Journal of Applied Meteorology and Climatology* **47**(7), 1940–1961.

Künsch, H. R. (1989), 'The Jackknife and the Bootstrap for General Stationary Observations', *The Annals of Statistics* **17**(3), 1217–1241.

Kurdzo, J. M., Bodine, D. J., Cheong, B. L. and Palmer, R. D. (2015), 'High-Temporal Resolution Polarimetric X-band Doppler Radar Observations of the 20 May 2013 Moore, Oklahoma Tornado', *Monthly Weather Review* **143**(7), 2711–2735.

Lahiri, S. N. (2003), *Resampling Methods for Dependent Data*, Springer Science & Business Media.

Liu, R. Y. and Singh, K. (1992), Moving Blocks Jackknife and Bootstrap Capture Weak Dependence, *in* R. LePage and Y. Billard, eds, 'Exploring the Limits of Bootstrap', Wiley, New York, pp. 225–248.

Marchand, R., Beagley, N., Thompson, S. E., Ackerman, T. P. and Schultz, D. M. (2006), 'A Bootstrap Technique for Testing the Relationship between Local-Scale Radar Observations of Cloud Occurrence and Large-Scale Atmospheric Fields', *Journal of the Atmospheric Sciences* **63**(11), 2813–2830.

Marshall, T. P. (2002), 'Tornado Damage Survey at Moore, Oklahoma', *Weather and Forecasting* **17**(3), 582–598.

Maruyama, T. and Noda, M. (2012), 'Tornado-Borne Debris', *Journal of Applied Wind Engineering* **37**, 124–129.

Melnikov, V. M. and Zrnić, D. S. (2004), 'Simultaneous Transmission Mode for the Polarimetric WSR-88D: Statistical Biases and Standard Deviations of Polarimetric Variables', *NOAA/NSSL Report* pp. 1–84.

Meymaris, G., Williams, J. K. and Hubbert, J. C. (2009), Performance of a Proposed Hybrid Spectrum Width Estimator for the NEXRAD ORDA, *in* '25th Conference on International Interactive Information and Processing Systems for Meteorology, Oceanography and Hydrology', American Meteororological Society, Phoenix, AZ.

Moisseev, D. N. and Chandrasekar, V. (2007), 'Nonparametric Estimation of Raindrop Size Distributions from Dual-Polarization Radar Spectral Observations', *Journal of Atmospheric and Oceanic Technology* **24**(6), 1008–1018.

Moisseev, D. N. and Chandrasekar, V. (2009), 'Polarimetric Spectral Filter for Adaptive Clutter and Noise Suppression', *Journal of Atmospheric and Oceanic Technology* **26**(2), 215–228.

Moisseev, D. N., Chandrasekar, V., Unal, C. M. H. and Russchenberg, H. W. J. (2006), 'Dual-Polarization Spectral Analysis for Retrieval of Effective Raindrop Shapes', *Journal of Atmospheric and Oceanic Technology* **23**(12), 1682–1695.

NCDC (2014), Summary of Natural Hazard Statistics for 2013 in the United States, Technical report, NWS Office of Climate, Water and Weather Services.
URL: *http://www.nws.noaa.gov/om/hazstats/sum13.pdf*

NWS Weather Forecast Office Norman, O. (2010), 'Information About the May 10, 2010 Tornado Outbreak in Oklahoma'.
URL: *http://www.srh.noaa.gov/oun/?n=events-20100510*

NWS Weather Forecast Office Norman, O. (2013), 'The Tornado Outbreak of May 20, 2013'.
URL: *http://www.srh.noaa.gov/oun/?n=events-20130520*

Overeem, A., Buishand, T. A. and Holleman, I. (2009), 'Extreme Rainfall Analysis and Estimation of Depth-Duration-Frequency Curves using Weather Radar', *Water Resources Research* **45**(10), 1–15.

Palmer, R. D., Bodine, D. J., Kumjian, M. R., Cheong, B. L., Zhang, G., Cao, Q., Bluestein, H. B., Ryzhkov, A. V., Yu, T.-Y. and Wang, Y. (2011), 'Observations of the 10 May 2010 Tornado Outbreak using OU-PRIME: Potential for New Science with High-Resolution Polarimetric Radar', *Bulletin of the American Meteorological Society* **92**(7), 871–891.

Papoulis, A. and Pillai, S. U. (2002), *Probability, Random Variables, and Stochastic Processes*, McGraw-Hill.

Politis, D. N. and Romano, J. P. (1994), 'The Stationary Bootstrap', *Journal of the American Statistical Association* **89**(428), 1303–1313.

Richards, P. J. (2012), 'Dispersion of Windborne Debris', *Journal of Wind Engineering and Industrial Aerodynamics* **104**, 594–602.

Ryzhkov, A. V., Burgess, D. W., Zrnić, D. S., Smith, T. and Giangrande, S. E. (2002), Polarimetric Analysis of a 3 May 1999 Tornado, *in* 'Preprints, 21st Conference on Severe Local Storms', American Meteororological Society, vol. 14, San Antonio, TX.

Ryzhkov, A. V., Schuur, T. J., Burgess, D. W. and Zrnić, D. S. (2005), 'Polarimetric Tornado Detection', *Journal of Applied Meteorology* **44**(5), 557–570.

Scharfenberg, K. A., Miller, D. J., Schuur, T. J., Schlatter, P. T., Giangrande, S. E., Melnikov, V. M., Burgess, D. W., Andra, D. L., Foster, M. P. and Krause, J. M. (2005), 'The Joint Polarization Experiment: Polarimetric Radar in Forecasting and Warning Decision Making', *Weather and Forecasting* **20**(5), 775–788.

Schultz, C. J., Carey, L. D., Schultz, E. V., Carcione, B. C., Darden, C. B., Crowe, C. C. and Knupp, K. R. (2012*a*), 'Dual-Polarization Tornadic Debris Signatures Part I: Examples and Utility in an Operational Setting', *Electronic Journal Of Operational Meteorology* **13**, 120–137.

Schultz, C. J., Carey, L. D., Schultz, E. V., Carcione, B. C., Darden, C. B., Crowe, C. C. and Knupp, K. R. (2012*b*), 'Dual-Polarization Tornadic Debris Signatures Part II: Comparisons and Caveats', *Electronic Journal of Operational Meteorology* **13**, 138–150.

Spek, A. L. J., Unal, C. M. H., Moisseev, D. N., Russchenberg, H. W. J., Chandrasekar, V. and Dufournet, Y. (2008), 'A New Technique to Categorize and Retrieve the Microphysical Properties of Ice Particles above the Melting Layer Using Radar Dual-Polarization Spectral Analysis', *Journal of Atmospheric and Oceanic Technology* **25**(3), 482–497.

Stoica, P. and Moses, R. L. (1997), *Introduction to Spectral Analysis*, Prentice Hall, Upper Saddle River, New Jersey.

Thomson, D. J. (1982), 'Spectrum Estimation and Harmonic Analysis', *Proc. IEEE* **70**, 1055–1096.

Torres, S. M. and Curtis, C. D. (2006), Design Considerations for Improved Tornado Detection using Super-Resolution Data on the NEXRAD Network, *in* 'Preprints, Third European Conference on Radar Meteorology and Hydrology (ERAD)', Copernicus, Barcelona, Spain.

Torres, S. M. and Warde, D. A. (2014), 'Ground Clutter Mitigation for Weather Radars Using the Autocorrelation Spectral Density', *Journal of Atmospheric and Oceanic Technology* **31**(10), 2049–2066.

Torres, S. M. and Zrnić, D. S. (1999), 'Ground Clutter Canceling with a Regression Filter', *Journal of Atmospheric and Oceanic Technology* **16**(10), 1364–1372.

Torres, S. M. and Zrnić, D. S. (2003), 'Whitening of Signals in Range to Improve Estimates of Polarimetric Variables', *Journal of Atmospheric and Oceanic Technology* **20**(12), 1776–1789.

Unal, C. M. H. (2009), 'Spectral Polarimetric Radar Clutter Suppression to Enhance Atmospheric Echoes', *Journal of Atmospheric and Oceanic Technology* **26**(9), 1781–1797.

Varian, H. (2005), 'Bootstrap Tutorial', *Mathematica Journal* **9**(4), 768–775.

Wang, Y. and Yu, T.-Y. (2015), 'Novel Tornado Detection Using an Adaptive Neuro-Fuzzy System with S-Band Polarimetric Weather Radar', *Journal of Atmospheric and Oceanic Technology* **32**(2), 195–208.

Welch, P. D. (1967), 'The Use of Fast Fourier Transform for the Estimation of Power Spectra: A Method Based on Time Averaging Over Short, Modified Periodograms', *IEEE Transactions on Audio and Electroacoustics* **15**(2), 70–73.

Yanovsky, F. J. (2011), Inferring Microstructure and Turbulence Properties in Rain Through Observations and Simulations of Signal Spectra Measured with Doppler-Polarimetric Radars, *in* M. I. Mishchenko, Y. S. Yatskiv, V. K. Rosenbush and G. Videen, eds, 'Polarimetric Detection, Characterization, and Remote Sensing', Springer, pp. 501–542.

Yu, T.-Y., Le, H., Wang, Y., Ryzhkov, A. V. and Kumjian, M. R. (2013), Application of Spectral Polarimetry to a Hailstorm at Low Elevation Angle, *in* '36th Conference on Radar Meteorology', American Meteororological Society, Breckenridge, CO.

Yu, T.-Y., Rondinel, R. R. and Palmer, R. D. (2009), 'Investigation of Non-Gaussian Doppler Spectra Observed by Weather Radar in a Tornadic Supercell', *Journal of Atmospheric and Oceanic Technology* **26**(3), 444–461.

Yu, T.-Y., Xiao, X. and Wang, Y. (2012), 'Statistical Quality of Spectral Polarimetric Variables for Weather Radar', *Journal of Atmospheric and Oceanic Technology* **29**(9), 1221–1235.

Zoubir, A. M. and Iskander, R. D. (2004), *Bootstrap Techniques for Signal Processing*, Cambridge University Press.

Zrnić, D. S. (1975), 'Simulation of Weatherlike Doppler Spectra and Signals', *Journal of Applied Meteorology* **14**(4), 619–620.

Zrnić, D. S. and Doviak, R. J. (1975), 'Velocity Spectra of Vortices Scanned with a Pulse-Doppler Radar', *Journal of Applied Meteorology* **14**(8), 1531–1539.